UNIVERSITÉ DU QUÉBEC À TROIS-RIVIÈRES

NOUVEAUX LIGANDS À BASE DE BENZÈNE, TRIPHÉNYLÈNE ET AZACORONÈNE POUR LA CHIMIE DE COORDINATION

NOVEL BENZENE, TRIPHENYLENE AND AZACORONENE-BASED LIGANDS FOR COORDINATION CHEMISTRY

THÈSE PRÉSENTÉE

COMME EXIGENCE PARTIELLE DU

DOCTORAT EN SCIENCES DE L'ÉNERGIE ET DES MATÉRIAUX

PAR

ALBORZ BAVANDSAVADKOUHI

AOÛT 2025

UNIVERSITÉ DU QUÉBEC À TROIS-RIVIÈRES

DOCTORAT EN SCIENCES DE L'ÉNERGIE ET DES MATÉRIAUX (PH. D.)

Direction de recherche :

Professeur Benoit Daoust	Directeur de recherche

Jury d'évaluation de la thèse :

Professeur Benoit Daoust	Directeur de recherche
Professeur François Brouillette	Président de jury
Professeur Thomas Auvray	Évaluateur interne
Professeur Jonathan Gagnon	Évaluateur

Acknowledgment

This work would not have been possible without the support, guidance, and encouragement of many individuals. I am deeply grateful to those who have helped me throughout this journey, as well as the professors who inspired me during my bachelor's and master's studies, shaping my academic path and motivating me to pursue higher education.

First and foremost, I extend my deepest gratitude to my PhD supervisor, professor Benoit Daoust, for his invaluable guidance, patience, kindness, and continuous support throughout my PhD. His expertise and encouragement have played a crucial role in shaping my research and academic development. I am also grateful for his motivation and for helping me learn French.

I would also like to sincerely thank professor Mihaela Cibian for her kindness, knowledge, and unwavering support, as well as professor Adam Duong for his assistance in my academic progression.

I would like to express my profound gratitude to the dean of research, Mr Jean-François Millaire, for his invaluable support, leadership, and dedication, which have greatly contributed to my academic journey.

I would like to express my sincere gratitude to Mrs. Catarina Leote Franco Pio for her kindness, support, and invaluable advice throughout my PhD.

I am especially grateful to professor Hooshang Vahedi, my master's supervisor, with whom I started my research journey. I deeply appreciate his knowledge, help, kindness, and encouragement, which played a significant role in motivating me to continue my studies.

I also want to acknowledge professor Mohammad Hasan Ganji, my father's professor, a true legend who encouraged me to continue my studies and inspired me with his unique character.

I extend my appreciation to professor Marc Beauregard, professor Phuong Nguyen-Tri, Mr. Jocelyn Bouchard, Mr. Jean-Philippe Marineau, Mr. Francis Lafontaine, professor Simon Ricard, professor Thierry Maris Mrs. Anick Hamel, Mrs. Anik Surprenant, Mr. Raphaël Gervais Lavoie, Mrs. Marie-Ève Marchand-Lamarche, and Mr. Benjamin Angers for their support.

I am also grateful to the jury members, professor François Brouillette, professor Jonathan Gagnon, and professor Thomas Auvray, for their time and valuable feedback.

A special thanks to my colleagues and friends: Dr. Love Karan, Dr. Mohamed Essalhi, Mr. Heriniaina Randriamiharisoa, Dr. Erman Eloge Nzaba Madila, Dr. Sanil Rajak and Mr. Tuan Doan, for their support and collaboration throughout this journey.

I humbly dedicate this thesis to the soul of my parents, whose love, sacrifices, and guidance have been the foundation of my journey. Their unwavering belief in me continues to inspire my path, and this work is a tribute to their memory, values, and the dreams they nurtured within me.

I also extend my deepest gratitude to my beloved sisters, Negin and Mahsa, for their support throughout this journey.

Résumé

Les structures métallo-organiques (MOF) font partie des matériaux les plus prometteurs, avec de nombreuses applications dans les domaines de la science des matériaux et de l'énergie. Elles sont composées de nœuds métalliques et de liants organiques, qui sont reliés entre eux par des liaisons de coordination. Ces deux composants jouent un rôle essentiel dans la détermination des propriétés du MOF final.

Les liants organiques, en particulier, se composent de deux parties clés: le noyau et les motifs de coordination. Ces deux éléments influencent considérablement les propriétés du MOF obtenu. Dans cette recherche, nous avons conçu et synthétisé de nouveaux liants organiques avec des noyaux aromatiques tels que le benzène, le triphénylène et les azacoronènes, en utilisant des méthodes simples. Les systèmes aromatiques et les systèmes conjugués sont connus pour améliorer la stabilité et les propriétés optiques des MOF finaux. De plus, nous avons incorporé une variété de motifs de coordination qui sont célèbres dans les réactions de coordination, notamment la diamino triazine, la carboxypyridine, l'acide carboxylique, l'amidepyridine et la cyanopyridine. Ces motifs étaient attachés symétriquement au noyau, améliorant la probabilité de formation réussie du MOF.

Dans ce projet, nous avons exploré différents isomères des motifs de coordination. Cette approche visait à mettre en évidence l'influence significative du positionnement des hétéroatomes, non seulement sur les réactions de coordination mais aussi sur les propriétés des composés résultants.

Ces lieurs organiques ont été caractérisés à l'aide de diverses techniques, notamment la spectroscopie UV-Vis, la RMN, l'IR et la SC-DRX. Les interactions intermoléculaires et intramoléculaires des lieurs organiques ont été évaluées par liaison hydrogène et analyse de surface de Hirshfeld à l'état solide. Les résultats ont révélé que la position des motifs de coordination et la

nature de leurs hétéroatomes jouent un rôle crucial dans ces interactions. Les spectres UV-Vis ont montré des décalages vers le rouge, attribués aux systèmes de conjugaison étendus des composés. De plus, l'analyse thermogravimétrique (ATG) a démontré la grande stabilité thermique de ces composés aromatiques.

Pour les réactions de coordination, nous avons sélectionné des composés avec des groupes fonctionnels et des isomères spécifiques qui ont démontré un potentiel élevé de formation de liaison de coordination. Grâce à de multiples tentatives de synthèse, nous avons réussi à synthétiser un complexe à base de diaminotriazine. Ce dimère comprend deux ligands diaminotriazine, deux groupes hydroxyles, quatre ions formiate et quatre ions zinc. Le complexe présentait un réseau de liaisons hydrogène fortes et faibles et démontrait une excellente stabilité thermique, résistant à des températures allant jusqu'à 341 °C.

De plus, au cours de ces réactions de coordination, nous avons observé qu'une oxydation pouvait se produire, conduisant à l'hydrolyse du groupe cyano en groupe amide et à la conversion du méthanol en formate.

Mots-clés : [MOF, le benzène, le triphenylene, l'azacoronène, la diamino triazine, la carboxypyridine, l'amidepyridine et la cyanopyridine, ion zinc, and le complexe]

Abstract

Metal-Organic Frameworks (MOFs) are among the most promising materials, with extensive applications in material science and energy. They are composed of metal nodes and organic linkers, which are connected to each other through coordination bonds. Both components play a critical role in determining the properties of the final MOF.

Organic linkers, in particular, consist of two key parts: the core and the coordination motifs. Both these elements significantly influence the properties of the resulting MOF. In this research, we designed and synthesized new organic linkers with aromatic cores such as benzene, triphenylene, and azacoronenes. Aromatic systems and conjugated systems are known to enhance the stability and optical properties of the final MOFs. Additionally, we incorporated a variety of coordination motifs, including diaminotriazine, carboxypyridine, carboxylic acid, amidepyridine, and cyanopyridine. These motifs are widely used in coordination reactions and contribute to the formation of stable coordination compounds.

To maximize the potential for obtaining MOFs or coordination polymers, we symmetrically attached these organic motifs to the aromatic cores. This symmetry improves the likelihood of successful MOF formation.

In this project, we added three isomers of cyanopyridine, three isomers of amide pyridine, two isomers of carboxypyridine, one isomer of carboxylate pyridine, and one isomer of diaminotriazine to benzene cores. Additionally, we incorporated four isomers of cyanopyridine on triphenylene cores and attached methyl benzoate to an azacoronene core. By adding different isomers, we aimed to demonstrate that the position of heteroatoms plays a crucial role not only in coordination reactions but also in influencing the properties of the resulting compounds. Additionally, by

introducing various functional groups, we showcased the importance of different coordination motifs.

It is noticeable that all compounds were purified using simple methods, avoiding the need for column chromatography. The purification process involved washing with solvents followed by filtration.

These organic linkers have been characterized and investigated using various techniques, including UV-Vis spectroscopy, NMR, IR, and single-crystal X-ray diffraction (SC-XRD). To gain deeper insight into the intermolecular and intramolecular interactions of the organic linkers, hydrogen bonding analysis and Hirshfeld surface studies were conducted in the solid state. The results revealed that the position of coordination motifs and the nature of their heteroatoms play a crucial role in these interactions. The UV-Vis spectra exhibited red shifts, attributed to the extended conjugation systems of the compounds. Additionally, thermogravimetric analysis (TGA) demonstrated the high thermal stability of these aromatic compounds.

For coordination reactions, we selected compounds with specific functional groups and isomers that exhibited a high potential to form MOFs. Several attempts were made to synthesize MOFs, ultimately leading to the formation of a diaminotriazine-based complex. In this process, we highlighted the critical role of solvents, which actively participate in the coordination process.

The resulting complex is a dimer composed of two diaminotriazine ligands, two hydroxyl groups, four formate ions, and four zinc ions serving as the metal nodes. In the solid state, the complex displayed various strong and weak hydrogen bonds and demonstrated high thermal stability, withstanding temperatures up to 341 °C. Furthermore, during these coordination reactions, we

observed that oxidation could occur, leading to the hydrolysis of the cyano group into an amide group and the conversion of methanol into formate.

Key words: [MOF, complex, Benzene, triphenylene, azacoronene, diaminotriazine, amide pyridine, cyanopyridine, carboxypyridine, coordination, and Zn ion]

Table of contents

Acknowledgment ..... **I**

List of figures ..... **XIV**

List of schemes ..... **XXI**

List of abbreviations ..... **XXIII**

1.1 The global energy consumption **2**

1.2 Problem: Fossil fuels and their effect on the environment **2**

1.3 Possible solutions: Renewable energy resources **3**

1.3.1 Metal-organic frameworks (MOFs) and complexes for energy applications **5**

1.3.1.1 Organic linker 6

1.4 The objective of my project: synthesis and characterization new organic linkers for coordination reaction and the development of metal-organic frameworks (MOFs) **8**

2.1 Benzene core ligands **10**

2.1.1 Benzene-1,4- dicarboxylic acid (BDC) (2) **11**

2.1.1.1 Synthesis 11

2.1.1.2 Coordination 13

2.1.2 2,5-Dihydroxyterephthalic acid (10) **17**

2.1.2.1 Synthesis 17

2.1.2.2 Coordination 19

2.1.3 1,3,5-Benzenetricarboxylic acid (BTC) (18) **20**

2.1.3.1 Synthesis 21

2.1.3.2 Coordination 22

2.1.4 4,4'-Dicarboxydiphenyl ether 25 ..... **24**

2.1.4.1 Synthesis 25

2.1.4.2 Coordination 25

2.1.5 4,4′,4′′-[1,3,5-Benzenetriyltris(oxy)]tris[benzoic acid] (H_3TCPB) (34) 28
2.1.5.1 Synthesis 29
2.1.5.2 Coordination 29
2.2 Triphenylene core ligands 32
2.2.1 2,3,6,7,10,11-Hexathioltriphenylene (THT) (42) 33
2.2.1.1 Synthesis 34
2.2.1.2 Coordination 35
2.2.2 2,3,6,7,10,11-hexahydroxytriphenylene (HHTP) (49) 36
2.2.2.1 Synthesis 37
2.2.2.2 Coordination 38
2.2.3 Triphenylene-2,6,10-tricarboxylic acid (H_3TTCA) (52) 40
2.2.3.1 Synthesis 40
2.2.3.2 Coordination 41
2.3 Coronene core ligands 43
2.3.1 1,2,3,4,5,6,7,8,9,10,11,12-Perthiolated coronene (PTC) (61) 44
2.3.1.1 Synthesis 45
2.3.1.2 Coordination 46
2.3.2 Hexahydroxy triazacoronene (6OH-TAC) (69) 49
2.3.2.1 Synthesis 49
2.3.2.2 Coordination 50
2.4 Coordination motifs 50
2.4.1 Cyanopyridine-based coordination motifs (73-75) 51
2.4.2 Pyridine carboxamide-based coordination motifs (87-89) 54
2.4.3 Pyridine carboxylic acid-based coordination motifs 57
2.4.4 [1,3,5] Triazine-2,4-diamine-based coordination motifs (119) 60
2.5 Conclusion 63
3.1 Introduction 65

3.2 Compounds 131, 132, 133, 134, 135, 136, 137, 139, and 141 67

3.2.1 Synthesis 67

3.2.1.1 Neocleophilic substitution reaction 67

3.2.1.2 Hydrolysis of cyanopyridines 68

3.2.2 Results and discussion 70

3.2.2.1 Comparison of 131-133 70

3.2.2.2 Comparison of 134-136 73

3.2.2.3 Comparison of 137, 141, and 139 75

3.2.2.4 Comparison of the ^{1}H NMR Spectra of Compounds **131**, **134**, and **137** 77

3.2.2.5 Comparison of IR in **131**, **132**, **133**, **134**, **135**, **136**, **137**, **139**, and **141** (cyano, amide, and carboxylic acid) 78

3.2.2.6 Single Crystal X-ray Diffraction (SCXRD) of 131, 132, 134, and 137 79

3.2.2.7 UV 83

3.2.2.8 TGA 85

3.2.2.9 Fluorescence 87

3.2.2.10 Hydrogen bond simulation of 131, 132, 134, and 137 90

3.2.2.11 Hirshfeld surface analysis of 131, 132, 134, and 137 93

3.3 Compound 145 97

3.3.1 Synthesis of compound 145 97

3.3.2 Result and discussion 98

3.3.2.1 NMR and IR of compound 145 98

3.3.2.2 UV of compound 145 100

3.3.2.3 TGA of compound 145 101

3.4 Conclusion 102

4.1 Introduction 106

4.2 Synthesis 108

4.3 Result and discussion 108

4.3.1 IR, TGA, and NMR 108

4.3.2 UV absorption and emission properties **114**

4.3.3 X-ray structure determination **117**

4.3.4 Hydrogen bonding **119**

4.3.5 Hirshfeld surface analysis **124**

4.4 Conclusion **125**

5.1 Introduction **128**

5.2 Synthesis **129**

5.3 Result and discussion **130**

5.3.1 IR and NMR **130**

5.3.2 UV **132**

5.3.3 TGA **133**

5.4 Conclusion **134**

6.1 Introduction **136**

6.2 Synthesis **136**

6.3 Result and discussion of compound 169 ..... **146**

6.3.1 IR **146**

6.3.2 UV **147**

6.3.3 TGA **148**

6.3.4 Single crystal x-ray diffraction (SCXRD) **149**

6.3.5 Hydrogen bonding **153**

6.3.6 Hirshfeld **155**

6.4 Conclusion **157**

8.1 Chemicals and instruments **166**

8.2 General synthesis methods **167**

8.2.1 General synthesis method for 131-133 167

8.2.2 General synthesis method for 134, 136, 137, and 139 168

8.2.3 General synthesis method for 135 and 141 170

8.2.4 Synthesis method of 145 172

8.2.5 General synthesis method for compounds 150-153 173

8.2.6 Synthesis method of 2,3,6,7,10,11-hexamethoxytriphenylene (52) 175

8.2.7 Synthesis method of 1,5,9-trinitro-2,3,6,7,10,11-hexamethoxytriphenylene (165). 176

8.2.8 Synthesis method for 2,3,6,7,10,11-hexamethoxytriphenylene-1,5,9-triamine (166) 177

8.2.9 Synthesis method of compound 165 178

8.2.10 Synthesis method of 169 179

References:..... ii

List of figures

Figure 1.1 Renewable energies.[7] 5

Figure 2. 1 Benzene **1**. 10
Figure 2. 2 Structure of compound **2**. 11
Figure 2. 3 Structure of compound **10**. 17
Figure 2. 4 Structure of compound **17**. 21
Figure 2. 5 Structure of compound **24**. 24
Figure 2. 6 Structure of compound **33**. 28
Figure 2. 7 Triphenylene **40**. 33
Figure 2. 8 Structure of compound **41**. 34
Figure 2. 9 Structure of compound **48**. 37
Figure 2. 10 Structure of compound **51**. 40
Figure 2. 11 Coronene **59.** 44
Figure 2. 12 Structure of compound **60**. 45
Figure 2. 13 Structures of compounds **68** and **69.** 49
Figure 2. 14 Cyanopyridine **(72).** 51
Figure 2. 15 Connectivity patterns of cyanopyridine compounds $[MX_2(CNpy)_x]_n$, (M= Mn, Fe, Co, Ni, Cu) (X=Br and Cl).[99] 52
Figure 2. 16 nicotinamide **(86)**, picolinamide **(87)**, and isonicotinamide **(88)**. 54
Figure 2. 17 Structure of compounds **89** and **90** and their coordination patterns (R = diisopropyl).[107] 56
Figure 2. 18 Structures of **91**, **92**, and **93** linkers. 57
Figure 2. 19 Isonicotinic acid **100**, picolinic acid **101**, and nicotinic acid **102**. 57
Figure 2. 20 Structures of **103**, **104**, and **105**. 58
Figure 2. 21 (a) 1D Chain Structure of Co-MOF 1 **110** (b) 1D Chain Structure of Co-MOF 2 **111**.[111] 59
Figure 2. 22 Structures of **112-117**.[112] 60
Figure 2. 23 [1,3,5] Triazine-2,4-diamine **118**. 60

Figure 2. 24 Coordination of **118** to Metal Ions (M= Co, Ni, Cu, and Zn).[114] 61
Figure 2. 25 Molecular Structures of the Ligands **123** and **124**.[115] 62

Figure 3. 1 Molecular structure of **33**, **129**, **130**, **131**, **132**, **133**, **134**, **135**, **136**, **137**, **138**, **139**, **140**, **141**, **143**, and **118**. 66
Figure 3. 2 ^{1}H NMR of **129-131** in DMSO-d6. 72
Figure 3. 3 IR spectra of **129-131**. 72
Figure 3. 4 ^{1}H NMR of **132**, **133**, and **134** in DMSO-d6. 74
Figure 3. 5 IR spectra of **132**, **133**, and **134**. 75
Figure 3. 6 ^{1}H NMR of **135, 139**, and **137** in DMSO-d6. 76
Figure 3. 7 IR spectra of **135**, **139**, and **137**. 77
Figure 3. 8 Comparison of ^{1}H NMR of **129**, **132**, and **135** in DMSO-d6**.** 78
Figure 3. 9 UV spectra of compounds **129**, **130**, **131**, **132**, **133**, **134**, **135**, **137**, and **139** in DMF at room temperature. 84
Figure 3. 10 Thermogravimetric analysis of compounds **129**, **130**, **131**, **132**, **133**, **134**, **135**, **137**, and **139** (TGA). 86
Figure 3. 11 Fluorescence spectra of compounds **129**, **130**, **131**, **132**, **133**, **134**, **135**, **137**, and **139** in DMF at room temperature, λ_{ex} = 270 nm. 88
Figure 3. 12 The hydrogen bonding configurations in molecules **129**, **130**, **132**, and **135** are depicted. Dashed lines represent the hydrogen bonds. Carbon atoms are depicted in gray, hydrogen atoms in white, nitrogen atoms in blue, oxygen atoms in red, and sulfur atoms in yellow. 93
Figure 3. 13 Hirshfeld surface of molecules **129**, **130**, **132**, and **135** with d_{norm} mapping for visualizing intermolecular interactions. 94
Figure 3. 14 Percentage contribution of intermolecular interaction for molecules **129**, **130**, **132**, and **135**. 96
Figure 3. 15 ^{1}H NMR of **143** in DMSO-d_6. 99
Figure 3. 16 IR spectrum of compound **143**. 100
Figure 3. 17 The UV spectrum of compound **143** in acetonitrile. 101
Figure 3. 18 Thermogravimetric analysis (TGA) for compound **143**. 102

Figure 4. 1 Molecular structures of **144-147**. 107

Figure 4. 2 FT-IR spectra of compounds **144-147**. 112
Figure 4. 3 Thermogravimetric analysis (TGA) for compounds **144-147** (30 to 700 °C, heating rate of 10 °C/ min, N_2 atmosphere)..... 113
Figure 4. 4 ^{1}H NMR spectra of **144-147** in DMSO-d_6 with tentative assignment..... 114
Figure 4. 5 UV absorption (left) and emission (right) spectra of compounds **144-147** in acetonitrile at room temperature. 116
Figure 4. 6 The solid-state structures of molecules **144** and **145** are depicted in (a_1) and (a_2) (top views), and (b_1) and (b_2) (side views) of individual molecules. Stereoviews displaying molecular packing are presented in (c_1) and (c_2). Atom color code: C gray, H white, N blue, and O red. To enhance clarity in molecule **144**, a green layer highlights the packing, and DMSO molecules are depicted in yellow (c_1). In molecule **145**, a yellow layer marks the packing (c_2). 121
Figure 4. 7 Hydrogen bonding patterns in the crystal structures of **144** and **145**. The hydrogen bonds are shown by dashed lines. Atom color code: C gray, H white, N blue, O red, and S yellow. 122
Figure 4. 8 Hydrogen bonding patterns in the crystal structures of **51**[161] and **156**[162]. The hydrogen bonds are shown by dashed lines. Atom color code: C gray, H white, and O red. 124
Figure 4. 9 Molecular packing in the solid state structures of **51**[161] (a) and **156**[162] (b). For better visualization, one of the layers is shown in yellow. Atom color code: C gray, H white, N blue, O red, and S yellow. 123
Figure 4. 10 Hirshfeld surfaces for the molecular unit of **144** and **145**. d_{norm} mapping in **144** (a); percentage contribution of intermolecular interaction in **144** (b); d_{norm} mapping in **145** (c); percentage contribution of intermolecular interaction in **145** (d). 125

Figure 5. 1 Structure of compounds **68** and **157**. 128
Figure 5. 2 a: ^{1}H NMR of **159** in $CDCl_3$-d6 and b: ^{1}H NMR of **157** in $CDCl_3$-d6. 131
Figure 5. 3 IR spectra of **157**..... 132
Figure 5. 4 UV absorption spectrum of compound **157** in acetonitrile at room temperature. ... 133
Figure 5. 5 Thermogravimetric analysis (TGA) for compound **157**. 134

Figure 6. 1 Structure of compound **135**. 137
Figure 6. 2 Structures of compounds **144** and **145**. 139

Figure 6. 3 Crystal structure of compound **163**. Dashed lines represent the coordination bonds. Carbon atoms are depicted in gray, hydrogen atoms in white, nitrogen atoms in blue, oxygen atoms in red, cobalt atom in pink, and bromine atoms in purple. 139
Figure 6. 4 FT-IR spectra of compounds **143** and **162.** 147
Figure 6. 5 The UV–vis spectrum of compound **162** in the solid state. 148
Figure 6. 6 Thermogravimetric analysis (TGA) for compound **162**. 149
Figure 6. 7 Solid-state structures of molecule **162** in (a_1) and (b_1) are shown, with stereoviews illustrating molecular packing in (c_1). Solid-state structures of molecule **165** in (a_2) and (b_2) are shown, with stereoviews illustrating molecular packing in (c_2). The atom color scheme is as follows: Zn is pink, C is gray, H is white, N is blue, and O is red. 152
Figure 6. 8 The hydrogen bonding configuration in molecule **162** is depicted. Dashed lines represent the hydrogen bonds. Carbon atoms are depicted in gray, hydrogen atoms in white, nitrogen atoms in blue, oxygen atoms in red, and zinc atoms in pink. 155
Figure 6. 9 Hirshfeld surfaces for the molecular unit of **162** and **165**. d_{norm} mapping in **162** (a); percentage contribution of intermolecular interaction in **162** (b); d_{norm} mapping in **165** (c); percentage contribution of intermolecular interaction in **165** (d). 156

Figure 7. 1 Structure of compound **165**, **166**, **167**, and **168**. 163
Figure 7. 2 Structure of compound **169**, **170**, **171**. 163

Figure 8. 1 Structures of compounds **131**, **132**, and **133**. 167
Figure 8. 2 Structures of compounds **134**, **136**, **137**, and **139**. 169
Figure 8. 3 Structures of compounds **135** and **141**. 171
Figure 8. 4 Structure of compound **145**. 172
Figure 8. 5 Structures of compounds **150**-**153**. 173
Figure 8. 6 Structure of compound **52**. 176
Figure 8. 7 Structure of compound **165**. 176
Figure 8. 8 Structure of compound **166**. 177
Figure 8. 9 Structure of compound **165**. 178
Figure 8. 10 Structure of compound **169**. 179
Figure 8. 11 Photo of crystal of compound **169**. 180

Figure S. 1 ^{1}H NMR (400 MHz) spectrum of compound **131**. Solvent: DMSO-d_6. ..... b
Figure S. 2 ^{13}C NMR (100 MHz) spectrum of compound **131**. Solvent: DMSO-d_6. c
Figure S. 3 ^{1}H NMR (400 MHz) spectrum of compound **132**. Solvent: DMSO-d_6. ..... d
Figure S. 4 ^{13}C NMR (100 MHz) spectrum of compound **132**. Solvent: DMSO-d_6. .....e
Figure S. 5 ^{1}H NMR (400 MHz) spectrum of compound **133**. Solvent: DMSO-d_6. ..... f
Figure S. 6 ^{13}C NMR (100 MHz) spectrum of compound **133**. Solvent: DMSO-d_6. ..... g
Figure S. 7 ^{1}H NMR (400 MHz) spectrum of compound **134**. Solvent: DMSO-d_6. ..... h
Figure S. 8 ^{13}C NMR (100 MHz) spectrum of compound **134**. Solvent: DMSO-d_6. i
Figure S. 9 ^{1}H NMR (400 MHz) spectrum of compound **135**. Solvent: DMSO-d_6. ..... j
Figure S. 10 ^{13}C NMR (100 MHz) spectrum of compound **135**. Solvent: DMSO-d_6. ..... k
Figure S. 11 ^{1}H NMR (400 MHz) spectrum of compound **136**. Solvent: DMSO-d_6..... l
Figure S. 12 ^{13}C NMR (100 MHz) spectrum of compound **136**. Solvent: DMSO-d_6. ..... m
Figure S. 13 ^{1}H NMR (400 MHz) spectrum of compound **137**. Solvent: DMSO-d_6. ..... n
Figure S. 14 ^{13}C NMR (100 MHz) spectrum of compound **137**. Solvent: DMSO-d_6. ..... o
Figure S. 15 ^{1}H NMR (400 MHz) spectrum of compound **139**. Solvent: DMSO-d_6. ..... p
Figure S. 16 ^{13}C NMR (100 MHz) spectrum of compound **139**. Solvent: DMSO-d_6. ..... q
Figure S. 17 ^{1}H NMR (400 MHz) spectrum of compound **141**. Solvent: DMSO-d_6. ..... r
Figure S. 18 ^{13}C NMR (100 MHz) spectrum of compound **141**. Solvent: DMSO-d_6. ..... s
Figure S. 19 ^{1}H NMR (400 MHz) spectrum of compound **145**. Solvent: DMSO-d_6. ..... t
Figure S. 20 ^{13}C NMR (100 MHz) spectrum of compound **145**. Solvent: DMSO-d_6. ..... u
Figure S. 21 ^{1}H NMR (200 MHz) spectrum of compound **150**. Solvent: DMSO-d6..... v
Figure S. 22 ^{13}C NMR (100 MHz) spectrum of compound **150**. Solvent: DMSO-d_6. ..... w
Figure S. 23 ^{1}H NMR (200 MHz) spectrum of compound **151**. Solvent: DMSO-d_6. x
Figure S. 24 ^{13}C NMR (100 MHz) spectrum of compound **151**. Solvent: DMSO-d_6. ..... y
Figure S. 25 ^{1}H NMR (200 MHz) spectrum of compound **152**. Solvent: DMSO-d_6. .....z
Figure S. 26 ^{13}C NMR (100 MHz) spectrum of compound **152**. Solvent: DMSO-d_6. .....aa
Figure S. 27 ^{1}H NMR (200 MHz) spectrum of compound **153**. Solvent: DMSO-d_6. ..... bb
Figure S. 28 ^{13}C NMR (100 MHz) spectrum of compound **153**. Solvent: DMSO-d_6. cc
Figure S. 29 ^{1}H NMR (400 MHz) spectrum of compound **164**. Solvent: $CDCl_3$-d_6. ..... dd
Figure S. 30 ^{13}C NMR (100 MHz) spectrum of compound 164. Solvent: $CDCl_3$-d_6. .....ee

Figure S. 31 Emission spectra of compounds **131**, **132**, **133**, **134**, **135**, **136**, **137**, and **139** in Acetonitrile at room temperature. ..... ff
Figure S. 32 Emission spectra of compounds **131**, **132**, **133**, **134**, **135**, **136**, **137**, and **139** in Acetonitrile at room temperature. λ_{ex} = 240 nm. ..... gg
Figure S. 33 Emission spectra of compounds **131**, **132**, **133**, **134**, **135, 136**, **137**, and **139** in acetonitrile at room temperature at different concentrations. λ_{ex} = 240 nm..... hh

List of Tables

Table 3. 1 Reaction conditions and yields for the hydrolysis of cyano compounds **131**, **132,** and **133**..... 70
Table 3. 2 Crystallographic data for **131**, **132**, **134**, and **137**. 82
Table 3. 3 The mean bond distances for compounds **131**, **132**, **134**, and **137**..... 83
Table 3. 4 Infrared spectral data, maximum absorption wavelengths (λ_{max}), and decomposition temperatures for compounds **131, 132, 133, 134, 135, 136, 137, 139, 141**, **34**, **144**, **146**, and **147**. 87
Table 3. 5 Fluorescence spectroscopy data of compounds **131, 132, 133, 134, 135, 136, 137, 139,** and **141**..... 90
Table 3. 6 The hydrogen bonding patterns in molecules **131**, **132**, **134**, and **137**. The angle (Θ) between the donor and acceptor atoms, as well as the length (d) of the hydrogen bond..... 93
Table 3. 7 IR data, λ_{max}, and TGA for compounds **131**, **119**, and **145**..... 102

Table 4. 1 FTIR data, λ_{max} absorption and emission values, and decomposition temperatures for **150-153** and selected relevant reported triphenylene-based compounds **158-161a**. 110
Table 4. 2 Crystal data and structure refinement details for **150** and **151.**..... 118
Table 4. 3 Bond lengths (Å) in **150** and **151**. 119
Table 4. 4 The type of hydrogen bonds in **150** and **151.** 120

Table 6. 1 Reaction conditions for the coordination of compounds **136**, **145**, **150**, and **151** with different metal salts..... 141
Table 6. 2 Crystallographic data of compound **169**..... 150
Table 6. 3 The average coordination bond lengths of compounds **169** and **172**. 151
Table 6. 4 The hydrogen bonding patterns in molecules **169** and **172**. The angle (Θ) between the donor and acceptor atoms, as well as the length (d) of the hydrogen bond..... 154

List of schemes

Scheme 2. 1 Reaction conditions. (i) $FeCl_3$, TBACl (tetrabutylammonium chloride), Cl_3CCH_2OH, MeCN, irradiation with blue LEDs (390 nm, 100 W), 1 atm of O_2 (balloon) at room temperature.92% yield. 12

Scheme 2. 2 (i) Co/Mn/Br catalyst (Co/Mn ratio 10:1), glacial acetic acid, 190°C, 17 atm, 3 h. 12

Scheme 2. 3 (i) (1) NaOH, water/DMSO, 120°C, 12 h (2) HCl. 12

Scheme 2. 4 (i) $KMnO_4$, pyridine, H_2O 81% (ii) Na_2CO_3, pyridine, CuBr, H_2O, 60% yield. 18

Scheme 2. 5 (i) CO_2, K_2CO_3, HCO_2H. 18

Scheme 2. 6 (i) (1) Cu $(OAc)_2.H_2O$, 65°C, 20 min, dioxane (2) Pd $(OAc)_2$, Et_3N, toluene, 20 h, 100°C, 97% yield. 21

Scheme 2. 7 (i) H_2SO_4/ CrO_3. 22

Scheme 2. 8 Reaction conditions. (i) $Co_2(CO)_8$, propylene oxide, K_2CO_3. 25

Scheme 2. 9 Reaction conditions. (i) KNO_2, Na_2CO_3, and $AcNMe_2$ (ii) NaOH, H_2O. 25

Scheme 2. 10 Reaction conditions. (i) (1) K_2CO_3, N-Methyl-2-pyrrolidone, 3 h, 180 °C (2) HCl, H_2O. 29

Scheme 2. 11 (i) (1) Sodium methylthiolate, dimethylimidazolidinone 70°C, 4 h (2) 110°C, 30 min (3) Methyl iodide, rt, 15 min (ii) (1) Li, NH_3 (liq.), −78°C, 3.5 h (2) CH_3OH, rt, 1.5 h; (3) HCl, H_2O, Et_2O, CH_2Cl_2. 35

Scheme 2. 12 Synthetic route: (i) $(CH_3)_2SO_4$, K_2CO_3, Acetone, reflux (ii) (1) $FeCl_3$, CH_2Cl_2, rt; (2) CH_3OH, rt (iii) HBr/HOAc, reflux. 37

Scheme 2. 13 (i) $PhI(OCOCH_3)_2$ (PIDA), CH_3SO_3H, $(CF_3)_2CHOH$, r.t. 38

Scheme 2. 14 Synthetic route: (i) $ZrCl_4$, reflux (ii) Pd/C, triglyme, reflux (iii) $NaCr_2O_7/H_2O$, 250°C /autoclave). 40

Scheme 2. 15 Reaction conditions: (i) $AlCl_3$, ICl, CCl_4, 81 °C, 48 h, 93% (ii) benzyl mercaptan, NaH, DMI, 0 °C to rt, 16 h, 62%; (iii and iv) Li, THF, methanol, NH_3, -78 °C to rt, 4 h; HCl/H_2O_2/water, rt, 61% (v) $NaBH_4$.[91] 46

Scheme 2. 16 (i) pyridine hydrocholoride, 200 °C, 4 h. 49

Scheme 3. 1 Synthesis route for synthesising **129**, **130**, **131**, **132**, **133**, **134**, **135**, **137**, and **139**. (i) corresponding bromopyridine carbonitrile, K_2CO_3, DMF/Toluene, reflux (ii) KOH, H_2O reflux (iii) HCl. 68

Scheme 3. 2 Synthetic route to prepare compound **143**. (i) (a) Dicyandiamide, KOH, 2-methoxyethanol, 4 hr reflux (b) H_2O, HCl 37%. 98

Scheme 4. 1 Synthetic route to prepare **144-147**. Reagents and conditions: i. $FeCl_3$, HCl/H_2SO_4, CH_2Cl_2, reflux, 2 h (87%).[154] ii. HBr, acetic acid (75%).[153] iii. Corresponding bromopyridinecarbonitrile**148-151**, K_2CO_3, DMF/Toluene, reflux (**144**, 90%, **145**, 87%, **146**, 92% and **147**, 89%). 109

Scheme 5. 1 (i) 1. HCl, H_2SO_4, $FeCl_3$, CH_2Cl_2, 2 hr reflux 2. MeOH. 30 min reflux (ii) $PhSO_2Cl$, $AgNO_3$, Bu_4N^+, $CHCl_3$, 3d reflux, 60 °C (iii) 1. Ni $(OAc)_2$, MeOH, THF, 5 min, rt 2. $NaBH_4$ (iv) 4-formylbenzoate 160, DMF, Ar 140 24 hr. 130

Scheme 6. 1 Synthetic route to prepare **162**. (i) DMF/MeOH, 80 °C, 48 hr. 145
Scheme 6. 2 Sequential oxidation of methanol to formic acid by perchlorate. 146

List of abbreviations

Å	Angstrom
atm	Atmosphere
BDC	Benzene-1,4-dicarboxylate
BET	Brunauer-Emmett-Teller
BTC	1,3,5-Benzenetricarboxylic acid
CCDC	Cambridge Crystallographic Data Centre
cm	Centimeter
d (NMR)	Doublet
d (bond)	Length of the bond in hydrogen bonding
dd	Doublet of Doublets
DAT	2,4-Diamino-l,3,5-triazine
DCM	Dichloromethane
δ (delta)	Chemical shift
DMF	Dimethyl formamide
DMI	1,3-Dimethyl-2-imidazolidinone
DMSO	Dimethyl sulfoxide
EA	Elemental analysis
eq	Equivalent
F	Structure Factor
FTIR	Fourier Transform Infrared Spectroscopy
g	Gram
GHG	Greenhouse gases
HFIP	Hexafluoroisopropanol
HHTP	2,3,6,7,10,11-Hexahydroxytriphenylene
H_3TCPB	4,4′,4″-[1,3,5-Benzenetriyltris(oxy)]tris[benzoic acid]
HRMS	High-resolution mass spectrometry
HRMS-ESI	High-resolution mass spectrometry - electrospray ionization
h	Hour
HER	Hydrogen evolution reaction
IEA	International Energy Agency
IR	Infrared
J	Coupling constant
K	Kelvin
kg	Kilogram
LnOFs	Lanthanide–organic frameworks
LSG	Laser-scribed graphene
LED	Light-Emitting Diode
λ (lambda)	Wavelength
min	Minute

MHz	Megahertz
m	Meter
mA	Milliampere
mg	Milligram
mL	Milliliter
mmol	Millimole
mV	Millivolt
mp	Melting point
MOFs	Metal-organic frameworks
µL	Microliter
N_{CN}	Nitrogen of cyano
NMR	Nuclear Magnetic Resonance
N_{py}	Nitrogen of pyridine
nm	Nanometer
d_{norm}	Normalized distance
ν (nu)	Frequency
OER	Oxygen evolution reaction
ORR	Oxygen reduction reaction
pH	Potential of hydrogen
PE	Petroleum ether
PET	Polyethylene terephthalate
ppm	Parts per million
PTC	1,2,3,4,5,6,7,8,9,10,11,12-Perthiolated coronene
PV	Photovoltaic panels
pta	Phthalic acid
r.t.	Room temperature
R	Residual factor
s (time)	Seconds
s (NMR)	Singlet
S	Siemens
SCXRD	Single Crystal X-ray Diffraction
STP	Standard Temperature and Pressure
Td	Decomposition temperature
TBACl	Tetrabutylammonium chloride
TGA	Thermogravimetric analysis
THF	Tetrahydrofuran
THT	2,3,6,7,10,11-Hexathioltriphenylene
θ (theta)	Angle between bonds in hydrogen bonding
2θ (two-theta)	Angle of diffraction (two-theta)
W	Watt

V	Volt
V_{cell}	Volume of the unit cell
wR2	Weighted R-Factor
XRD	X-ray Diffraction

Chapter 1

Introduction

1.1 The global energy consumption

One of the main components of every development program is energy. Currently, the primary energy sources in the world are fossil fuels like coal, oil, and natural gas. Based on the international energy agency (IEA) report 2020, ~ 78% of energy was generated by fossil fuels (34% oil, 30.6% natural gas, 13.2% coal).[1] However, fossil fuels are non-renewable resources that form deep beneath the Earth's surface over millions of years. We are utilizing them so quickly that they will be finished soon.

Multiple reports indicate an increasing demand for energy. For example, a study shows that global energy consumption rose from 8,588.9 million tonnes of oil equivalent (Mtoe) in 1995 to 13,147.3 Mtoe in 2015.[2] This trend highlights the growing dependence on energy to support economic growth and development. In addition, according to the IEA report, it is predicted that the amount of energy demand will increase between 2015 and 2040 by 28%.[1]

1.2 Problem: Fossil fuels and their effect on the environment

The intergovernmental panel on climate change claims that fossil fuel emissions are the main contributor to global warming. The combustion of fossil fuel produces CO_2 which is one of the main components of greenhouse gases (GHG). CO_2 by trapping heat in the atmosphere causes global warming and global warming causes lots of problems like extreme weather, species extinction, food scarcity, sea level rise, and poverty in poor countries. [3]

The environmental impacts of fossil fuels extend beyond GHG emissions. The extraction and combustion of fossil fuels lead to land degradation, water contamination, and air pollution. A research highlights that while fossil fuel industries bring immediate economic benefits, such as job creation and infrastructure development, they also introduce environmental degradation, health hazards from pollutants, and social disruptions from forced displacements.[4] For instance, surface mining for coal involves stripping away vast expanses of topsoil, leading to reduced agricultural productivity and food security issues for local communities.[5]

Water contamination is another critical issue associated with fossil fuels. Mining activities can result in acid mine drainage, where rainwater reacts with exposed minerals to produce highly acidic water laden with heavy metals.[6] This toxic concoction can contaminate local water sources, rendering them unsafe for consumption and leading to severe health issues such as neurological disorders and cancers.[4]

In addition, oil spills, both on land and in marine environments, have catastrophic consequences, affecting agriculture, local ecosystems, and marine life.[7]

1.3 Possible solutions: Renewable energy resources

Due to global warming, future energy demands would be impossible to meet with fossil fuels. Therefore, it is essential to create certain energy sources that are sustainable, clean, and renewable. Clean energy comes in many forms, including solar, biomass, wind, geothermal energy, and others (Figure 1.1).[8]

One of the promising solutions for energy demand is solar energy. The most plentiful and sustainable energy source in the world is solar energy. In solar technology, photovoltaic panels (PV) turn sunlight into electrical energy. There are several steps to change the light of the sun to electricity and it needs different instruments like panels, inverter(s), racking, and solar battery storage unit. Although it is safe energy it has some drawbacks like high upfront cost, the size of the system being limited by available space, needing sunny weather to work efficiently, manufacturing solar panels can be harmful to the environment, low rate of energy conversion, and solar panels cannot be used during the night.[9]

Wind energy is renewable and sustainable energy and has very smaller bad effects on the environment than fossil fuels. Wind energy defines the process by which the wind is used to generate mechanical power or electricity. To produce electricity from the wind the nacelle, the foundation, the tower, the rotor, and the hub (which includes three blades) are needed. There are

some difficulties with wind energy such as unpredictability, it is a threat to birds and wildlife, it makes noise, and wind turbines need special locations to work properly.[10]

Hydro energy is a form of clean energy that harnesses the power of water in motion like water flowing to generate electricity. Hydro energy produced a sixth of the world's total electricity in 2020.[11] Producing electricity from hydro requires a dam on the running water, a hydraulic turbine, and a hydroelectric generator. This energy has some limitations like high initial costs and impact on animals and plants which are under the water.[12]

Tidal energy is a term used to describe a type of power produced by the rise and fall of tides. Turbines and energy generators are required as the fundamental infrastructure for this energy. There are some issues with this energy like expensive infrastructures, and it requires access to the sea.[13]

Geothermal energy is heat that is produced beneath the earth's surface. Geothermal energy is transported to the earth's surface via water and/or steam. It can be utilized to produce clean electricity or be used for heating and cooling. To exploit this energy, the steam turbine, generator, condenser, cooling tower, gas removal system, and hydrogen sulfide abatement system are necessary. It has some difficulties like high initial costs, and it can cause earthquakes.[14]

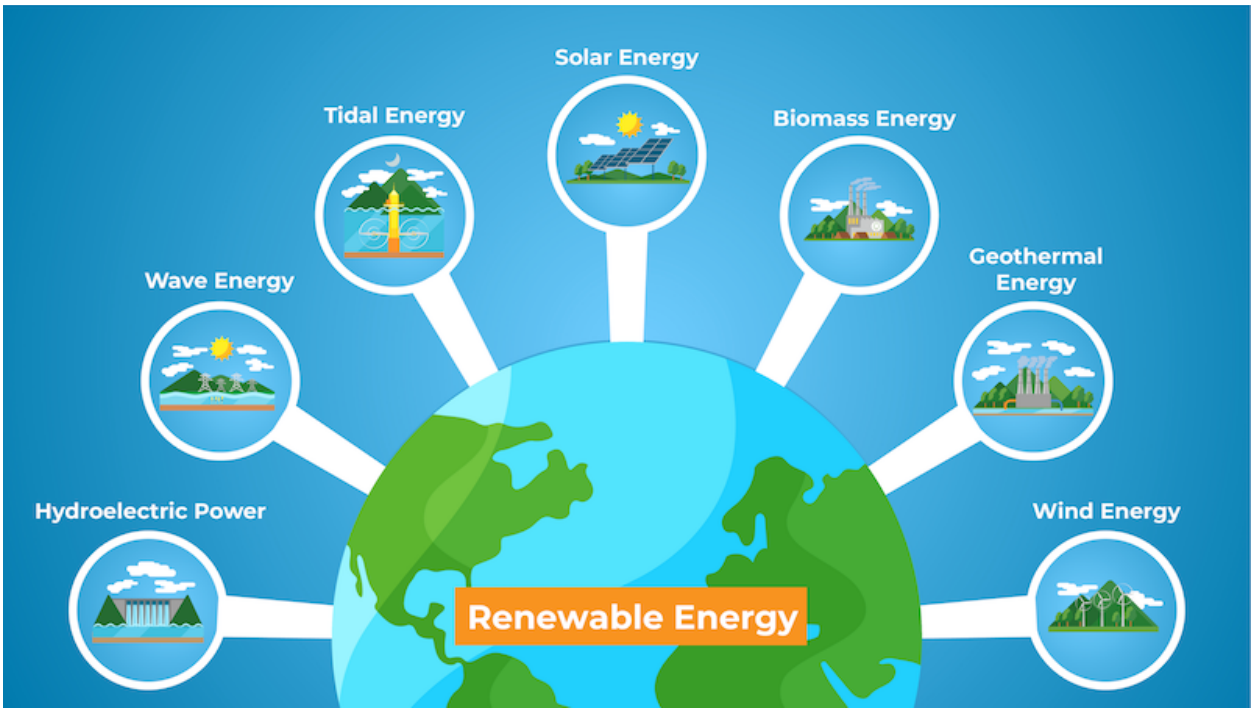

Figure 1.1 Renewable energies.[8]

One of the promising approaches to addressing the challenges posed by fossil fuels lies in material science. Rather than serving as a direct alternative, material science offers solutions to mitigate the negative impacts of fossil fuel usage and to enhance the efficiency of alternative energy technologies. Material science can be used for energy conversion systems, energy storage technologies, and clean and sustainable energy sources.[15] Therefore, materials with energy applications are in high demand to decrease the rising global energy and environmental problems.

1.3.1 Metal-organic frameworks (MOFs) and complexes for energy applications

Metal-organic frameworks (MOFs) are a class of porous crystalline materials composed of metal ions connected to organic linkers through coordination bonds (Scheme 1.1). Their highly ordered structures and tunable porosity make them ideal candidates for a range of energy-related applications.

Although MOFs are not direct alternatives to fossil fuels, they support the development of cleaner energy systems. For example, they are widely used in gas storage and separation, including hydrogen storage and carbon dioxide capture—both crucial for reducing greenhouse gas emissions.[16,17].

Furthermore, MOFs and related coordination complexes have been integrated into fuel cells, solar cells, batteries, and other energy devices, where they contribute to improved efficiency and performance.[18–22] Their versatility and structural tunability make them important materials in advancing sustainable energy technologies.

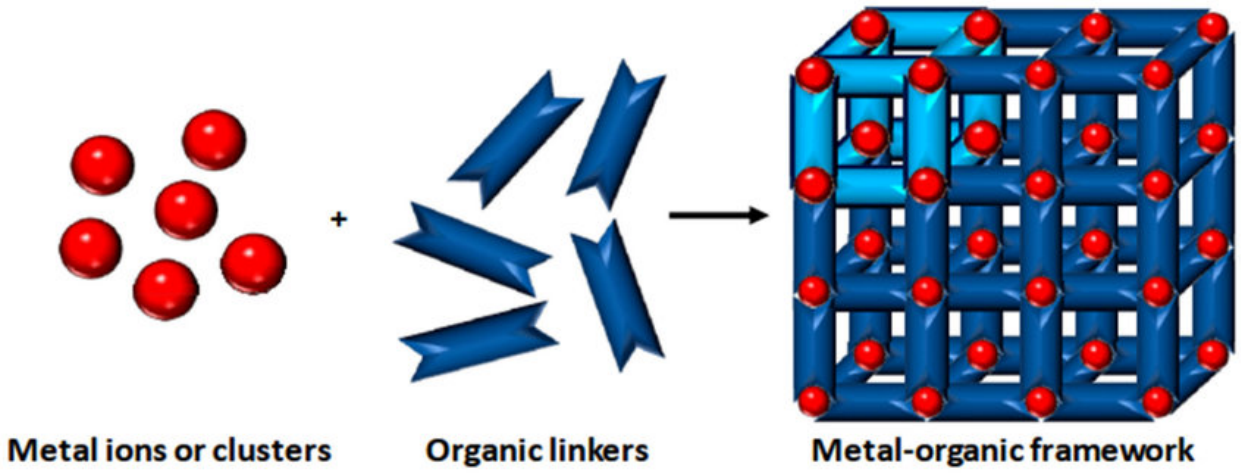

Scheme 1. 1 The preparation of a MOF.[23]

1.3.1.1 Organic linker

One of the primary components of MOFs or complexes, alongside metal ions, is the organic linker, which plays a pivotal role in shaping the structure, morphology, and properties of the final compound.[24] Organic linkers are composed of core and coordination motifs, both of which significantly influence the characteristics of the resulting MOFs or complexes.

The core of the ligand is generally located at the center of the organic linker (Scheme 1.2). Aromatic cores such as benzene, triphenylene, and azacoronene enhance the stability and optical properties of the resulting coordination compounds.[25]

Aromatic molecules are defined as cyclic, planar systems with conjugated π-electron networks that follow Hückel's rule, possessing (4n + 2) π-electrons, where *n* is a non-negative integer.

However, some compounds like azacoronene, although they do not strictly follow Hückel's rule, are still considered aromatic due to extensive π-electron delocalization. This delocalization imparts high thermodynamic stability and contributes to the unique electronic and chemical properties of these aromatic cores.

Coordination motifs are typically attached to the cores of ligands and contain heteroatoms that facilitate the formation of coordination bonds between the metal and ligand (Scheme 1.2). The symmetry of these coordination motifs is particularly important for the successful construction of MOFs. Well-designed coordination motifs enable the formation of strong coordination bonds, contributing to the overall stability of the coordination compound. Furthermore, the heteroatoms in these motifs can engage in hydrogen bonding, both intramolecularly and intermolecularly. Such interactions can profoundly influence the properties of the final compound, making it highly suitable for applications such as gas storage and separation.

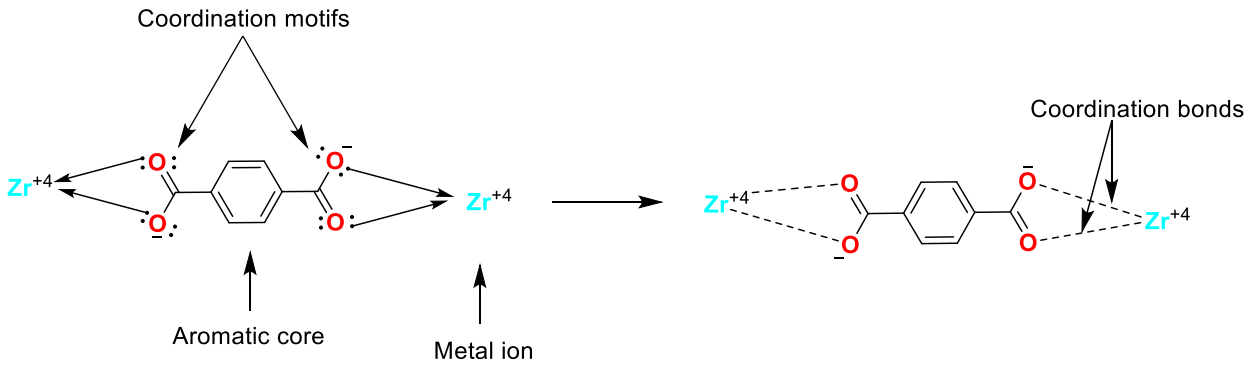

Scheme 1. 2 Organic linker with an aromatic core (benzene) and symmetrically attached coordination motifs (carboxylate), showing coordination bonds.

1.4 The objective of my project: synthesis and characterization new organic linkers for coordination reaction and the development of metal-organic frameworks (MOFs)

This project focuses on synthesizing organic compounds with benzene, triphenylene, and azacoronene cores, chosen for their aromatic nature and extended conjugated systems, which provide stability and enhance the optoelectronic properties of the final coordination compounds. Additionally, this project incorporates various coordination motifs into the ligands, including cyanopyridine, pyridinecarboxamide, carboxypyridine, carboxylic acid, and diaminotriazine groups. These motifs are symmetrically positioned on the cores and are rich in nitrogen and oxygen heteroatoms.

In the following chapter, I will introduce various organic linkers featuring benzene, triphenylene, and azacoronene cores, detailing their synthesis methods and applications in coordination reactions. Additionally, I will discuss common coordination motifs observed in coordination chemistry. Subsequent chapters will then focus on novel organic linkers and coordination compounds which were synthesized in this project (chapter 6).

Chapter 2

A review of the synthesis and coordination reactions of organic linkers with benzene, triphenylene, and azacoronene cores for MOF design

As mentioned in Chapter 1, this chapter introduces organic linkers based on benzene, triphenylene, and azacoronene cores, with a focus on their application in MOF synthesis. It also highlights that in MOF synthesis, multiple coordination sites and the symmetrical arrangement of these sites on the core of organic linkers are important for forming the MOF network. In addition, it presents some notable coordination motifs.

2.1 Benzene core ligands

Benzene (**1)** (Figure 2.1) is an aromatic organic compound with a molecular formula C_6H_6, It follows Hückel's rule and is characterized by a planar structure with delocalized π-electrons.

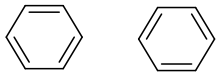

Figure 2. 1 Resonance structures of benzene **1**.

In the field of material science, benzene derivatives are highly valued for their exceptional stability and unique optical properties.[26] These attributes make benzene an ideal core structure for organic linkers in the synthesis of metal-organic frameworks (MOFs) and complexes. By incorporating benzene derivatives into organic linkers, researchers can enhance the stability and tailor the properties of the resulting MOFs and complexes.

This versatility has made benzene derivatives a cornerstone in coordination chemistry, where they play a pivotal role in creating materials with superior performance in energy-related applications. Notable uses include gas storage and separation, as well as components in fuel cells, solar cells, electrodes, and batteries.[27–31]

Several organic compounds with a benzene core have been synthesized for coordination reactions. In this section, we will introduce some of the most commonly used benzene-based ligands, discussing their synthesis and coordination reactions.

2.1.1 Benzene-1,4- dicarboxylic acid (BDC) (2)

Compound **2** is an organic molecule composed of a benzene ring with two carboxylic acid groups which are symmetrically located at the 1 and 4 positions (Figure 2.2). These carboxylic acid groups serve as excellent coordination motifs, which will be discussed further in the coordination motifs section (2. 4 Coordination motifs). The compound features a conjugated system and is primarily used as a precursor in the production of polyethylene terephthalate (PET) **4,** which is widely utilized in fibers and plastics.[32] Additionally, it has been extensively employed in various coordination reactions for making MOFs.

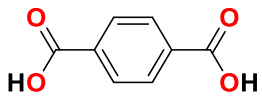

Figure 2. 2 Structure of compound **2**.

2.1.1.1 Synthesis

Several articles have reported the synthesis of compound **2** using various methods and oxidants. For instance, one report described the synthesis of compound **2** in excellent yield via a photocatalytic reaction. In this process, para-xylene **5** and oxygen were used as reactants, with $FeCl_3$ and 2,2,2-trichloroethanol serving as catalysts. The reaction was conducted under blue LED irradiation (390 nm) (Scheme 2.1).[33]

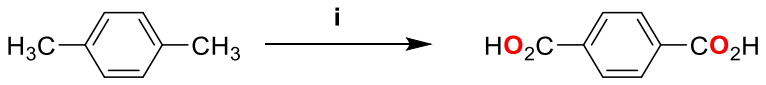

5 **2**

Scheme 2. 1 Synthetic route of **2**. (i) $FeCl_3$, TBACl (tetrabutylammonium chloride), Cl_3CCH_2OH, MeCN, irradiation with blue LEDs (390 nm, 100 W), 1 atm of O_2 (balloon) at room temperature.92% yield.

In another study, p-xylene **5** was oxidized using a Co-Mn catalyst, resulting in a 97% yield of terephthalic acid **2** (Scheme 2.2). In this reaction, the catalyst was separated by centrifugation, and the organic phase containing the products was subsequently analyzed by gas chromatography.[34]

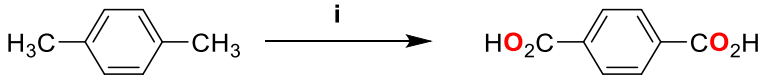

5 **2**

Scheme 2. 2 Synthetic route of **2**. (i) Co/Mn/Br catalyst (Co/Mn ratio 10 :1), glacial acetic acid, 190°C, 17 atm, 3 h. 97% yield.

In another research, 1,4-phenylenedimethanol **6** was dehydrogenated using a ruthenium-based complex as a catalyst. The reaction was conducted at 120°C under a continuous flow of nitrogen gas, yielding 100% of the final compound (Scheme 2.3). In this reaction, to obtain a pure compound the sodium salt was acidified with hydrochloric acid to obtain the free carboxylic acid form, which is compound **2**.[35]

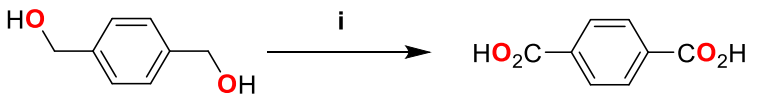

6 **2**

Scheme 2. 3 Synthetic route of **2**. (i) (1) NaOH, water/DMSO, 120°C, 12 h (2) HCl. 100% yield.

In addition, waste polyethylene terephthalate (PET) **4** was hydrolyzed using an alkaline hydrolysis process. In this reaction, potassium hydroxide was used as the hydrolysis agent, and the reaction was conducted at 100°C for 30 minutes, yielding 99.6% terephthalic acid **2**. In this reaction, after hydrolysis, the resulting potassium terephthalate was acidified with hydrochloric acid (HCl) to precipitate the pure terephthalic acid **2**.[36] Also, the depolymerization of PET **4** was performed via hydrolysis, using t-$BuNH_2$ as a catalyst and NaCl as a Lewis acid in the catalytic system. This reaction occurred under both conventional heating and microwave radiation, yielding 100% terephthalic acid **2** in just 10 minutes.[37]

2.1.1.2 Coordination

There are several examples of MOFs with compound **2** (BDC) as a ligand. For instance, UiO-66 **7** (Figure 2.3), a MOF that was constructed from compound **2** and Zr (iv), demonstrates exceptional thermal stability, remaining stable up to 540°C. It maintains its structural integrity under mechanical pressure up to 10,000 kg/cm² and is resistant to solvents such as water, DMF, benzene, and acetone. The pore sizes of UiO-66 **7** are estimated based on the largest sphere that can fit through the window openings, with linkers creating openings of 6 Å, 8 Å, and 10 Å, depending on their lengths. The surface area of UiO-66 **7** is 1187 m²/g, but extending the linkers can increase this surface area significantly, reaching up to 3000 m²/g with two ring linkers and 4170 m²/g with three ring linkers. UiO-66 **7** is employed in various applications, including gas storage, petrochemistry, catalysis, and selective separation.[38]

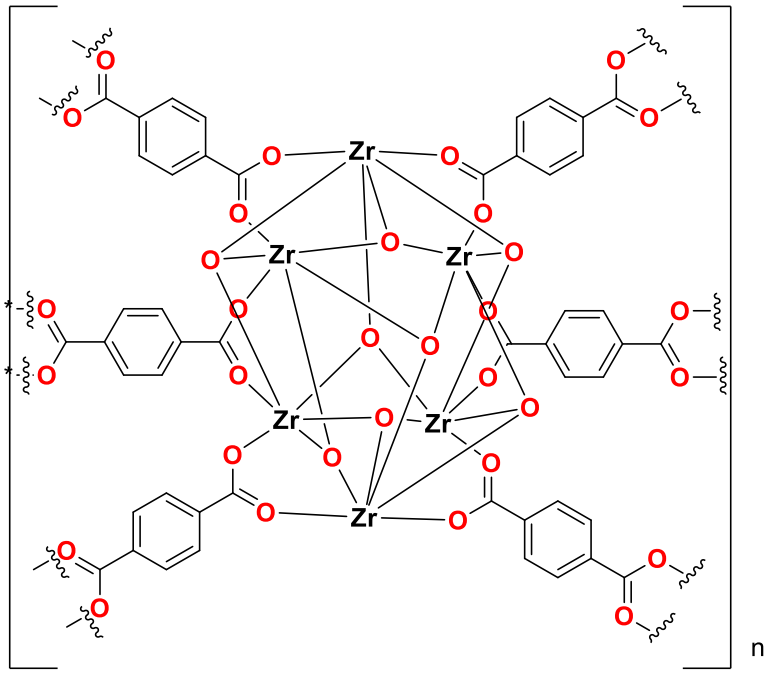

Figure 2. 3 Structure of UiO-66 **7.** The wavy lines indicate the repetition and spatial extension of the framework beyond the illustrated segment.

MIL-53 **8** (Figure 2.4) is a MOF that was constructed from compound **2** and Cr (III). It demonstrates thermal stability up to 375°C. It has large pores, roughly 8.6 × 8.6 Å in size, and boasts a surface area greater than 1500 m^2/g. This material exhibits unique properties, including zeolitic behavior, magnetic properties, high thermal stability, and notable sorption capacities.[39]

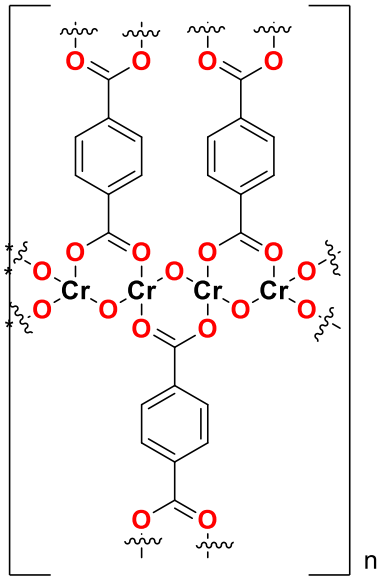

Figure 2. 4 Structure of MIL-53 **8**. The wavy lines indicate the repetition and spatial extension of the framework beyond the illustrated segment.

MIL-101 **9** (Figure 2.5), a MOF that was also constructed from compound **1** and Cr (III), has a different structure from MIL-53 **7**. It exhibits thermal stability up to 275°C and features a range of extra-large pore sizes, approximately 30 to 34 Å, and a surface area of about 5900 m^2/g. MIL-101 **9** holds potential applications as a nano mold for creating monodisperse nanomaterials and possesses high adsorption capacities, making it suitable for the adsorption of gases and large molecules.[40]

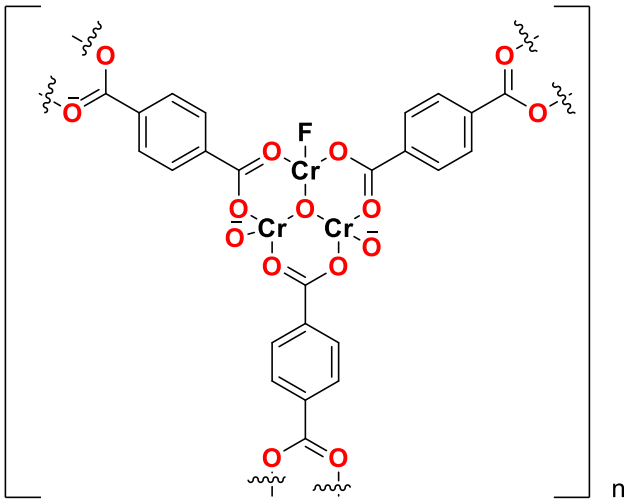

Figure 2. 5 Structure of MIL-101 **9**. The wavy lines indicate the repetition and spatial extension of the framework beyond the illustrated segment.

MOF-5 **10** (Figure 2.6), a MOF that was constructed from compound **2** and Zn (II), shows high thermal stability, withstanding temperatures between 300°C and 400°C. Its structure possesses a significant surface area, ranging from 2500 to 3000 m^2/g. In hydrogen storage application, MOF-5 **10** demonstrated the ability to adsorb up to 4.5 weight percent of hydrogen at 78 K, and 1.0 weight percent at room temperature and a pressure of 20 bar.[41]

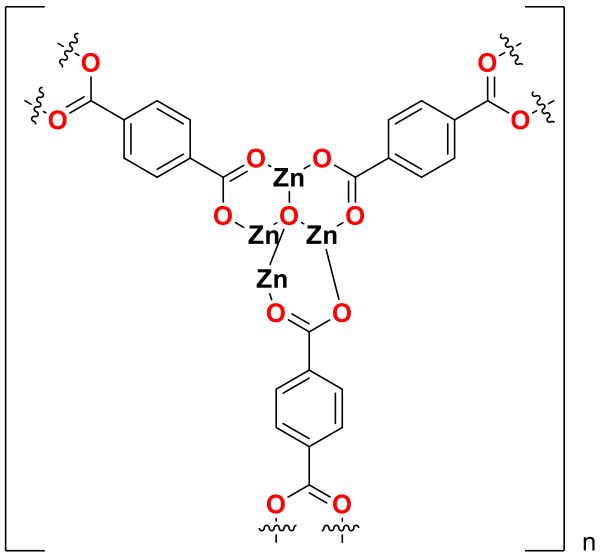

Figure 2. 6 Structure of MOF-5 **10**. The wavy lines indicate the repetition and spatial extension of the framework beyond the illustrated segment.

2.1.2 2,5-Dihydroxyterephthalic acid (11)

Compound **11** is another example of an organic compound with a benzene core, derived from terephthalic acid **2**, with two hydroxyl groups attached at positions 2 and 5 (Figure 2.7). It features a conjugated system and has been used in the production of polymers and polyesters.[42,43] In addition, it has been used as an organic linker in several coordination reactions for making MOFs.

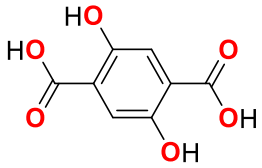

Figure 2. 7 Structure of compound **11**.

2.1.2.1 Synthesis

Several methods and oxidizing agents have been employed to synthesize compound **11**. For example, compound **11** was obtained by first oxidizing 2,5-dibromo-1,4-dimethylbenzene **11** using potassium permanganate ($KMnO_4$) as the oxidizing agent, resulting in an 81% yield of the

intermediate compound **13** (Scheme 2.4). The final compound **11** was then synthesized via copper-catalyzed hydroxylation and subsequently purified by crystallization from water.[44]

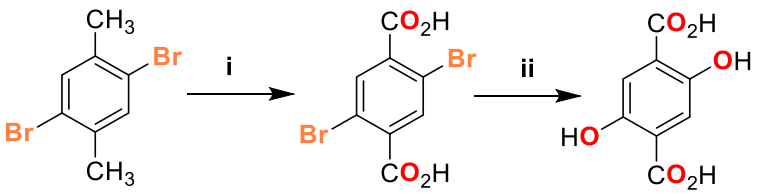

12 **13** **11**

Scheme 2. 4 Synthetic route of **11**. (i) $KMnO_4$, pyridine, H_2O, 81% yield (ii) Na_2CO_3, pyridine, CuBr, H_2O, 60% yield.

In another study, the synthesis process of compound **11** started from hydroquinone **14**. In this reaction, hydroquinone **14** was carboxylated using carbon dioxide (CO_2), with formic acid as the solvent and potassium carbonate (K_2CO_3) as a base to neutralize the acid formed during the reaction (Scheme 2.5) and compound **11** was purified by filtration after acidification.[45]

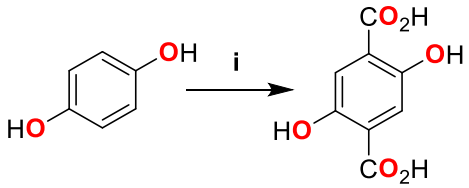

14 **11**

Scheme 2. 5 Synthetic route of **11**. (i) CO_2, K_2CO_3, HCO_2H.

2.1.2.2 Coordination

As it mentioned earlier compound **11** has been used in several MOFs. For instance, MOF-74, a MOF that was made from compound **11** and various metal ions like Ni, Zn, and Cu. MOF-74(Ni) **15** (Figure 2.8) is a metal-organic framework synthesized from Ni^{2+} and compound **11**. The MOF has a specific surface area of 1233 m^2/g, determined using the Brunauer-Emmett-Teller (BET) method. It features pore sizes around 11.7 Å and exhibits thermal stability up to 360°C under a nitrogen atmosphere. Additionally, MOF-74(Ni) **15** has shown potential for methane storage, with one of the highest reported storage capacities among MOFs, achieving 214 cm^3 (STP) at 25°C and 35 bars.[46]

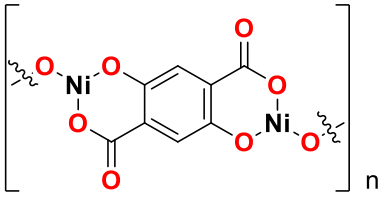

Figure 2. 8 Structure of MOF-74(Ni) **15**. The wavy lines indicate the repetition and spatial extension of the framework beyond the illustrated segment.

MOF-74(Cu) **16** (Figure 2.9) is a metal-organic framework synthesized from Cu^{2+} and compound **11** through a solvothermal reaction. This MOF exhibits high CO_2 adsorption due to its highly porous structure. Additionally, MOF-74(Cu) **16** shows enhanced photocatalytic performance for the reduction of CO_2 to methane under visible light.[47]

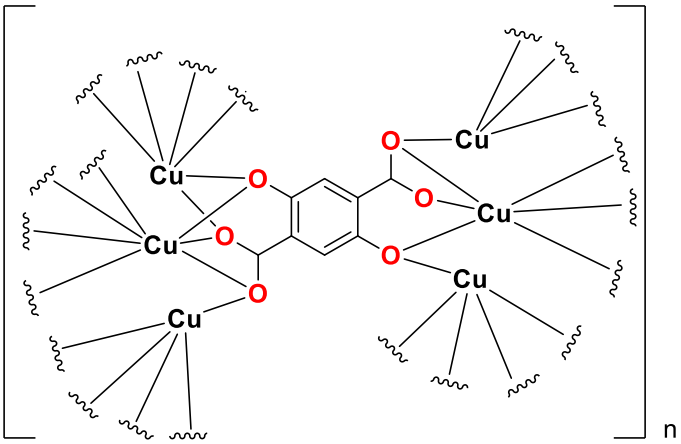

Figure 2. 9 Structure of MOF-74(Cu) **16**. The wavy lines indicate the repetition and spatial extension of the framework beyond the illustrated segment.

MOF-74(Zn) **17** (Figure 2.10) is a metal-organic framework synthesized from Zn^{2+} and compound **11**. The MOF is thermally stable up to 240°C. It was used to enhance the performance of zinc-ion batteries by improving long-term cycling stability and rate performance.[48]

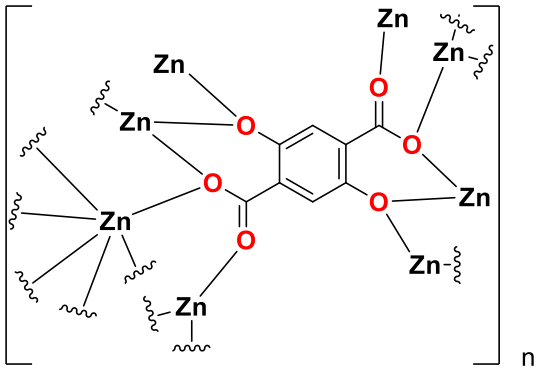

Figure 2. 10 Structure of MOF-74(Zn) **17**. The wavy lines indicate the repetition and spatial extension of the framework beyond the illustrated segment.

2.1.3 1,3,5-Benzenetricarboxylic acid (BTC) (18)

Compound **18** is an organic compound consisting of a benzene ring with three carboxylic acid groups which are symmetrically attached at positions 1, 3, and 5 (Figure 2.11). In our project, we have a similar structure, but instead of the carboxyl groups, we use a carboxypyridine unit linked to the benzene ring through an ether bond. Compound **18** features a conjugated system and has

been used as an organic linker in several coordination reactions for making MOFs. Compared to compound **2**, compound **18** offers an additional coordination site.

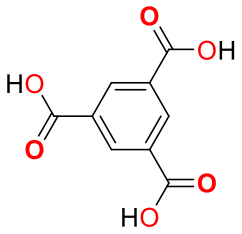

Figure 2. 11 Structure of compound **18**.

2.1.3.1 Synthesis

Several methods and oxidizing agents have been employed to synthesize Compound **18**. For instance, compound (**18**) was synthesized through a silyloxycarbonylation reaction of 1,3,5-tribromobenzene **19**. In this reaction, $Pd(OAc)_2$ and $Cu(OAc)_2$ were used as catalysts, and Et_3N was employed as a base. CO_2 served as the carbonyl source, resulting in a 97% yield (Scheme 2.6).[49]

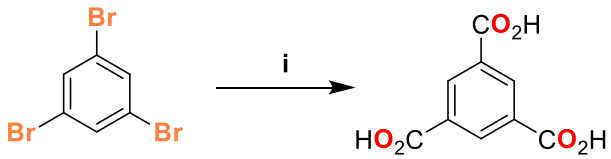

19 **18**

Scheme 2. 6 Synthetic route of **18**. (i) (1) $Cu(OAc)_2.H_2O$, 65°C, 20 min, dioxane (2) $Pd(OAc)_2$, Et_3N, toluene, 20 h, 100°C, 97% yield.

In another report, 1,3,5-trichlorobenzene **20** was used as the raw material, with $Co_2(CO)_8$ as the catalyst and NaOH as the base. The reaction was conducted under pressurized carbon monoxide (CO) at 2 kg/cm² and heated to 65°C. Additionally, the reaction was photostimulated using a high-pressure mercury lamp (500 W) placed about 30 cm from the autoclave.[50]

In another study, 1,3,5-trimethylbenzene (mesitylene) **21** was converted to compound **18** through a Jones oxidation reaction, using CrO_3 and H_2SO_4 as the oxidizing agents, yielding 46% (Scheme 2.7) and the pure compound was achieved by recrystallization.[51]

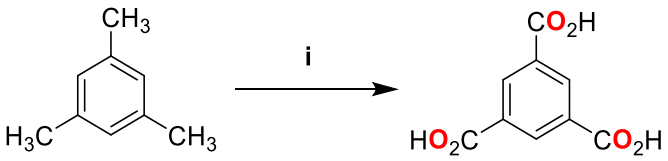

21 **18**

Scheme 2. 7 Synthetic route of **18**. (i) H_2SO_4/ CrO_3, 46% yield.

2.1.3.2 Coordination

As mentioned earlier, compound **18** has been used in several MOFs. For instance, Co-BTC **22** (Figure 2.12), a MOF that was made from compound **18** and cobalt ion, is investigated for its hydrogen storage capabilities, demonstrating excellent performance attributed to its porous structure and high surface area. Additionally, Co-BTC **22** MOF was employed as electrode materials for electrochemical capacitors, offering high capacitance due to their extensive surface area and porosity, which improve their electrochemical efficiency. The specific surface area of Co-BTC MOFs **22** varies depending on the synthesis methods and conditions.[52]

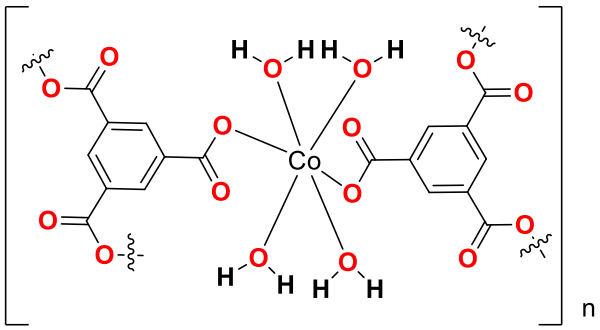

Figure 2. 12 Structure of Co-BTC **22**. The wavy lines indicate the repetition and spatial extension of the framework beyond the illustrated segment.

Cu-BTC **23** (Figure 2.13), a MOF that was made from 1,3,5-benzenetricarboxylic acid **17** and copper ion, is a framework known for its favorable hydrogen storage properties, attributed to its porous structure and high surface area. Furthermore, Cu-BTC **23** is effective in capturing benzothiophene from various fuels, demonstrating its versatility in multiple applications.[53]

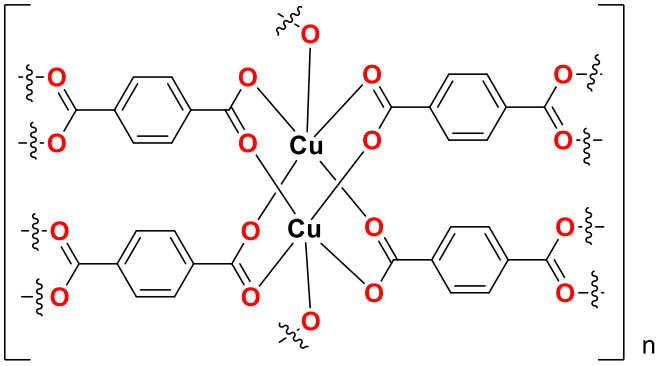

Figure 2. 13 Structure of Cu-BTC **23**. The wavy lines indicate the repetition and spatial extension of the framework beyond the illustrated segment.

MIL-100(Fe) **24** (Figure 2.14) as a MOF, which was made from compound **18** and Fe ion, demonstrates excellent gas adsorption performance for removing volatile organic compounds like toluene and p-xylene. The saturation adsorption capacity for toluene on MIL-100(Fe)_A2 **24** is

523.3 mg/g at 298 K, while for p-xylene, it is 560.2 mg/g at 298 K. The material exhibits decomposition temperatures around 450°C, and the BET surface area of MIL-100(Fe)_A2 **24** is 1011 m^2/g.[54]

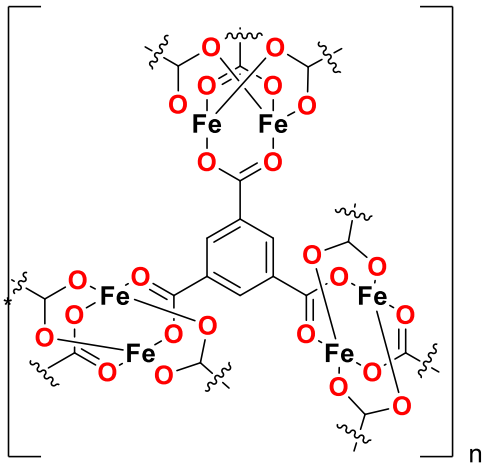

Figure 2. 14 Structure of MIL-100(Fe) **24**. The wavy lines indicate the repetition and spatial extension of the framework beyond the illustrated segment.

2.1.4 4,4'-Dicarboxydiphenyl ether 25

Compound **25** is an organic compound consisting of two benzene rings connected by an ether linkage, with carboxylic acid groups attached to the para positions on each benzene ring (Figure 2.15). It has a long-conjugated system and has been used as an organic linker in several coordination reactions for making MOFs.

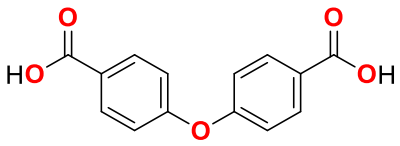

Figure 2. 15 Structure of compound **25**.

2.1.4.1 Synthesis

Several methods have been employed to synthesize compound **25**. For instance, compound **25** was synthesized through the carbonylation of the corresponding aryl halide **26**. In this reaction, CO was used as the carbonyl source, $Co_2(CO)_8$ served as the catalyst, epoxide was employed as a cocatalyst to activate the cobalt carbonyl complex, and K_2CO_3 was used as the base (Scheme 2.8) and the final compound was purified by recrystallization from water.[55]

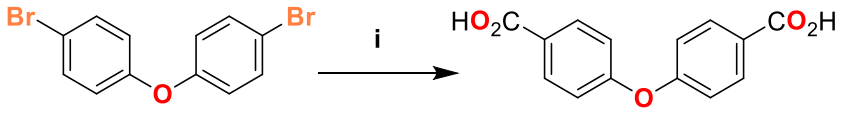

26 **25**

Scheme 2. 8 Synthetic route of **25**. (i) $Co_2(CO)_8$, propylene oxide, K_2CO_3, 93% yield.

In another study, the process began with 4-nitrophenylacetonitrile ($4\text{-}O_2NC_6H_4CN$) **27** (Scheme 2.9). This compound reacted with KNO_2 and Na_2CO_3 in dimethylacetamide ($AcNMe_2$) at 170-175°C to yield 4,4'-dicyanodiphenyl ether ($NCC_6H_4OC_6H_4CN\text{-}4$) **28**. The intermediate was then hydrolyzed with NaOH in aqueous solution to obtain the final compound **24**.[56]

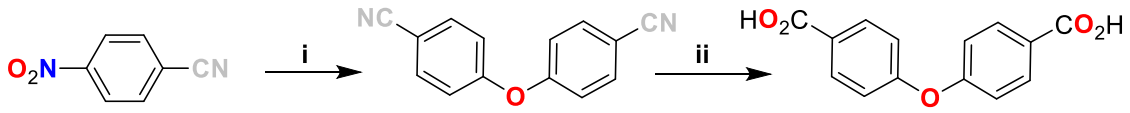

27 **28** **25**

Scheme 2. 9 Synthetic route of **25**. (i) KNO_2, Na_2CO_3, and $AcNMe_2$ (ii) NaOH, H_2O, 78.2% yield.

2.1.4.2 Coordination

As previously mentioned, compound **25** has been utilized in various MOFs and complexes. For example, the complex Eu(**25**)$_2$(**30**) **29** (where **25** = 4,4′-oxybis(benzoic acid) and **30** = 1,10-phenanthroline**)** (Figure 2.16) was synthesized using compound **25** and Eu ions through a

hydrothermal method. The complex demonstrates outstanding luminescence properties, making it suitable for use in materials that necessitate photoluminescence.[57]

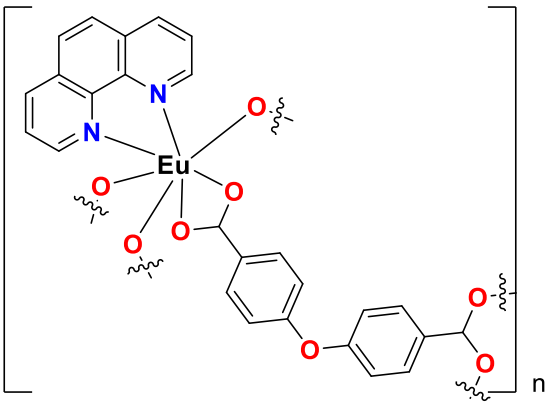

Figure 2. 16 Structure of Eu(**25**)$_2$(**30**) **29**. The wavy lines indicate the repetition and spatial extension of the framework beyond the illustrated segment.

The series of lanthanide–organic frameworks [Ln(H_2**25**)(**30**)(**33**)$_{0.5}$]$_n$ **31**(Figure 2.17) (where **25**= 4,4′-oxybis(benzoic acid), **30** = 1,10-phenanthroline **,** and **32** = oxalate) were synthesized from compound **25** and lanthanide ions under hydrothermal conditions. These frameworks exhibit thermal stability up to approximately 248°C in an air atmosphere. Their high luminescence efficiency, narrow bandwidth, and extended luminescence lifetime make these LnOFs **31** outstanding candidates for applications in luminescent devices, fluoroimmunoassays, and optical displays.[58]

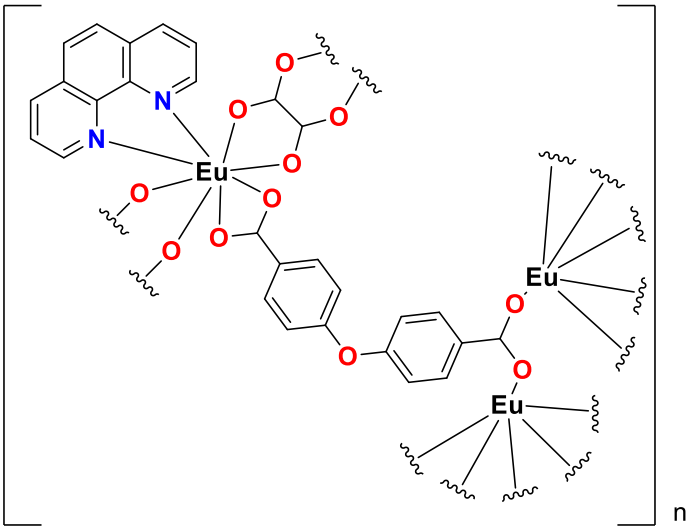

Figure 2. 17 Structure of [Eu(H_2**25**)(**30**)(**32**)$_{0.5}$]$_n$ **31**. The wavy lines indicate the repetition and spatial extension of the framework beyond the illustrated segment.

[(UO_2)($C_{15}H_8O_5$)(DMF)]n **33** (Figure 2.18), a one-dimensional uranyl coordination polymer, was synthesized through a solvothermal reaction from compound **25** and uranyl. Thermogravimetric analysis (TGA) reveals that the material loses its coordinated DMF ligand at 200°C. The compound maintains its crystallinity in various solvents with different polarities when exposed to 120°C for three days.[59]

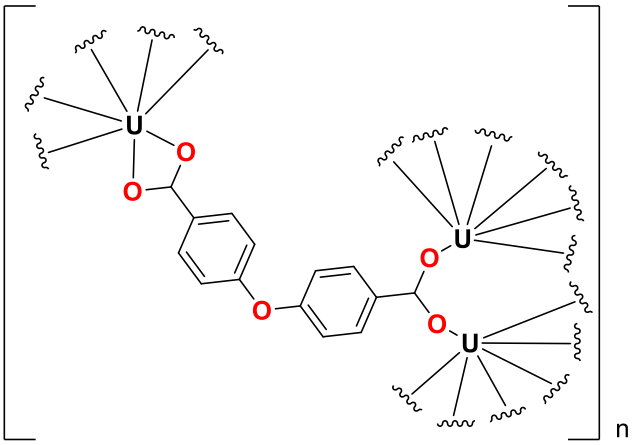

Figure 2. 18 Structure of [(UO_2)($C_{15}H_8O_5$)(DMF)]n **33**. The wavy lines indicate the repetition and spatial extension of the framework beyond the illustrated segment.

2.1.5 4,4′,4′′-[1,3,5-Benzenetriyltris(oxy)]tris[benzoic acid] (H_3TCPB) (34)

Compound **34** is an organic compound with a central benzene ring linked symmetrically to three benzoic acid groups via ether bonds (Figure 2.19). In our project, we have a similar structure, but instead of the benzoic acid branch, we use a carboxypyridine unit. Compound **34** features a conjugated system and has been widely used as a ligand in various coordination reactions for making MOFs.[60–64]

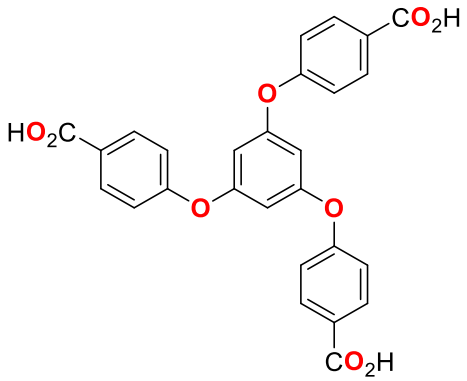

Figure 2. 19 Structure of compound **34**.

2.1.5.1 Synthesis

Compound **34** can be produced through some methods. For instance, in one work, it was synthesized via a nucleophilic reaction between 1,3,5-trihydroxybenzene **35** and 4-fluorobenzonitrile **36**, followed by hydrolysis using hydrochloric acid, yielding 78% (Scheme 2.10) and the acidification step facilitated obtaining the pure compound.[60,65,66]

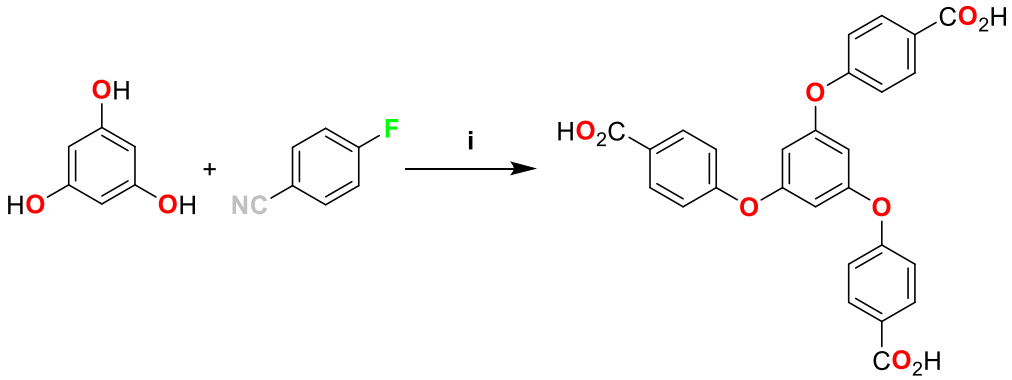

35 **36** **34**

Scheme 2. 10 Synthetic route of **34**. (i) (1) K_2CO_3, N-Methyl-2-pyrrolidone, 3 h, 180 °C (2) HCl, H_2O, 78% yield.

In another study, it was synthesized via a nucleophilic reaction between 1,3,5-trihydroxybenzene **35** and 4-nitrobenzonitrile **37**, followed by hydrolysis using hydrochloric acid, yielding 63%. The final compound was recrystallized from water and methanol.[66]

2.1.5.2 Coordination

Compound (H_3TCPB) **34** has been used in several coordination reactions. For instance, it reacted with uranium nitrate through a solvothermal process to produce [$C_{29}H_{23}NO_{11}U$] (UTCPB) **38** (Figure 2.20) with a yield of 86%. The MOF **38** was explored for its potential as a sensor, particularly for detecting Ru^{3+} ions, exhibiting strong luminescence quenching in the presence of Ru^{3+}, making it a promising candidate for sensing applications. Additionally, the complex was tested for its ability to adsorb organic dyes, such as methyl violet, from aqueous solutions.[67]

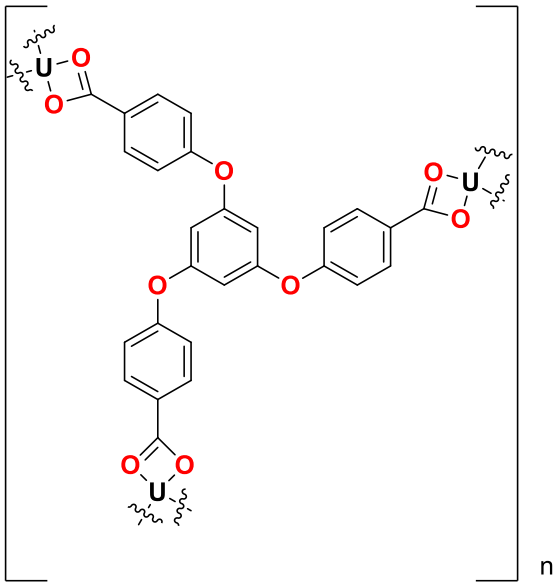

Figure 2. 20 Structure of **38**. The wavy lines indicate the repetition and spatial extension of the framework beyond the illustrated segment.

In another report, compound **34** reacted with $Zn(NO_3)_2 \cdot 6H_2O$ through a solvothermal reaction to produce a MOF **39** (Figure 2.21) in which the ligand coordinated with the oxygen atoms of the carboxylic acid groups. The synthesized MOF was explored for its luminescent properties and potential applications in the detection of both aromatic and aliphatic nitro explosives. The MOF **39** exhibited significant fluorescence quenching when exposed to these explosives, indicating high sensitivity and efficiency in detecting these hazardous substances. The quenching efficiency was reported to be as high as 86% for nitrobenzene and 57% for dimethoxy nitrobenzene, highlighting the MOF's effectiveness in practical sensing applications.[66]

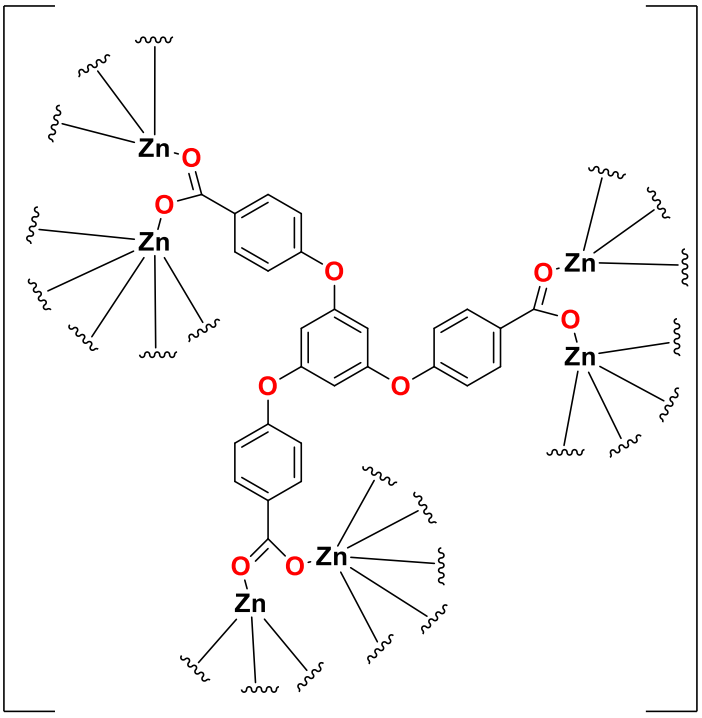

Figure 2. 21 Structure of **39**. The wavy lines indicate the repetition and spatial extension of the framework beyond the illustrated segment.

As mentioned in other research, compound **34** was also coordinated with zinc (II) and copper (II) thorough solvothermal reaction. The final MOFs were used for gas adsorption. The BET surface area for the activated 1-Cu MOF **40** (Figure 2.22) was significantly higher than that of 1-Zn, indicating enhanced gas adsorption capacity. The 1-Cu MOF **40** demonstrated effective gas adsorption for N_2, O_2, and CO_2, making it suitable for gas storage and separation applications.[65]

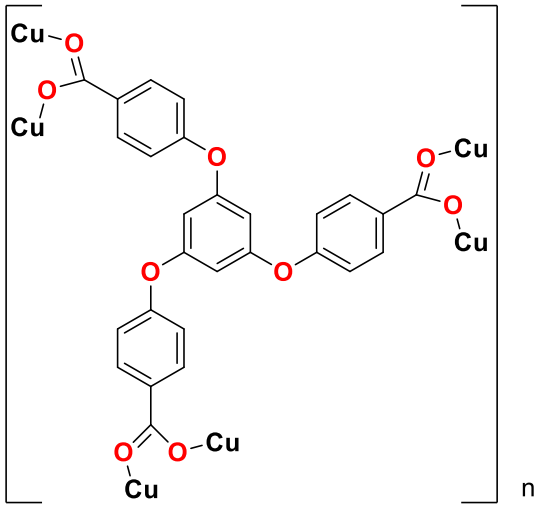

Figure 2. 22 Structure of **40**.

All of these organic linkers with a benzene core are effective for coordination reactions. However, there is potential to enhance the coordination motifs by introducing flexible arms, such as etheric bonds, to the benzene core **1**, as seen in compound **34**. In addition, we aim to replace benzoic acids branches in compound **34** with the carboxypyridines, which provides three additional coordination sites compared to compound **34** (see chapter 3). As a result, the ligand will be able to coordinate not only through the carboxylic acid group but also via the nitrogen of the pyridine ring. Additionally, we intend to replace the carboxylic acid group in the branched pyridine with other groups, such as DAT, amide, and cyano groups, all of which are excellent coordination motifs (see chapter 3). This should increase the likelihood of obtaining stable coordination compounds.

2.2 Triphenylene core ligands

Triphenylene **41** is a planar organic compound composed of four fused benzene rings, forming an 18-π-electron aromatic system with extensive delocalization in accordance with Hückel's rule (Figure 2.23). Compared to benzene **1**, triphenylene **41** exhibits a higher degree of conjugation due to its larger, more interconnected π-electron system, leading to enhanced electronic properties. The compound has the molecular formula $C_{18}H_{12}$ and exhibits D_3h symmetry.

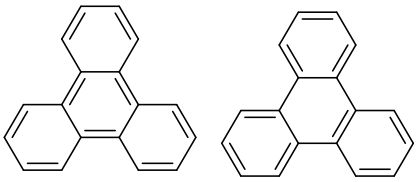

Figure 2. 23 Two resonance structures of triphenylene **41**.

In the field of material science, triphenylene derivatives are highly valued as ligands for creating metal-organic frameworks (MOFs) and complexes due to their exceptional stability and optical properties.[68–70] These characteristics make triphenylene derivatives particularly suitable for applications where both structural integrity and functional optical properties are crucial. Their unique molecular structure allows for the formation of robust frameworks with potential applications in areas such as gas storage, catalysis, and optoelectronic devices.[71–73] Additionally, the extended π-conjugation in triphenylene derivatives contributes to enhanced electronic properties, making them ideal for use in photovoltaic cells and light-emitting devices.[74]

Several organic compounds with triphenylene core have been synthesized for coordination reactions. In this section, I will introduce some of the most commonly used triphenylene-based ligands, discussing their synthesis and coordination reactions.

2.2.1 2,3,6,7,10,11-Hexathioltriphenylene (THT) (42)

Compound **42** is an organic compound with a triphenylene core. In compound **42** six thiol groups are symmetrically linked at positions 2, 3, 6, 7, 10, and 11 (Figure 2.24). It was used in several coordination reactions for making MOFs and complexes.

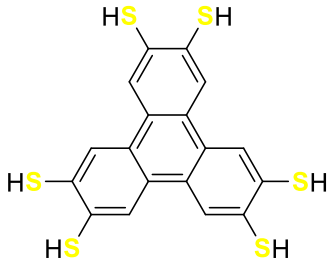

Figure 2. 24 Structure of compound **42**.

2.2.1.1 Synthesis

To synthesize compound **42**, one report describes starting from hexabromotriphenylene **43**, which underwent a nucleophilic aromatic substitution reaction with sodium sulfite **44** to produce hexamethylthiotriphenylene **45**. Compound **45** was then treated with lithium in ammonia, where lithium acted as the reducing agent. After the reduction, hydrochloric acid (HCl) was added for acidification and the yield was 91%. For purification, the solid product was washed with diethyl ether and dichloromethane (Scheme 2.11).[75]

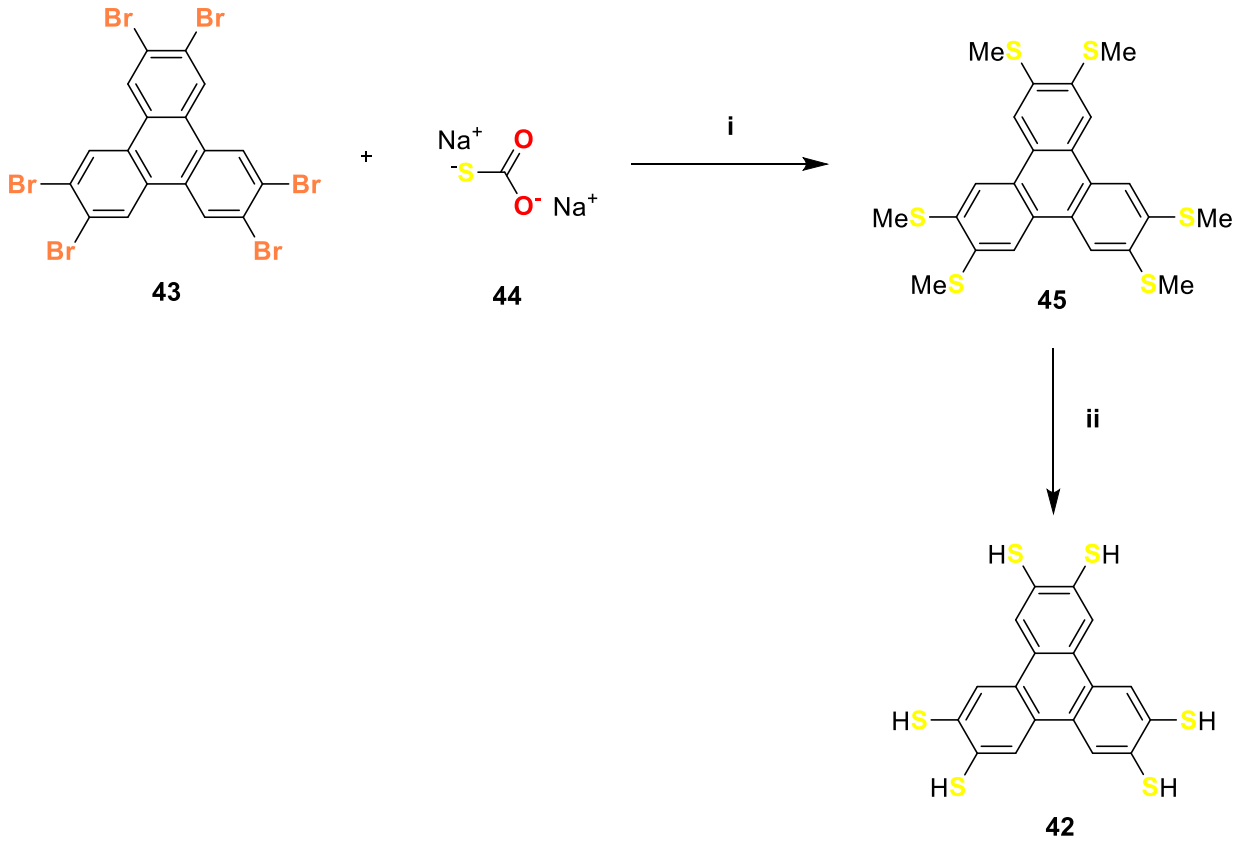

Scheme 2. 11 Synthetic route of **42**. (i) (1) Sodium methylthiolate, dimethylimidazolidinone 70°C, 4 h (2) 110°C, 30 min (3) Methyl iodide, rt, 15 min (ii) (1) Li, NH_3 (liq.), −78°C, 3.5 h (2) CH_3OH, rt, 1.5 h; (3) HCl, H_2O, Et_2O, CH_2Cl_2, 91% yield.

2.2.1.2 Coordination

Compound **42** has been utilized in various coordination reactions. For example, the MOF THTNi **46** (Figure 2.25) was synthesized through the reaction between nickel bis(dithiolene) complex and compound **42**. This MOF forms a 2D supramolecular polymer and exhibits excellent electrocatalytic performance in hydrogen evolution reactions (HER), with a Tafel slope of 80.5 mV/decade and an operating overpotential of 333 mV at a current density of 10 mA/cm. [76]

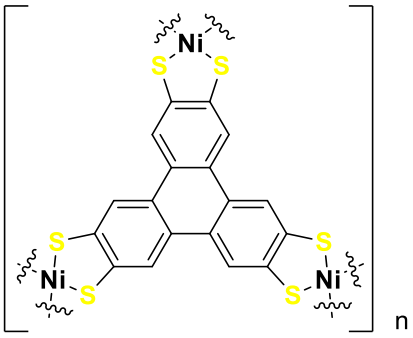

Figure 2. 25 Structure of THTNi **46**. The wavy lines indicate the repetition and spatial extension of the framework beyond the illustrated segment.

In another research, compound **42** was used as a ligand in a coordination reaction with $[Co(MeCN)_6][BF_4]_2$ **47** to produce a MOF **48** (Figure 2.26). This MOF was applied in hydrogen evolution reactions (HER), achieving notable catalytic current densities of 31 mA/cm² at –0.8 V at pH 1.3. Additionally, at pH 2.6, it demonstrated a faradaic efficiency of 97% for hydrogen production from water. The MOF exhibited high stability under acidic conditions, making it a promising catalyst for HER.[77]

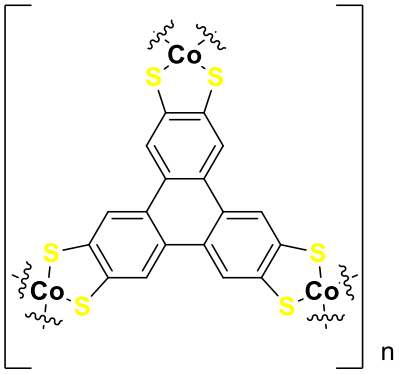

Figure 2. 26 Structure of **48**. The wavy lines indicate the repetition and spatial extension of the framework beyond the illustrated segment.

2.2.2 2,3,6,7,10,11-hexahydroxytriphenylene (HHTP) (49)

Compound **49** is an organic compound with a triphenylene core **41**, to which six hydroxy groups are symmetrically linked at positions 2, 3, 6, 7, 10, and 11 (Figure 2.27). It was used in several coordination reactions for making MOFs.

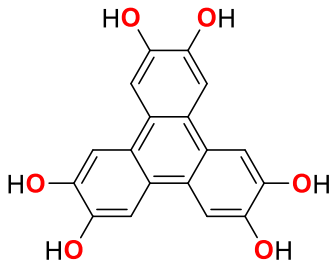

Figure 2. 27 Structure of compound **49**.

2.2.2.1 Synthesis

To produce compound **49**, various methods have been used. For instance, in one approach, the starting material was pyrocatechol **50**, which was first alkylated to synthesize 1,2-dimethoxybenzene **51**. This was followed by oxidative trimerization ($FeCl_3$) to form 2,3,6,7,10,11-hexamethoxytriphenylene **52**. Finally, the 2,3,6,7,10,11-hexamethoxytriphenylene **52** was demethylated using a mixture of hydrobromic acid and acetic acid to produce the pure compound **49** (Scheme 2.12).[78]

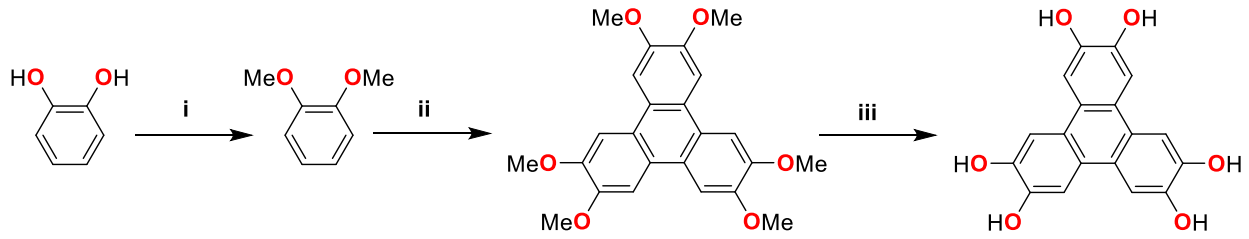

Scheme 2. 12 Synthetic route of **49**: (i) $(CH_3)_2SO_4$, K_2CO_3, Acetone, reflux (ii) (1) $FeCl_3$, CH_2Cl_2, rt; (2) CH_3OH, rt (iii) HBr/HOAc, reflux, 75% yield.

In another study, the synthesis started with **50**, which was subjected to oxidative trimerization using phenyliodine(III) bis(trifluoroacetate) (PIFA) in hexafluoroisopropanol (HFIP) as the solvent. The reaction was conducted under mild conditions with methanesulfonic acid (CH_3SO_3H) as the acid catalyst, yielding 65%. The final compound was purified by washing it with water.

Additionally, in this study, 2,2-dimethyl-1,3-benzodioxole **53** was also used as a starting material, yielding 45% (Scheme 2.13).[79]

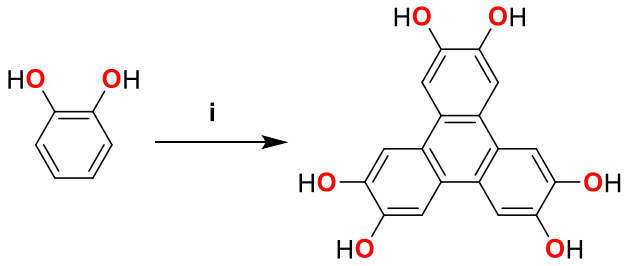

50 **49**

Scheme 2. 13 Synthetic route of **49**. (i) $PhI(OCOCH_3)_2$ (PIDA), CH_3SO_3H, $(CF_3)_2CHOH$, r.t, 45% yield.

2.2.2.2 Coordination

Compound **49** has been employed in various coordination reactions. One notable example is the synthesis of Cu_3(**49**)$_2$ **50** (Figure 2.28), a coordination compound formed from Cu (II) ions and HHTP **49**, which exhibits a high surface area and a capacitance of 22 μF/cm². This compound has been successfully used as an electrode material in batteries, where it exhibited excellent performance, retaining 75% of its initial capacity even after 500 charge-discharge cycles.[80]

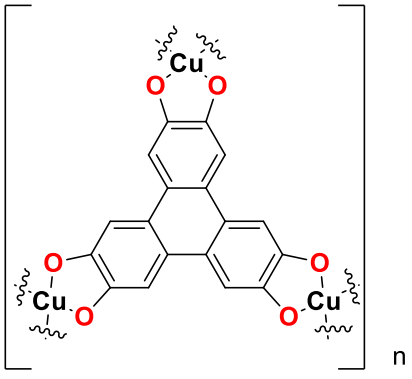

Figure 2. 28 Structure of Cu_3(**49**)$_2$ **50**. The wavy lines indicate the repetition and spatial extension of the framework beyond the illustrated segment.

The MOF Ni_9(**49**)$_4$ **51** (Figure 2.29), synthesized from HHTP **49** and Ni(II) ions and grown on 3D porous laser-scribed graphene (LSG) interdigitated electrodes on polyimide substrates, was utilized in supercapacitors, achieving a capacitance of 15.2 mF/cm² and an energy density of 4.1 μWh/cm².[81]

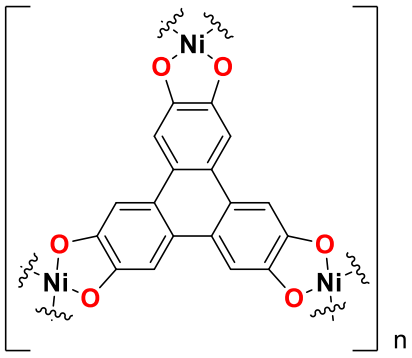

Figure 2. 29 Structure of Ni_9(**49**)$_4$ **51**. The wavy lines indicate the repetition and spatial extension of the framework beyond the illustrated segment.

MOF Cu_3(**49**)$_2$ **50**, and MOF Ni_3(**49**)$_2$ **51** were used as electrocatalysts for the oxygen reduction reaction (ORR), demonstrating high activity due to their excellent electrical conductivity and redox activity.[82]

MOF Cu_3(**49**)$_2$ **50** has been utilized as a semiconductor in photovoltaic solar cells due to its excellent charge transfer capabilities and high stability. It maintains its structure and properties under ambient conditions. The charge mobility for Cu_3(**49**)$_2$ **50** was measured at 40 °C and 70 °C, and it was 0.364 and 0.298 $cm^2 \cdot V^{-1} \cdot s^{-1}$, respectively. This high mobility facilitates efficient charge transport within the solar cell.[83]

2.2.3 Triphenylene-2,6,10-tricarboxylic acid (H_3TTCA) (52)

Compound **(52)** is an organic compound with a triphenylene core, featuring three carboxyl groups symmetrically linked at positions 2, 6, and 10 (Figure 2.30). It has been used in several coordination reactions as an organic linker for making MOFs.

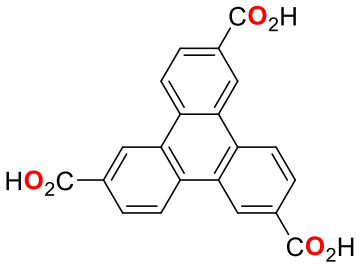

Figure 2. 30 Structure of compound **52**.

2.2.3.1 Synthesis

Compound **52** was synthesized through several steps (Scheme 2.14). First, 4-methylcyclohexanone **53** was reacted with $ZrCl_4$ as a catalyst to yield 2,6,10-trimethyl-dodecahydrotriphenylene **54**. Then, this intermediate underwent dehydrogenation using 10% Pd/C (palladium on carbon) as a catalyst to produce 2,6,10-trimethyltriphenylene **55**. Finally, 2,6,10-trimethyltriphenylene **55** was oxidized by using $Na_2Cr_2O_7 \cdot 2H_2O$ as an oxidizing agent, and hydrochloric acid was added to precipitate compound **52**, yieling 20% (Scheme 2.15).[84]

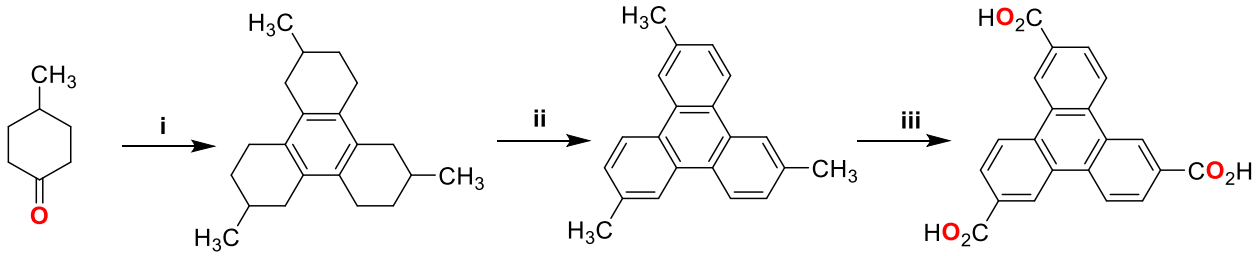

53 **54** **55** **52**

Scheme 2. 14 Synthetic route of **52**. (i) $ZrCl_4$, reflux (ii) Pd/C, triglyme, reflux (iii) $NaCr_2O_7/H_2O$, 250°C /autoclave), 20% yield.

2.2.3.2 Coordination

Compound **52** has been used as a ligand in various coordination reactions. For instance, $(Me_2NH_2)_3[Pb_2K(\mathbf{52})_2Cl_2]$ **56** (Figure 2.31) is a metal-organic framework (MOF) synthesized from compound **52** and Pb through a solvothermal reaction. This MOF exhibits photoluminescent properties, with a maximum emission when excited by light at 410 nm, making it useful for optical materials. Additionally, $(Me_2NH_2)_5[Cd_2Na(\mathbf{52})_2(H\mathbf{52})_2]\cdot 4DMF\cdot 2H_2O$ **57** is another MOF synthesized from compound **52** and Cd via a solvothermal reaction, which emits light with a maximum wavelength when excited at 400 nm.[84]

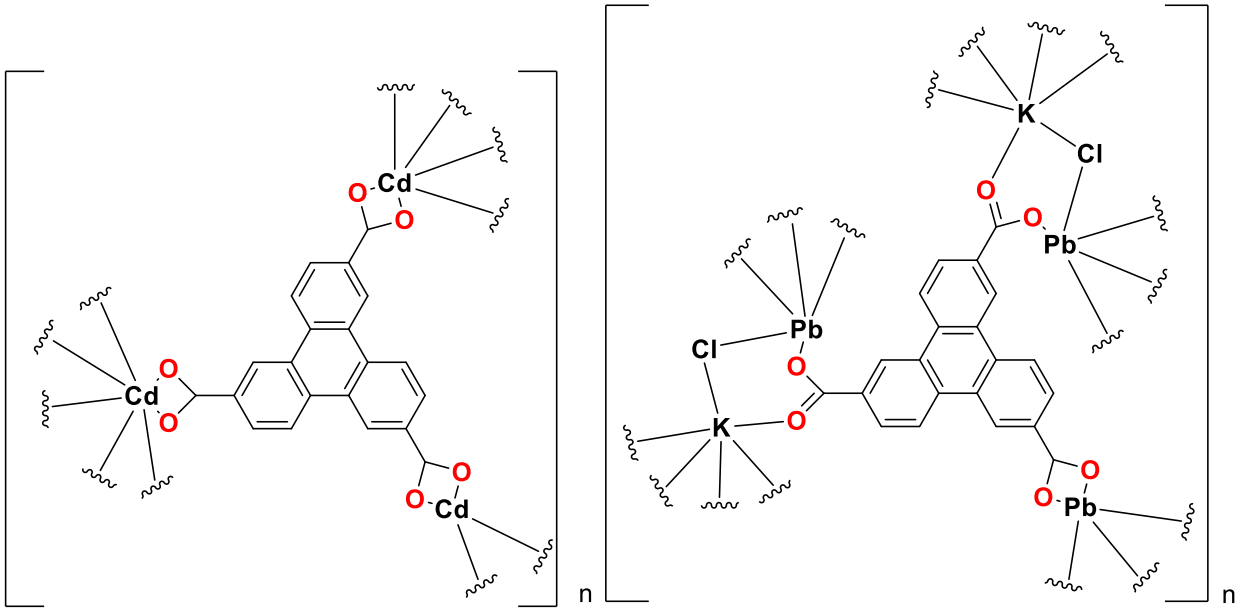

56 **57**

Figure 2. 31 Structures of compounds **55** and **56**. The wavy lines indicate the repetition and spatial extension of the framework beyond the illustrated segment.

In another study, MOF $[Tb(\mathbf{52})(DMA)(H_2O)]\bullet 7DMA\bullet 9.5H_2O$ **58** (Figure 2.32) was synthesized using compound **52** and Tb via a solvothermal reaction. This MOF is stable up to 500°C and has a porosity of 72.4%. It exhibits strong emission at wavelengths of 490 nm, 546 nm, 585 nm, and 624 nm when excited at 370 nm. Its strong luminescence makes it ideal for use as a fluorescent

sensor. The MOF was tested for detecting nitroaromatic explosives, demonstrating its potential for sensing applications.[85]

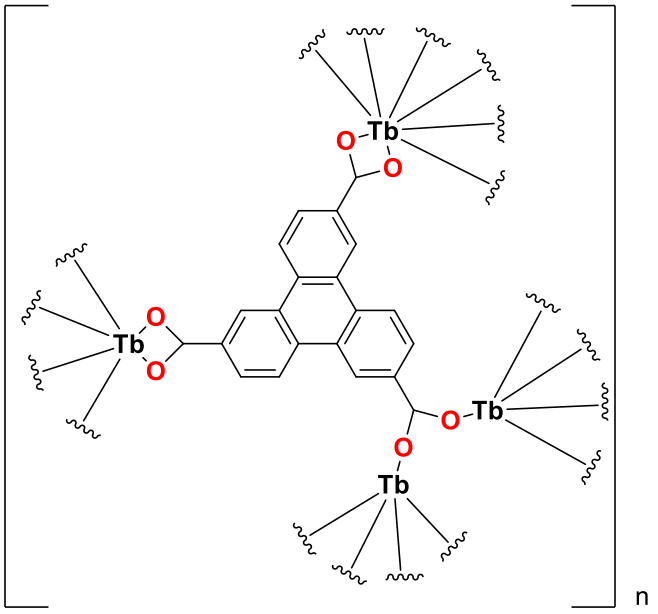

Figure 2. 32 Structure of compound **58**. The wavy lines indicate the repetition and spatial extension of the framework beyond the illustrated segment.

MOF $(Me_2NH_2)_3(MV)_{1.5}[Cd_9(\mathbf{52})_8]\cdot 15EtOH$ **59** (Figure 2.33) was synthesized from compound **52** and Cd through a solvothermal reaction. This MOF demonstrated high sensitivity to oxygen, changing color from black to dark yellow within 5 seconds upon exposure to oxygen, indicating its potential for use as a rapid oxygen sensor.[86]

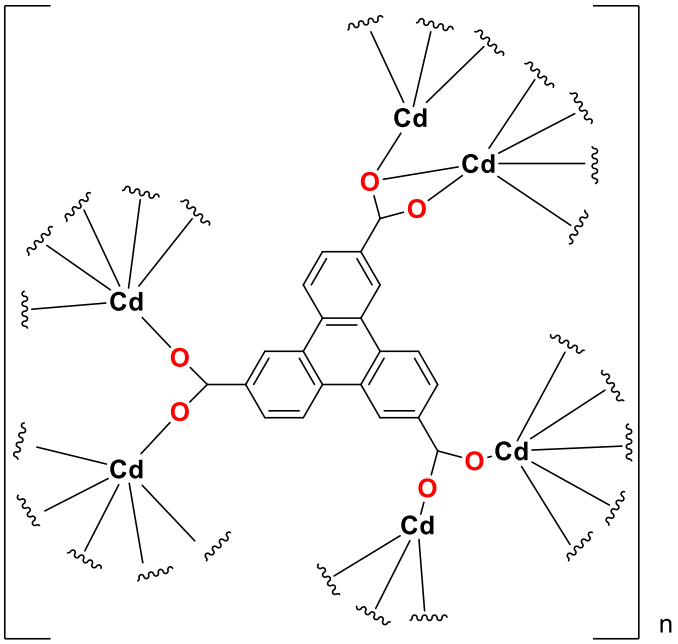

Figure 2. 33 Structure of compound **59**. The wavy lines indicate the repetition and spatial extension of the framework beyond the illustrated segment.

All of these organic linkers with a triphenylene core **41** are effective for coordination reactions. However, there is potential to enhance the coordination motifs by introducing flexible arms, such as etheric bonds, to the triphenylene core. In this project, we intend to add six etheric bonds to the triphenylene core, along with cyanopyridine substitutions on these etheric bonds (see chapter 4). This approach introduces flexibility to the triphenylene core while incorporating cyanopyridine as coordination motifs, allowing coordination through the nitrogen atoms of both the pyridine rings and the cyano groups. Additionally, we aim to hydrolyze the cyano groups into amide, carboxylic acid, and DAT groups in future work, as these functional groups are excellent for coordination chemistry.

2.3 Coronene core ligands

Coronene **60** is a planar organic molecule composed of seven fused benzene rings, forming a highly conjugated system with 24 delocalized π-electrons and approximately 20 resonance

structures (Figure 2.34). Although it does not strictly follow Hückel's rule, it is still considered aromatic due to the delocalization of π-electrons across the fused rings. It has the molecular formula $C_{24}H_{12}$ and displays D_6h symmetry. Coronene is soluble in common solvents such as toluene, dichloromethane (CH_2Cl_2), and benzene.

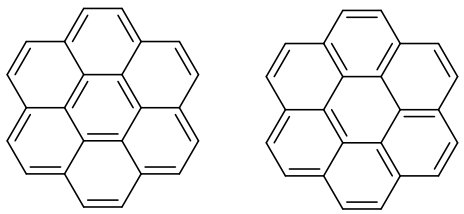

Figure 2. 34 Two resonance structures of coronene **60**.

In the field of materials science, coronene derivatives are highly valued for their extensive conjugated systems and exceptional optoelectronic properties.[87–90] However, they are used less frequently as ligands compared to benzene and triphenylene. Incorporating coronene in coordination reactions can lead to the formation of metal-organic frameworks (MOFs) with unique optical properties.[91]. In this section, I will introduce some coronene-based ligands, discussing their synthesis and coordination reactions.

2.3.1 1,2,3,4,5,6,7,8,9,10,11,12-Perthiolated coronene (PTC) (61)

Compound **61** is an organic compound featuring a coronene core, where twelve thiol groups are symmetrically attached at positions 1, 2, 3, 4, 5, 6, 7, 8, 9, 10, 11, and 12 (Figure 2.35). This structure has been employed in several coordination reactions, forming metal-organic frameworks (MOFs).

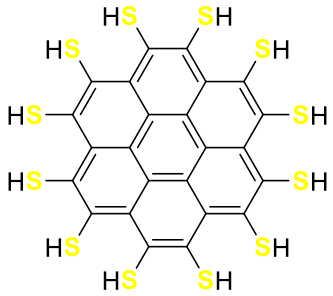

Figure 2. 35 Structure of compound **61**.

2.3.1.1 Synthesis

Compound **(61)** was synthesized through a multi-step process. It started from coronene **60**, which underwent chlorination by reacting with aluminum chloride ($AlCl_3$) and iodine chloride (ICl), producing dodecachlorocoronene **62**. Then, a nucleophilic substitution reaction was performed using benzyl mercaptan and sodium hydride (NaH), yielding dodecakis(benzylthio)coronene **63**. Through reductive cleavage of the benzyl groups, dodecathiolate coronene **64** was achieved. Finally, dodecathiolate coronene **64** was reacted with sodium borohydride ($NaBH_4$) to break the disulfide bonds, yielding compound **(61)** which was purified by washing with methanol (Scheme 2.15).[92]

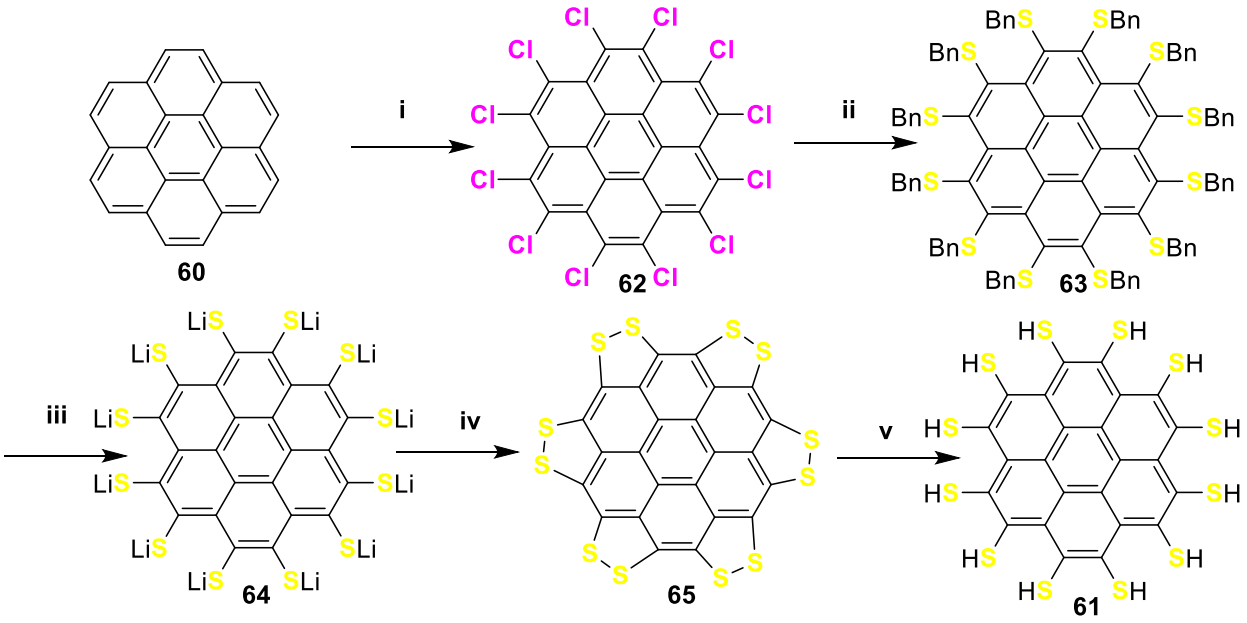

Scheme 2. 15 Synthetic route of **61**. (i) $AlCl_3$, ICl, CCl_4, 81 °C, 48 h, 93% (ii) benzyl mercaptan, NaH, DMI, 0 °C to rt, 16 h, 62%; (iii and iv) Li, THF, methanol, NH_3, -78 °C to rt, 4 h; HCl/H_2O_2/water, rt, 61% yield. (v) $NaBH_4$.[92]

2.3.1.2 Coordination

Several metal-organic frameworks (MOFs) incorporating compound **61** as a ligand have been reported. For example, Fe-PTC **66** (Figure 2.36), a MOF synthesized from compound **61** and Fe, has demonstrated catalytic activity in hydrogen evolution reaction (HER), oxygen evolution reaction (OER), and oxygen reduction reaction (ORR) with overpotentials of -0.23 V, 0.89 V, and 0.44 V, respectively. Its efficiency is comparable to that of Pt-based catalysts and Co_3O_4.[93]

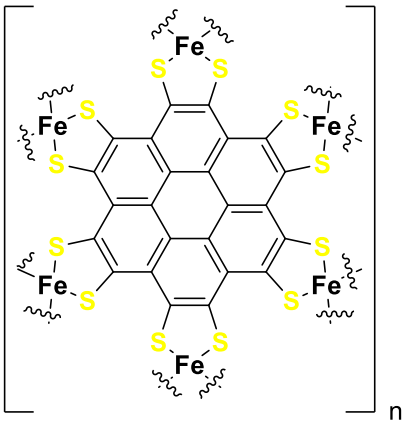

Figure 2. 36 Structure of Fe-PTC **66**. The wavy lines indicate the repetition and spatial extension of the framework beyond the illustrated segment.

In another research, Co-PTC **67** (Figure 2.37), a 2D MOF which was formed from compound **61** and Co, demonstrated excellent electrocatalytic performance for the hydrogen evolution reaction (HER), exhibiting an overpotential of 227 mV at a current density of 10 mA cm^{-2} and a Tafel slope of 189 mV/decade. The material showed high stability in acidic solutions, maintaining a stable current density of approximately 10 mA cm^{-2} for 40 hours at a constant voltage. Additionally, it retained stability after 2000 cycling tests. Co-PTC **67** also displayed impressive electrical conductivity, measuring 45 S cm^{-1} at room temperature.[94]

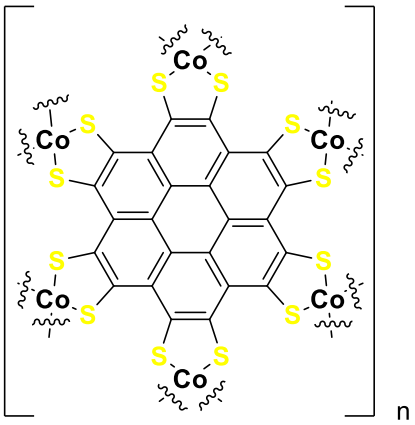

Figure 2. 37 Structure of Co-PTC **67**. The wavy lines indicate the repetition and spatial extension of the framework beyond the illustrated segment.

Ni-PTC **68** (Figure 2.38) as another example of coronene MOF, which was made from compound **61** and Ni, has been used for hydrogen evolution reaction HER, OER, and ORR, with overpotentials of -0.31 V, 0.91 V, and 0.46 V, respectively. It demonstrated high stability during these catalytic reactions.[93]

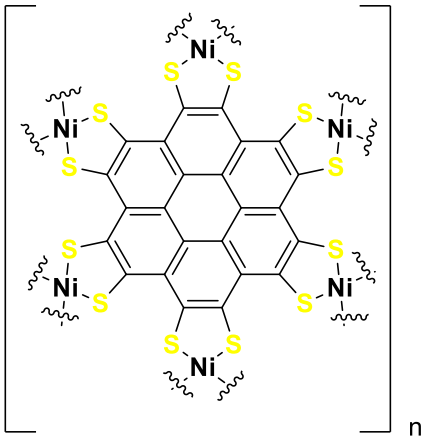

Figure 2. 38 Structure of Ni-PTC **68**. The wavy lines indicate the repetition and spatial extension of the framework beyond the illustrated segment.

2.3.2 Hexahydroxy triazacoronene (6OH-TAC) (69)

Compound **69** is an organic compound with an azacoronene core **70**, where three nitrogen atoms are positioned at the 1, 5, and 9 positions of the coronene ring and six hydroxyl groups are attached at positions 2, 3, 6, 7, 10, and 11 (Figure 2.39). The nitrogen atoms in azacoronene **69** enable potential coordination through the nitrogen sites within the azacoronene ring. Compound **69** has been used in coordination reaction for making MOF.

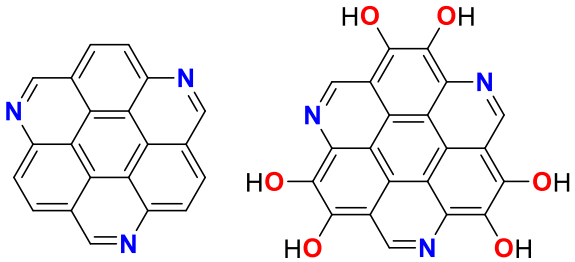

70 **69**

Figure 2. 39 Structures of compounds **69** and **70.**

2.3.2.1 Synthesis

Compound **(69)** was synthesized through the demethoxylation of 3,4,7,8,11,12-Hexamethoxy-1,5,9-triazacoronene **71 (**Scheme 2.16**).** Compound **71** was reacted with pyridine hydrochloride at 200°C for 4 hours, yielding 90% of compound **(69)** which was purified by washing with deionized water.[95]

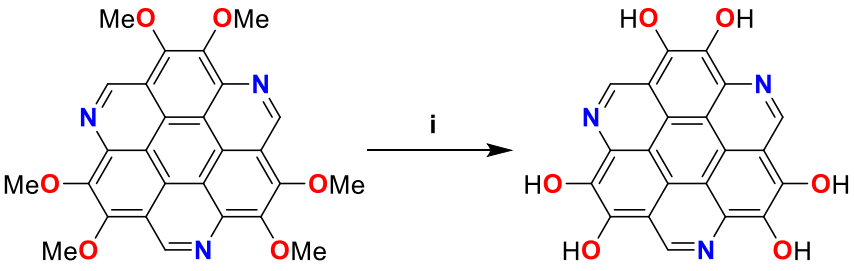

71 **69**

Scheme 2. 16 Synthetic route of **69.** (i) pyridine hydrocholoride, 200 °C, 4 h, 90% yield.

2.3.2.2 Coordination

Cu-TAC **72** (Figure 2. 40) is a 2D metal-organic framework (MOF) formed by coordination of compound **69** and copper ions. This MOF has been used as an anode material for lithium-ion batteries, where it demonstrates a superior reversible capacity of 772.4 mAh g^{-1} at 300 mA g^{-1}. Additionally, Cu-TAC **72** retains 83% of its capacity after 600 cycles at 300 mA g^{-1}, emphasizing its excellent long-term stability.[95]

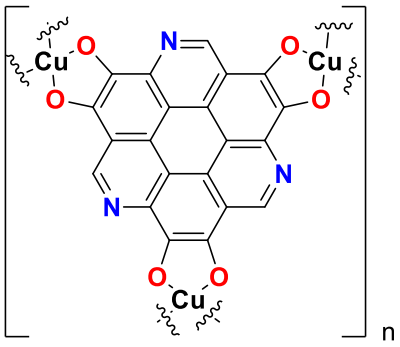

Figure 2. 40 Structure of Cu-TAC **72**. The wavy lines indicate the repetition and spatial extension of the framework beyond the illustrated segment.

These organic linkers with coronene **60** and azacoronene **70** cores are effective for coordination reactions, but there is a potential to further enhance their coordination motifs. In this project, we added three benzoic acid groups to the 2, 6, and 10 positions of 1, 5, 9-azacoronene **70** (see chapter 5). Attaching benzoic acid to the azacoronene core increases the conjugated system, while introducing carboxylic acid group, which is an excellent coordination motif, provides additional coordination sites. There is the potential to coordinate through the nitrogen atoms of the azacoronene core and the oxygen atoms of the carboxylic acid groups. These coordination sites, combined with the extended conjugation, will contribute to forming stable coordination compounds.

2.4 Coordination motifs

For coordination reactions and the synthesis of MOFs and complexes, specific coordination motifs are essential for linking organic linkers to metal centers. Several coordination motifs are

commonly used in these reactions, most of them contain heteroatoms such as nitrogen and oxygen. In this section, I will introduce the coordination motifs used in this project, which include carboxylic acid, pyridine carboxamide, cyanopyridine, and diaminotriazine. Several articles have reported coordination compounds incorporating these motifs. They contain multiple heteroatoms and possess conjugated systems that can extend conjugation with the core of the organic linker. These features facilitate the formation of coordination bonds between the organic linkers and metal ions.

2.4.1 Cyanopyridine-based coordination motifs (73-75)

Cyanopyridine **(72-74)** compounds are organic molecules consisting of a cyano group attached to a pyridine ring (Figure 2.41). These compounds have emerged as versatile building blocks with a range of biological activities, including anticancer, antibacterial, insecticidal properties, and kinase inhibition.[96] Additionally, they are considered valuable coordination motifs in coordination chemistry.[97–99]

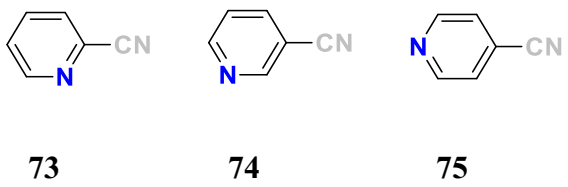

73 **74** **75**

Figure 2. 41 Structure of cyanopyridine **(73-75).**

Cyanopyridines **(73-75)** exhibit versatile coordination behavior, acting either as monodentate or bridging ligands in the synthesis of MOFs and complexes (Figure 2.42). They can coordinate through both the nitrogen of the nitrile group (N_{CN}) and the nitrogen of the pyridine ring (N_{py}).[100]

For instance, 3-cyanopyridine **74** can coordinate with metal centers through the nitrogen of the pyridine ring (N_{py}), functioning as a monodentate ligand. Alternatively, 3-cyanopyridine **74** can serve as a bridging ligand by coordinating through both the nitrogen of the nitrile group (N_{CN}) and the nitrogen of the pyridine ring (N_{py}). This dual coordination capability enables 3-cyanopyridine **(74)** to efficiently link metal centers.[100]

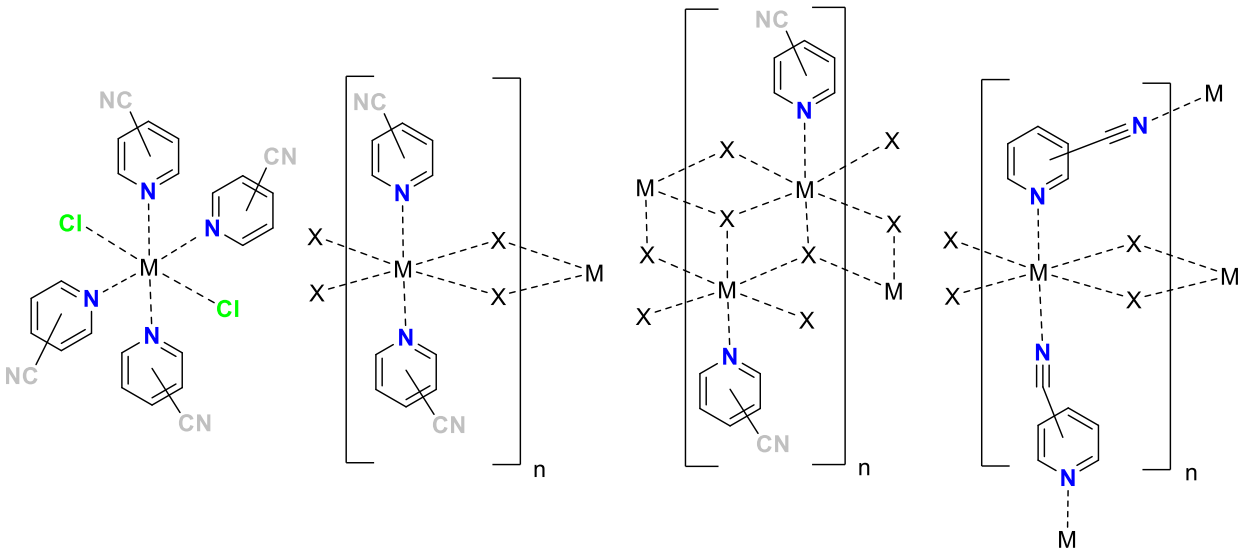

$[MX_2(CNpy)_4]_n$ $[MX_2(CNpy)_2]_n$ $[MX_2(CNpy)_1]_n$ $[MX_2(CNpy)_1]_n$

Figure 2. 42 Connectivity patterns of cyanopyridine compounds $[MX_2(CNpy)_x]_n$, (M= Mn, Fe, Co, Ni, Cu) (X=Br and Cl).[100]

In another study, the complex $[Ag_2(\mathbf{73})_2(NO_3)_2]_n$ **76** was synthesized using 2-cyanopyridine **73** as bidendate ligand and Ag (I) ions, with coordination occurring through both the pyridine nitrogen (N_{py}) and the cyano nitrogen (N_{CN}), each binding to different Ag centers. This complex exhibited a conductivity of 3.1×10^{-7} $S \cdot cm^{-1}$ at room temperature. Additionally, they reported that the complex $[Ag_4(\mathbf{73})_8(SiF_6)_2(H_2O)_2]_n$ **77**, synthesized from 3-cyanopyridine **74** and Ag (I) ions, forms a two-dimensional network. In this polymer, ligand **74** acts as a monodentate ligand, coordinating exclusively through the pyridine nitrogen (N_{py}). Furthermore, the complex $[Ag(\mathbf{74})_2(NO_3)]_n$ **78**,

synthesized from 3-cyanopyridine **78** and Ag (I) ion, features a one-dimensional helical chain in which ligand **74**, acting as a monodentate, coordinates exclusively through the pyridine nitrogen (N_{py}). It exhibits a conductivity ranging from 1×10^{-11} to 1×10^{-13} $S\cdot cm^{-1}$, classifying it as an insulator.[101]

One study explores the coordination of mixed ligands 4-cyanopyridine **75** and phthalic acid (where H_2pta= phthalic acid) with Ag(I), resulting in various complexes. These include [Ag(**75**)$_2$(Hpta)] **79**, a zero-dimensional (0D) mononuclear molecule; [Ag_2(**75**)$_2$$(Hpta)_2$] **80**, a zero-dimensional (0D) tetranuclear motif; [Ag_4(**75**)$_2$$(pta)_2(H_2O)]_n$ **81**, a two-dimensional (2D) coordination polymer; and [Ag_2(**89**)$_2$$(pta)_3(H_2O)]_n$ **82**, a one-dimensional (1D) chain structure. In all these structures, Ag(I) exclusively coordinates with the nitrogen atom of the pyridine ring, while the nitrogen of the cyano group remains non-coordinated, and cyanopyridine functions as a monodentate ligand. The resulting structures are dependent on the pH.[102]

[$Cd(NCS)_2$(**73**)$_2]_n$ **83** is a one-dimensional (1D) coordination polymer in which Cd is coordinated to 3-cyanopyridine **74.** In this polymer, **74** acts as a monodentate ligand, coordinating solely through the nitrogen atom of the pyridine ring.[103]

[$Mn(NCS)_2$(**75**)$_2]_n$ **84** forms a one-dimensional (1D) chain structure in which Mn (II) is octahedrally coordinated by two terminal N-bonded thiocyanate anions and two 4-cyanopyridine **75** ligands. Ligand **75** acts as a monodentate ligand and coordinates to Mn solely through the nitrogen atom of the pyridine ring.[104]

In complex $Zn(NCS)_2$(**74**)$_4$ **85**, the Zn(II) ion is octahedrally coordinated by four nitrogen atoms from the pyridine rings of four 3-cyanopyridine **(74)** ligands and two nitrogen atoms from terminally bonded thiocyanate anions. While in complex $Zn(NCS)_2$(**74**)$_2$ **86**, the Zn(II) ion forms

a tetrahedral complex, where it is coordinated by two nitrogen atoms from the pyridine rings of two 3-cyanopyridine **74** ligands and two nitrogen atoms from terminally bonded thiocyanate anions. In both complexes, ligand **74** is a monodentate ligand and coordinates to the metal solely through the nitrogen atom of the pyridine ring.[105]

In this project, we synthesized three novel isomers of cyanopyridine with a benzene core and four isomers of cyanopyridine with a triphenylene core (see chapters 3 and 4). These compounds can coordinate through both the nitrogen of the nitrile group (N_{CN}) and the nitrogen of the pyridine ring (N_{py}) (Figure 2.16).[100]

2.4.2 Pyridine carboxamide-based coordination motifs (87-89)

Pyridine carboxamide compounds are organic molecules featuring an amide group connected to a pyridine ring (Figure 2.43). These compounds are a form of vitamin B3 (niacin) and are vital in numerous biological processes.[106] Additionally, they serve as excellent coordination motifs. In all isomers of pyridine carboxamide, including nicotinamide, picolinamide, and isonicotinamide, the coordination sites are the nitrogen atom in the pyridine ring and the oxygen and nitrogen atoms in the carboxamide group.[107]

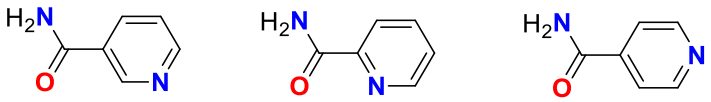

87 **88** **89**

Figure 2. 43 Structure of nicotinamide **(87)**, picolinamide **(88)**, and isonicotinamide **(89)**.

There are numerous examples of complexes and coordination polymers that employ pyridine carboxamide ligands, and the position of the amide group on the pyridine ring plays a crucial role in determining the types of coordination bonds formed (Figure 2.44). For instance, [Co(**90**)$_2$Cl$_2$] **91** is a complex where the Co (II) ion is coordinated by the nitrogen atoms of the pyridine rings and the oxygen atoms of the amide groups of the (**90)** ligands, forming a distorted octahedral environment and demonstrating high thermal stability up to 200°C. In complex [Zn(**90**)$_2$(ClO$_4$)$_2$] **92**, the Zn (II) ion is coordinated by the nitrogen atoms of the pyridine rings and the oxygen atoms of the amide groups of the (**90)** ligands as bidentate ligands. Complex [Ag(**90**)$_2$NO$_3$] **93** features the Ag(I) ion coordinated by the nitrogen atoms of the pyridine rings from two **90** ligands. The dimeric complex [Ag$_2$(**91**)$_2$(μ−**91**)$_2$]$_2$ClO$_4$·2H$_2$O **94** has each Ag(I) ion coordinated by the nitrogen atoms of the pyridine rings from two **91** ligands and one oxygen atom from the amide group of a third centrosymmetric ligand, forming a trigonal coordination geometry with both monodentate and bidentate bridging ligands. Complex [Cu(**91**)$_2$(ClO$_4$)$_2$] **95** involves the Cu (II) ion coordinated by the nitrogen atoms of the pyridine rings and the oxygen atoms of the amide groups of the **91** ligands as bidentate ligands. In complex [Cu(**90**)$_2$(NO$_3$)$_2$(H$_2$O)$_{1.5}$] **96**, the Cu (II) ion is coordinated by the nitrogen atoms of the pyridine rings from two **90** ligands, two nitrate anions, and water molecules. Complex [Co(**91**)$_2$(H$_2$O)$_2$]$_n$·2NO$_3$ **97** forms a one-dimensional (1D) polymeric complex where the Co(II) ion is coordinated by the nitrogen atoms of the pyridine rings from two **91** ligands and two water molecules. Lastly, complex [Zn$_2$(**91**)$_2$(μ−**91**)$_2$(NO$_3$)$_4$] **98** is a two-dimensional (2D) coordination polymer where the Zn (II) ion is coordinated by the nitrogen atoms of the pyridine rings from two **91** ligands and oxygen atoms from nitrate anions (Figure 2.44).[108]

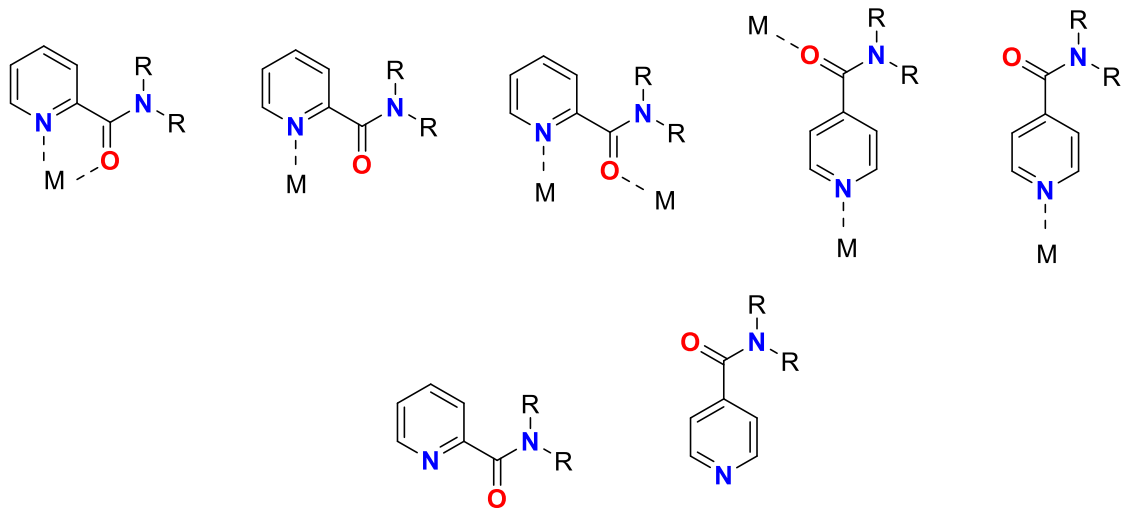

Figure 2. 44 Structures of compounds **90** and **91** and their coordination patterns (R = diisopropyl).[108]

In another study, pyridine carboxamides **92**, **93**, and **94** (Figure 2.45) were coordinated with metal ions, resulting in diverse coordination chemistries. [Tb_3(**92**)$_4$(**18**)$_3$(H_2O)$_3$] **95** is a MOF where Tb (III) ions are coordinated to the carboxylate groups of **18** and the nitrogen atoms of the pyridine rings of ligand **92**. [Zn(**92**)$_2Cl_2$] **96** is a complex where Zn (II) ion is coordinated to the nitrogen atoms of two **92** ligands and two chloride ions. [Cu(**92**)$_2$(SCN)$_2$(H_2O)] **97** is a coordination polymer where Cu (II) ions are coordinated to two nitrogen atoms from two **92** ligands, one water molecule, and two thiocyanate groups. [Cu(**92**)$_2Cl_2$] **97** is a complex where Cu (II) ions are coordinated to two nitrogen atoms of ligand **92** and two chloride ions. [Eu(**93**)$_3$(H_2O)$_3$] **98** is a complex where Eu (III) ion is coordinated to the nitrogen atoms of the pyridine rings and the oxygen atoms of the amide groups of ligand **93**. [Cu(**94**)$_2Cl_2$] **99** is a complex where Cu (II) ion is coordinated to the nitrogen atoms of two **94** ligands and two chloride ions. [Cu(**94**)$_2$(SCN)$_2$] **100** is a coordination polymer where Cu (II) ions are coordinated to the nitrogen atoms of two **92** ligands and two thiocyanate groups.[109]

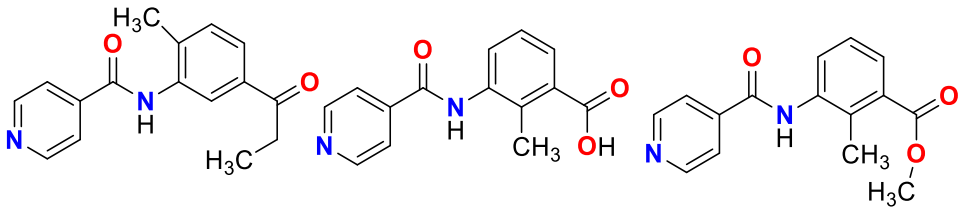

92 **93** **94**

Figure 2. 45 Structures of **92**, **93**, and **94** linkers.

In this project, we synthesized three novel isomers of pyridine carboxamide with a benzene core (see chapter 3). As previously mentioned, these compounds can coordinate through the nitrogen atom of the pyridine ring, as well as the oxygen and nitrogen atoms of the amide group.[107]

2.4.3 Pyridine carboxylic acid-based coordination motifs

Pyridine carboxylic acids are organic molecules distinguished by a carboxyl group attached to a pyridine ring (Figure 2.46). They are considered among the best coordination motifs. In all isomers of pyridine carboxylic acids, including isonicotinic acid **101**, picolinic acid **102**, and nicotinic acid **103**, the coordination sites are the nitrogen atom in the pyridine ring and the oxygen atoms in the carboxyl group.[110]

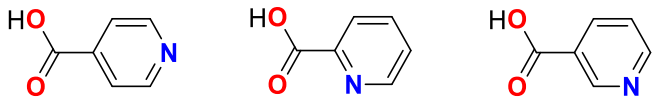

101 **102** **103**

Figure 2. 46 Structures of isonicotinic acid **101**, picolinic acid **102**, and nicotinic acid **103**.

Several complexes and MOFs have been synthesized using pyridine carboxylic acids (Figure 2.47) as coordination motifs. For example, in a particular study, pyridine-2,6-dicarboxylic acid **104** was employed as a ligand to coordinate with Cu (II) ions. The coordination involved nitrogen atoms from the pyridine ring and oxygen atoms from the carboxylate groups, resulting in the formation of a metal-organic framework (MOF) with the composition [Cu(**105**)(**104**)] **107**. Additionally, **104**, thiocyanate (SCN), and water (H_2O) were used as ligands to coordinate with Cu (II), resulting in [Cu(**104**)$_2$(SCN)$_2$(H_2O)] **108**, a coordination polymer. In this polymer, nitrogen atoms from the pyridine ring of **104**, nitrogen atoms from the thiocyanate ions, and oxygen atoms from the water molecule are coordinated to the metal ion. Another example is complex [Zn(**104**)$_2$$Cl_2$] **109**, was synthesized using **104**, chloride (Cl), and Zn (II) ion, where the ligands coordinated through nitrogen atoms from the pyridine ring of **104** and chloride ions. Lastly, Eu (III) was coordinated with **104** and water (H_2O) through nitrogen atoms of the pyridine ring, oxygen atoms of the carboxylic groups, and oxygen atoms from water molecules to form [Eu(**104**)$_3$(H_2O)$_3$] **110**.[11187]

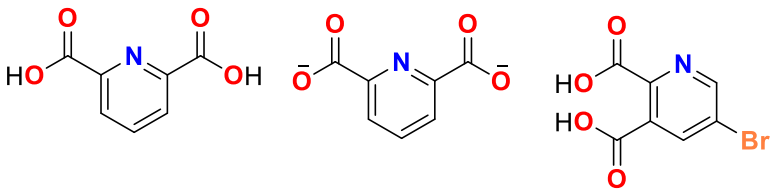

104 **105** **106**

Figure 2. 47 Structures of **104**, **105**, and **106**.

In another research, Co-MOF 1 **111** (Figure 2.48-a), a metal-organic framework (MOF) consisting of 5-bromopyridine-2,3-dicarboxylic acid **106** and water molecules as ligands, was synthesized by a solvothermal reaction. In this MOF, Co (II) is coordinated with two oxygen atoms and one nitrogen atom from the ligand, as well as three oxygen atoms from coordinated water molecules. It exhibited high thermal stability, remaining stable up to about 280°C. Conversely, Co-MOF 2 **112** (Figure 2.48-b), also synthesized by a solvothermal reaction, is a MOF in which the Co (II)

ion is coordinated with two carboxyl oxygen atoms and one nitrogen atom from the ligand, along with three oxygen atoms from coordinated water molecules. This MOF demonstrated stability up to 190°C.[112]

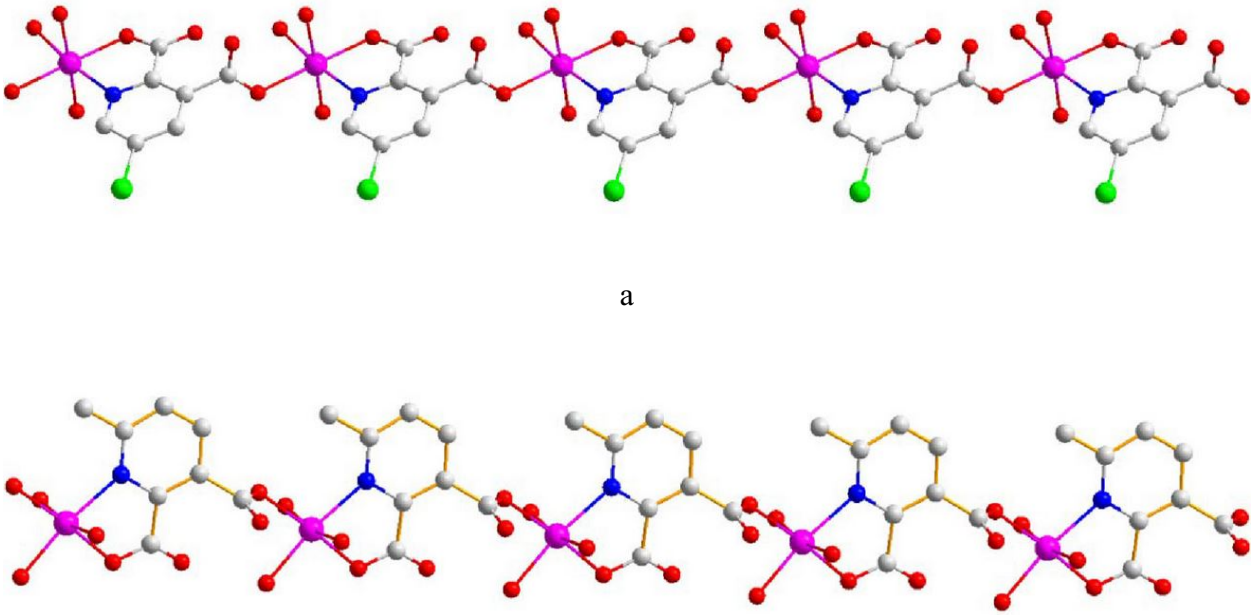

a

b

Figure 2. 48 (a) 1D chain structure of Co-MOF 1 **111** (b) 1D Chain structure of Co-MOF 2 **112**. Atom color code: C gray, Co pink, O red, and N blue.[112]

In another study, Pd(II) and Pt(II) ions were coordinated with 2,2′-bipyridyl-5,5′-dicarboxylic acid **113** and 2,2′-bipyridyl-4,4′-dicarboxylic acid **114** under hydrothermal conditions. In all synthesized complexes [Pd(**113**)$Cl_2 \cdot 2H_2O$] **115**, [Pt(**113**)$Cl_2 \cdot 2H_2O$] **116**, [Pd(**114**)$Cl_2 \cdot H_2O$] **117**, and [Pt(**114**)$Cl_2 \cdot H_2O$] **118** the metal ions were coordinated to two nitrogen atoms from the bipyridyl ligands and two chlorine atoms (Figure 2.49).[113]

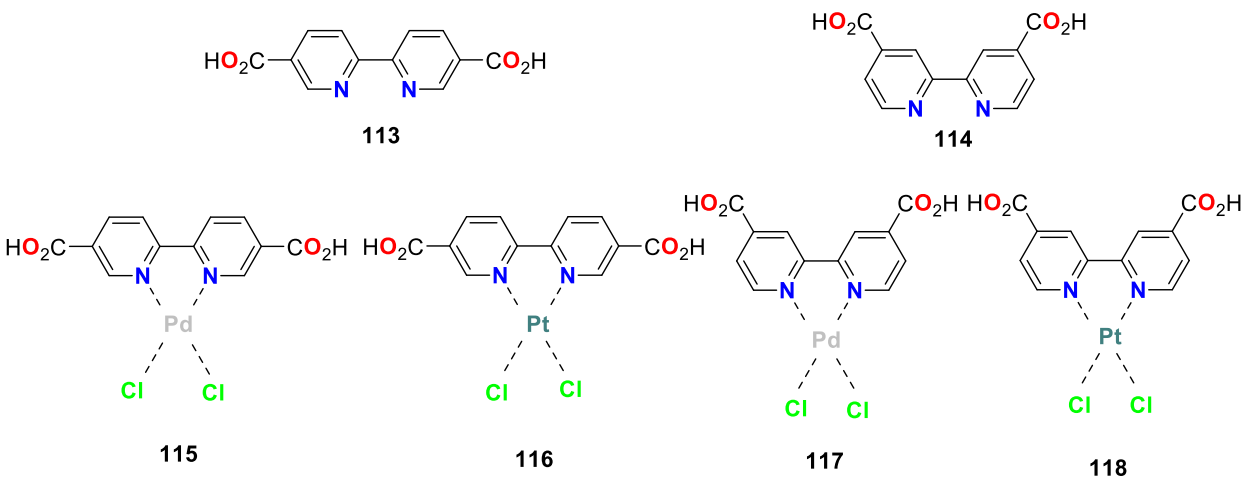

Figure 2. 49 Structures of **113-118**.[113]

In this project, we synthesized three novel isomers of pyridine carboxylic acids with a benzene core (see chapter 3). As previously mentioned, these compounds can coordinate through the nitrogen atom of the pyridine ring and the oxygen atoms of the carboxyl group.[110]

2.4.4 [1,3,5] Triazine-2,4-diamine-based coordination motifs (119)

[1,3,5]triazine-2,4-diamine **119** is a heterocyclic compound characterized by the presence of both a pyridine ring and a triazine ring (Figure 2.50). The triazine ring in this compound has two amine groups (-NH_2) located at position 2 and position 4, and a pyridine ring is attached at position 6. This compound can be used in various chemical applications, including materials science and pharmaceuticals, due to its unique structural properties.[114]

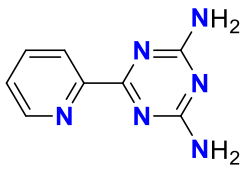

Figure 2. 50 Structure of [1,3,5] triazine-2,4-diamine **119**.

Several coordination compounds have been synthesized using [1,3,5] triazine-2,4-diamine **119** derivatives. These compounds exhibit various coordination sites, including nitrogen atoms in the triazine ring, amine groups, and nitrogen atoms in the pyridine ring. For instance, in a study, various metal ions were coordinated with **119**, resulting in the formation of the complexes [Co(**119**)$_2$(NO$_3$)$_2$] **120**, [Ni(**119**)$_2$(NO$_3$)$_2$] **121**, [Cu(**119**)$_2$(NO$_3$)$_2$] **122**, and [Zn(**119**)$_2$(NO$_3$)$_2$] **123**. In all these complexes, the coordination sites include two nitrogen atoms from the pyridine rings, two nitrogen atoms from the triazine rings, and two oxygen atoms from nitrate ions (Figure 2.51).[115]

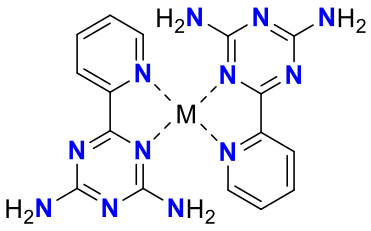

Figure 2. 51 Coordination of **119** to Metal Ions (M= Co, Ni, Cu, and Zn).[115]

In another study, copper (II) was coordinated with 6-chloro-N,N,N',N'-tetrakis-pyridin-2-ylmethyl-[1,3,5]triazine-2,4-diamine **124** and 6-chloro-N,N'-bis-pyridin-2-ylmethyl-N,N'-bis-thiophen-2-ylmethyl-[1,3,5]triazine-2,4-diamine **125** (Figure 2.52). In the complex [Cu$_2$Cl$_4$(**124**)] ·3MeOH **126**, the copper (II) ion is coordinated by three nitrogen atoms from the dipicolylamine unit of **124** and two chloride anions. In complex [Cu$_4$(NO$_3$)$_8$(**124**)$_2$] ·2.07CH$_2$Cl$_2$·0.93MeOH **127**, copper (II) ions are coordinated by three nitrogen atoms from the dipicolylamine moiety of **124** and two nitrate ions. For complex [Cu$_2$Cl$_4$(**125**)$_2$] **128**, the copper (II) ion is coordinated by two pyridine nitrogens, one nitrogen from the triazine unit, and two chloride anions. Lastly, in complex [Cu(NO$_3$)$_2$(**125**)]·CH$_2$Cl$_2$ **129**, the copper(II) ion is coordinated by two nitrate oxygens, two pyridine nitrogens, and one nitrogen from the triazine ring.[116]

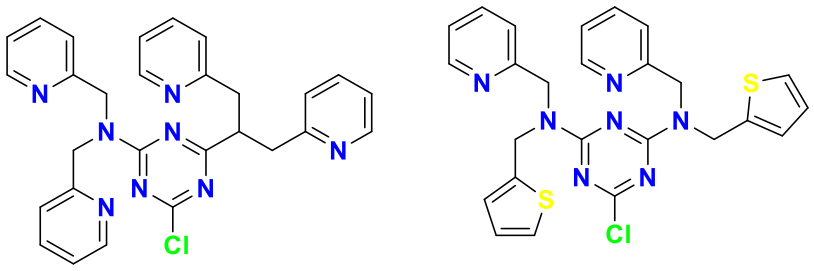

124 **125**

Figure 2. 52 Molecular structures of the ligands **124** and **125**.[116]

In a different report, DAT-MOF-1, constructed from compound **130** (Figure 2.53) and Cu (II) ions, features copper centers coordinated to both a nitrogen atom of the triazine ring and an oxygen atom of the carboxylate group. This MOF was designed for the selective separation of benzene from cyclohexane. Ideal adsorbed solution theory (IAST) calculations revealed an adsorption selectivity for equimolar benzene/cyclohexane mixtures exceeding 200, highlighting the material's high efficiency in hydrocarbon separation.[117]

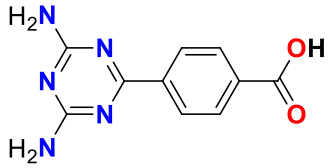

Figure 2. 53 Structure of compound **130**.

In this project, we synthesized a novel [1,3,5]-triazine-2,4-diamine, in which two [1,3,5]-triazine-2,4-diamine units are linked to a benzene core through etheric bonds (see chapter 3). As previously mentioned, this compound can coordinate with metal ions through the nitrogen atoms of the triazine ring, amine groups, and nitrogen atoms of the pyridine ring.[115]

2.5 Conclusion

In conclusion, this literature review demonstrated that organic linkers with benzene, triphenylene, and coronene cores have been employed in various coordination reactions, showcasing unique properties and highly conjugated systems. Furthermore, the study revealed that coordination motifs such as carboxylic acid, [1,3,5]triazine-2,4-diamine, pyridine carboxylic acids, pyridine carboxamide, and cyanopyridine can effectively facilitate coordination reactions, leading to the formation of stable MOFs and complexes. In addition, it is essential to have organic linkers with multiple coordination motifs that are symmetrically connected to the cores.

In this project, we intend to add etheric bonds to the benzene core to increase flexibility and the conjugated system, along with adding DAT groups, pyridine carboxamide, cyanopyridine, and pyridine carboxylic acids as coordination motifs. Similarly, we plan to add etheric bond to the triphenylene core to enhance flexibility and conjugation, along with adding cyanopyridines as coordination motifs. Furthermore, we intend to attach benzoic acid groups to an azacoronene core to increase the conjugated system and improve the coordination motifs. In all these designed compounds, the symmetry of the coordination motifs on the cores was considered to enhance the likelihood of obtaining MOFs.

In the following sections in different chapters, I will introduce the benzenes, triphenylenes, and azacoronene synthesized in this project for coordination chemistry.

Chapter 3

Organic linkers with benzene cores

3.1 Introduction

Benzene serves as the core structure of ligands that have been utilized in various coordination compounds. In this chapter, we present the synthesis and characterization of ten novel organic linkers based on the benzene core. The design of these molecules incorporates multiple coordination motifs symmetrically positioned on the benzene core. This symmetry enhances the likelihood of forming coordination polymers or metal-organic frameworks (MOFs).

These molecules include three isomers of 1,3,5-tri-cyanopyridine-benzene (compounds **121**-**133**), three isomers of 1,3,5-tri-pyridinecarboxamide-benzene (compounds **134**-**136**), two isomers of 1,3,5-tri-carboxypyridine-benzene (compounds **137** and **139**), 1,3,5-tri-carboxylatepyridine-benzene (compound **141**), and diamino triazine (compound **145**) (Figure 3.1).

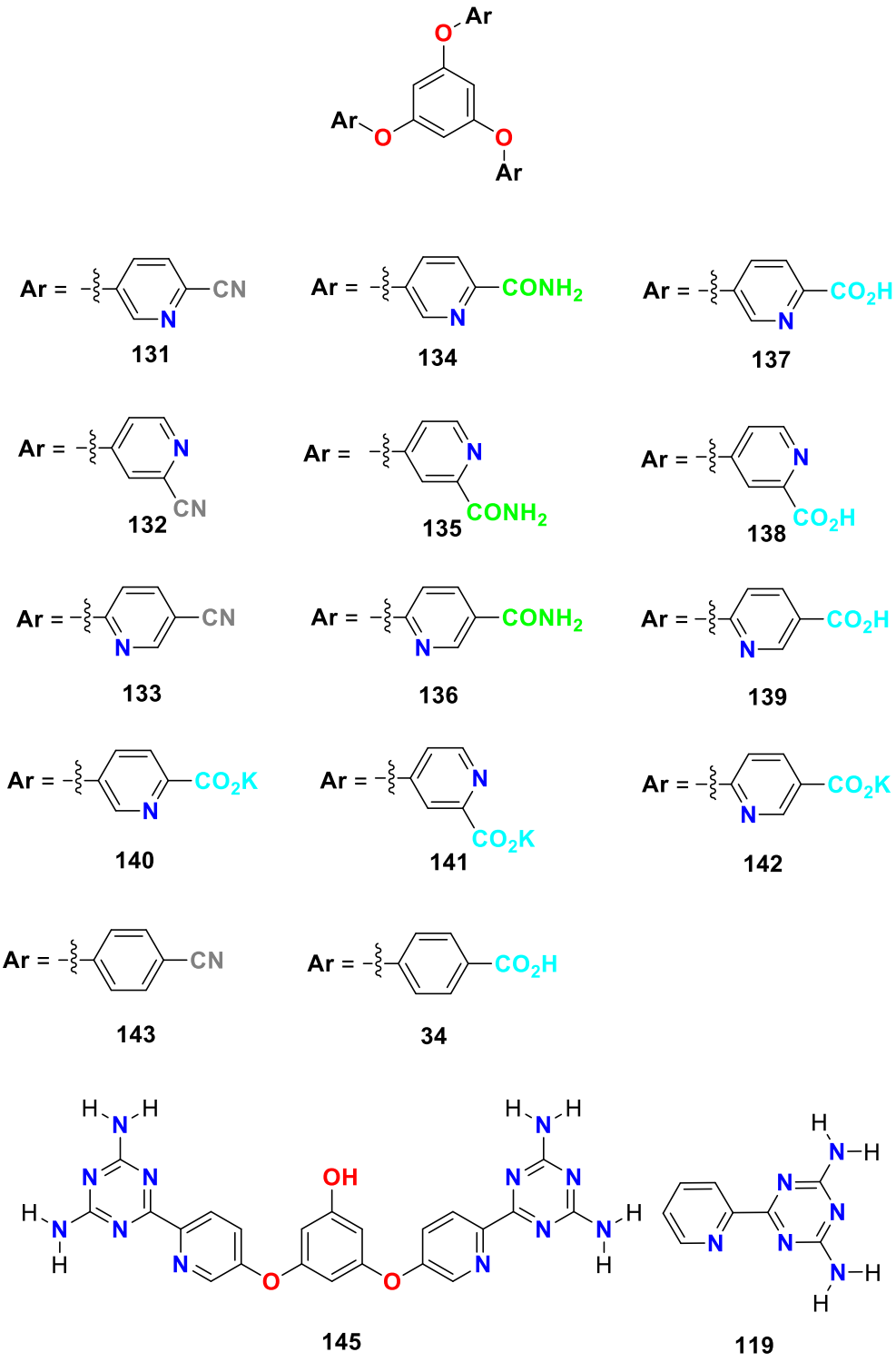

Figure 3. 1 Molecular structure of **34**, **131**, **132**, **133**, **134**, **135**, **136**, **137**, **138**, **139**, **140**, **141**, **142**, **143**, **145**, and **119**.

3.2 Compounds 131, 132, 133, 134, 135, 136, 137, 139, and 141

4,4′,4″-[1,3,5-benzenetriyltris(oxy)]tris[benzoic acid**] 34** (Figure 3.1) is an organic compound with a central benzene ring linked to three symmetrically distributed benzoic acid groups via ether bonds. This compound has been widely used as a ligand in various coordination reactions, efficiently coordinating through the oxygen atoms of its carboxylic acid groups (as mentioned in chapter 2).[60–64]

In this research, we aim to introduce novel organic linkers with additional coordination sites by replacing all three benzene rings, which act as branches, with pyridine rings **137**-**139** (Figure 3.1). This modification will enhance the coordination capabilities of **34** by enabling coordination through both the nitrogen atoms of the pyridine rings and the oxygen atoms of the carboxylic acid groups like other carboxypyridine compounds.[118–121]

3.2.1 Synthesis

3.2.1.1 Neocleophilic substitution reaction

As described in chapter two (section 2.1.5.1), compound **143** was synthesized via various nucleophilic substitution reactions.[60,66] In this research to synthesize compounds **137**-**139**, we first prepared 1,3,5-tri-cyanopyridine-benzenes **131**-**133** through nucleophilic substitution reactions, as illustrated in (Scheme 3.1). In this reaction, benzene-1,3,5-triol **35** was reacted with the corresponding cyano-bromo-pyridines, producing cyanopyridines **131**-**139**. These compounds were purified by extraction with dichloromethane, followed by evaporation of the CH_2Cl_2 under reduced pressure to yield a solid residue. The residue was further purified by washing with diethyl ether. The yields of **131**-**133** were 67%, 65%, and 68% respectively. Cyanopyridine compounds **131**-**133** are characterized by the presence of a cyano group (-CN) attached to a pyridine ring. Besides serving as precursors to the target carboxylic acids **137**-**139**, these derivatives are excellent candidates for coordination reactions, coordinating through both the nitrogen atom of the pyridine ring and the nitrogen of the cyano group.[122–124] Furthermore, these compounds exhibit potential

biological activities, including anticancer, antibacterial, insecticidal activities, and kinase inhibition.[125–127]

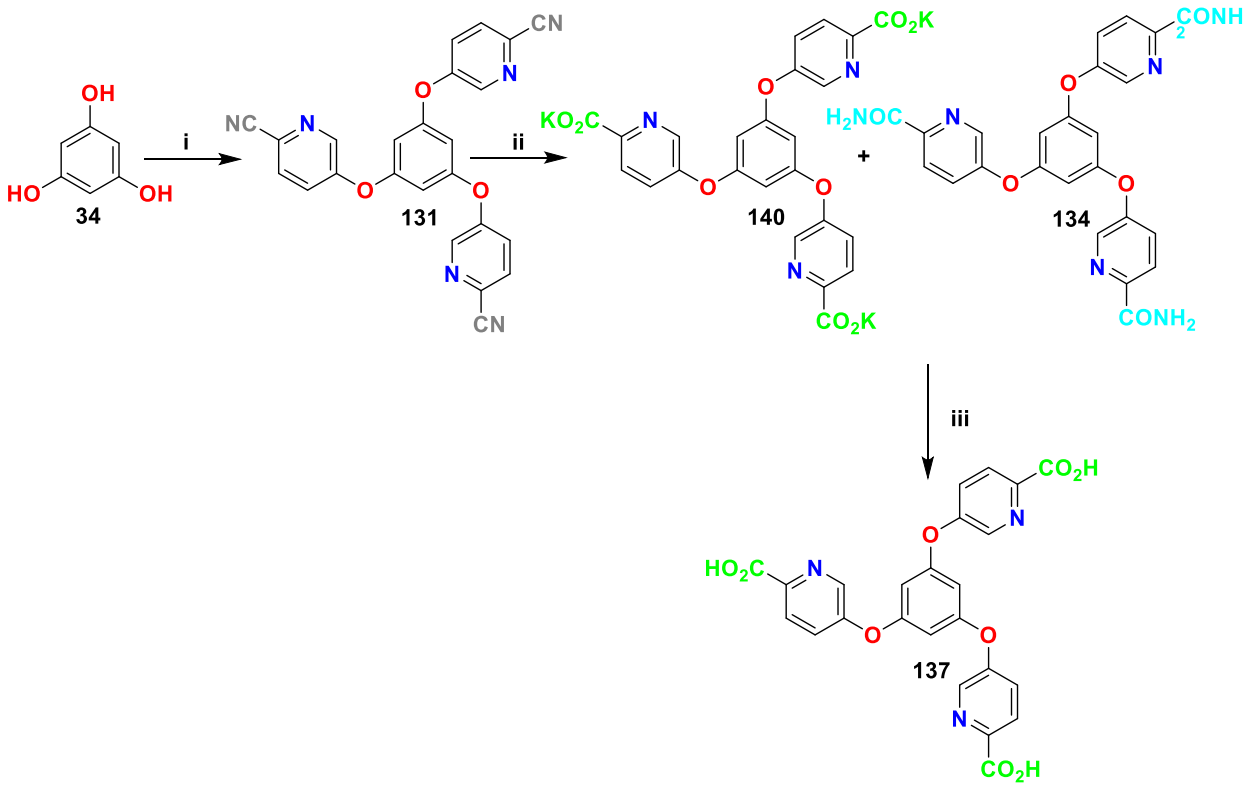

Scheme 3. 1 Synthesis route for synthesizing **131**, **134**, and **137**. (i) corresponding bromopyridine carbonitrile, K_2CO_3, DMF/Toluene, reflux (ii) KOH, H_2O reflux (iii) HCl.

3.2.1.2 Hydrolysis of cyanopyridines

Several methods have been used to hydrolyze the cyano group. Cyano compounds can be hydrolyzed in acidic, basic, and catalytic conditions.[128–130] In this research, basic conditions were chosen, avoiding both acidic conditions and catalysts. Basic hydrolysis is milder than acidic hydrolysis, resulting in fewer side reactions, and it also eliminates the challenges associated with catalyst separation. An additional advantage of the basic conditions used in this project is that they allowed for the synthesis of both amide and carboxylic acid derivatives, which were easily

purified. In contrast, the acidic conditions reported in previous studies (section 2.1.5.1) yielded only carboxylic acid derivatives.[60,66]

Compounds **131**-**133** were hydrolyzed under basic conditions and formed amidepyridines **134**-**136**, carboxylicacidpyridine **137** and **139**, and carboxylate **141** (Scheme 3.1). Compounds **134**-**136** also serve as effective coordination motifs, offering the potential for coordination bonds between metal ions, amide groups, and the nitrogen atoms of the pyridine rings.[131–133]

In hydrolysis reactions, reaction time is an important factor affecting the yield of the final compounds. The results reveal that after four hours, cyanopyridine was entirely consumed, yielding only amide and carboxylate salt (Table 3.1). After the consumption of all cyano groups, the amide group is converted to carboxylate group. Therefore, after 24 hours, the percentage of carboxylate increases while the percentage of the amide group decreases.

Additionally, the hydrolysis of the cyano compounds was investigated using different equivalents of KOH (Table 3.1). The results show that increasing the KOH equivalent from 5 to 10 led to a significant increase in the yield of carboxylate, while the yield of the amide decreased. This suggests a direct conversion of the amide to carboxylate, highlighting the impact of KOH equivalence on the reaction pathway.

It is noticeable that, upon acidification, all carboxylate groups **140**-**142** precipitated to produce carboxylic acids. However, the carboxylate salt of compound **138** did not precipitate and remained in its carboxylate form compound **141**.

Table 3. 1 Reaction conditions and yields for the hydrolysis of cyano compounds **131**, **132,** and **133**.

Compound			Reaction conditions : 4h, 5 eq. KOH, reflux, 200 µL HCl 37%		Reaction conditions : 24h, 5 eq. KOH, reflux, 200 µL HCl 37%		Reaction conditions : 24h, 10 eq. KOH, reflux, 300 µL HCl 37%	
Cyano compound hydrolysed	Amid formed	Acid formed	Yield of amide (%)	Yield of acid (%)	Yield of amide (%)	Yield of acid (%)	Yield of amide (%)	Yield of acid (%)
131	**134**	**137**	26	40	22	46	~1	63
132	**135**	**138**	24	-	20	-	~1	-
133	**136**	**139**	30	29	23	33	~1	52

3.2.2 Results and discussion

3.2.2.1 Comparison of 131-133

1,3,5-tri-cyanopyridine-benzenes **131-133** were synthesized by a nucleophilic reaction between bromo cyanopyridines and benzene-1,3,5-triol **34.**[134] In all three isomers, there are four distinct types of protons, each with its unique characteristics (Figure 3.2). In all isomers, the Hd protons of the benzene core are less deshielded compared to the others, peaking at 7.10, 7.24, and 7.10 ppm for isomers **131**, **132**, and **133**, respectively. The Hd protons in compounds **131** and **133** exhibit the same deshielding effect due to their identical conjugation and chemical environment. In molecule **131**, Hc, with a doublet pattern peaked at 8.08 ppm. Hb displays a doublet of doublets pattern at 7.77 ppm. Ha is showing a doublet peak at 8.64 ppm. In molecule **132**, Hb is observed as a doublet of doublets at 7.48 ppm, Ha as a doublet peaked at 7.92 ppm and Hc as a doublet peaked at 8.65 ppm. In molecule **133**, Hc is identified as a doublet of doublets at 8.34 ppm. Hb presents itself as a doublet at 7.29 ppm. Ha appears as a doublet at 8.70 ppm. These chemical shift values are within the standard range.[135]

One can see that protons in pyridine rings are more deshielded compared to those in benzene rings. While benzene protons are mainly deshielded by the ring's π electrons, pyridine's protons face additional deshielding due to the nitrogen atom within the ring. Particularly, protons at the α-position of the N-pyridyl group experience heightened deshielding. Therefore, Ha in isomer **131** (8.64 ppm) and **133** (8.70 ppm) and Hc in isomer **132** (8.65 ppm) are more deshielded than the others (7.29 to 8.34 ppm). In addition, it is observed that the ^{3}J coupling constant in molecule **132** (5.8 Hz) is lower than in molecules **131** and **133** (~8.6 Hz) because the nitrogen atom in the pyridine ring of molecule **132** is closer to Hc. This difference highlights the variation in chemical environments of protons among the isomers.[136]

Furthermore, based on the IR spectra of all three isomers of cyanopyridine benzene **131-133** (Figure 3.3) (Table 3. 4), the presence of peaks around 2235 cm^{-1} indicates the existence of a cyano group similar to those observed in compounds **143**[137] and **144**[138] and the peaks at around 1120 cm^{-1} in all isomers indicate the formation of the C-O bond similar to those observed in compounds **146**[139] and **34**[140].

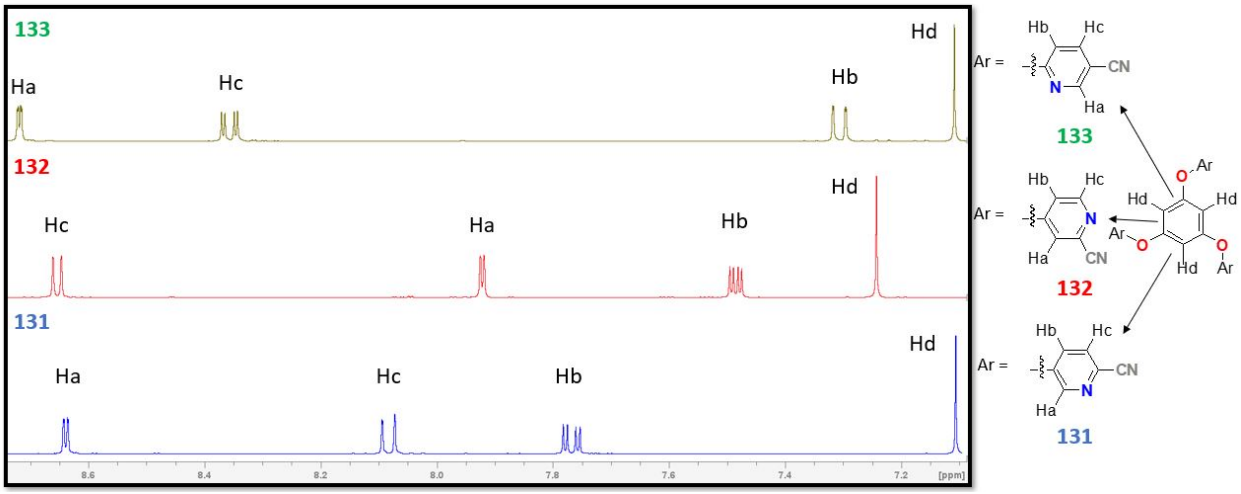

Figure 3. 2 ^{1}H NMR for molecules **131-133** in DMSO-d_6.

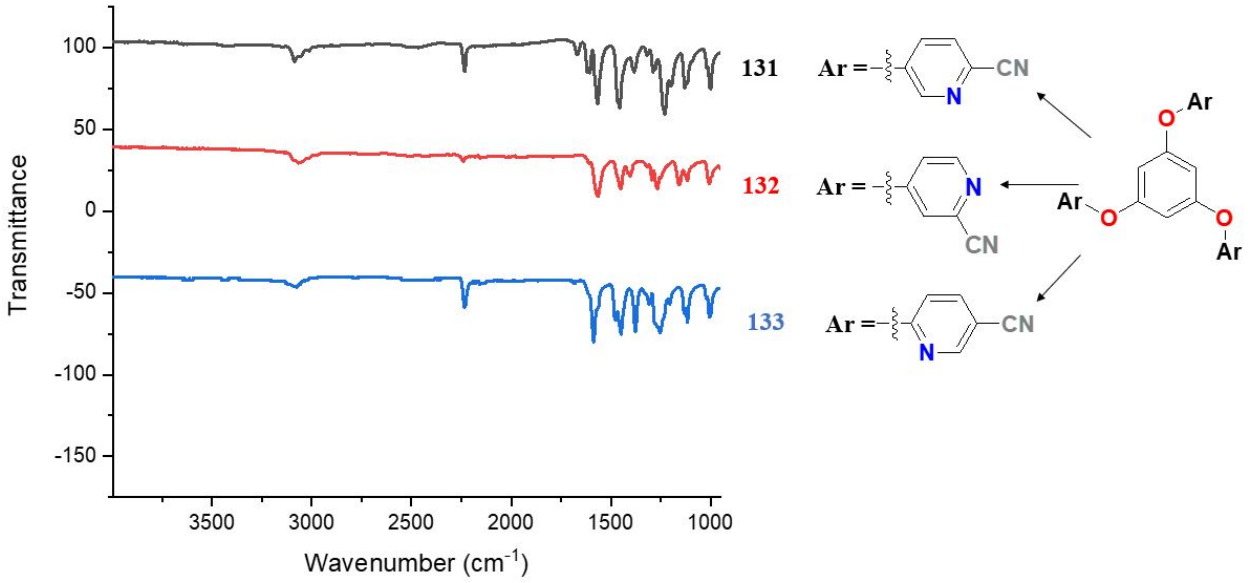

Figure 3. 3 IR spectra for molecules **131-133**.

3.2.2.2 Comparison of 134-136

1,3,5-tri-pyridinecarboxamide-benzene derivatives **134-136** were synthesized by the hydrolysis of the respective cyanopyridine derivatives **131**-**133**. They were characterized by ^{1}HNMR as shown in (Figure 3.4). Differences in the chemical shifts of the amide protons are observed in all isomers and can be attributed to the influence of hydrogen bonding, including both intramolecular and intermolecular interactions. These factors restrict the rotation of the amide groups, resulting in differing degrees of deshielding for the protons of NH_2. As a result, the protons in the amide groups exhibit distinctive chemical shifts in the NMR spectra. Similar behavior has also been observed in related compounds.[139] In compounds **134**-**136**, like in **131**-**133**, the Hd protons of the benzene ring are less deshielded compared to the protons of the pyridine ring, peaking at 6.87, 7.14, and 6.94 ppm respectively.

In molecule **134**, two singlet peaks are detected at chemical shifts of 7.59 ppm and 8.02 ppm, attributed to the protons within the amide functional group HN_2. Hb displays a doublet of doublets at a chemical shift of 7.68 ppm, while Hc appears as a doublet peak at 8.05 ppm. Ha is also observed as a doublet peak with a chemical shift of 8.46 ppm. In molecule **135**, Hb exhibits a doublet of doublet at 7.29 ppm. Ha is a doublet peak located around 7.61 ppm. Two singlet peaks at chemical shifts of 7.72 ppm and 8.16 ppm are attributed to the protons within the amide functional group. Hc is observed as a doublet peak at 8.55 ppm. In molecule **136**, Hb is observed at a chemical shift of 7.15 ppm, appearing as a doublet peak. Two singlet peaks at chemical shifts of 7.50 ppm and 8.07 ppm are attributed to the protons within the amide functional group. Hc appears as a doublet of doublets peak at 8.27 ppm, while Ha is observed as a doublet peak at 8.66 ppm. These chemical shift values are in close to those reported for structurally similar compounds.[139]

In amide pyridine, analogous to cyanopyridine, the deshielding of protons in pyridine rings exceeds that of benzene rings. Notably, protons at the α-position of the N-pyridyl group undergo more intensified deshielding. Therefore, Ha in isomer **134** (8.46 ppm) and **136** (8.66 ppm) and Hc

in isomer **135** (8.55 ppm) are more deshielded than the others (7.29 to 8.27 ppm). In addition, it is observed that the ^{3}J coupling constant in molecule **135** (~5.5 Hz) is lower than in molecules **134** and **136** (~8.6 Hz) because the nitrogen atom in the pyridine ring of molecule **135** is closer to Hc. This difference highlights the variation in chemical environments of protons among the isomers.[136]

Furthermore, based on the IR spectra amide pyridine benzenes **134** and **136** (Figure 3.5) (Table 3. 4), the presence of peaks at ~ 3159 cm^{-1} and ~ 3400 cm^{-1} indicates the existence of a NH_2 group close to compound **146** which is 3204 cm^{-1} and 3374 cm^{-1} and the peaks at ~ 1674 cm^{-1} in all isomers indicate the formation of the conjugated C=O bond consistent with the value observed for compound **146** (1674 cm^{-1}).[139]

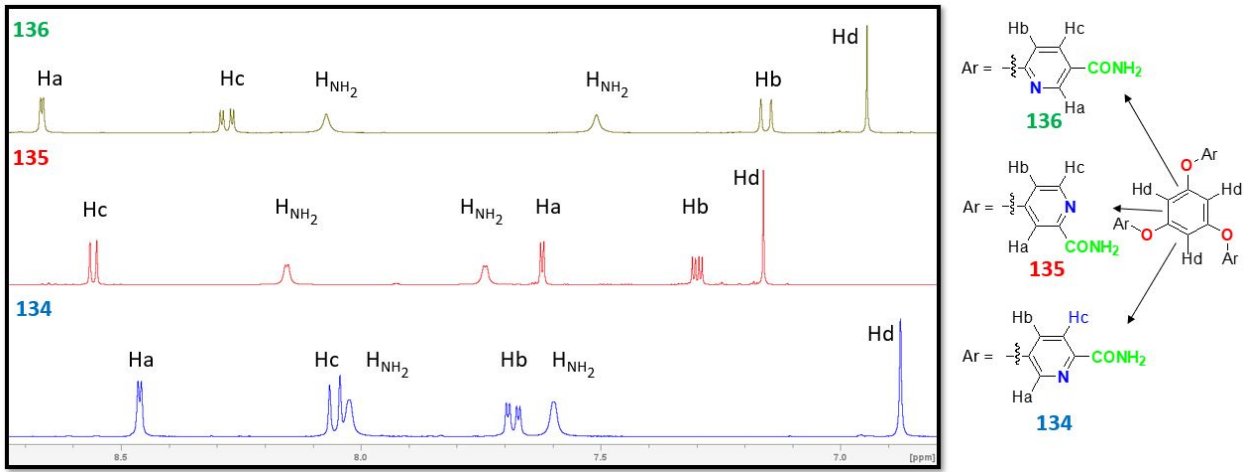

Figure 3. 4 ^{1}H NMR for molecules **134**, **135**, and **136** in DMSO-d_6.

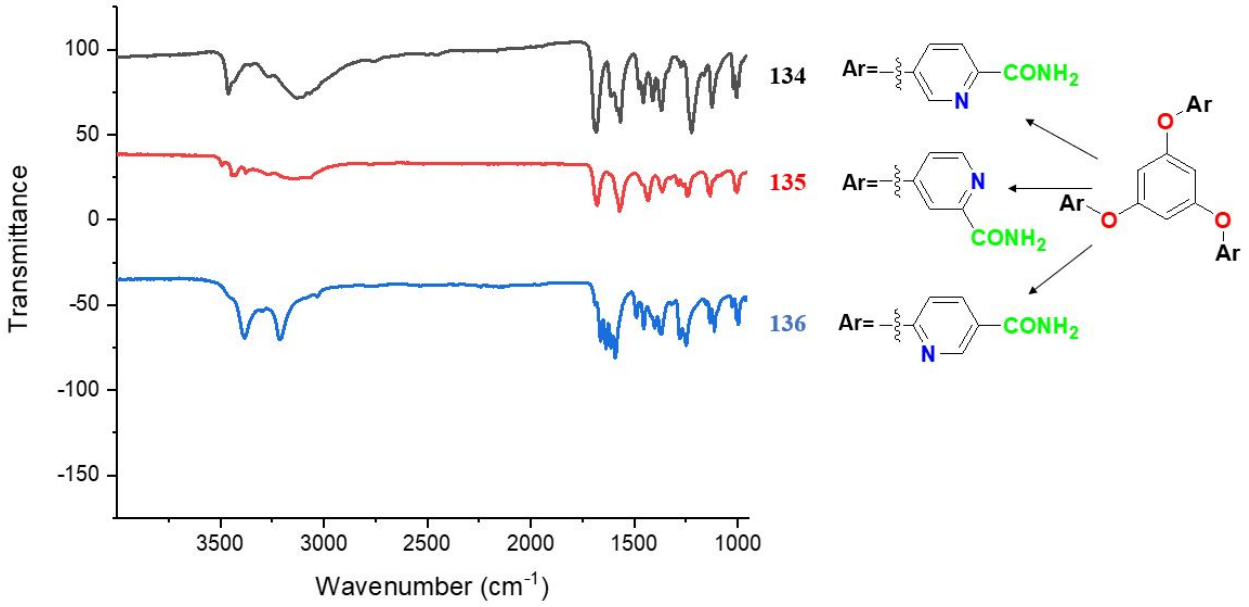

Figure 3. 5 IR spectra for molecules **134**, **135**, and **136**.

3.2.2.3 Comparison of 137, 141, and 139

Compounds **137, 141,** and **139** were synthesized through the hydrolysis of their corresponding cyanopyridine benzenes **131-133**. In each of the three isomers, there are four different proton types, each displaying its own unique characteristics (Figure 3.6). Across all isomers, the Hd protons within the benzene core show less deshielding compared to the others, reaching peaks at 6.96, 7, and 7.03 ppm for isomers **137**, **141**, and **139**, respectively. In molecule **7**, Hb is observed as a doublet of doublets, peaking at 7.66 ppm. Hc is a doublet, peaked at 8.07 ppm. Ha is another doublet, peaking at 8.54 ppm. In molecule **141**, Hb is observed as a doublet of doublets, peaking at 7.14 ppm. Hc is a doublet, peaked at 7.51 ppm. Ha is another doublet, peaking at 8.49 ppm. In molecule **139**, Hb is a doublet and peaked at 7.18 ppm. Hc is a doublet of doublets, peaking at 8.31 ppm. Ha is a doublet detected at 8.72 ppm. These chemical shift values are close to reported for similar compounds.[141]

Furthermore, the IR spectra for all compounds **137**, **141**, and **139** (Figure 3.7) (Table 3. 4) reveal significant features. The presence of a broad peak exceeding 3300 cm^{-1} signifies the presence of the hydroxyl (OH) group in the carboxylic moiety, while the peaks around ~1700 cm^{-1} in all isomers indicate the presence of the conjugated C=O bond. These observations are consistent with those reported for compound **147**.[142] Additionally, the characteristic peak of the cyano group at approximately 2235 cm^{-1} has disappeared, indicating the conversion of all cyanopyridines into amide or carboxylic acids.

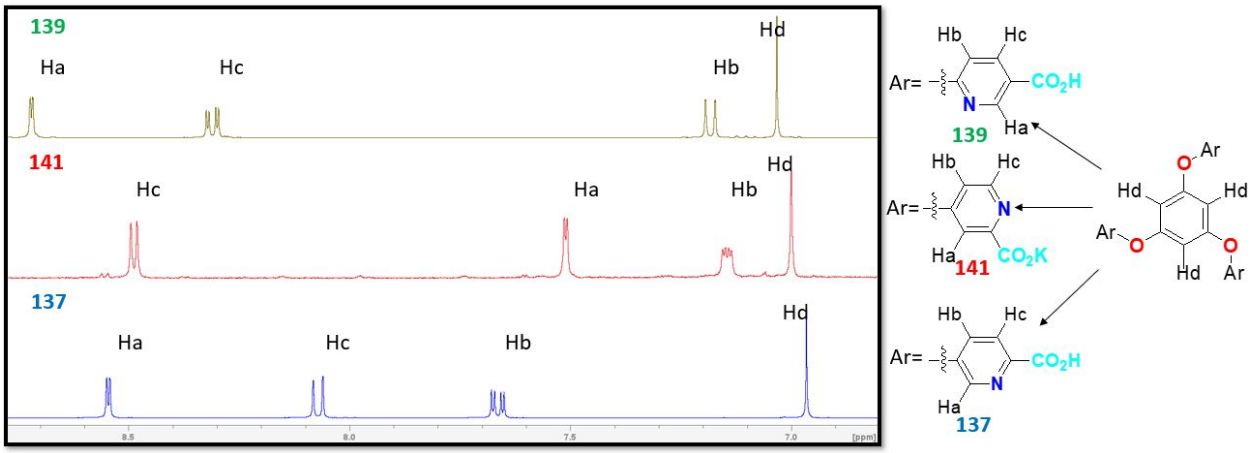

Figure 3. 6 ^{1}H NMR for molecules **137, 141**, and **139** in DMSO-d_6.

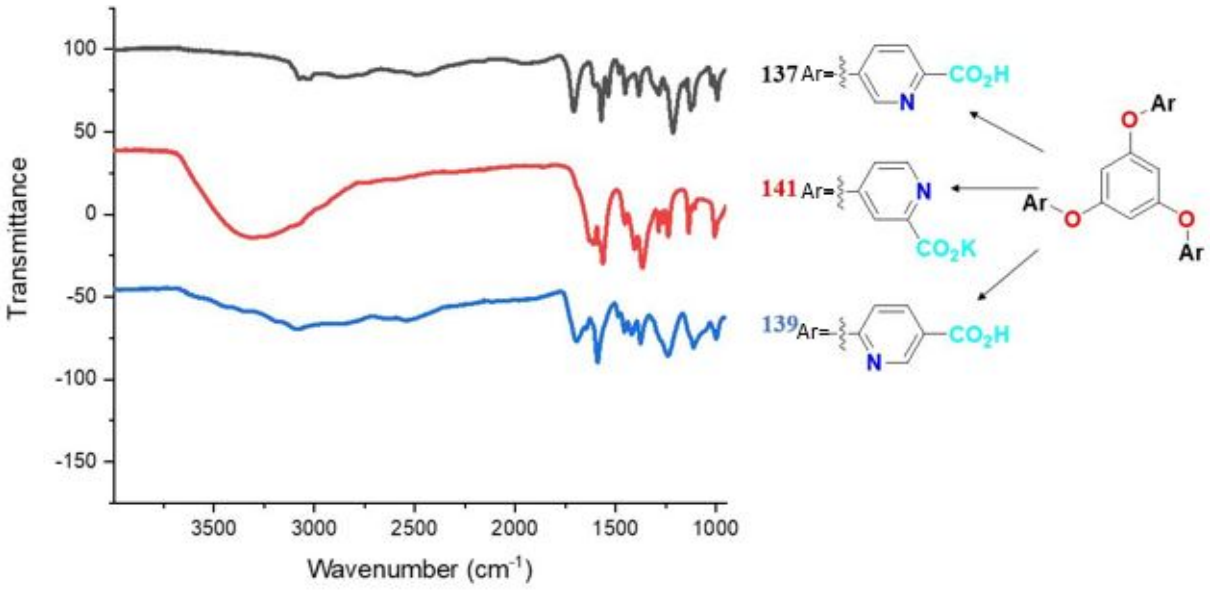

Figure 3. 7 IR spectra for molecules **137**, **141**, and **139**.

3.2.2.4 Comparison of the ^{1}H NMR Spectra of Compounds **131**, **134**, and **137**

As shown in (Figure 3.8), among compounds **131**, **134**, and **137** which have different functional groups at the same position on the same pyridine rings, Ha proton in molecule **131** (8.64 ppm) which has a cyano group is more deshielded than Ha protons in **134** (8.46 ppm) and **137** (8.54 ppm). Also Ha in molecule **137** which has a carboxylic acid group is more deshielded than Ha proton in **134**. It shows cyano group is the strongest electron-withdrawing group among the three (cyano, carboxylic acid, and amide) and carboxylic group is stronger electron-withdrawing group than amide group.

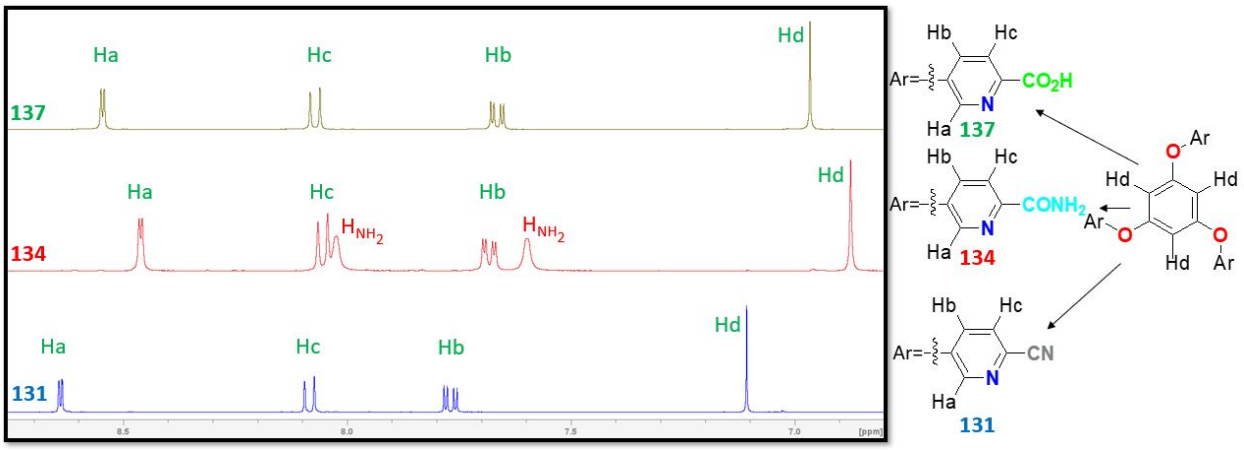

Figure 3. 8 ^{1}H NMR comparison of molecules **131**, **134**, and **137** in DMSO-d_6**.**

3.2.2.5 Comparison of IR in **131**, **132**, **133**, **134**, **135**, **136**, **137**, **139**, and **141** (cyano, amide, and carboxylic acid)

The IR data (Table 3.4) for compounds **131**, **132**, and **133** include values at 2233, 2240, and 2233 cm^{-1}, respectively, corresponding to the presence of cyano (CN) groups. These values fall within the expected range and can be compared to compound **144**, which exhibits a CN stretching band at 2217 cm^{-1}.[143] In the IR spectra of compounds **134**, **135**, and **136**, the characteristic cyano (C≡N) stretching bands have disappeared, and new absorption bands appear at 1682, 1678, and 1662 cm^{-1}, respectively. These values indicate the formation of carbonyl (C=O) groups and are comparable to the C=O stretch observed in compound gg, which appears at 1675 cm^{-1}.[139] Additionally, two values are listed at (3351 and 3462 cm^{-1}), (3337 and 3444 cm^{-1}), and (3212 and 3382 cm^{-1}) for molecules **134**, **135**, and **136**, respectively, indicating the presence of NH_2 groups, suggesting the formation of amide groups and these values are comparable to compound **146** (3204 and 3374 cm^{-1}).[139]

For molecules **137**, **141**, and **139**, the IR data show carbonyl (C=O) values at 1736, 1630, and 1698 cm^{-1}, with no CN and NH_2 values, indicating the formation of carboxylic groups. The C=O stretching band for compound cc appears at 1735 cm^{-1}, providing a comparable reference.[142] These

changes in the IR data suggest the successful transformation of the initial cyano groups (compounds **131**–**133**) into amide groups (compounds **134**–**136**), and subsequently into carboxylic groups (compounds **137**, **141**, and **139**). In addition, compounds **131** and **133** (CN group in the para position) exhibited peaks at lower wavelengths than compound **132** (CN group in the meta position). This difference arises because the cyano group at the meta position cannot participate in conjugation with the oxygen atom of the ether group, whereas in the para position, conjugation is possible. Additionally, the inductive effect of the cyano group may also contribute to the observed differences.

3.2.2.6 Single Crystal X-ray Diffraction (SCXRD) of 131, 132, 134, and 137

Single crystal x-ray diffraction (SCXRD) analysis has been conducted on well formed crystals of compounds **131**, **132**, **134**, and **137** to determine the molecular structure and the precise spatial arrangement of atoms within these crystals. Regrettably, appropriate crystals required for conducting XRD analysis were not obtained for the remaining compounds. The precise determination of atomic positions and coordination motifs is essential for understanding and predicting coordination reactions. Detailed crystallographic data for these molecules can be found in Table 3.2. Crystal structure of **131**, **132**, **134**, and **137** (Figure 3.9) show that compounds **131** and **132**, a cyanopyridine moiety with an etheric bond is linked to the benzene ring. Compound **134** features an amide pyridine with an etheric bond attached to the benzene ring, while in compound **137**, a carboxypyridine with an etheric bond is linked to the benzene ring. In all these compounds, the substituent branches are oriented out of the plane of the benzene ring. Since similar compounds (**34** and **143**) have not been characterized by SCXRD, no direct crystallographic comparison was made with literature references.

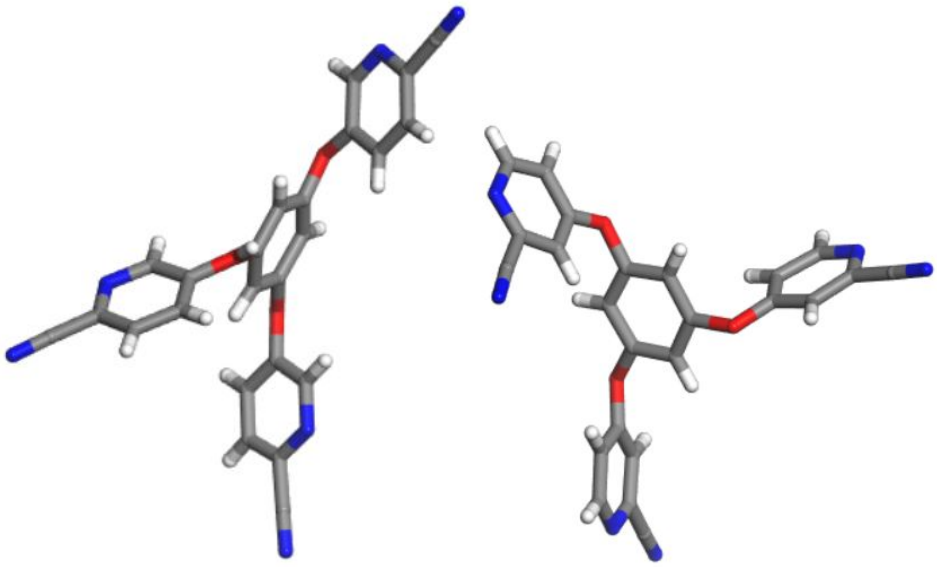

131 **132**

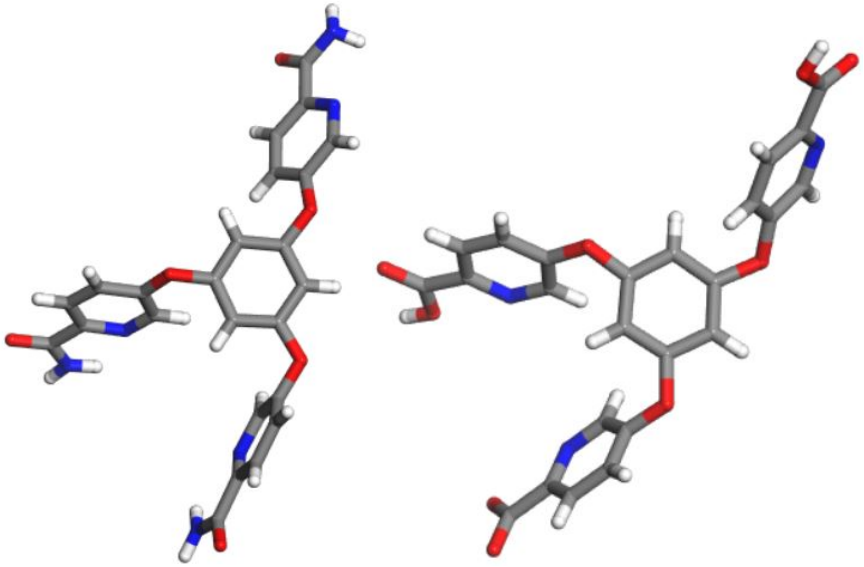

134 **137**

Figure 3. 9 Crystal structures of compounds **131**, **132**, **134**, and **137**. Carbon atoms are depicted in gray, hydrogen atoms in white, nitrogen atoms in blue, oxygen atoms in red.

In crystallography, crystals are categorized into seven crystal systems based on unit cell geometry, specifically the lengths of the cell axes (a, b, c) and the angles between them (α, β, γ). Compounds **131**, **132**, and **134** crystallized in the triclinic system, while compound **137** crystallized a monoclinic system, despite all being crystallized from DMF. This difference is likely attributed to variations in molecular structure and the resulting intermolecular interactions, such as hydrogen bonding and packing arrangements.

Beyond the crystal system, the symmetry of a crystal is described by its space group. Crystals are classified into 230 distinct space groups. Compounds **131**, **132**, and **134** belong to the space group P-1, whereas compound **137** crystallizes in the space group P21/n, reflecting differences in molecular structure and the resulting molecular interactions.

The number of formula units per unit cell, denoted as the Z value, is 2 for compounds **131** and **134**, and 4 for compounds **132** and **137**. Notably, isomers **131** and **132**, although similar in composition, exhibit different lattice parameters. This reflects subtle differences in atomic positions that affect unit cell dimensions and overall crystal geometry.

The total number of electrons in the unit cell, represented by F (000), is 444, 888, 1008, and 1272 for compounds **131**, **132**, **134**, and **137**, respectively.

The average bond lengths of molecules **131**, **132**, **134**, and **137**, as listed in Table 3.3, fall within the anticipated and normal range, underscoring the uniformity and stability observed in their molecular structures.

Table 3. 2 Crystallographic data for **131**, **132**, **134**, and **137**.

Compound	**131**	**132**	**134**	**137**
Empirical formula	$C_{24}H_{12}N_6O_3$	$C_{24}H_{12}N_6O_3$	$C_{48}H_{36}N_{12}O_{12}$	$C_{29}H_{29}N_5O_{10}$
Formula weight	432.4	432.4	972.89	607.57
Temperature/K	293(2)	150	100	150
Crystal system	triclinic	Triclinic	triclinic	monoclinic
Space group	P-1	P-1	P-1	$P2_1/n$
a/Å	7.3661(7)	8.1235(6)	9.8017(6)	7.0998(2)
b/Å	11.6507(8)	14.0498(10)	14.5623(9)	13.5450(4)
c/Å	11.8113(5)	18.1664(13)	17.5635(9)	30.0098(8)
α/°	101.881(5)	95.021(3)	108.110(5)	90
β/°	92.179(6)	101.662(3)	98.989(5)	91.492(2)
γ/°	93.556(7)	90.878(4)	105.535(5)	90
Volume/Å^3	988.68(12)	2021.6(3)	2215.8(2)	2884.97(14)
Z	2	4	2	4
ρ_{calc}g/cm^3	1.452	1.421	1.458	1.399
μ/mm^{-1}	0.833	0.518	0.908	0.577
F(000)	444	888	1008	1272
Crystal size/mm^3	0.2 × 0.1 × 0.05	0.15 × 0.11 × 0.07	0.2 × 0.1 × 0.05	0.15 × 0.09 × 0.06
Radiation	Cu Kα (λ = 1.54184)	Ga Kα (λ = 1.34139)	Cu Kα (λ = 1.54184)	Ga Kα (λ = 1.34139)
2Θ range for data collection/°	7.66 to 144.97	6.682 to 121.698	5.484 to 144.146	7.65 to 121.464
Index ranges	-9 ≤ h ≤ 8, -13 ≤ k ≤ 14, -12 ≤ l ≤ 14	? ≤ h ≤ ?, ? ≤ k ≤ ?, ? ≤ l ≤ w?	-11 ≤ h ≤ 11, -17 ≤ k ≤ 16, -15 ≤ l ≤ 21	-9 ≤ h ≤ 9, -17 ≤ k ≤ 17, -38 ≤ l ≤ 38
Reflections collected	6472	9264	15234	42818
Independent reflections	3634 [R_{int} = 0.0390, R_{sigma} = 0.0523]	9264 [R_{int} = 0.0456, R_{sigma} = 0.0264]	8488 [R_{int} = 0.0337, R_{sigma} = 0.0532]	6636 [R_{int} = 0.0910, R_{sigma} = 0.0615]
Data/restraints/parameters	3634/0/310	9264/0/595	8488/0/651	6636/103/464
Goodness-of-fit on F^2	1.139	1.053	1.027	1.035
Final R indexes [I>=2σ (I)]	R_1 = 0.0652, wR_2 = 0.1792	R_1 = 0.0453, wR_2 = 0.1291	R_1 = 0.0508, wR_2 = 0.1232	R_1 = 0.0588, wR_2 = 0.1519
Final R indexes [all data]	R_1 = 0.0866, wR_2 = 0.2173	R_1 = 0.0489, wR_2 = 0.1324	R_1 = 0.0738, wR_2 = 0.1369	R_1 = 0.1014, wR_2 = 0.1819

F(000): Total number of electrons in the unit cell contributing to scattering

T = Data collection temperature (K)

V = Volume of the unit cell (in Å³)

Table 3. 3 The mean bond distances for compounds **131**, **132**, **134**, and **137**.

	Bond lengths* (Å)				
Bond	**131**	**132**	**134**	**137**	**Literature**
C=C	1.38	1.38	1.39	1.38	1.41 (61)[144]
C=O	-	-	1.23	1.23	1.25(78)[145]
C-O	1.38	1.38	1.38	1.38	1.37 (77)[146]
C≡N	1.14	1.15	-	-	1.15 (0.9)[147]

*Bond lengths are given as average values.

3.2.2.7 UV

The UV spectroscopy of molecules **131**, **132**, **133**, **134**, **135**, **136**, **137**, and **139** (Table 3.4) (Figure 3.9) reveals a distinct sharp peak around 270 nm, attributed to the $\pi \rightarrow \pi^*$ transition of the benzene cores. Among molecules **131** to **133**, which are isomers of cyano pyridines, the structures of molecules **131** and **133** bear closer resemblance, with their λ_{max} values closely aligned at 271 nm for **131** and 272 nm for **133**. In molecule **132**, where the position of the cyano group is altered, the peak shifts to 267 nm. This shift indicates that the position of the cyano group on the pyridine ring affects the UV spectra. When the cyano group is in the para position, there is a longer conjugated system, causing the UV spectra to shift to lower energy. Similar trends have been observed for corresponding amide **134**-**136** and carboxylic acid derivatives **137** and **139**. In addition, molecule **143**, which has a benzene ring instead of a pyridine ring and has greater aromaticity, exhibits a $\pi \rightarrow \pi^*$ transition at 305 nm, showing a red shift compared to compound **131** (271 nm).[148] The UV spectrum of compound **141** differs from the other compounds. It exhibits a peak at 310 nm, attributed to the $\boldsymbol{\pi \rightarrow \pi^*}$ transition, and a peak at 358 nm, corresponding to the $\mathbf{n \rightarrow \pi^*}$ transition. The $\pi \rightarrow \pi^*$ transition of compound **141** shows a red shift compared to the other compounds. This arises from the delocalization of charge on the oxygen atoms of the carboxylate group. This delocalization facilitates conjugation, reduces the energy gap between the π and π^* molecular orbitals, and shifts the $\pi \rightarrow \pi^*$ transition to lower energy compared to other molecules.

Additionally, the delocalized charge on the oxygen atoms lowers the energy of the non-bonding (n) orbital, facilitating the n → π* transition.

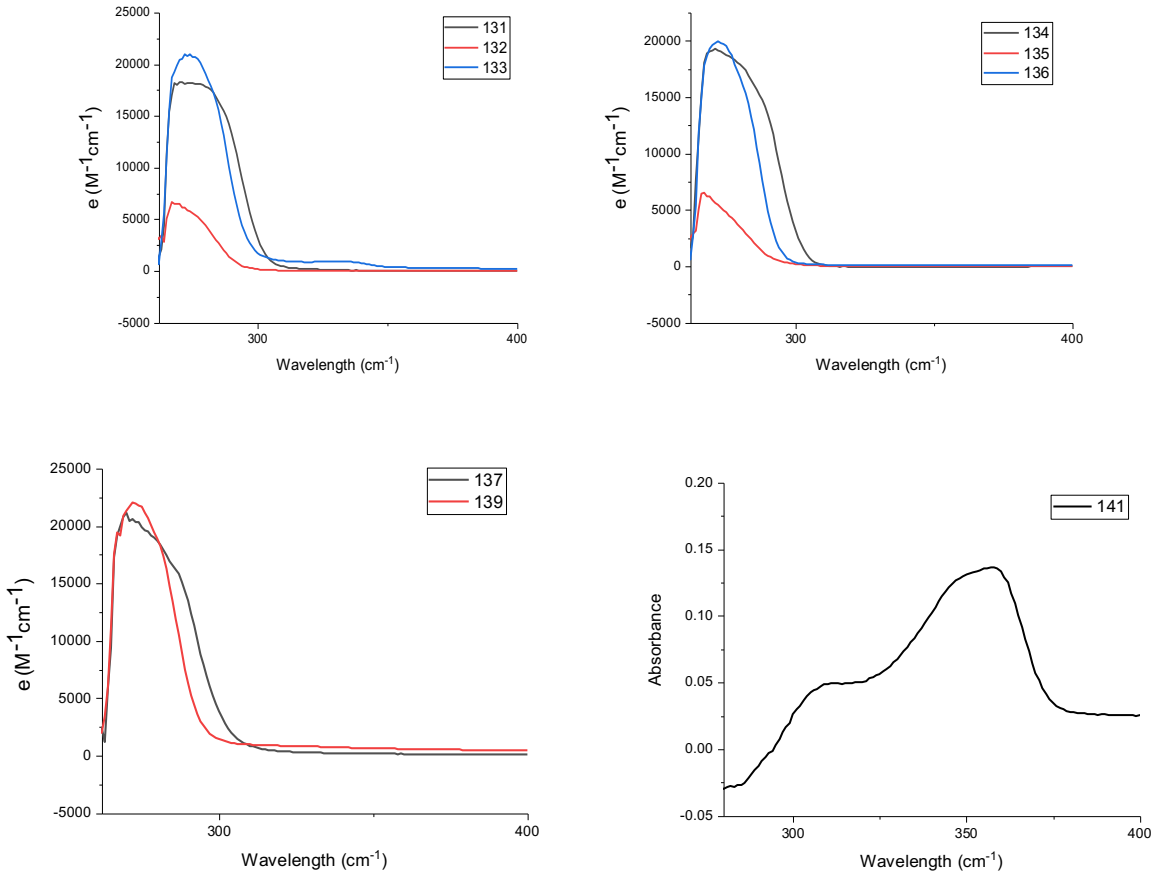

Figure 3. 10 UV spectra of compounds **131**, **132**, **133**, **134**, **135**, **136**, **137**, **139**, and **141** in DMF at room temperature.

The molar absorptivity coefficient (ε) values indicate that compound **132** and compound **135**, which feature cyano and amide groups substituted at the meta position, respectively, have lower ε values compared to compounds with substitutions at the para position. This is likely due to the longer conjugated system afforded by para substitution, which enhances electron delocalization and increases the molar absorptivity.

To examine solvent effects, the UV spectra of compounds **131**, **132**, **133**, **134**, **135**, **136**, **137**, and **139** were also recorded in acetonitrile (Figure S31). Compared to their spectra in DMF, all peaks exhibited a blue shift, accompanied by an additional shoulder, which can be attributed to a $\pi \rightarrow \pi^*$ transition. Due to the low solubility of compound **141** in acetonitrile, its UV spectrum could not be recorded in this solvent.

3.2.2.8 TGA

The thermogravimetric analysis (TGA) data (Table 3.4) (Figure 3.10) for compounds **131**, **132**, **133**, **134**, **135**, **136**, **137**, **139**, and **141** indicate that these compounds exhibit high thermal stability, with decomposition temperatures ranging from 200°C to 419°C. A comparison between compounds **131** (288°C), **134** (363°C), and **137** (292°C), which share the same core structure but differ in their functional groups, suggests that the type of functional group, along with its moiety and hydrogen bonding interactions, can significantly influence the thermal stability of the compounds.[149] Compound **131** exhibits more stability compared to the similar Compound **143**, which contains a benzene ring in place of a pyridine ring. This difference in stability may be attributed to the nitrogen atoms in the pyridine ring of Compound **131**, which can form more hydrogen bonds than Compound **143**.[148]

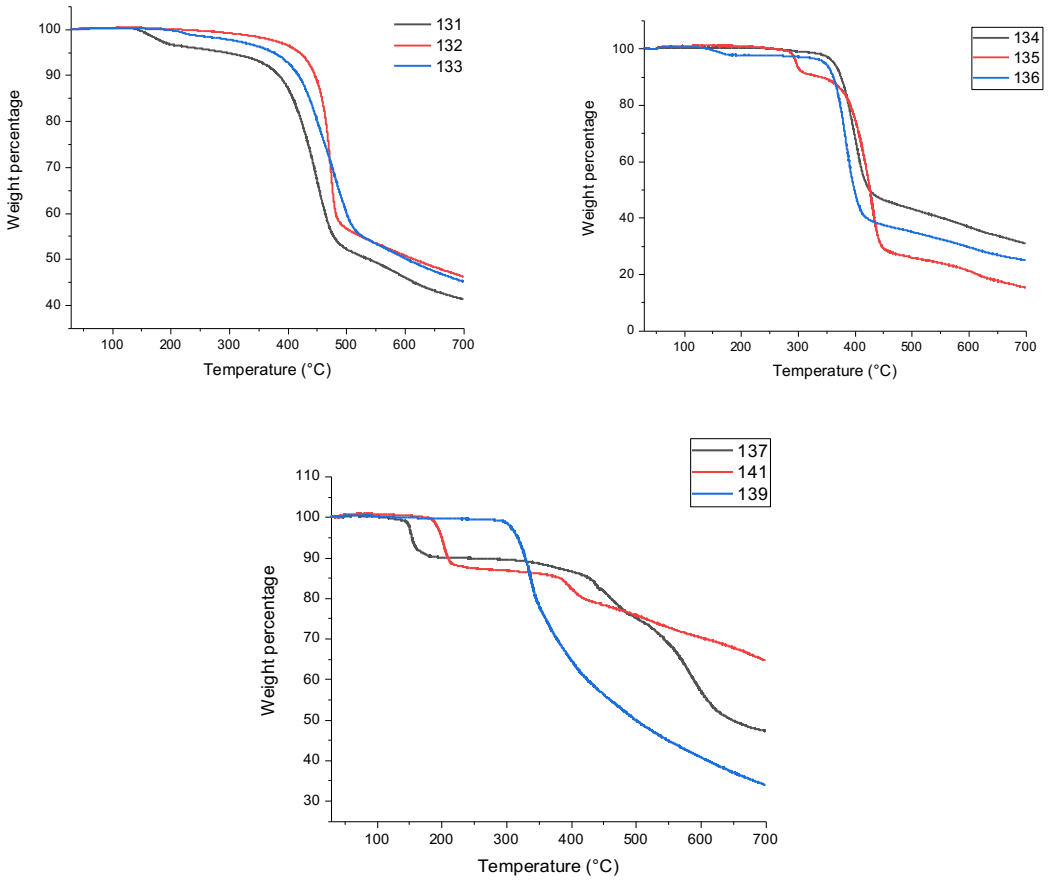

Figure 3. 11 Thermogravimetric analysis of compounds **131**, **132**, **133**, **134**, **135**, **136**, **137**, **139**, and **141** (TGA).

Table 3. 4 Infrared spectral data, maximum absorption wavelengths (λ_{max}), and decomposition temperatures for compounds **131, 132, 133, 134, 135, 136, 137, 139, 141**, **34**, **144**, **146**, and **147**.

Cpd.	FTIR data						λmax abs (nm) / ε ($M^{-1}cm^{-1}$)	Td [a] (TGA) (°C)
	-CN group (cm^{-1})	C-N aromatic (cm^{-1})	C-O ether (cm^{-1})	C=O (cm^{-1})	O-H (cm^{-1})	NH_2 (cm^{-1})		
131	2233	1567	999	---	---	---	271/ 18224	288
132	2240	1564	1006	---	---	---	267 / 6617	419
133	2233	1586	1006	---	---	---	272/ 20909	374
134	---	1614	1004	1682	---	3351-3462	271/ 19275	363
135	---	1570	1004	1678	---	3337-3444	267/ 6550	297
136	---	1591	1004	1662	---	3212-3382	272/ 19902	346
137	---	1570	993	1736	3025	---	270/ 21153	292
141	---	1563	1007	1630	---	---	310-443/---	200
139	---	1590	998	1698	3315	---	272/ 21987	317
143[148]	~ 2300	---	~ 1000	---	---	---	365	200
34[65]	---	---	~ 1010	1689		---	---	---
144[b136]	2217	1587	---	---	---	---	---	---
146c[139]	---	1586	1022	1674	---	3204-3374	---	---
147d[142]	---	---	---	1735	3075	---	---	---

a Td - decomposition temperature at 5 % weight loss measured by thermogravimetric analysis (TGA).
b BZ4 CYBR (**144**) is referenced from Manohara et al. (2019).
c 3-Methoxypicolinamide (3j) (**146)** is referenced from Han et al. (2016).
d BA-4 (**147)** is referenced from Han et al. (2014).

3.2.2.9 Fluorescence

The emission properties of cyanopyridine benzene isomers were studied using an excitation wavelength of 270 nm (chosen due to the highest absorption at this wavelength) (Table 3.5) (Figure 3.12) under air. The fluorescence intensity observed can be lower or higher depending on the quantum yield, which may be quenched by factors such as oxygen or influenced by the molecular structure.[150] Compound **131** exhibited peaks at 313 nm and 412 nm, while Compound **132** showed

peaks at 312 nm, 365 nm, and 414 nm. This demonstrates that the position of the nitrogen in the pyridine ring significantly influences the optical properties of these compounds. Additionally, compound **132** displayed peaks at 311 nm and 422 nm, indicating that the positions of both the nitrogen atom in the pyridine ring and the cyano group affect the emission characteristics. Notably, the second peak is shifted to a higher wavelength.

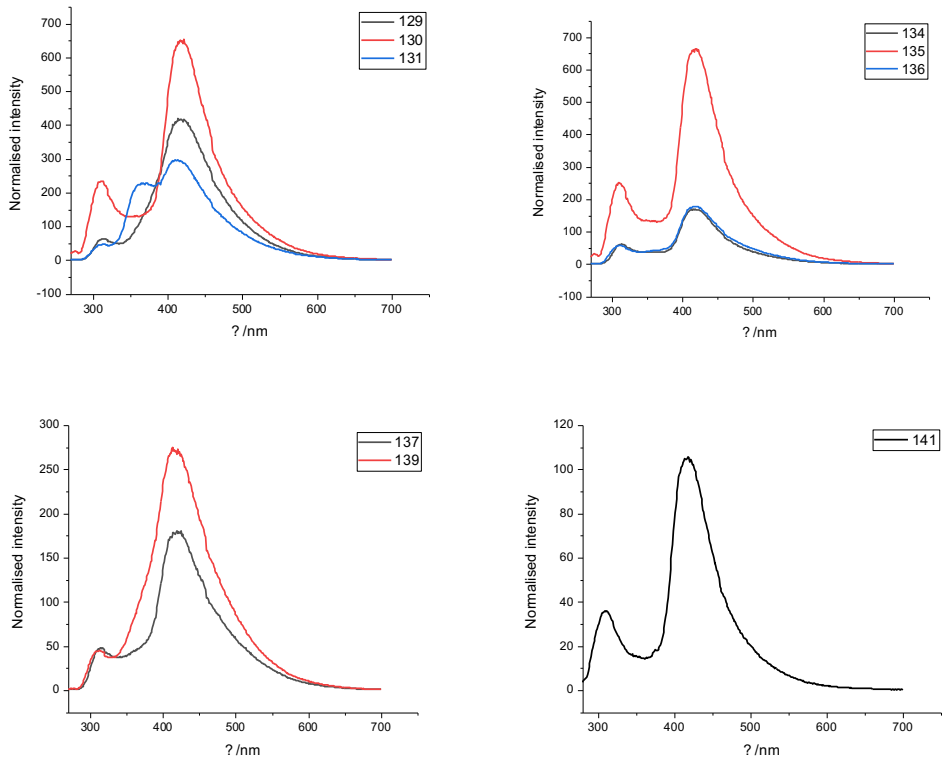

Figure 3. 12 Fluorescence spectra of compounds **131**, **132**, **133**, **134**, **135**, **136**, **137**, **139**, and **141** in DMF at room temperature, λ_{ex} = 270 nm.

The emission properties of the amide pyridine isomers **134-136** were investigated using 270 nm as the excitation wavelength (Table 3.5) (Figure 3.12). Compound **134** exhibited peaks at 314 nm and 414 nm, while Compound **135** showed peaks at 310 nm and 423 nm, and Compound **136** peaked at 311 nm and 416 nm. Notably, in compound **135**, similar to compound **132**, the second peak is shifted to a higher wavelength. These results indicate that changing the functional group from cyano to amide does not significantly affect the emission properties of these compounds.

The emission properties of carboxypyridine isomers were investigated using the same excitation wavelength of 270 nm (Table 3.5) (Figure 3.12). Compound **137** exhibited peaks at 314 nm and 419 nm, while Compound **141**, which is a carboxylate, showed peaks at 309 nm and 418 nm. Compound **139** displayed peaks at 312 nm and 414 nm. These findings indicate that changes in the functional group from cyano to carboxylate do not significantly alter the emission properties of these compounds.

In addition, to evaluate the effect of solvent on the emission properties, fluorescence measurements were performed on compounds **131**, **132**, **133**, **134**, **135**, **136**, **137**, **139**, and **141** in acetonitrile. These compounds exhibited emission peaks around 308 nm, showing a blue shift compared to those measured in DMF. Notably, the emission peak of compound **131** observed around 363 nm in DMF disappeared or was integrated into the aggregation band when measured in acetonitrile (Figure S32). To assess the possibility of aggregation, fluorescence spectra were recorded at different concentrations. The spectra at different concentrations showed broad emission bands around 400 nm, which are attributed to aggregation-induced emission (Figure S33). For compound **141**, due to its low solubility in acetonitrile, the emission spectrum could not be recorded.

In conclusion, the position of functional groups (cyano, amide, and carboxylic acid) on the pyridine ring has a greater influence on the emission spectra than the nature of the functional group itself. Changing the solvent can also lead to spectral shifts. Fluorescence measurements at different concentrations revealed a broad emission peak around 400 nm, which is attributed to aggregation-induced emission.

Table 3. 5 Fluorescence spectroscopy data of compounds **131, 132, 133, 134, 135, 136, 137, 139,** and **141**.

Compound	Peak (nm)
131	313, 412
132	311, 422
133	312, 365, 414
134	314, 414
135	310, 423
136	311, 416
137	314, 419
141	309, 418
139	312, 414

3.2.2.10 Hydrogen bond simulation of 131, 132, 134, and 137

Hydrogen bond simulations in the solid state reveal diverse interactions among different molecules **131**, **132**, **134**, and **137** (Figure 3.12) (Table 3.6). In the comparison between compounds **131** and **132**, which are isomers, the hydrogen bonding is different. In compound **131**, there is only a weak hydrogen bond between the proton of the benzene core and the nitrogen of the cyano group. However, in compound **132**, hydrogen bonding is observed between the protons of the pyridine ring and the nitrogen of the cyano group, and between the protons of the pyridine ring and the nitrogen of the pyridine ring.

In compound **134**, which has more diverse types of hydrogen bonds, there are hydrogen bonds between the protons of the benzene core and the oxygen of the amide group, the protons of the amide group and the nitrogen of the pyridine ring, the protons of the amide group and the oxygen of another amide, and finally between the protons of the pyridine ring and the oxygen of the etheric bond.

In compound **137**, which has more diverse types of hydrogen bonds, hydrogen bonding occurs between the hydrogen of the pyridine ring and the oxygen of the carbonyl group, the hydrogen of

the benzene core and the oxygen of the carbonyl group, and between the proton of the carboxylic group and the oxygen of the carbonyl group.

These data show that compounds **131** and **132** exhibit distinct hydrogen bonding patterns, highlighting that the position of atoms can influence the formation of hydrogen bonds. Additionally, as seen in compounds **131**, **134**, and **137**, different functional groups and heteroatoms lead to varying hydrogen bonding patterns. Furthermore, it is predicted that compounds **131** and **132**, with only weak hydrogen bonds, are likely to result in less stable coordination compounds. In contrast, compounds **134** and **137**, with stronger hydrogen bonds, are predicted to form more stable coordination compounds due to the presence of stronger hydrogen bonding.[151] Moreover, hydrogen bonding behavior in solution differs from that in the solid state. This is evidenced by the proton NMR, where the protons of the benzene core in solution exhibit the same chemical shift, indicating uniform bonding interactions. However, in the solid state, only one proton of the benzene core participates in hydrogen bonding.

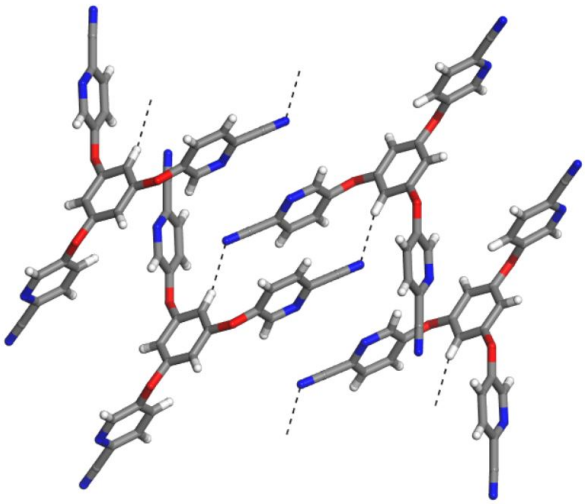

131

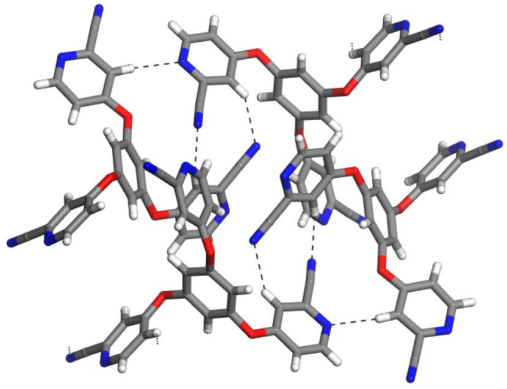

132

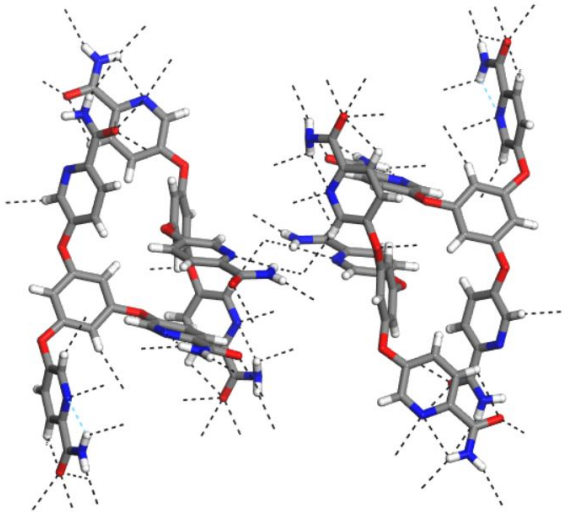

134

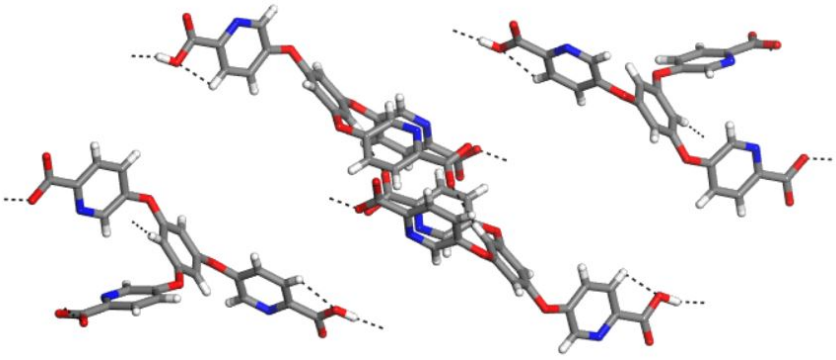

137

Figure 3. 13 The hydrogen bonding configurations in molecules **131**, **132**, **134**, and **137** are depicted. Dashed lines represent the hydrogen bonds. Carbon atoms are depicted in gray, hydrogen atoms in white, nitrogen atoms in blue, oxygen atoms in red, and sulfur atoms in yellow.

Table 3. 6 The hydrogen bonding patterns in molecules **131**, **132**, **134**, and **137**. The angle (Θ) between the donor and acceptor atoms, as well as the length (d) of the hydrogen bond.

Cpd.	Bond	θ (°)	d (Å)	Type of hydrogen bond
131	N_{CN}…H-C_{Bn}	158.98	2.47	Weak
132	N_{Py}…H-C_{Py}	162.42	2.42	Weak
	N_{CN}…H-C_{Py}	145.73–156.88	2.44–2.49	Weak
134	$O_{Carbonyl}$…H-C_{Bn}	157.47–172.46	2.32–2.43	Weak
	N_{Py}…H-N	103.89–154.61	2.28–2.49	Weak
	$O_{Carbonyl}$…H-N	149.49–144.99	2.27–2.29	Weak
	O_{Ether}…H-C_{Py}	167.77	2.32	Weak
	$O_{Carbonyl}$…H-N	153.83–168.34	2.04–2.09	Strong
	N_{Py}…H-N	148.28	2.1	Strong
137	$O_{Carbonyl}$…H-C_{Py}	98.81	2.42	Weak
	$O_{Carbonyl}$…H-C_{Bn}	171.4	2.32	Weak
	$O_{Carbonyl}$…H-O	164.17–165.73	1.58–1.77	Strong

3.2.2.11 Hirshfeld surface analysis of 131, 132, 134, and 137

In the context of metal-organic frameworks (MOFs) and complexes, the organic linkers play a crucial role in determining the overall structure and properties of the material. By using Hirshfeld surface analysis, we visualized the molecular packing and quantified the close contacts of organic linkers **131**, **132**, **134**, and **137** within the crystal lattice (Figure 3.14).

As indicated in Figure 3.15, compound **131** exhibits a predominant interaction of 34.9% for N···H, 17% for H···H, and 15.3% for C···H. In contrast, compound **132** displays a higher percentage of 40.2% for N···H, 16.2% for C···H, and 13% for H···H. Compound **134** demonstrates a notable presence of 28.9% for N···H, 23% for H···H, and 15.4% for C···H. Compound **137**, shows 35.2% for O···H, 28% for H···H, and 15.2% for C···H.

These findings suggest that the positioning of nitrogen in the pyridine rings and the cyano group can influence the close contacts, as evidenced by the variations between compounds **131** and **132**, which are isomers. Furthermore, a comparison between compounds **131**, **134**, and **137** underscores the importance of functional groups in modulating interactions.

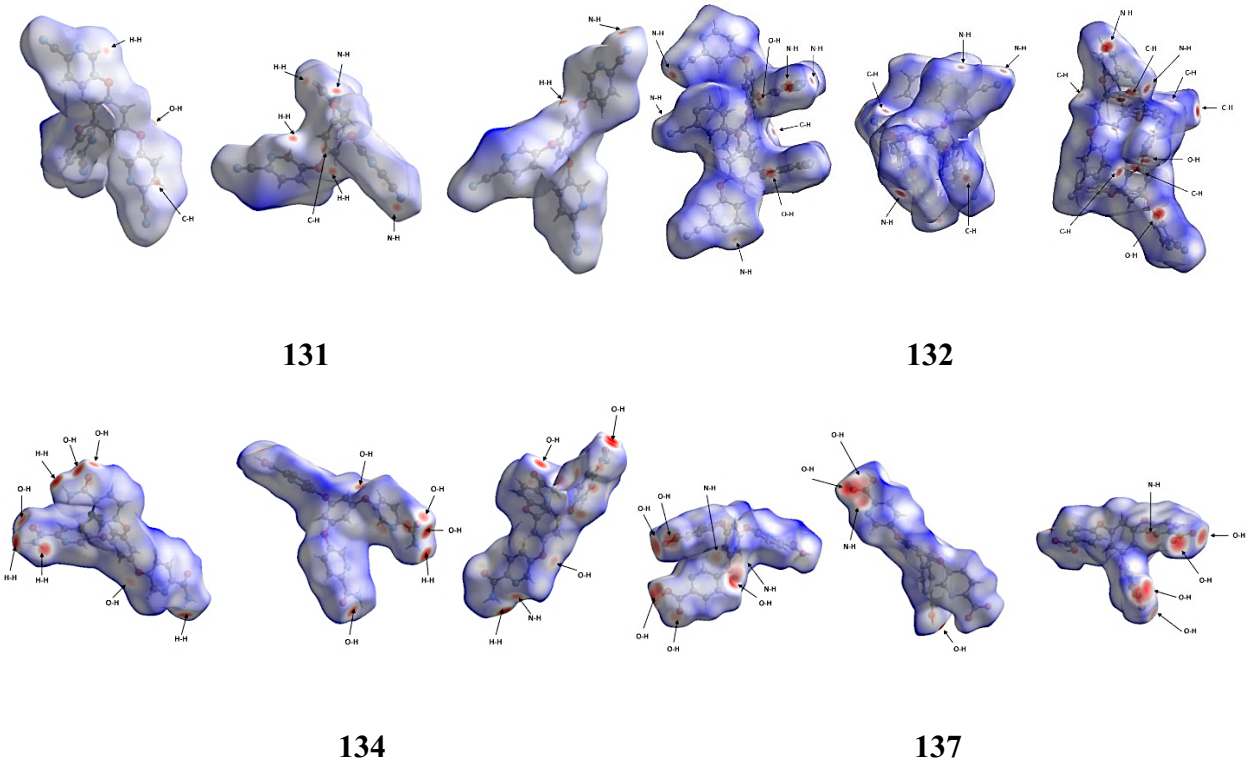

Figure 3. 14 Hirshfeld surface of molecules **131**, **132**, **134**, and **137** with d_{norm} mapping for visualizing intermolecular interactions.

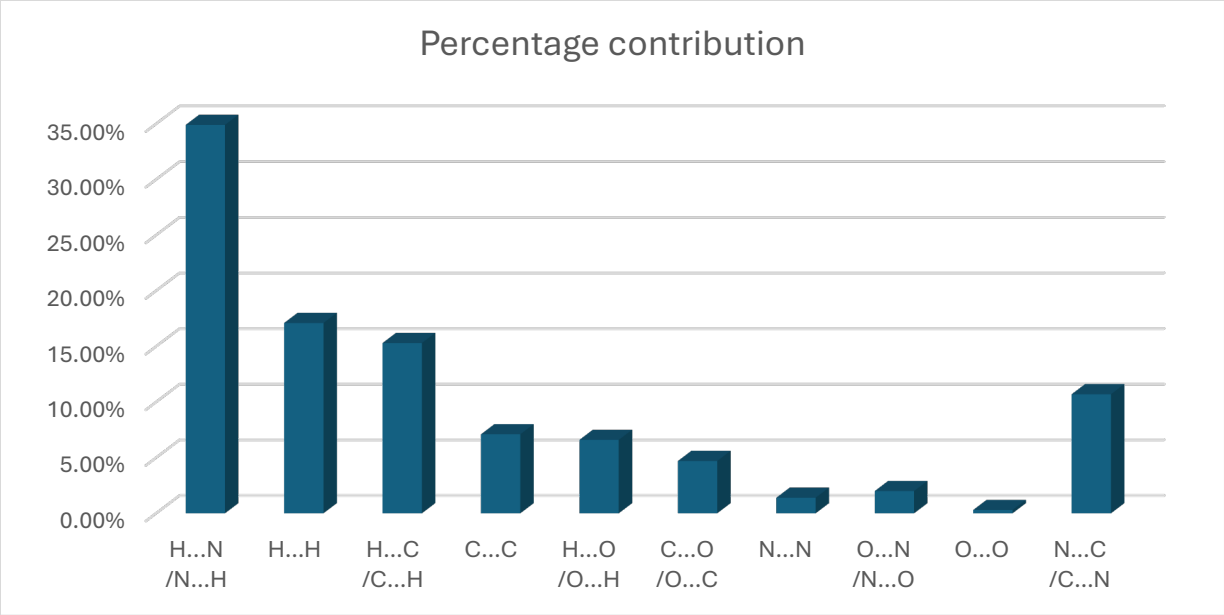
Percentage contribution
35.00%
30.00%
25.00%
20.00%
15.00%
10.00%
5.00%
0.00%
H...N /N...H
H...H
H...C /C...H
C...C
H...O /O...H
C...O /O...C
N...N
O...N /N...O
O...O
N...C /C...N

131

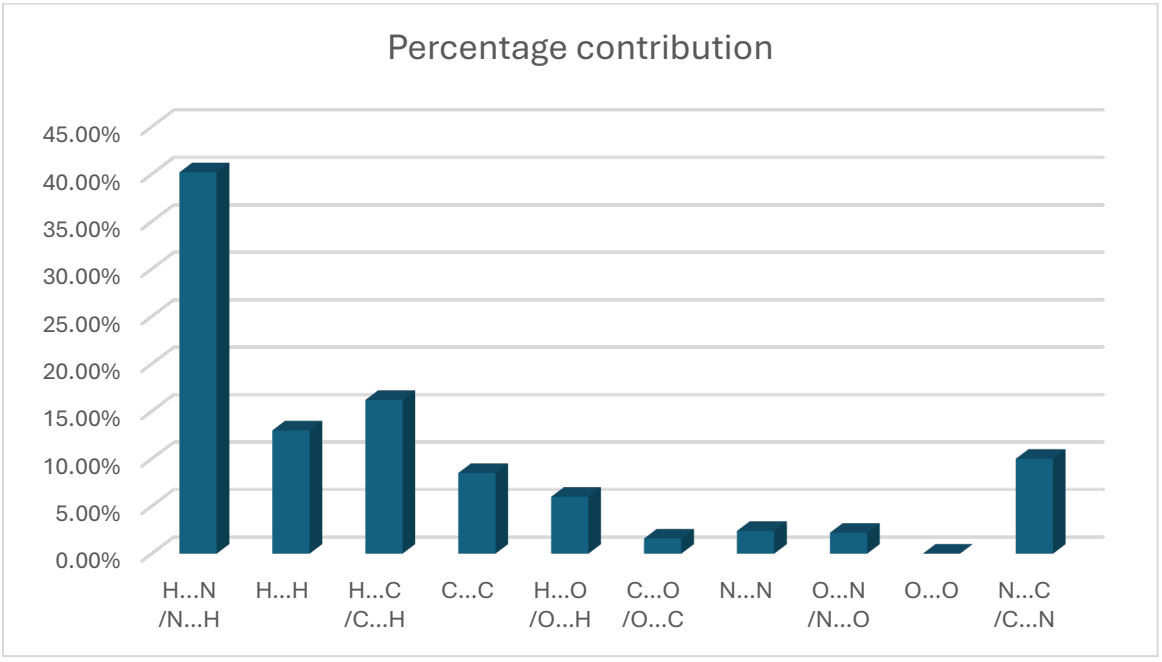
Percentage contribution
45.00%
40.00%
35.00%
30.00%
25.00%
20.00%
15.00%
10.00%
5.00%
0.00%
H...N /N...H
H...H
H...C /C...H
C...C
H...O /O...H
C...O /O...C
N...N
O...N /N...O
O...O
N...C /C...N

132

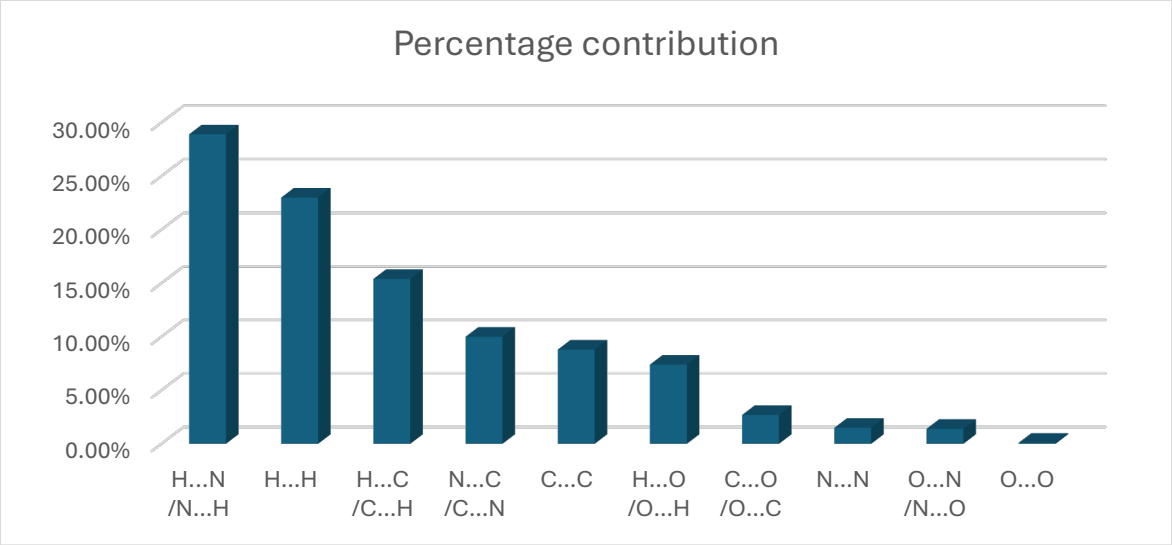

134

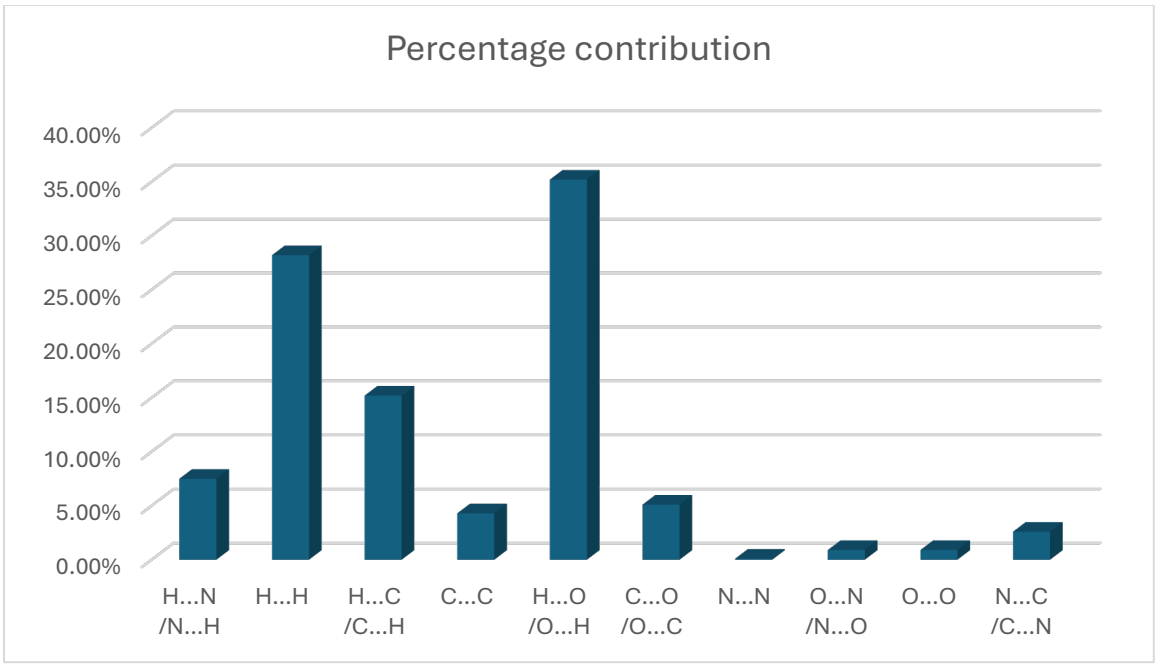

137

Figure 3. 15 Percentage contribution of intermolecular interaction for molecules **131**, **132**, **134**, and **137**.

3.3 Compound 145

Another coordination motif suitable for linking to a benzene core to create an effective coordination linker is pyridine diamino triazine (compound **119**), as discussed in Chapter 2 (Figure 3.1). This motif coordinates to metal atoms through the nitrogen atoms of both the pyridine ring and the diamino triazine group. In this project, we propose a new diamino triazine with a benzene core (compound **145**) (Figure 3.1), featuring a longer conjugated system and more coordination sites compared to previous pyridine diamino triazine (compound **119**), thereby enhancing its potential for coordination applications.[30]

3.3.1 Synthesis of compound 145

Compound **143** was synthesized following a previously reported method, which is known to provide a high yield.[152] In this reaction, one equivalent of compound **129**, three equivalents of dicyandiamide, and three equivalents of KOH were refluxed in 2-methoxyethanol for four hours. After the reaction, water was added, followed by hydrochloric acid, which led to the precipitation of pure compound **143** with a yield of 72% (Scheme 3.2).

Our goal was to obtain compound **148** (Scheme 3.2) bearing three pyridine–diamino triazine branches. Mass spectrometry confirmed the formation of the fully substituted intermediate containing all three pyridine–triazine groups. However, under the reaction conditions, a nucleophilic substitution occurred in which a hydroxide ion attacked the β-position carbon of one of the pyridine–diamino triazine branches, leading to the cleavage of that unit and the loss of a pyridine–diamino triazine group. The reaction stopped at this stage, likely due to a decrease in the

electrophilicity of the remaining sites, possibly caused by the accumulation of negative charge, which hindered further substitution.

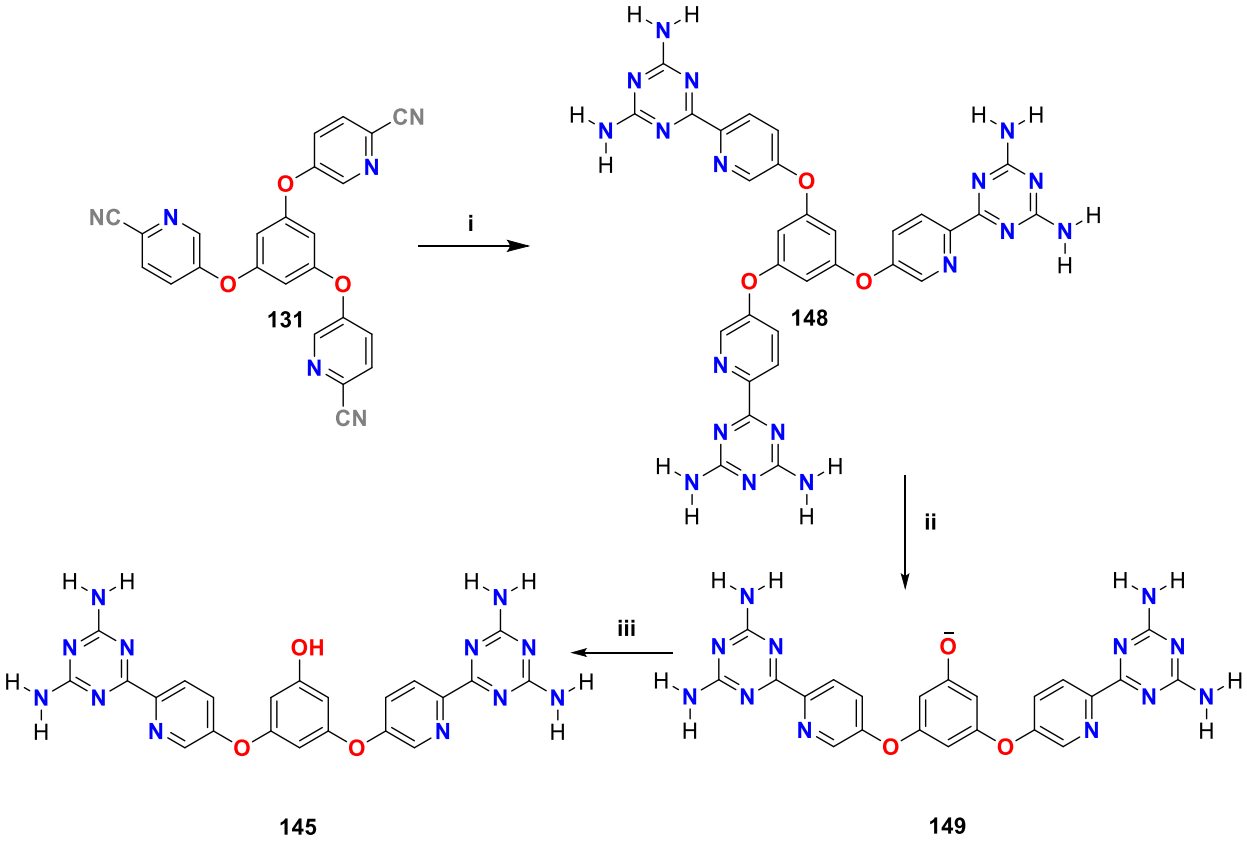

Scheme 3. 2 Synthetic route to prepare compound **145**. (i) (a) Dicyandiamide, KOH, 2-methoxyethanol, 4 hr reflux (ii) KOH (iii) H_2O, HCl 37%. (ii)

3.3.2 Result and discussion

3.3.2.1 NMR and IR of compound 145

In the proton NMR spectrum of compound **145**, seven distinct types of protons are identified. As illustrated in (Figure 3.15). He and Hd protons (from the benzene rings) are observed as singlets at 6.33 ppm and 6.36 ppm, respectively. There is a broad peak, which corresponds to the overlapping signals of the Hf protons from the amine group ($-NH_2$) and the Hg proton from the hydroxyl group (-OH). These protons are seen as a broad peak around 6.64–7.03 ppm, due to possible hydrogen bonding and proton exchange. The Hb proton appears as a doublet of doublets

at 7.58 ppm. The Hc proton resonates as a doublet at 8.24 ppm, showing coupling with Hb and Ha. The Ha proton appears as a doublet at 8.46 ppm showing coupling with Hb. Ha proton is more deshielded than the other protons because it is closer to the nitrogen atom in the pyridine ring. Hb proton is less deshielded than Hc proton because it is farther from the nitrogen atom in the pyridine ring compared to Hc. All proton NMR signals fall within the expected chemical shift range and are comparable to those of compound **119**.[153]

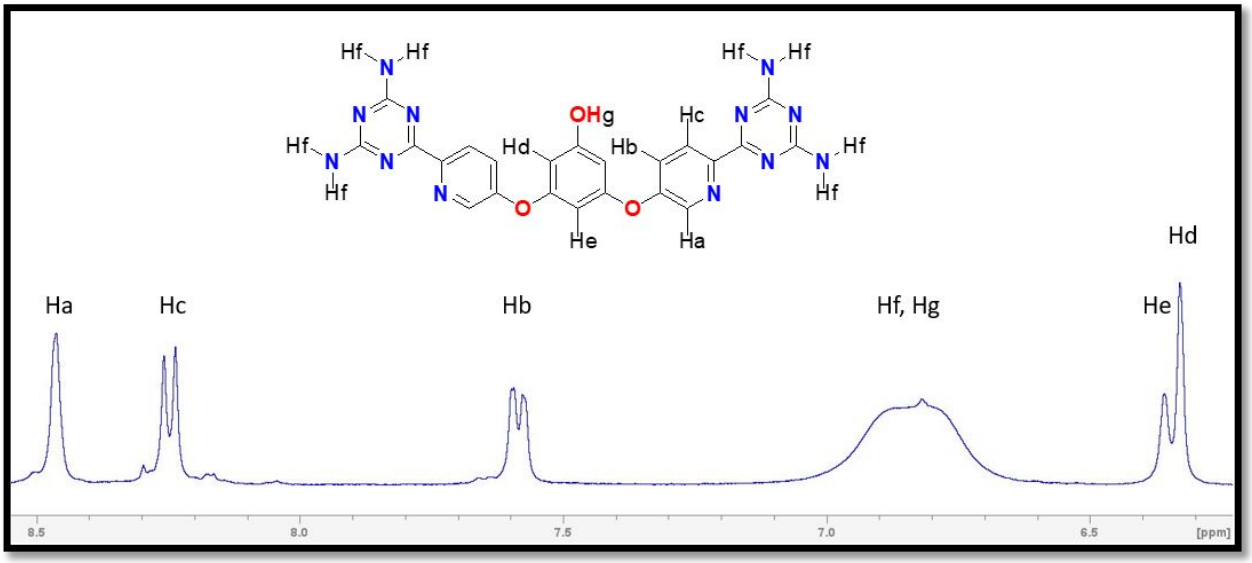

Figure 3. 16 ^{1}H NMR of **145** in DMSO-d_6.

Based on the IR spectrum of compound **145** (Figure 3.16) (Table 3.7), the cyano peak observed in compound **131** has disappeared, and new peaks have emerged at 3313 and 3470 cm^{-1}, indicating the presence of NH_2 groups and suggesting the formation of amide groups. Additionally, a broad peak at 3188 cm^{-1} suggests the formation of a hydroxyl group. The IR data fall within the expected range and are consistent with those observed for the similar compound **119** (Table 3.7).

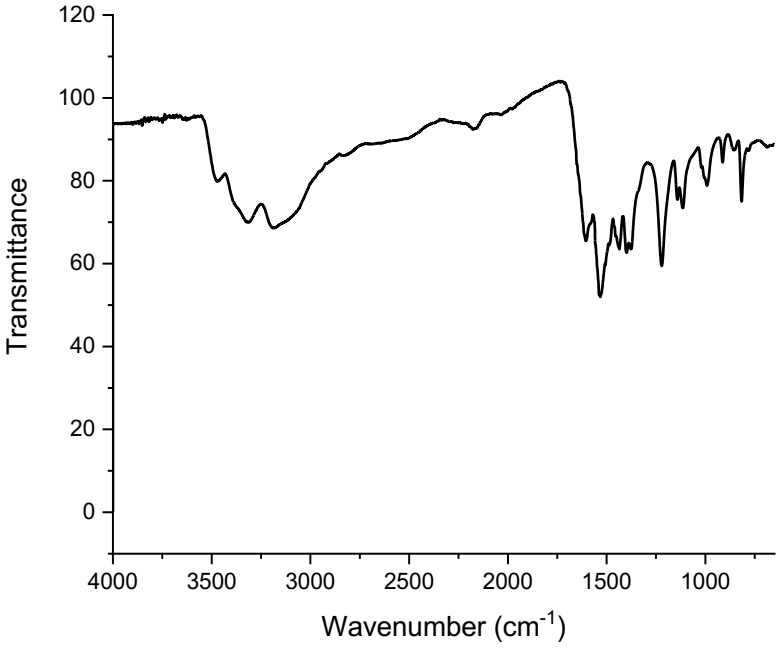

Figure 3. 17 IR spectrum of compound **145**.

3.3.2.2 UV of compound 145

Compound **145**, with an extended conjugated system, was analyzed for its absorption properties using UV spectroscopy (Figure 3.17) (Table 3.7). A characteristic $\pi \rightarrow \pi^*$ electronic transition was observed, with a maximum absorption wavelength (λ_{max}) at 300 nm and a molar absorptivity coefficient (ε) of 18,987 $M^{-1}cm^{-1}$ (Table 6), both of which are higher than those of compounds **131** and **119**. This red shift and increased molar absorptivity coefficient (ε) are attributed to the longer conjugated system in compound **145**.[154]

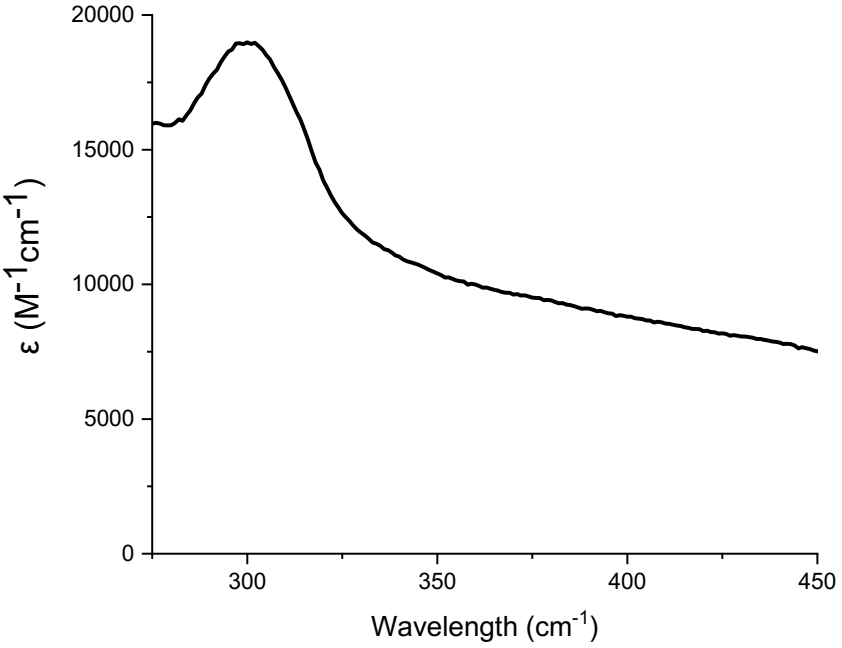

Figure 3. 18 The UV spectrum of compound **145** in acetonitrile.

3.3.2.3 TGA of compound 145

Thermogravimetric analysis shows that compound **145** exhibits high thermal stability, with decomposition occurring at 310°C, which is higher than that of compound **131** (Figure 3.18) (Table 3.7). This enhanced stability can be attributed to the more extensive conjugated system and the increased number of heteroatoms, which promote additional hydrogen bonding in compound **145**.

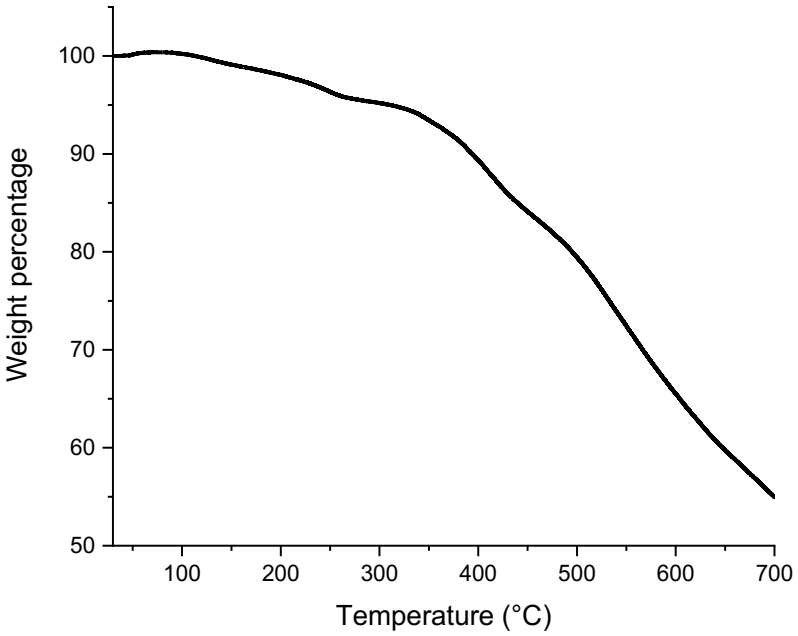

Figure 3. 19 Thermogravimetric analysis (TGA) for compound **145**.

Table 3. 7 IR data, λ_{max}, and TGA for compounds **131**, **119**, and **145**.

Cpd.	FTIR data				λmax abs (nm) / ε ($M^{-1}cm^{-1}$)	Td [a] (TGA) (°C)
	-CN group (cm^{-1})	C-O ether (cm^{-1})	O-H (cm^{-1})	NH_2 (cm^{-1})		
131	2233	1229	---	---	271/ 18224	288
119	---	---	---	3398, 3464	265/12100	---
145	---	1221	3188	3313, 3470	300 / 18987	310
a Td - decomposition temperature at 5 % weight loss measured by thermogravimetric analysis (TGA).						

3.4 Conclusion

In this study, we synthesized three isomers of cyanopyridine benzenes with yields exceeding 65%. Subsequently, we hydrolyzed them to amide and carboxylic groups in aqueous basic conditions

without using any catalyst. The resulting amide and nicotinic acid were purified without using any organic solvents or column chromatography. The yields of the amide and carboxylic acid derivatives vary depending on reaction conditions, such as reaction time and the amount of base used. Hydrogen bonding simulations in the solid state were conducted to show the effect of the position of heteroatoms in different isomers on molecular interaction. In addition, the results indicated that in the cyano isomers, only weak hydrogen bonds were observed. In contrast, the amide and carboxylic acid isomers exhibited both weak and strong hydrogen bonds, highlighting the influence of functional groups on the nature and strength of the hydrogen bonding network. Furthermore, Hirshfeld studies were conducted to show close contact between atoms.

The reaction time and the equivalents of base were investigated, showing that after four hours, all cyano groups convert to amide and carboxylic acid. Over time, the amide further converts to carboxylic acid, with the percentage of amide decreasing and carboxylic acid increasing. Additionally, using more equivalents of base increased the yield of carboxylic acid. UV spectra revealed that when cyano, amide, and carboxylic groups are in para positions, the higher conjugation system causes a red shift in λ_{max} compared to when they are in meta positions. In compound **141** the delocalized charge on the oxygen atoms of the carboxylate group causes a red shift in the $\pi \rightarrow \pi^*$ transition and facilitates the $n \rightarrow \pi^*$ transition. Proton NMR showed that protons of the pyridine ring closer to the nitrogen of the pyridine ring experience greater deshielding than other protons. TGA analysis shows all compounds **131**, **132**, **133**, **134**, **135**, **136**, **137**, **139**, and **141** have high thermal stability and hydrogen bonding can influence the thermal stability. The fluorescence results demonstrated that changes in the position of heteroatoms can alter the emission properties and also indicate aggregation.

In addition, compound **145** was synthesized with a yield of 72% and characterized using NMR, IR, UV spectroscopy, and mass spectrometry. The UV spectrum revealed a red shift compared to compounds **131** and **119**, attributed to the extended conjugated system of compound **145**. Thermal gravimetric analysis (TGA) demonstrated that the high degree of conjugation in compound **145**

contributes to its superior thermal stability, withstanding temperatures up to 341°C, compared to compound **131**.

All these compounds—cyano, amide, carboxylic, and diamino triazine—have significant potential for coordination reactions and the synthesis of metal-organic frameworks (MOFs) and complexes.

Chapter 4

Organic linkers with triphenylene cores

4.1 Introduction

In the field of molecular materials, triphenylene scaffold has received wide interest. It is a symmetrical and flat polyaromatic hydrocarbon consisting of four fused benzene rings.[155–163] These compounds have diverse properties that depend on the substituents introduced on the triphenylene core.[156,157,164] They are used in a wide range of applications such as organic light-emitting diodes (OLEDs), optical compensation films for liquid crystal display (LCD), organic field-effect transistors (OFET), photovoltaic solar cells, gas sensors, and so forth.[155,156,158–163,165–174] Although they are well-exploited in the field of functional materials, triphenylene derivatives are less used as a platform for coordination chemistry. Even though these compounds have been studied for more than a century, to the best of our knowledge, oxytriphenylenes with pyridine substituents (TPOPy) have never been reported (Figure 4. 1, top).

In this chapter, we present the synthesis and characterization of four novel organic linkers (Figure 4.1) based on the triphenylene core. These compounds feature six cyanopyridyl groups symmetrically substituted on a hexaoxytriphenylene platform. This symmetrical arrangement increases the likelihood of forming coordination polymers or metal-organic frameworks (MOFs).

According to the structures reported for substituted triphenylenes, the cyanopyridine arms of **150-153** should ideally protrude out of the triphenylene plane, thereby orienting the ligating sites in three directions.[175–180] Cyanopyridine contains two nitrogen donors (the N_{py} and the $N_{C\equiv N}$ atoms) capable of serving as coordination sites.[181] [181] In addition, the cyano group in this series of compounds has the potential to be oxidized to a carboxylic group, which could further enhance their value and versatility for coordination reactions.[182] Although numerous triphenylene derivatives have been documented, those incorporating cyanopyridines remain unreported.[183–186] In this study, triphenylene was synthesized following a previously reported procedure.[187,188] Subsequently, a nucleophilic reaction was used to introduce cyanopyridine isomers onto the triphenylene core. Notably, high yields were obtained without resorting to flash chromatography for purification. Thus, our primary objective in designing these ligands: to access the compounds using a simple and straightforward method allowing good yields, is met. Furthermore, the compounds were characterized by Fourier transform infrared spectroscopy (FTIR), ^{1}H and ^{13}C

nuclear magnetic resonance (NMR) spectroscopy, high-resolution mass spectrometry - electrospray ionization (HRMS-ESI), and CHN elemental analysis. Their absorption and emission properties were determined by UV absorption and fluorescence spectroscopy and thermogravimetric analysis (TGA) was used to assess their thermal stability.

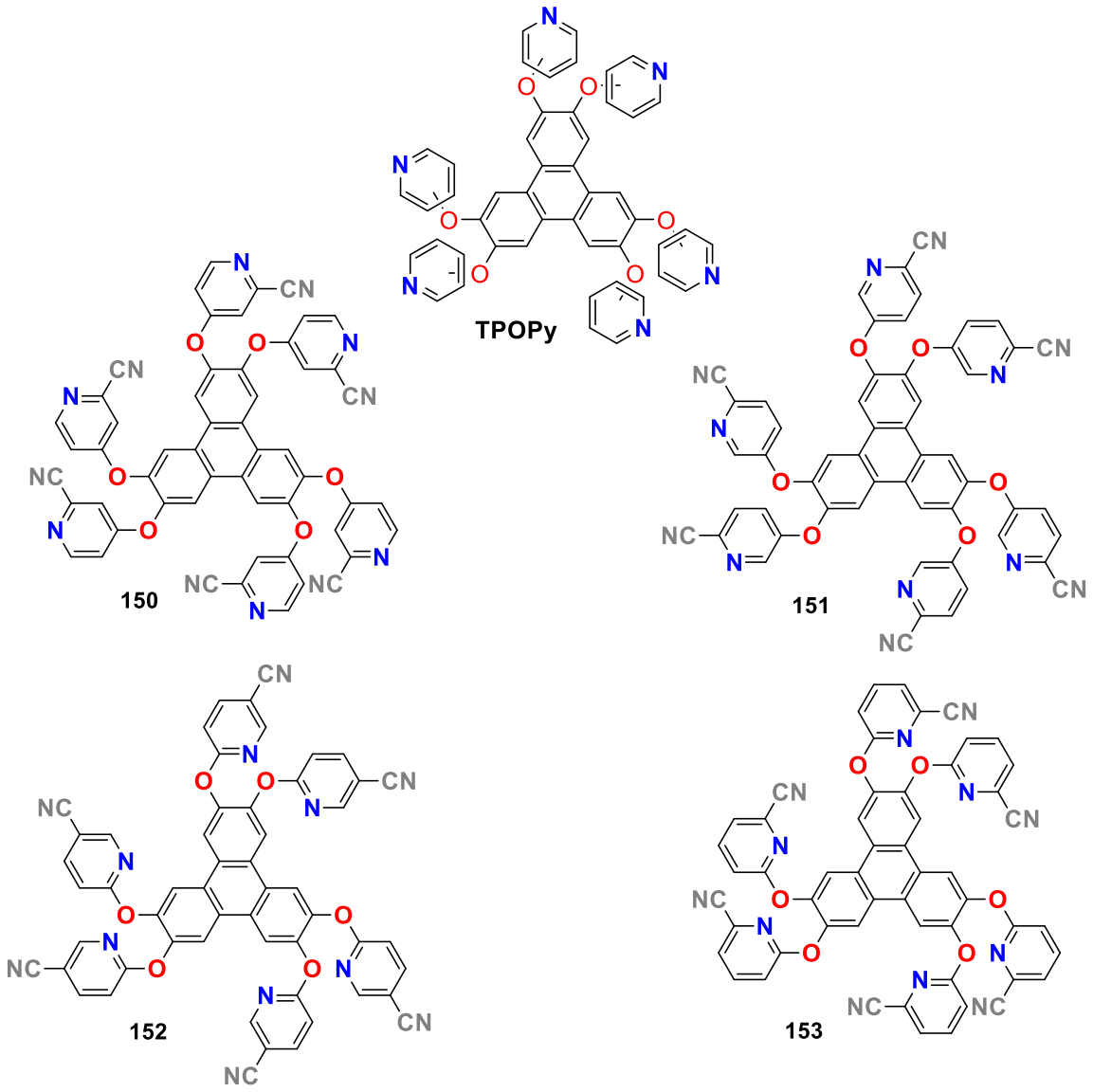

Figure 4. 1 Molecular structures of **150-153**.

4.2 Synthesis

2,3,6,7,10,11-hexahydroxy-triphenylene (HHTP) **49**, prepared in two synthetic steps following reported methods,[187,188] was reacted with 4-bromo-pyridine-2-carbonitrile **154**, 5-bromo-pyridine-2-carbonitrile **155**, 6-bromo-nicotinonitrile **156**, and 6-bromo-pyridine-2-carbonitrile **157**, respectively, to give, by nucleophilic substitution, the compounds **150**-**153** in very good yields (higher than 85%), as air stable pale beige powders (Scheme 4.1). Remarkably, no flash chromatography was required to isolate the pure products. Extraction and washing of the crude products were sufficient to isolate 2,3,6,7,10,11-hexamethoxy-triphenylene (HMTP) **52**, 2,3,6,7,10,11-hexahydroxy-triphenylene-(HHTP) **49**, and **150-153**. These compounds demonstrate significant solubility in various common solvents, such as DMF (dimethylformamide), DMSO (dimethyl sulfoxide), CH_2Cl_2 (dichloromethane), $CHCl_3$ (chloroform), and acetonitrile.

4.3 Result and discussion

4.3.1 IR, TGA, and NMR

The identities of **150-153** were confirmed by HRMS-ESI, in positive mode, for their molecular formula $C_{54}H_{24}N_{12}O_6$ (M) as $[M+H]^+$ ionized species and CHN elemental analysis was used to prove their purity (see Experimental section for details). Infrared spectra were recorded for **150-153** and confirm the presence of characteristic vibration frequencies of the -CN groups (2232 – 2241 cm^{-1}), C-N aromatic (1570 – 1596 cm^{-1}), C-O (1002 – 1013 cm^{-1}), and C-H bonds (3060 – 3088 cm^{-1}) (Figure 4.2 and Table 4.1).[143] In addition, ^1H and ^{13}C NMR spectroscopy data for **150-153** (Figures 4.4 and S21-S28) are in accordance with their expected formulated structures. Furthermore, as shown by TGA analysis (Table 4.1 and Figure 4.3), isomers **150-153** exhibit decomposition temperatures ranging from 359 to 402 °C, indicating their high thermal stability, which exceeds those of previously reported triphenylenes.[189]

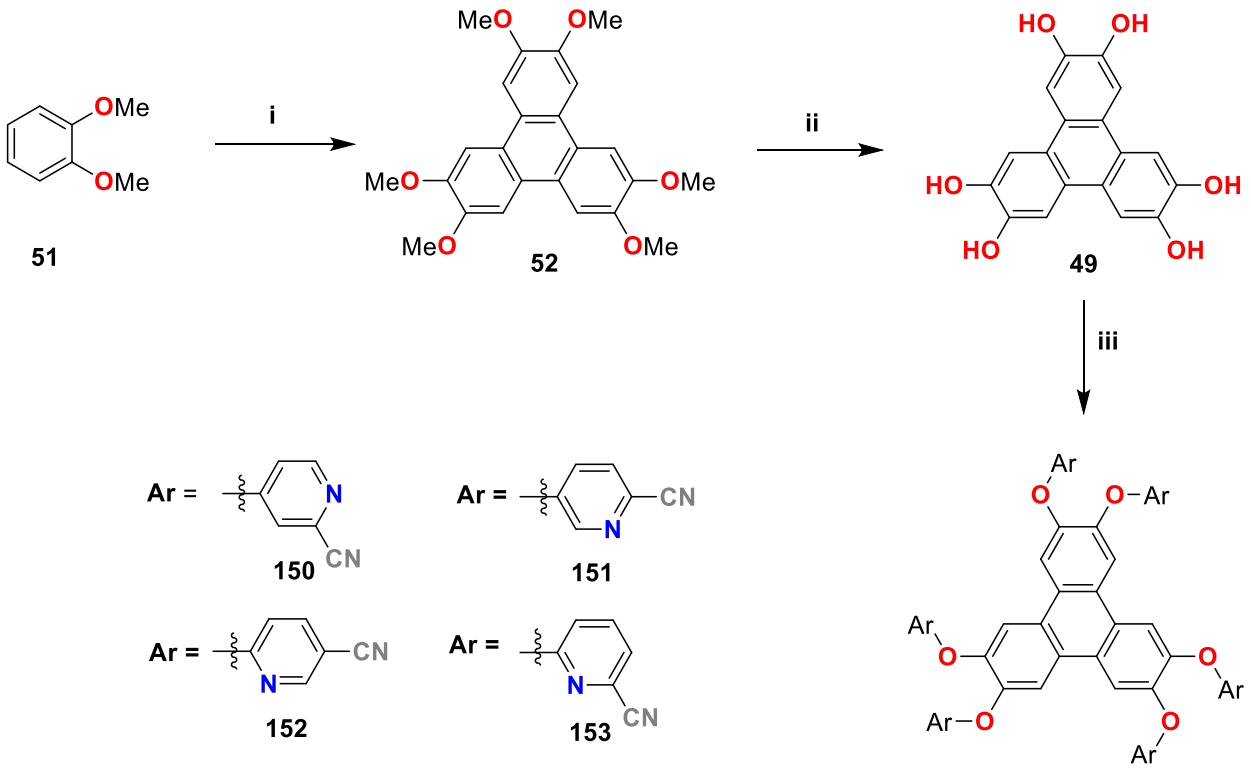

Scheme 4. 1 Synthetic route to prepare **150-153**. Reagents and conditions: i. $FeCl_3$, HCl/H_2SO_4, CH_2Cl_2, reflux, 2 h (87%).[188] ii. HBr, acetic acid (75%).[187] iii. Corresponding bromopyridinecarbonitrile **154-157**, K_2CO_3, DMF/Toluene, reflux (**150**, 90%, **151**, 87%, **152**, 92% and **153**, 89%).

Table 4. 1 FTIR data, λ_{max} absorption and emission values, and decomposition temperatures for **150-153** and selected relevant reported triphenylene-based compounds **158-161a**.

Cpd.	FTIR data ν (cm^{-1})				$\lambda_{max\ abs}$ (nm) / ε ($\times 10^5\ M^{-1}cm^{-1}$)[a]	$\lambda_{max\ em}$ (nm) (λ_{exc} = 270 nm)[a]			T_d [b] (TGA) (°C)
	-CN group	C-N aromatic	C-O	C-H aromatic		Main band	Shoulders	Other bands	
150	2241	1571	1007	3060	271 / 1.5	377	360, 396	-	397
151	2234	1570	1013	3061	275 / 1.2	380	363, 398	-	402
152	2232	1596	1002	3075	273 / 1.5	375	364, 393	-	400
153	2236	1590	1011	3088	269 / 1.3	374	362, 394	473	359
157[c, 143]	2217	1587	1019	2945	330	431	-	-	-
159[d, 189]	-	-	-	-	362, 407	460	-	-	305
160[e, 175]	-	-	-	-	-	305, 382	-	-	-
161[f, 190]	-	-	-	-	-	415, 430	-	525	-
162[g] 191	-	-	-	-	275 / 0.6	-	-	-	-

[a]in acetonitrile, at room temperature

[b]T_d - decomposition temperature at 5 % weight loss measured by thermogravimetric analysis (TGA)

[c]**158** is *BZ4 CYBR, a* triphenylene-based compound: $C_{29}H_{34}N_2O_3$ (Figure 4.2)

[d]**159** is PTPT, a triphenylene-based compound: $C_{46}H_{62}O_4$ (Figure 4.2)

[e]**160** is a triphenylene-based compound: $C_{342}H_{390}F_{54}N_{48}O_{72}$ (Figure 4.2)

[f]**161** is a triphenylene-based compound: $C_{102}H_{174}N_6O_{12}$ (Figure 4.2)

[g]**162** is compound 6a in ref. 185, a triphenylene-based compound: $C_{68}H_{107}NO_4S_2$ (Figure 4.2)

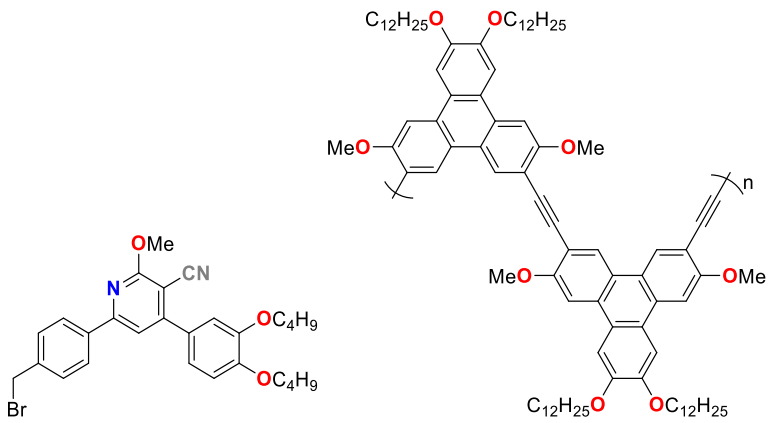

158 **159**

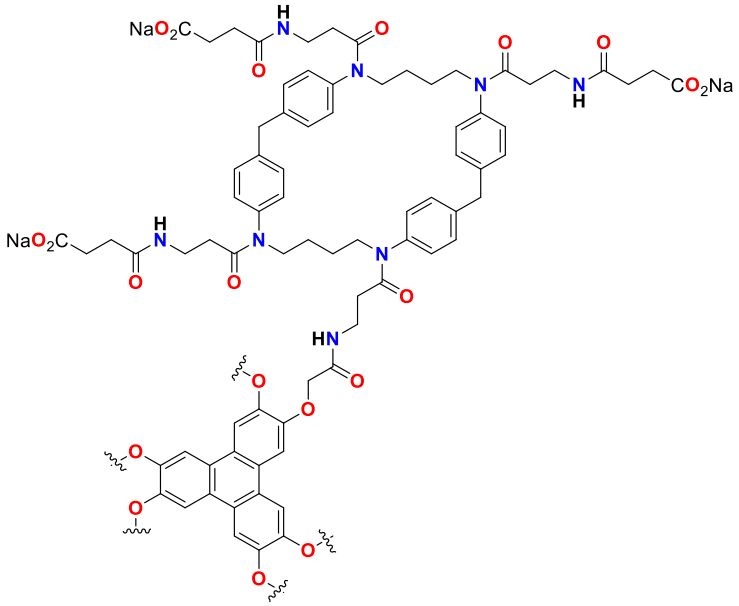

160

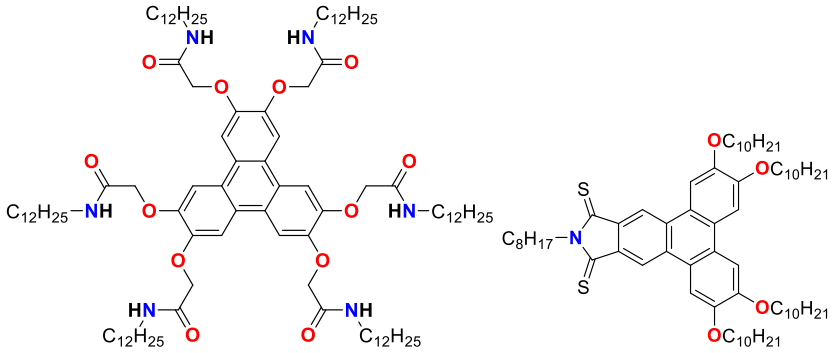

161 **162**

Figure 4. 2 Structure of compounds **158**[143], **159**[189], **160**[73], **161**[190], and **162**[190].

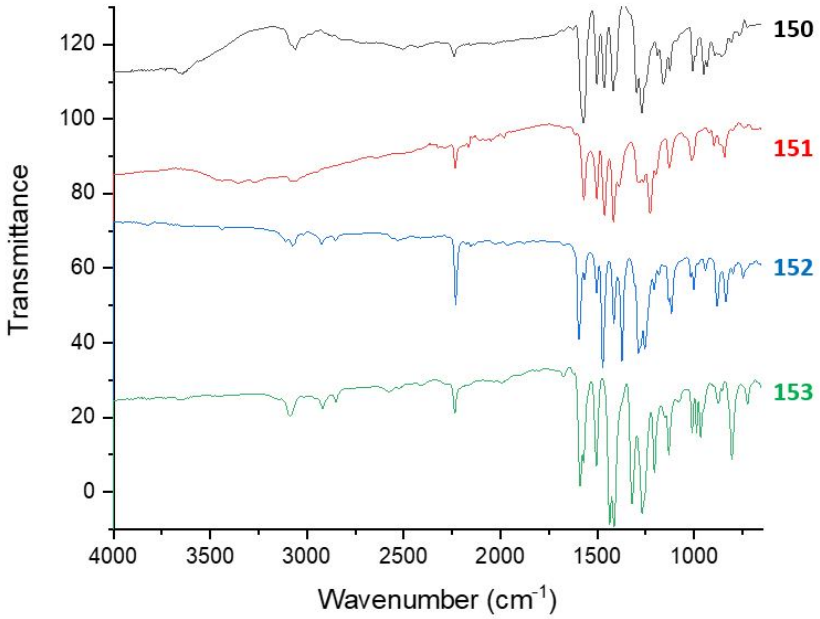

Figure 4. 3 FT-IR spectra of compounds **150-153**.

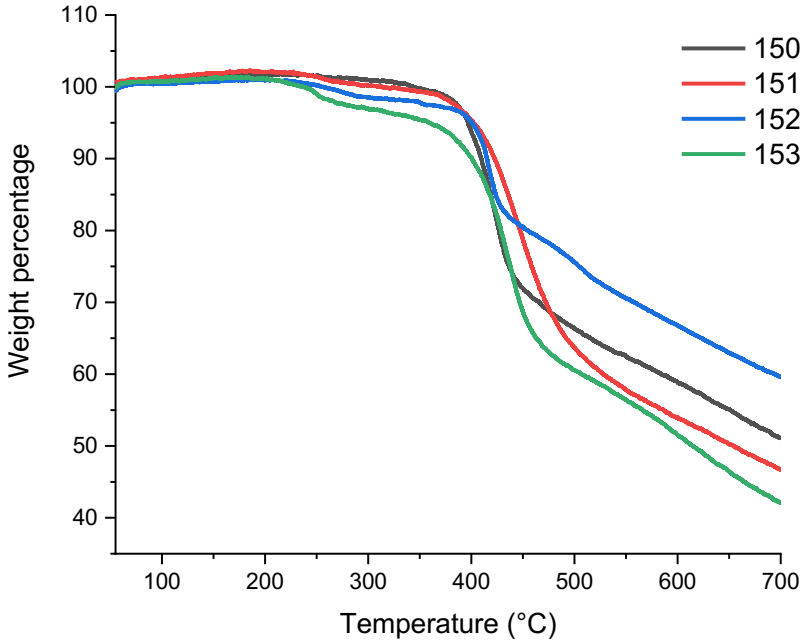

Figure 4. 4 Thermogravimetric analysis (TGA) for compounds **150-153** (30 to 700 °C, heating rate of 10 °C/ min, N_2 atmosphere).

The ^{1}H NMR spectra of isomers **150-153** reveal distinct proton resonance chemical shifts, coupling constants, and multiplicities (Figure 4.4). Each isomer presents the Hd protons belong to triphenylene cores as singlets, at different chemical shifts: **150**at δ 9.05 ppm (s, 6H), **151** at δ 8.96 ppm (s, 6H), **152** at δ 8.86 ppm (s, 6H), and **153** at δ 8.91 ppm (s, 6H). Isomer **150** exhibits two doublets: Hc proton at δ 8.56 ppm (d, ^{3}J = 5.8 Hz, 6H) and Ha proton at δ 7.82 ppm (d, ^{4}J = 2.5 Hz, 6H), together with a doublet of doublets at δ 7.31 ppm for Hb proton (dd, ^{3}J = 5.8, ^{4}J = 2.6 Hz, 6H). Isomer **151** displays two doublets: Ha proton at δ 8.48 ppm (d, ^{4}J = 2.5 Hz, 6H) and Hc proton at δ 7.98 ppm (d, ^{3}J = 8.7 Hz, 6H), along with a doublet of doublets for Hb proton at δ 7.58 ppm (dd, ^{3}J = 8.7, ^{4}J = 2.9 Hz, 6H). Isomer **152** shows two doublets: Ha proton at δ 8.59 ppm (d, ^{4}J = 1.9 Hz, 38H) and Hb proton at δ 7.13 ppm (d, ^{3}J = 8.7 Hz, 46H), along with a doublet of doublets for Hc proton at δ 8.26 ppm (dd, ^{3}J = 8.7, ^{4}J = 2.3 Hz, 47H). Isomer **153** exhibits three doublets of doublets: Hc proton at δ 8.01 ppm (dd, ^{3}J = 8.5, ^{3}J = 7.4 Hz, 6H), Ha proton at δ 7.73 ppm (dd, ^{3}J

= 7.3, ^4J = 0.7 Hz, 6H), and Hb proton at δ 7.31 ppm (dd, ^3J = 8.5, ^4J = 0.7 Hz, 6H), indicating coupling among Ha, Hb, and Hc protons. Moreover, all Hd protons in the triphenylene cores exhibit more deshielding than others due to the strong induced field of triphenylene. Furthermore, Hc proton in isomer **150**, Ha proton in isomer **151**, and Ha proton in isomer **152** are deshielded more than other protons of the pyridine rings, as they are located at the α-position of the N-pyridyl atom. These observations provide insights into the positional effects of protons relative to the N-pyridyl atom. Moreover, while isomers **150**, **151**, and **152** share identical splitting patterns, isomer **153** displays a different pattern due to the absence of a proton at the α-position of the N-pyridyl atom (Figures 4.5 and S21-S28).

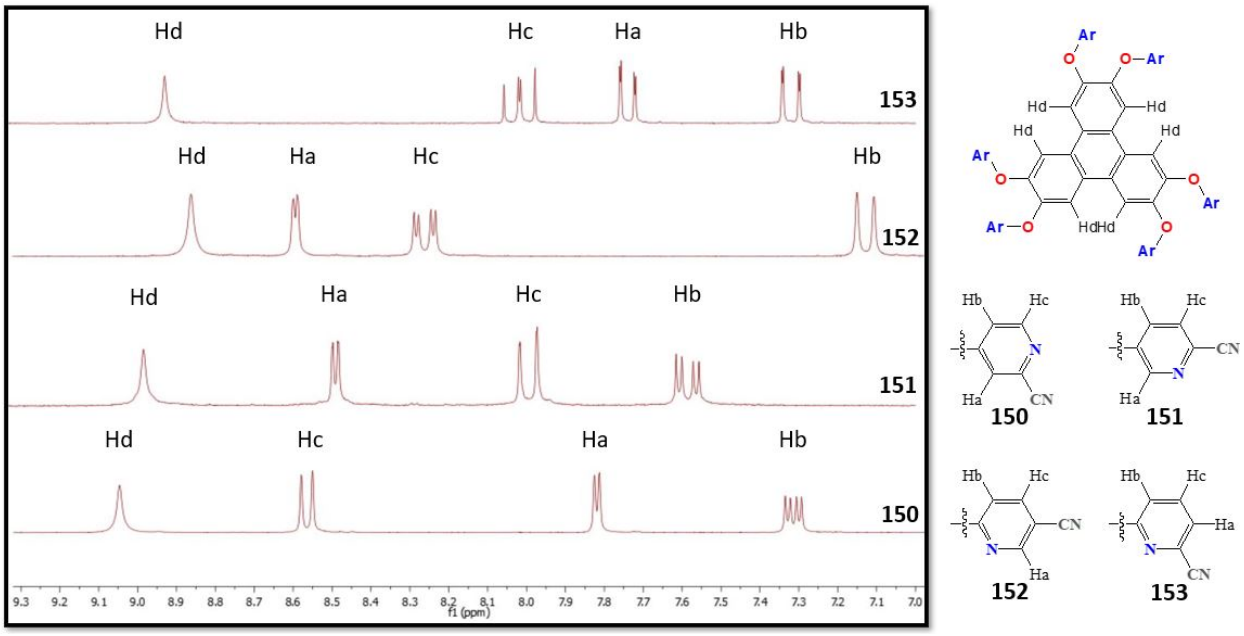

Figure 4. 5 ^{1}H NMR spectra of **150-153** in DMSO-d_6.

4.3.2 UV absorption and emission properties

Compounds **150-153**, characterized by the extended conjugated system of the triphenylene core, were examined for their absorption properties by UV spectroscopy (Table 4.1, Figure 4.6). Characteristic π → π* electronic transitions were found with maximum absorption wavelength ($\lambda_{max\ abs}$) and molar absorptivity coefficient (ε) values in the range of 269-275 nm and 1.2 ×10^5 –

1.5×10^5 $M^{-1}cm^{-1}$**,** respectively. These values align well with those found for other triphenylene chromophores (250–320 nm).[189] Slight differences in $\lambda_{max\ abs}$ observed for **150-153** are attributed to the effect of distinct substitutions on the triphenylene core. The placement of the cyano group in para position relative to the ether group (in **151** and **153**) results in an extended conjugated system compared to the situation when its placement is in meta position (in **150** and **153**). Consequently, a red shift of the $\lambda_{max\ abs}$ is observed for **151** and **153** vs. **150** and **153**. In addition, compounds **150**–**153** exhibited significantly higher molar extinction coefficients (120,000 to 150,000 $L \cdot mol^{-1} \cdot cm^{-1}$) compared to similar compounds (Table 4.1, cpd. **162**, 60,000 $L \cdot mol^{-1} \cdot cm^{-1}$)[191], attributed to an extended conjugated systems in compounds **150**–**153**. These findings highlight the impact of specific molecular modifications on the electronic structure and absorption properties of triphenylene derivatives. The improved absorption properties of the compounds herein suggest them as good candidates for light harvesting devices.

Fluorescence spectroscopy offers valuable insights into the molecular organization of compounds **150-153**. As depicted in Figure 4.6 (right), the fluorescence spectra of freshly prepared acetonitrile solutions, excited at 270 nm, reveal that all compounds exhibit a consistent pattern indicative of typical triphenylenes.[175] (a main band (350 to 425 nm) with $\lambda_{max\ em}$ in the interval 374-380 nm and two shoulders (360-364 nm and 393-398 nm) (Table 4.1). Interestingly, compound **153** demonstrates a distinct behavior, featuring an additional broad band at 473 nm, attributed to excimer emission. This phenomenon, also observed in other triphenylene derivatives, is ascribed to variations in aggregation/ packing arrangements of triphenylene moieties.[190,191] For compound **153**, the intensity of the emission feature at 400-550 nm increases *vs.* the emission intensity of the 350-400 nm band, with increasing concentration from 5 x 10^{-7} M to 1 x 10^{-5} M, supporting the assignment of the former as aggregation based (Figure 4.7). Measurements at higher concentrations are hindered by the poor soluibility of the compound. The position of the nitrogen atom in the pyridine ring with respect to the protons in the triphenylene core, as well as the position of the cyano group within the four isomers, dictate the force of intra- and intermolecular (hydrogen bonding) interactions (see also X-ray structure determination and Hirshfeld surface analysis sections, *vide infra*). As a result, the planarization degree of each isomer **150**-1**53**, and consequently its capacity to aggregate, are determined. The emissive properties of **153**, uniquely

displaying aggregation behaviour, can, thus, be rationalized by considering the combined effect of the above-mentioned structural features.

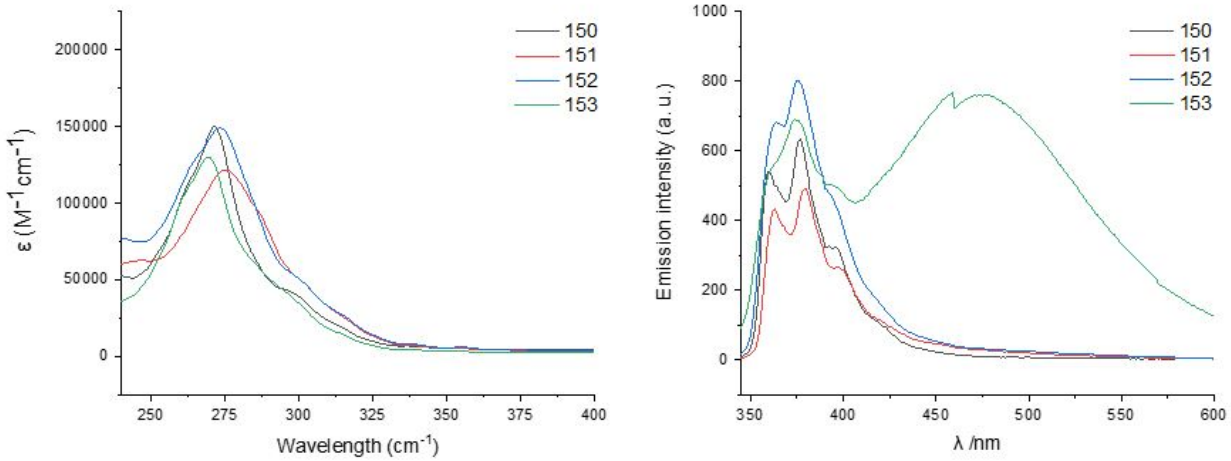

Figure 4. 6 UV absorption (left) and emission (right) spectra of compounds **150-153** in acetonitrile at room temperature.

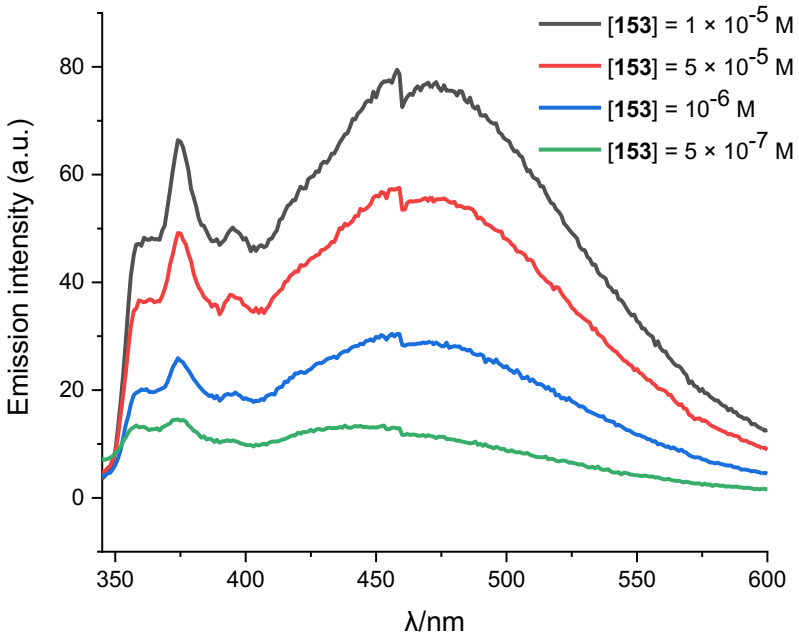

Figure 47 . Emission spectra of compound **153** in acetonitrile at room temperature at different concentrations.

4.3.3 X-ray structure determination

Single-crystal X-ray diffraction (SCXRD) analysis was carried out to elucidate the solid state structures of **150** and **151**. Yellowish crystals of **150** and **151** were grown by partial evaporation of DMSO and acetonitrile solutions of the compounds, respectively. It is worth noting that despite many attempts to crystallize compounds **152** and **153**, suitable crystals for SCXRD couldn't be obtained. Well-formed crystals of **150** are triclinic, space group P-1 (Z = 2), while crystals of **151** are monoclinic, space group $P2_1/c$ (Z = 4). Crystal data and structure refinement details for **150** and **151** are given in Table 4.2, and views of the structures are illustrated in Figure 4.8. The structures of compounds **150** and **151** reveal that the six cyanopyridine substituants are positioned out of the plane of the triphenylene core and are covalently bonded to the oxytriphenylene moiety, through etheric bonds. The average bond length of C=C[192], C-O[193], and C≡N[147] bonds in **150** and **151** are in the normal ranges (Table 4.3).[144,146,147]

Table 4. 2 Crystal data and structure refinement details for **150** and **151.**

Compound	**150**	**151**
CCDC no.	2379513	2379447
Empirical formula	$C_{54}H_{24}N_{12}O_6S_{0.5}$	$C_{54}H_{24}N_{12}O_6$
Formula weight	952.903	936.85
Temperature/K	100.00(10)	150.15
Crystal system	triclinic	monoclinic
Space group	P-1	$P2_1/c$
a/Å	10.4850(2)	5.9205(9)
b/Å	14.6692(3)	26.389(4)
c/Å	16.9754(5)	30.767(5)
α/°	73.345(2)	90
β/°	77.370(2)	95.092(8)
γ/°	77.189(2)	90
Volume/Å^3	2405.27(10)	4787.8(13)
Z	2	4
ρ_{calc}g/cm^3	1.316	1.3
μ/mm^{-1}	0.936	0.466
F(000)	979.6	1920
Crystal size/mm^3	0.19 × 0.03 × 0.02	0.2 × 0.02 × 0.02
Radiation	Cu Kα (λ = 1.54184)	GaKα (λ = 1.34139)
2Θ range for data collection/°	6.38 to 155.78	3.844 to 106.518
Index ranges	-13 ≤ h ≤ 10, -18 ≤ k ≤ 18, -21 ≤ l ≤ 21	-6 ≤ h ≤ 6, -31 ≤ k ≤ 31, -36 ≤ l ≤ 36
Reflections collected	31959	45617
Independent reflections	9688 [R_{int} = 0.0229, R_{sigma} = 0.0244]	8414 [R_{int} = 0.1041, R_{sigma} = 0.0873]
Data/restraints/parameters	9688/0/688	8414/156/662
Goodness-of-fit on F^2	1.039	1.023
Final R indexes [I>=2σ (I)]	R_1 = 0.0520, wR_2 = 0.1475	R_1 = 0.0788, wR_2 = 0.2243
Final R indexes [all data]	R_1 = 0.0585, wR_2 = 0.1530	R_1 = 0.1611, wR_2 = 0.2846

Table 4. 3 Bond lengths (Å) in **150** and **151**.

Bond	Bond lengths* (Å)		
	150	**151**	**Literature**
C=C	1.39 (51)	1.38 (57)	1.41 (61)[144]
C-O	1.38 (23)	1.38 (42)	1.37 (77)[146]
C≡N	1.15 (15)	1.13 (53)	1.15 (0.9)[147]

*Bond lengths are given as average values.

4.3.4 Hydrogen bonding

The hydrogen bonding pattern in **150** (Figure 4.7-a) reveals a combination of strong and weak hydrogen bonds (Table 4.4).[194] These bonds involve interactions between hydrogen atoms and both nitrogen and oxygen atoms of the molecule, as well as the co-crystallized solvent. In **151** (Figure 4.7-b), the presence of various weak and strong hydrogen bonds involving nitrogen atoms are found. These observations underscore the importance of atom positioning in the isomers and its impact on inter- and intramolecular interactions, as well as on packing arrangements. Of note, the crystal packing in **150** and **151** does not involve the columnar π-π stacking commonly observed in many other triphenylene derivatives (Figure 4.6). This deviation is attributed to the steric bulk created by the presence of cyanopyridyl substituents. Additionally, the existence of multiple interactions, in both **150** and **151**, such as hydrogen bonds involving cyanopyridyl substituents, partly hinders the columnar phenomenon (Figure 4.7). To contextualize the behavior of **150** and **151** in comparison to other derivatives exhibiting this columnar phenomenon of triphenylene, the crystal packing of compounds (2,3,6,7,10,11-hexamethoxytriphenylene)[195] **52** and (triphenylene-2,3,6,7,10,11-hexacarboxylic acid hexamethyl ester)[196] **163** (Figure 4.8) is analyzed. In these cases, a distinctive columnar packing arrangement is evident, explained by the relatively modest size of the methoxy and ester groups, which do not significantly disrupt the inherent columnar packing system of triphenylene. In the case of molecule **52**, a weak hydrogen bond is observed between the hydrogen of the methyl group and the oxygen atom (O···H–C(sp^3), d = 2.39(1) Å and θ = 154.3(1)°) (Figure 4.9). In molecule **163**, two weak hydrogen bonds are identified. One involves the hydrogen of triphenylene and oxygen (O···H–C(sp^2), d = 2.47(1) Å and θ = 123.3(1)°), while the other is between the hydrogen of the methyl group and the oxygen of the carbonyl group

(O···H–C(sp^3), d = 2.35(1) Å and θ = 100.7(1)°) (Figure 4.9). These interactions play a crucial role in maintaining the overall stability of crystal packing by influencing the arrangement of molecules within the lattice. Importantly, these effects are achieved, in case of **52** and **163**, without disrupting the columnar packing system of triphenylene (Figure 4.8).

Table 4. 4 The type of hydrogen bonds in **150** and **151.**

Cpd.	Bond	θ (°)	d (Å)	Type of hydrogen bond[197]
150	N···H-C	163.1(2)	2.4(3)	Weak
150	O···H-C	161.2(1)	2.2(3)	Strong
150	O···H-C	148.7(2)	2.1(4)	Strong
150	N···H-C	170.0(4)	2.3(4)	Weak
151	N···H-C	158.3(1)	2.4(4)	Weak
151	N···H-C	149.0(2)	2.2(4)	Strong
151	N···H-C	172.8(2)	2.4(3)	Weak
151	N···H-C	158.3(2)	2.4(3)	Weak

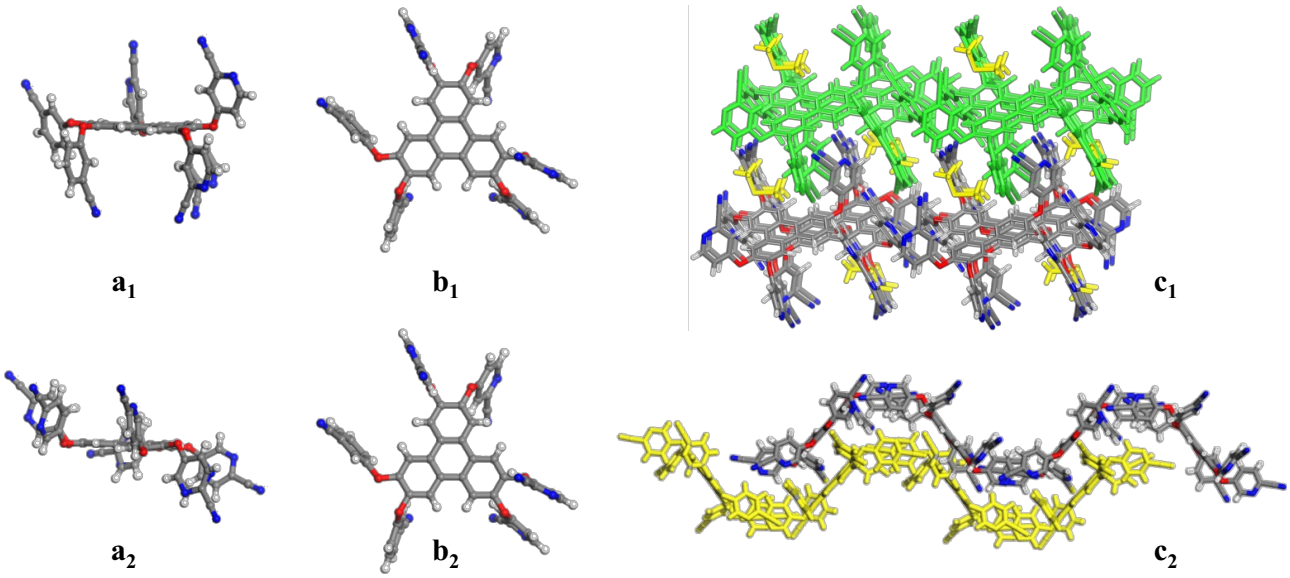

Figure 4. 8 The solid-state structures of molecules **150** and **151** are depicted in (a_1) and (a_2) (top views), and (b_1) and (b_2) (side views) of individual molecules. Stereoviews displaying molecular packing are presented in (c_1) and (c_2). Atom color code: C gray, H white, N blue, and O red. To enhance clarity in molecule **150**, a green layer highlights the packing, and DMSO molecules are depicted in yellow (c_1). In molecule **151**, a yellow layer marks the packing (c_2).

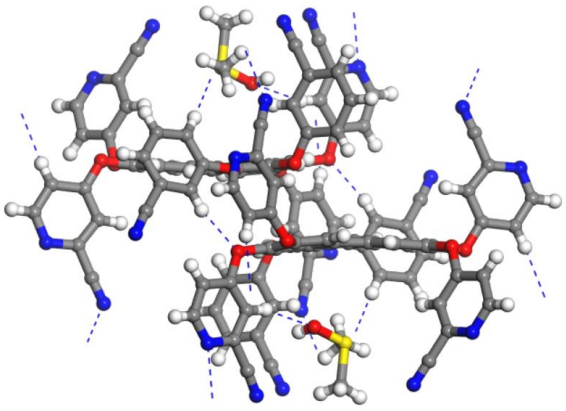

a

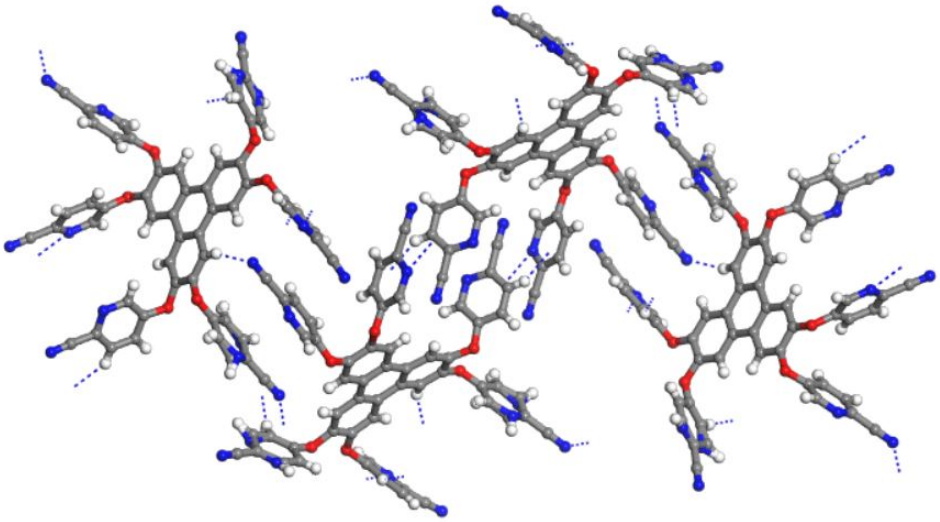

b

Figure 4. 9 Hydrogen bonding patterns in the crystal structures of **150** and **151**. The hydrogen bonds are shown by dashed lines. Atom color code: C gray, H white, N blue, O red, and S yellow.

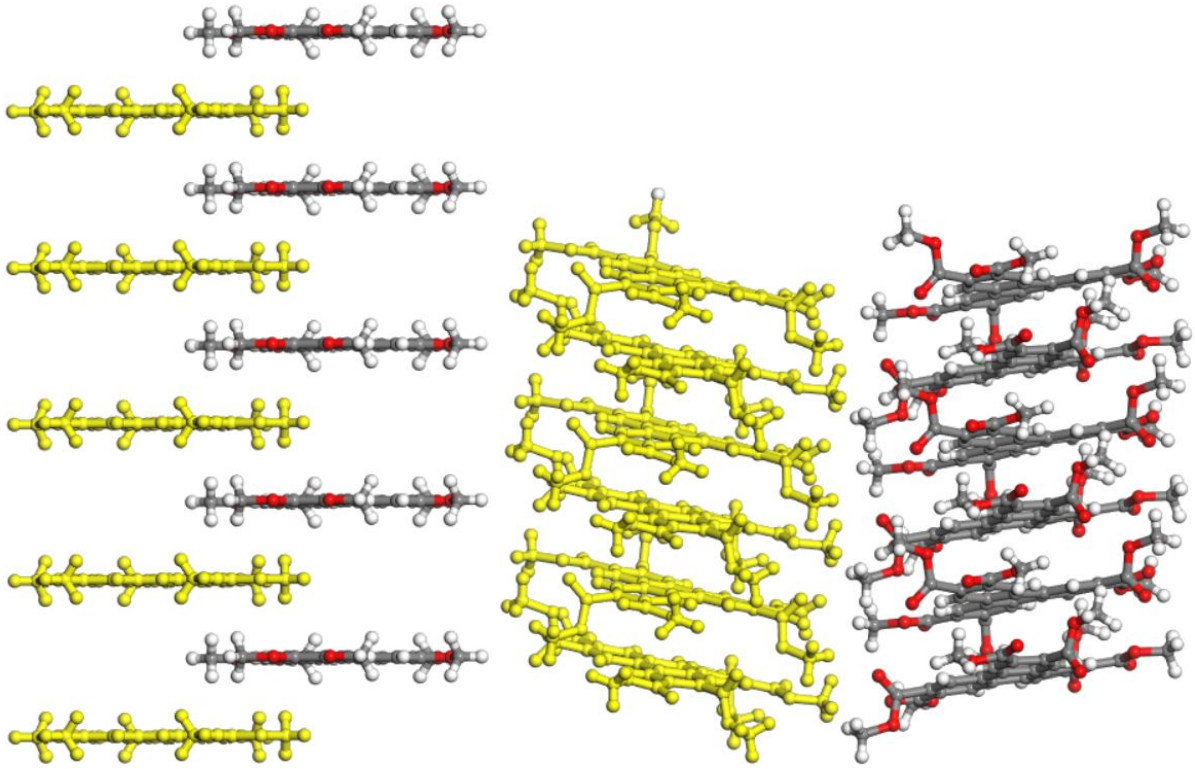

52 **163**

Figure 4. 8 Molecular packing in the solid state structures of **52**[195] and **163**[196]. For better visualization, one of the layers is shown in yellow. Atom color code: C gray, H white, N blue, O red, and S yellow.

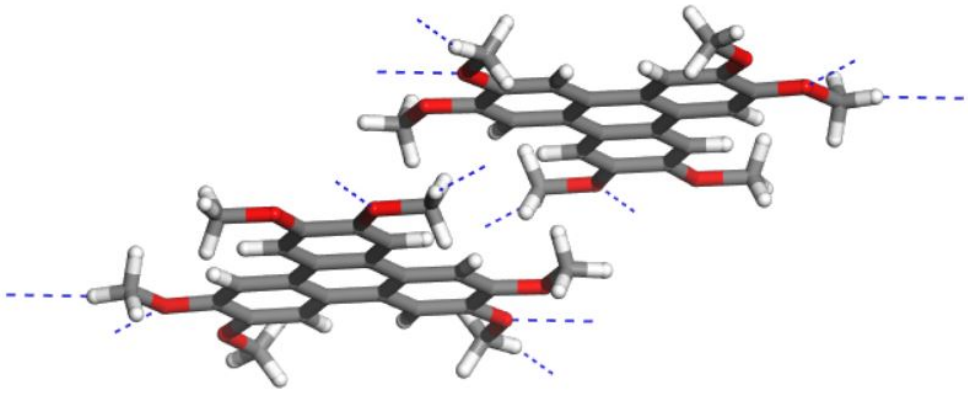

52

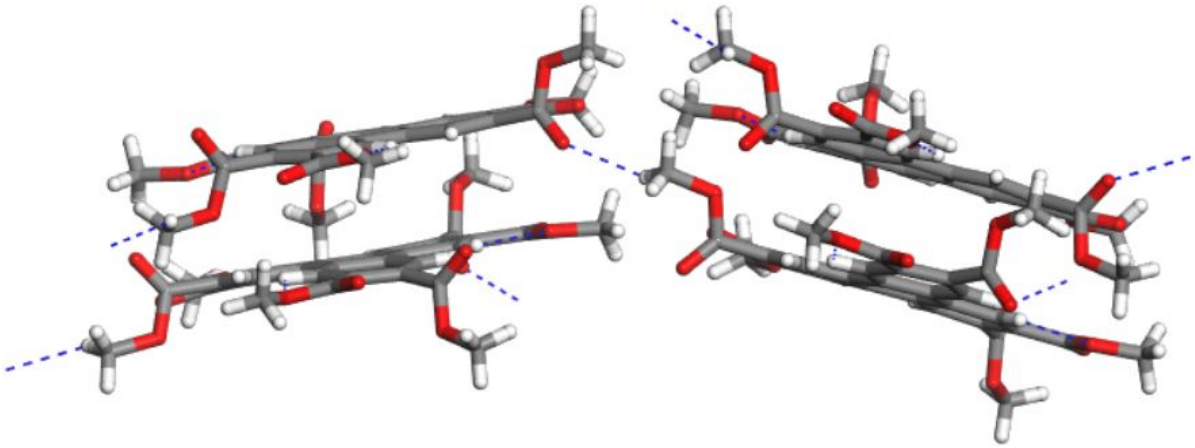

163

Figure 4. 9 Hydrogen bonding patterns in the crystal structures of **52**[195] and **163**[196]. The hydrogen bonds are shown by dashed lines. Atom color code: C gray, H white, and O red.

4.3.5 Hirshfeld surface analysis

To gain deeper insights into the molecular organization, the intermolecular interactions in the crystal packing of **150** and **151** have been further examined by Hirshfeld surface analysis (Figures 4.10 a-d and S14-15). Figures 4.10a and 4.10c show the d_{norm}, mapping in which short intermolecular contacts corresponding to N · · · H, O · · · H, and H · · ·H are represented by red spots. The overall fingerprint plot (Figures 4.10b and 4.10d) display prominent types of contacts corresponding to N · · · H (33.4%), H · · · H (17.5%), C · · · H (16.0%), C · · · N (10.7%), C · · · C (8.0%), O · · · H (7.8%), C · · · O (2.7%), N · · · N (1.9%), O · · · N (1.5%) and O · · · O (0.1%) for **150** and N · · · H (34.8%), H · · · H (20.6%), C · · · H (12.9%), C · · · N (11.6%), C · · · C (8.3%), O · · · H (4.4%), C · · · O (2.7%), N · · · N (2.7%), O · · · N (1.4%) and O · · · O (0.2%) for **151**.

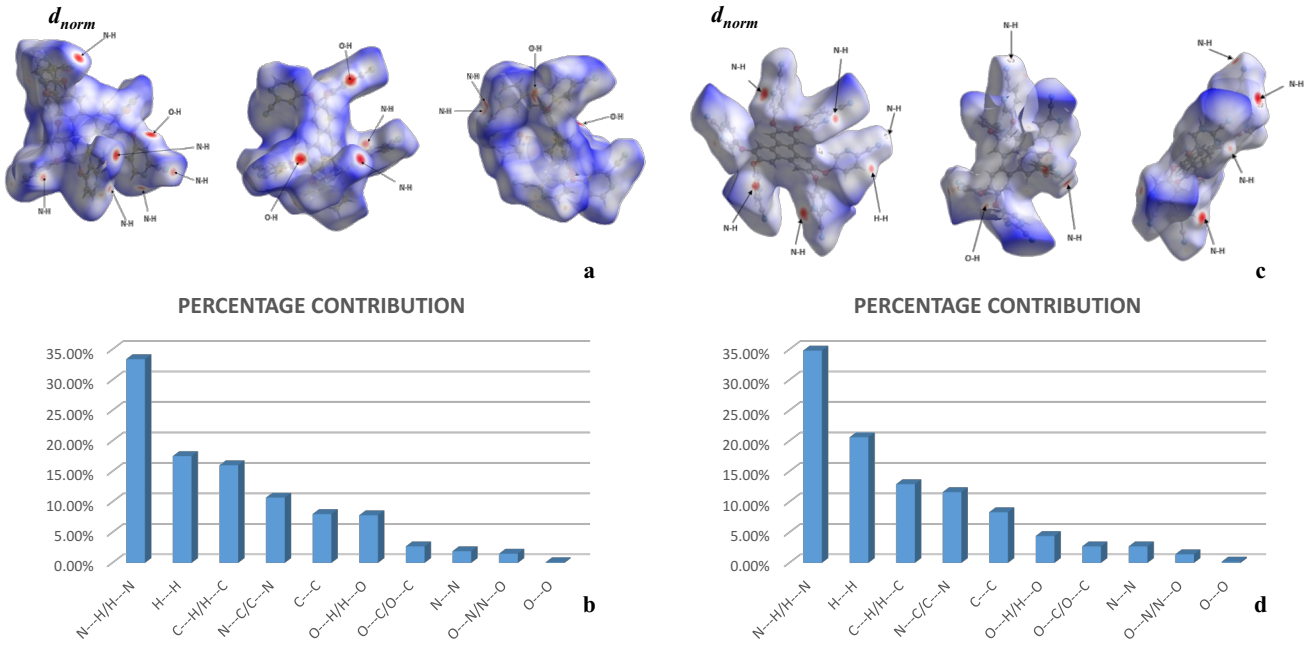

Figure 4. 10 Hirshfeld surfaces for the molecular unit of **150** and **151**. d_{norm} mapping in **150** (a); percentage contribution of intermolecular interaction in **150** (b); d_{norm} mapping in **151** (c); percentage contribution of intermolecular interaction in **151** (d).

Based on the percentage contribution of intermolecular interactions in compounds **150** and **151**, it is evident that most of the interactions involve nitrogen atoms. This highlights the significance of nitrogen in these interactions. Therefore, the position of the cyano group and the nitrogen in the pyridine ring likely plays an important role in influencing the intermolecular interactions.

4.4 Conclusion

In this study, we have successfully synthesized a novel series of hexaoxytriphenylene derivatives substituted with cyanopyridyl groups (**150-153**). Notably, the purification after each synthetic step is facile, consisting only of extraction and washing the crude product with solvents, thus greatly facilitating the isolation of final products **150-153** in very good yields (87 – 92%). The compounds are thermally stable (up to ~ 400 °C) and present exciting spectroscopic properties. In particular, all **150-153** derivatives exhibit triphenylene-based emission at around 375 nm, while interestingly,

isomer **153** displays an additional broad peak at 475 nm, attributed to aggregation effects. The solid state structures of **150** and **151** show that the columnar organization found in other triphenylene-based compounds is not observed due to the positioning of cyanopyridyl substituents out of the terphenylene core plane and their participation in multiple molecular interactions, as shown by packing and hydrogen bonding analysis, as well as by Hirshfeld surface analysis. These compounds are promising for designing ordered materials as they present the possibility of facile -CN group conversion into carboxylate[198] or diaminotriazinyl (DAT)[199] groups. They can also be used to develop new coordination polymers (CP) with tailored properties by linkage with metal ions, as evidenced by the synthesis of a cyanopyridine CP of Cd(II), used in humidity sensing.[200]

Chapter 5

Organic linker with azacoronene core

5.1 Introduction

In the field of material science, long conjugated systems have garnered significant attention due to their potential applications in organic optoelectronics, such as field-effect transistors, photovoltaic cells, and light-emitting diodes.[201–203] A longer conjugated system can induce a red shift in the UV spectrum[204] and enhance thermal stability.[205] One of the notable structures that has been extensively studied is coronene, known for its extended conjugated system. Azacoronene, a derivative of coronene, is an organic compound where one or more CH groups in the coronene core are replaced by nitrogen atoms. The substitution of carbon with a more electronegative atom like nitrogen can enhance electron transport within the conjugated system. Additionally, in the field of coordination chemistry, the presence of heteroatoms such as nitrogen increases the potential for coordination bonds, contributing to the formation of more stable metal-organic frameworks (MOFs) and complexes.[206]

In this research, our newly synthesized azacoronene, compound **164**, (Figure 5.1) demonstrates improved coordination sites and an extended conjugated system compared to hexahydroxy triazacoronene (compound **69**) by incorporating three benzoic acid groups at the 2, 6, and 10 positions of triazacoronene. These enhancements suggest the potential for increased stability and superior electronic properties in the resulting coordination compound.[25]

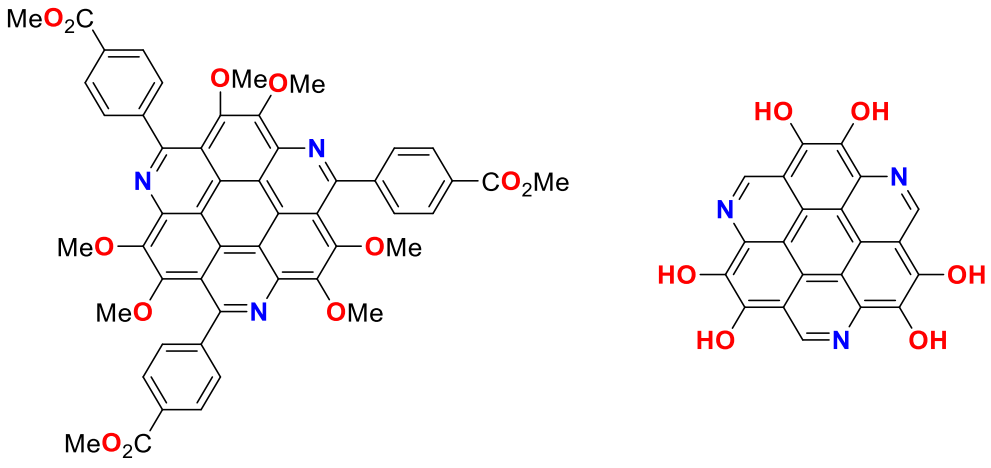

164 **69**

Figure 5. 1 Structure of compounds **69** and **164**.

Several methods have been employed for the synthesis of azacoronene derivatives. In this research, we utilized the 6π azaelectrocyclization strategy, a reported method involving an oxidative aromatization process. This approach offers several advantages, including simplicity, high yields, and broad substrate scope, while eliminating the need for any catalysts.[207]

5.2 Synthesis

In this research, we synthesized compound **164** (Scheme 5.1). The reaction began with oxidative aromatization of veratrole **51** using $FeCl_3$, leading to the synthesis of hexamethoxytriphenylene **52**. Following this, an electrophilic aromatic substitution reaction was carried out to introduce three nitro groups onto the hexamethoxytriphenylene **52**. The nitro groups were then reduced to amine groups using $Ni(OAc)_2$ and $NaBH_4$. Finally, a 6π azaelectrocyclization reaction between 1,5,9-triamino-2,3,6,7,10,11-hexamethoxytriphenylene **166** and 4-formylbenzoate resulted in the formation of compound **164**.

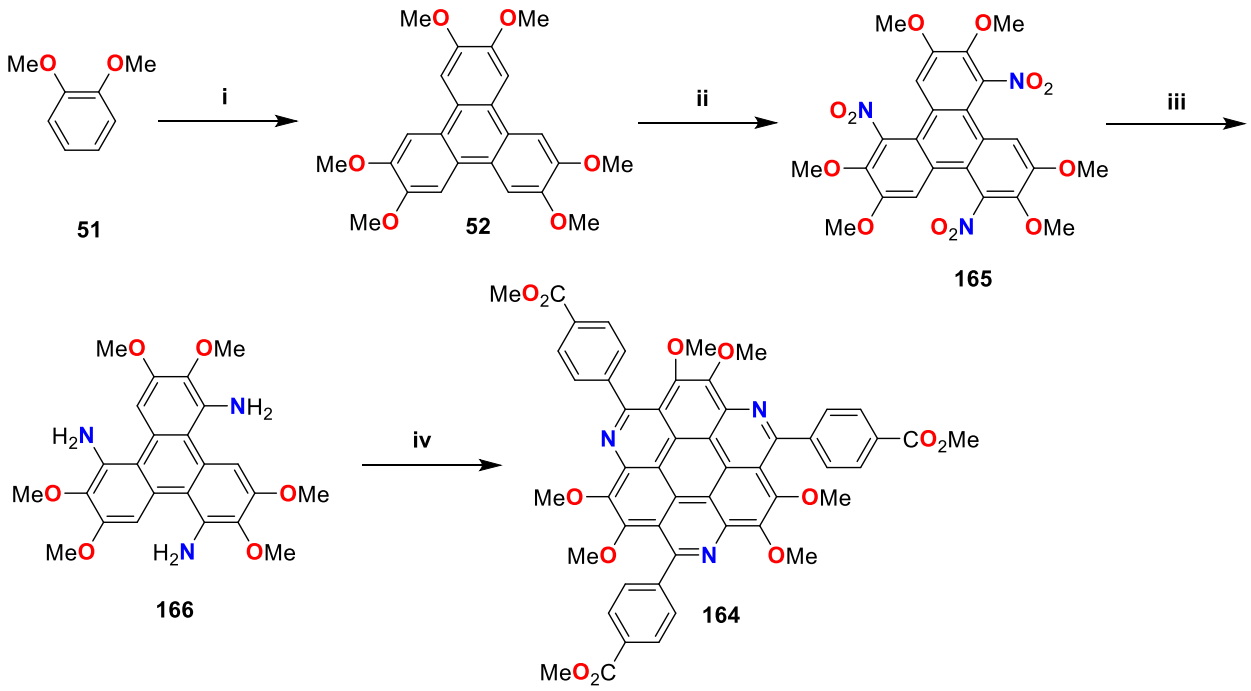

Scheme 5. 1 (i) 1. HCl, H_2SO_4, $FeCl_3$, CH_2Cl_2, 2 hr reflux 2. MeOH. 30 min reflux (ii) $PhSO_2Cl$, $AgNO_3$, Bu_4N^+, $CHCl_3$, 3d reflux, 60 °C (iii) 1. Ni $(OAc)_2$, MeOH, THF, 5 min, rt 2. $NaBH_4$ (iv) 4-formylbenzoate 150, DMSO, Ar 140 24 hr, O_2 at 120 °C.

5.3 Result and discussion

5.3.1 IR and NMR

Based on the proton NMR spectrum of compound **166** (Figure 5.2-a), four types of protons are identified. NH_2 protons peaked at 5.14 ppm, triphenylene protons (Hf) peaked at 8.10 ppm, and methoxy protons (Hc and Hb) peaked at 3.79 ppm and 3.90 ppm, respectively. In contrast, the spectrum of compound **164** (Figure 5.2-b and Figure S29) displays five types of protons. The benzene protons (Hd and He) appear as singlets at 8.33 and 7.99 ppm, respectively. The methoxy protons (Hb and Hc) also appear as singlets at 4.06 and 3.82 ppm, while the ester group protons (Ha) appear as a singlet at 4.53 ppm.

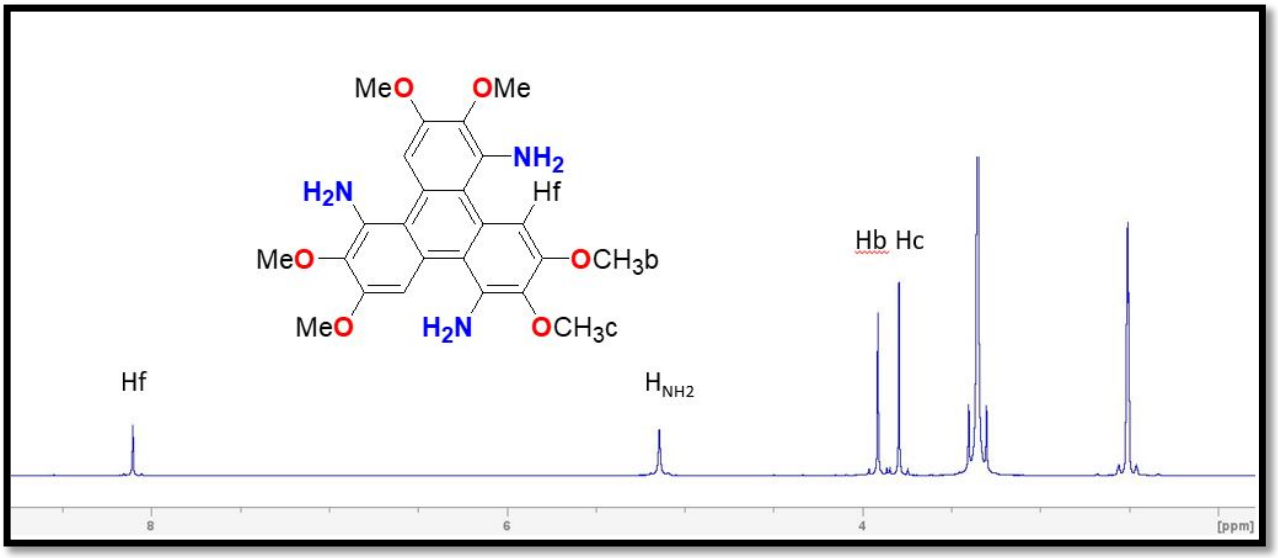

a

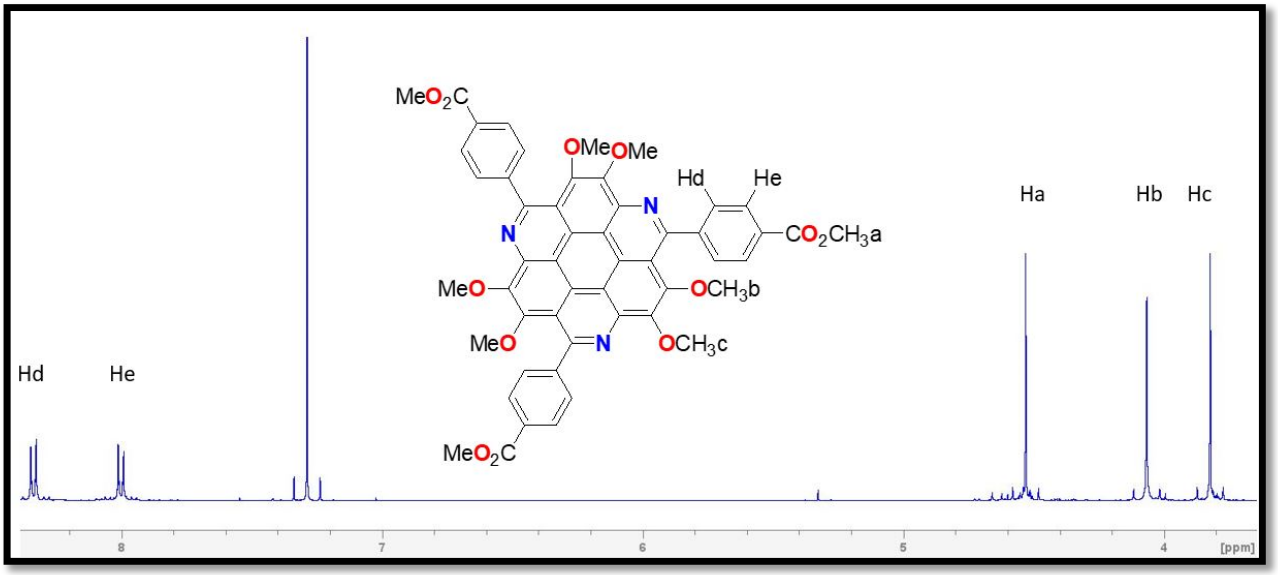

b

Figure 5. 2 a: ^{1}H NMR of **166** in DMSO-d_6 and b: ^{1}H NMR of **164** in $CDCl_3$-d_6.

The IR spectrum of compound **164** (Figure 5.3) reveals the absence of symmetric and asymmetric amine peaks and displays an ester carbonyl group peak at 1716 cm^{-1}.

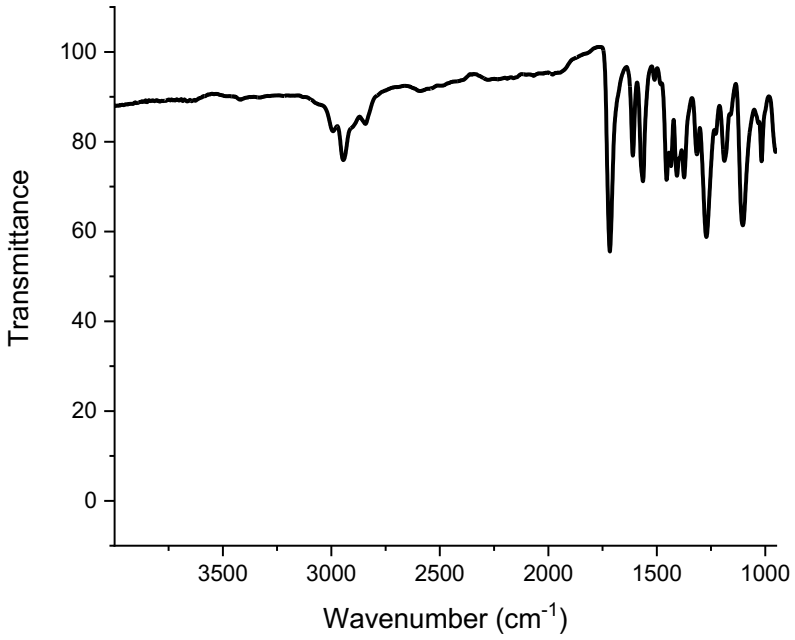

Figure 5. 3 IR spectra of **164**.

In conclusion, the absence of triphenylene protons in the ^{1}HNMR spectrum, along with the lack of symmetric and asymmetric amine peaks and the presence of an ester carbonyl group peak at 1716 cm^{-1} in the IR spectrum of compound **164**, indicates that the reaction proceeded as expected.

5.3.2 UV

Compound **164**, characterized by the extended conjugated system of the azacoronene core, was examined for its absorption properties using UV spectroscopy (Figure 5.4). Characteristic $\pi \rightarrow \pi^*$ electronic transitions were observed with maximum absorption wavelengths (λ_{max}) at 232, 274, and 366 nm, with corresponding molar absorptivity coefficients (ε) of 61543, 68103, and 55436 $M^{-1}cm^{-1}$, respectively. Like other azacoronene compounds, compound **164** exhibits multiple $\pi \rightarrow \pi^*$ transitions, which can be attributed to various functional groups within the conjugated system, such as ester and methoxy groups.[208] The UV spectrum of compound **69** has not been reported.

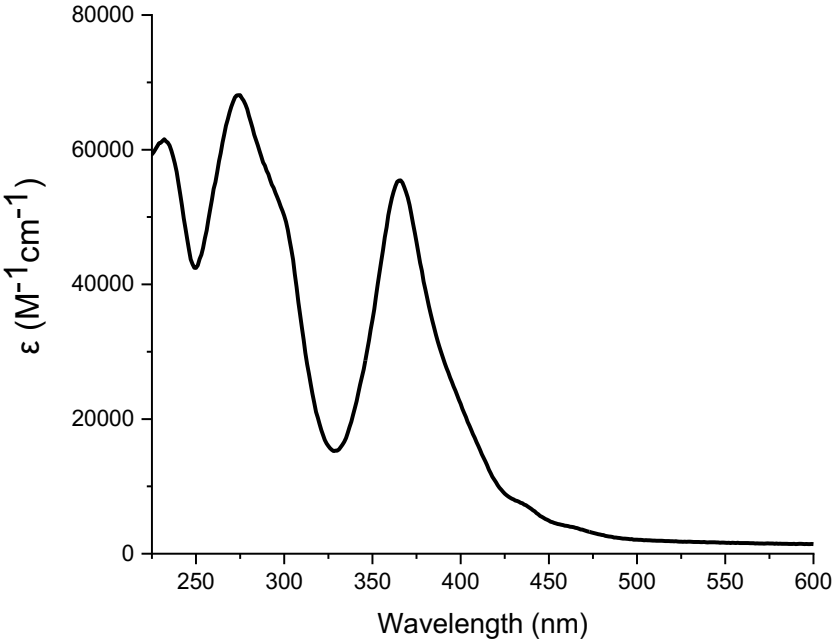

Figure 5. 4 UV absorption spectrum of compound **164** in acetonitrile at room temperature.

5.3.3 TGA

Thermogravimetric analysis (Figure 5.5) shows that compound **164**, like other azacoronenes[209], demonstrates high thermal stability, remaining stable up to 367 °C. This stability can be attributed to its highly conjugated structure and hydrogen bonding interactions.[148,209] The TGA data for compound **69** has not been reported.

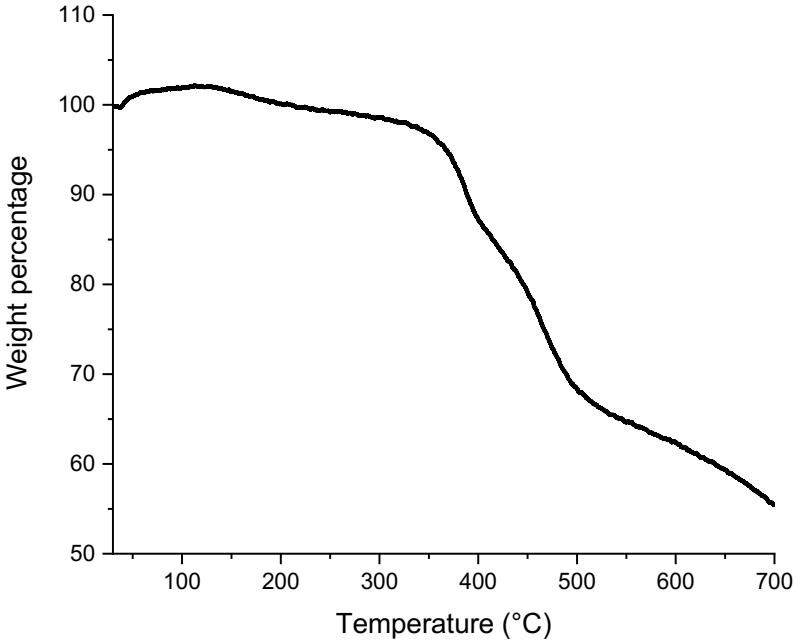

Figure 5. 5 Thermogravimetric analysis (TGA) for compound **164**.

5.4 Conclusion

In this study, we synthesized a novel azacoronene, compound **164**, which was characterized using NMR, IR, UV-Vis, and mass spectrometry. The NMR analysis revealed the presence of 15 distinct carbon environments and 5 types of protons. Thermogravimetric analysis (TGA) indicated high thermal stability up to 367 °C. The UV-Vis spectrum displayed multiple $\pi \rightarrow \pi^*$ transitions, likely attributed to various functional groups within the compound's conjugated system. Due to its extensive conjugation, compound **164** holds potential as a ligand for coordination reactions, offering promising applications in the development of metal-organic frameworks (MOFs) and complexes with optoelectronic properties.[210]

Chapter 6

Exploring Coordination Reactions for MOF Development

6.1 Introduction

Coordination compounds, such as MOFs or complexes, are composed of metal ions and organic linkers. The structure of the organic linker plays a key role in the formation of these materials. Specifically, the position and number of coordination motifs on the organic linkers are crucial in determining whether the resulting structure will form a complex, dimer, polymer, or MOF. In this project, we utilized multi-motif ligands. The strategy was to design MOFs by ensuring that all coordination motifs were symmetrically arranged on the cores (benzene, triphenylene, azacoronene). This symmetry in the organic linkers increases the likelihood of forming polymers or MOFs.

We attempted to coordinate the ligands synthesized in this project with several abundant metal ions available in our lab (Table 1), including Zr, Co, Cd, Zn, Cu, and Ni, which are widely studied in coordination chemistry and they have several catalytic applications.

6.2 Synthesis

In a coordination reaction, organic linkers and metal ions react to form coordination compounds. If the formation of coordination bonds between the metal ion and the organic linker occurs quickly, the resulting coordination compound is more likely to precipitate. However, if the process is slow, the final coordination compound may form as crystals.

Obtaining coordination compounds in crystal form is crucial because their structural characterization primarily relies on single-crystal X-ray diffraction (SCXRD). This technique provides precise information about the atomic arrangement and connectivity within the compound and requires single crystals rather than powdered samples. Other characterization methods, such as nuclear magnetic resonance (NMR) spectroscopy, are often less effective due to the poor solubility of most metal-organic frameworks (MOFs) and coordination complexes in common

solvents. Additionally, recrystallizing precipitates after a coordination reaction is challenging, making it essential to prevent early precipitation. Therefore, in this project, we employed solvothermal reactions, which offer scalability and a higher likelihood of obtaining crystalline products compared to other methods.[211]

As part of this approach, we decided to start coordination reactions with compound **137** (Figure 6.1) which has one of the best coordination motifs (pyridine carboxylic acids). Therefore, compound **137** was tested with various metal salts under different conditions (reactions 1–13 of table 6.1). Each reaction used one equivalent of the ligand and three equivalents of the metal salt, as compound **137** contains three pyridine carboxylic acid groups capable of coordinating with metal ions. Metal salts were selected based on their ability to remain soluble upon initial mixing with the ligand, thereby avoiding immediate precipitation at the start of the reaction. We used DMF as the primary solvent in reactions 1–3 (Table 6.1) because it effectively dissolves both the metal salts and compound **137**. Its high boiling point allows for high-temperature reactions, while its basic properties help activate the ligand by facilitating deprotonation. For reactions 4–13 (Table 6.1), we used varying percentages of water and methanol mixed with DMF to adjust the solution's polarity. Both water and methanol are miscible with DMF and have moderate boiling points, ensuring suitable reaction conditions. Considering all these factors, we obtained precipitates at the end of the reactions, possibly due to the rapid reaction between the metal ions and compound **137**.

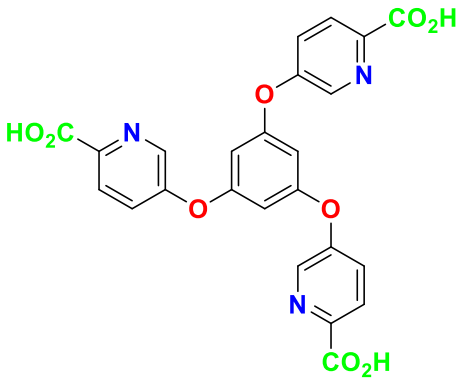

Figure 6. 1 Structure of compound **137**.

Other organic linkers chosen for coordination reactions were compounds **150** and **151** (Figure 6.2). These compounds were selected for coordination reactions because, compared to compound **137** (which features a carboxylic group at the same position), the cyano group is predicted to coordinate with metal ions more slowly. This slower coordination reduces the likelihood of precipitation, as the cyano group has a lower tendency to coordinate with metals than the carboxylic acid group. Additionally, there is a possibility that compounds **150** and **151** could undergo hydrolysis during the coordination reaction, converting the cyano group into an amide or carboxylic group, which could then coordinate with the metal ion.[182] It was anticipated that this process would take more time, increasing the likelihood of obtaining crystals compared to using a carboxylic acid directly. An interesting observation was made during reaction 24, compound **151** contained a small amount of impurity from its synthesis, identified as 5-bromo-pyridine-2-carbonitrile **170**. This impurity underwent hydrolysis to form an amide group, which then coordinated with cobalt, leading to the formation of compound **171** (Figure 6.3). The lack of reactivity of compound **145** with cobalt may be attributed to its low solubility in acetonitrile and significant steric hindrance, whereas compound **170**, being more soluble and less sterically demanding, was able to coordinate with the metal center. In this complex, cobalt is coordinated to two oxygen atoms from the nitrate groups, two nitrogen atoms from two pyridine rings, and two oxygen atoms from the amide groups of two ligands, resulting in an octahedral structure (Figure 6.3).

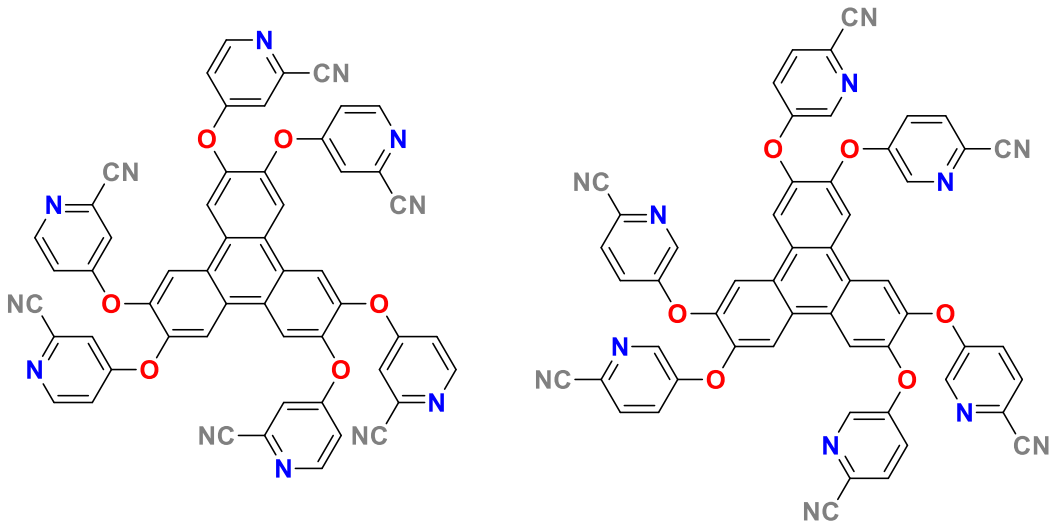

150 **151**

Figure 6. 2 Structures of compounds **144** and **145**.

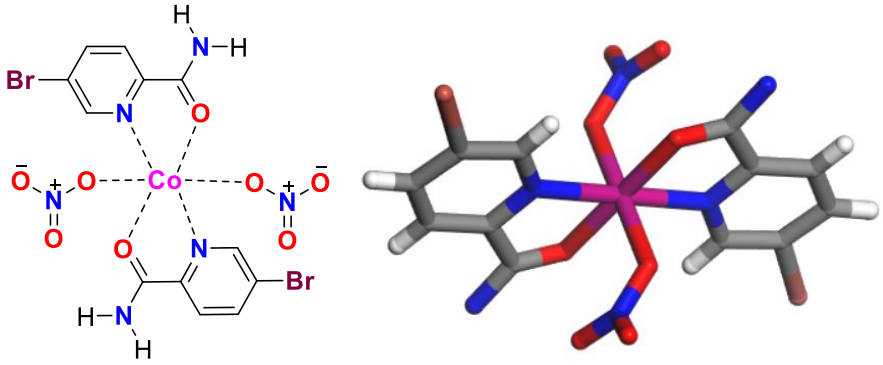

Figure 6. 3 Crystal structure of compound **171**. Dashed lines represent the coordination bonds. Carbon atoms are depicted in gray, hydrogen atoms in white, nitrogen atoms in blue, oxygen atoms in red, cobalt atom in pink, and bromine atoms in purple.

In all reactions involving compounds **150** and **151** (14–23 and 24–39 of table 6.1), one equivalent of the ligands and six equivalents of the metal salt were used, as these compounds contain six cyanopyridine groups.

Choosing an appropriate solvent for compounds **150** and **151** was challenging due to their limited solubility in common solvents. However, they were found to be soluble in DMSO, DMF, and slightly soluble in acetonitrile.

For compounds **150** and **151**, reactions (14–21 and 24–35 of table 6.1) were conducted at low temperatures to allow sufficient time for crystal formation. Additionally, experiments were performed at higher temperatures (22, 23, and 36-39 of table 6.1) with shorter reaction times to explore the possibility of forming coordination compounds.

Despite these conditions, crystalline materials, whether as complexes or MOFs, could not be obtained from **150** and **151**.

Another ligand used in this project is compound **145** (Figure 6.3) (reactions 40–75 in Table 6.1). This compound was selected because, unlike compound **139**—which reacts rapidly with metal ions and forms a precipitate rather than crystals—compound **145** reacts more slowly with metal salts, thereby increasing the likelihood of obtaining high-quality single crystals. Compound **145**, which features two diamino triazine rings at the α-position of the N-pyridyl atom and one hydroxy group, serves as an excellent coordination motif. Consequently, we used three equivalents of metal salt and one equivalent of compound **145** in all these reactions (40-75 of table 6.1).

We employed DMF as the main solvent (reactions 40–44 of table 6.1) due to its ability to solubilize both the metal salt and the ligand. For the remaining reactions (45-75 of table 6.1), we adjusted the solvent polarity by adding water, acetonitrile, and methanol to DMF. These solvents are miscible with DMF and are suitable for solvothermal reactions. Among all these reactions, reaction

52 (Table 6.1) yielded high-quality crystals. Under this optimized condition, a solution was prepared by dissolving one equivalent of compound **145** and three equivalents of $Zn(ClO_4)_2 \cdot 6H_2O$ **168** (in a mixture of 3 mL of DMF and 6 mL of methanol) (Scheme 6.1). This solution was transferred to a 25 mL sealed vial and heated in an oven at 80 °C for 48 hours. After heating, the vial was allowed to cool slowly to room temperature, leading to the formation of crystals of the final compound, **169**.

It is notable that during the reaction, methanol was oxidized to formic acid. It is proposed that methanol was oxidized by ClO_4^- to produce formic acid, hydroxyl groups, and chloric acid (ClO_3H) (Scheme 6.2). The ClO_3H generated could act as an oxidant, further contributing to the oxidation process. The presence of methanol as the solvent and ClO_4^- as the counterion plays a crucial role in the formation of compound **169**. This is because methanol is oxidized to formic acid and hydroxyl groups, which are subsequently coordinated to the metal ion.

Table 6. 1 Reaction conditions for the coordination of compounds **136**, **145**, **150**, and **151** with different metal salts.

Reaction	Cpd	metal salt	Eq of organic linker	Eq of metal salt	reaction time (day)	T (°C)	Solvent	Vial (ml)	Result
1	**137**	$Co(NO_3)_2 \cdot 6H_2O$	1	3	3	100	1.6mL DMF	5	×
2	**137**	$Co(OAC)_2 \cdot 4H_2O$	1	3	3	100	1.6mL DMF	5	×
3	**137**	$Cd(NO_3)_2 \cdot 4H_2O$	1	3	3	100	1mL DMF	5	×
4	**137**	$Zr(OCl_2) \cdot 8H_2O$	1	3	2	80	3mL DMF/3mL MeOH	25	×
5	**137**	$Zr(OCl_2) \cdot 8H_2O$	1	3	2	80	3mL DMF/6mL MeOH	25	×
6	**137**	$Zr(OCl_2) \cdot 8H_2O$	1	3	2	80	3mL DMF/3mL H_2O	25	×
7	**137**	$Zr(OCl_2) \cdot 8H_2O$	1	3	2	80	3mL DMF/6mL H_2O	25	×
8	**137**	$Zr(OCl_2) \cdot 8H_2O$	1	3	2	90	3mL DMF/3mL MeOH	25	×
9	**137**	$Zn(OAC)_2 \cdot 2H_2O$	1	3	2	80	3mL DMF/6mL MeOH	25	×
10	**137**	$Zn(NO_3)_2 \cdot 6H_2O$	1	3	2	80	3mL DMF/6mL MeOH	25	×

11	**137**	$Co(BF_4)_2 \cdot 6H_2O$	1	3	3	100	0.5mL DMF/0.5mL H_2O	5	×
12	**137**	$Co(NO_3)_2 \cdot 6H_2O$	1	3	3	100	0.5mL DMF/0.5mL H_2O	5	×
13	**137**	$Co(OAC)_2 \cdot 4H_2O$	1	3	3	100	0.5mL DMF/0.5mL H_2O	5	×
14	**150**	$CoCl_2$	1	6	14	25	10 mL DMSO	25	-
15	**150**	$Co(NO3)_2 \cdot 6H_2O$	1	6	14	25	5 mL DMF	25	-
16	**150**	$Co(OH)_2$	1	6	14	25	5 mL DMF	25	-
17	**150**	$CoCl_2$	1	6	14	25	10 mL DMF	25	-
18	**150**	$Ni(ClO_4)_2 \cdot 6H_2O$	1	6	14	25	10 mL DMF	25	-
19	**150**	$Ni(OAC)_2 \cdot 4H_2O$	1	6	14	25	10 mL DMF	25	-
20	**150**	$Cu(NO_3)_2 \cdot H_2O$	1	6	14	25	5 mL DMF	25	-
21	**150**	$Co(BF_4)_2 \cdot 6H_2O$	1	6	14	25	5 mL DMF	25	-
22	**150**	$Cu(NO_3)_2 \cdot H_2O$	1	6	1	90	15 mL DMSO	25	-
23	**150**	$CoCl_2$	1	6	3	90	5 mL DMF	25	-
24	**151**	$Co(NO_3)_2 \cdot 6H_2O$	1	6	14	25	10 mL Acetonitrile	25	✓
25	**151**	$Cu(ClO_4)_2 \cdot 6H_2O$	1	6	14	25	10 mL Acetonitrile	25	-
26	**151**	$Cu(ClO_4)_2 \cdot 6H_2O$	1	6	14	25	10 mL DMF	25	-
27	**151**	$Cu(ClO_4)_2 \cdot 6H_2O$	1	6	14	25	10 mL DMSO	25	-
28	**151**	$Co(BF_4)_2 \cdot 6H_2O$	1	6	14	25	10 mL DMSO	25	-
29	**151**	$Co(ClO_4)_2 \cdot 6H_2O$	1	6	14	25	10 mL DMSO	25	-
30	**151**	CuI	1	6	3	25	5 mL DMSO	25	-
31	**151**	$Cu(CH_3CN)_4PF_6$	1	6	14	25	10 mL DMSO	25	-
32	**151**	$Co(NO_3)_2 \cdot 6H_2O$	1	6	1	25	20 mL Acetonitrile	25	-
33	**151**	$Cd(NO_3)_2 \cdot 4H_2O$	1	6	1	25	10 mL DMSO	25	-
34	**151**	$Cd(NO_3)_2 \cdot 4H_2O$	1	6	3	25	20 mL Acetonitrile	25	-
35	**151**	CuI	1	6	14	25	5mL DMSO/5mL Acetonitrile	25	-
36	**151**	$Ni(OAC)_2 \cdot 4H_2O$	1	6	1	80	7 mL DMSO	25	-
37	**151**	$Zn(BF_4)_2 \cdot H_2O$	1	6	1	80	10 mL DMSO	25	-
38	**151**	$CoCl_2$	1	6	4	80	10 mL DMSO	25	-
39	**151**	$Cu(CH_3CN)_4BF_6$	1	6	2	80	10 mL DMSO	25	-
40	**145**	$Zn(NO_3)_2 \cdot 6H_2O$	1	3	3	80	5mL DMF	25	-
41	**145**	$Zn(NO_3)_2 \cdot 6H_2O$	1	3	3	100	5mL DMF	25	-

42	**145**	$Zn(BF_4)_2 \cdot H_2O$	1	3	3	90	5mL DMF	25	-
43	**145**	$Zn(ClO_4)_2 \cdot 6H_2O$	1	3	2	100	5mL DMF	25	-
44	**145**	$Co(OAC)_2 \cdot 4H_2O$	1	3	2	80	4mL DMF	25	-
45	**145**	$Zn(OAC)_2 \cdot 2H_2O$	1	3	3	80	3mL DMF/6mL MeOH	25	-
46	**145**	$Zn(OAC)_2 \cdot 2H_2O$	1	3	3	80	3mL DMF/6mL H_2O	25	-
47	**145**	$Zn(NO_3)_2 \cdot 6H_2O$	1	3	3	80	3mL DMF/2mL Acetonitrile	25	-
48	**145**	$Zn(NO_3)_2 \cdot 6H_2O$	1	3	3	80	3mL DMF/2mL H_2O	25	-
49	**145**	$Zn(ClO_4)_2 \cdot 6H_2O$	1	3	2	80	2mL DMF/4mL Acetonitrile	25	-
50	**145**	$Zn(ClO_4)_2 \cdot 6H_2O$	1	3	2	80	2mL DMF/6mL Acetonitrile	25	-
51	**145**	$Zn(ClO_4)_2 \cdot 6H_2O$	1	3	2	80	3mL DMF/2mL Acetonitrile	25	-
52	**145**	$Zn(ClO_4)_2 \cdot 6H_2O$	1	3	2	80	3mL DMF/6mL MeOH	25	✓
53	**145**	$Co(NO_3)_2 \cdot 6H_2O$	1	3	2	80	3mL DMF/3mL H2O/3mL EtOH	25	-
54	**145**	$Co(OAC)_2 \cdot 4H_2O$	1	3	2	80	3mL DMF/1mL H_2O	25	-
55	**145**	$Co(OAC)_2 \cdot 4H_2O$	1	3	2	80	3mL DMF/9mL H_2O	25	-
56	**145**	$Co(OAC)_2 \cdot 4H_2O$	1	3	2	80	3mL DMF/6mL Acetonitrile	25	-
57	**145**	$Co(OAC)_2 \cdot 4H_2O$	1	3	2	80	3mL DMF/3mL Acetonitrile	25	-
58	**145**	$Co(OAC)_2 \cdot 4H_2O$	1	3	2	80	3mL DMF/3mL EtOH	25	-
59	**145**	$Co(OAC)_2 \cdot 4H_2O$	1	3	2	80	3mL DMF/3mL H_2O	25	-
60	**145**	$Co(OAC)_2 \cdot 4H_2O$	1	3	2	80	3mL DMF/6mL H_2O	25	-
61	**145**	$Co(OAC)_2 \cdot 4H_2O$	1	3	2	80	3mL DMF/6mL MeOH	25	-
62	**145**	$CoCl_2 \cdot 6H_2O$	1	3	2	80	3mL DMF/6mL MeOH	25	-
63	**145**	$CoCl_2 \cdot 6H_2O$	1	3	2	80	3mL DMF/6mL H_2O	25	-
64	**145**	$Co(BF_4)_2 \cdot 6H_2O$	1	3	2	80	3mL DMF/3mL Acetonitrile	25	-
65	**145**	$Co(BF_4)_2 \cdot 6H_2O$	1	3	2	80	3mL DMF/3mL MeOH	25	-
66	**145**	$Co(BF_4)_2 \cdot 6H_2O$	1	3	2	80	3mL DMF/6mL MeOH	25	-
67	**145**	$Zr(OCl_2) \cdot 6H_2O$	1	3	2	90	3mL DMF/3mL MeOH	25	-
68	**145**	$Zr(OCl_2) \cdot 8H_2O$	1	3	2	80	3mL DMF/3mL MeOH	25	-

69	**145**	$Zr(OCl_2)\cdot 8H_2O$	1	3	2	80	3mL DMF/6mL MeOH	25	-
70	**145**	$Zr(OCl_2)\cdot 8H_2O$	1	3	2	80	3mL DMF/3mL H_2O	25	-
71	**145**	$Zr(OCl_2)\cdot 8H_2O$	1	3	2	80	3mL DMF/6mL H_2O	25	-
72	**145**	$Co(NO_3)_2\cdot 6H_2O$	1	3	2	80	3mL DMF/6mL H_2O	25	-
73	**145**	$Co(NO_3)_2\cdot 6H_2O$	1	3	2	80	3mL DMF/9mL H_2O	25	-
74	**145**	$Co(NO_3)_2\cdot 6H_2O$	1	3	2	80	3mL DMF/6mL Acetonitrile	25	-
75	**145**	$Co(NO_3)_2\cdot 6H_2O$	1	3	2	80	3ml DMF/6mL Acetonitrile	25	-
✓: Formation of crystals × Precipitation -: No crystallisation nor precipitation occured									

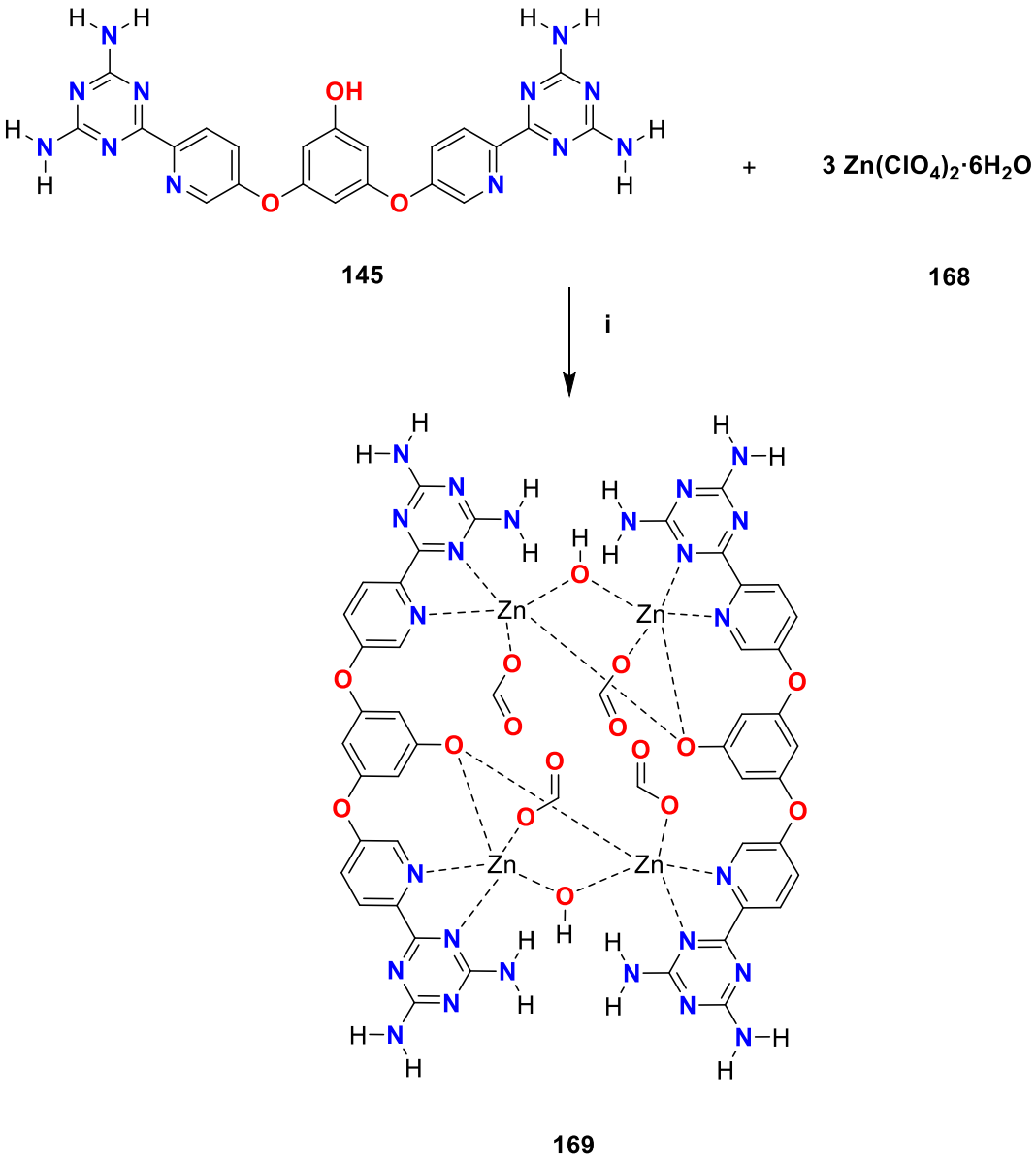

Scheme 6. 1 Synthetic route to prepare **169**. (i) DMF/MeOH, 80 °C, 48 hr.

Oxidation of methanol to formaldehyde:

$$\text{Ox: } CH_3OH \rightarrow CH_2O + 2H^+ + 2e^-$$

$$\underline{\text{Red: } ClO_4^- + 2H^+ + 2e^- \rightarrow ClO_3H + OH^-}$$

$$CH_3OH + ClO_4^- \rightarrow ClO_3H + CH_2O + OH^-$$

Oxidation of formaldehyde to formic acid:

$$\text{Ox: } CH_2O + H_2O \rightarrow HCO_2H + 2H^+ + 2e^-$$

$$\underline{\text{Red: } ClO_4^- + 2H^+ + 2e^- \rightarrow ClO_3H + OH^-}$$

$$CH_2O + H_2O \rightarrow HCO_2H + ClO_3H + OH^-$$

Oxidation of methanol to formic Acid:

$$2ClO_4^- + CH_3OH + H_2O \rightarrow 2ClO_3H + HCO_2H + 2OH^-$$

Scheme 6. 2 Proposed sequential oxidation of methanol to formic acid by perchlorate.

6.3 Result and discussion of compound 169

6.3.1 IR

Based on the IR spectra of compounds **145** and **169** (Figure 6.4), the C=N bond of the pyridine ring in compound **145** appears at 1605 cm^{-1}**,** while in compound **169**, it shifts to 1524 cm^{-1}. Similarly, the C=N bond of the triazine ring in compound **145** is observed at 1532 cm^{-1}, but in compound **169**, it shifts to 1492 cm^{-1}. Additionally, the IR spectrum of compound **169** shows a new peak at 1563 cm^{-1}**,** which corresponds to the carbonyl of the formate group. The peak of NH_2 in compound **169** appears broadened and shifted to a lower wavenumber, likely due to hydrogen bonding between the hydroxyl group and the NH_2 group**.** To conclude, the IR spectra reveal a shift in the C=N stretching frequencies, indicating coordination of the C=N groups to the metal ion, as well as the presence of new hydroxy and formate groups in the complex.

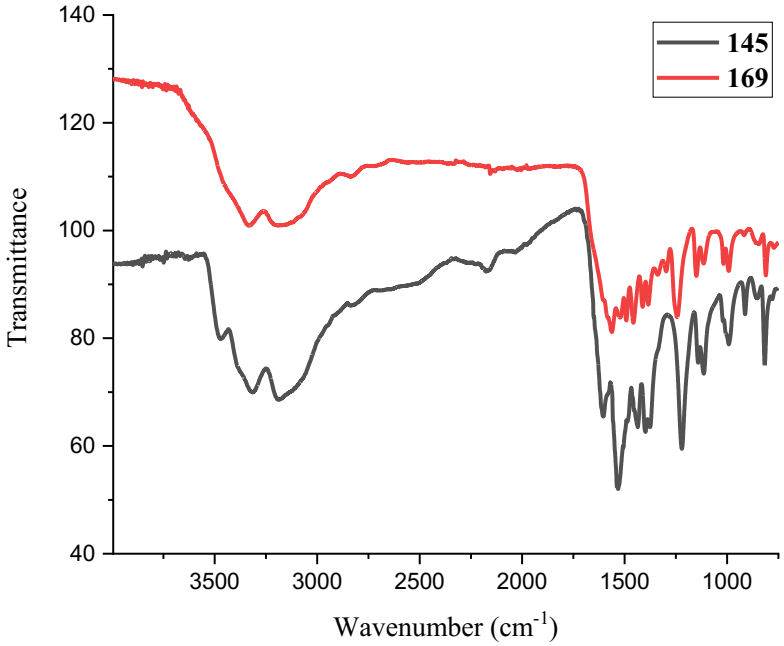

Figure 6. 4 FT-IR spectra of compounds **145** and **169.**

6.3.2 UV

In the UV spectrum of compound **169**, measured in a suspension in DMF (Figure 6. 5), a peak appears at 300 nm, attributed to the $\pi \rightarrow \pi^*$ electronic transition of ligand **145**. No d-d transition is observed, as the d orbitals of Zn are fully occupied. Similarly, in compound **172** (Figure 6. 7) (in compound **172**, compound **119** is coordinated with zinc) with Zn, no charge transfer occurs between the metal and the ligand.[212]

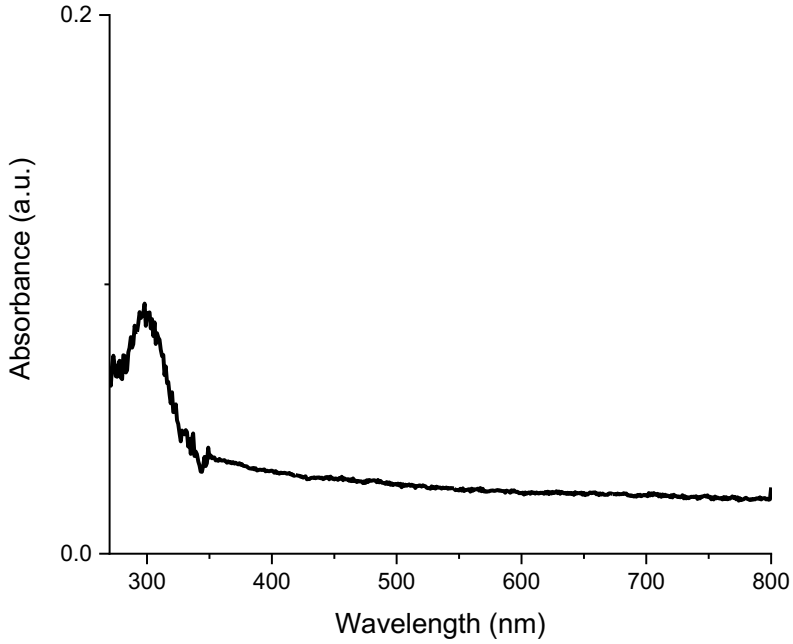

Figure 6. 5 The UV–vis spectrum of compound **169** in the solid state.

6.3.3 TGA

TGA analysis (Figure 6.6) reveals that compound **169** demonstrates high thermal stability, with decomposition occurring at 341 °C, closely comparable to the decomposition temperature of compound **172**, which decomposed at 345 °C. This stability is likely attributed to the presence of strong hydrogen bonding.[212]

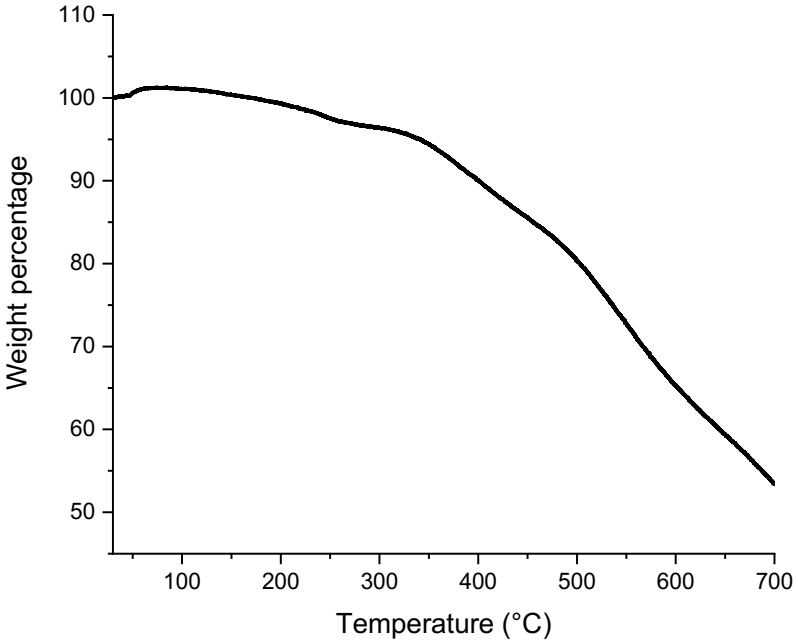

Figure 6. 6 Thermogravimetric analysis (TGA) for compound **169**.

6.3.4 Single crystal x-ray diffraction (SCXRD)

Single-crystal X-ray diffraction (SCXRD) was conducted on well-formed crystals of compound **169** to determine its solid-state structure. Compound **169** crystallized in the triclinic space group P-1 (Z = 1). The crystal data for compound **169** are summarized in (Table 6.2), with structural views and packing shown in (Figure 6.7).

The structure shows that compound **169** forms a dimer, with four Zn atoms. Each Zn is coordinated by nitrogen atoms from both the pyridine and diamino triazine rings, as well as oxygen atoms from the phenol, hydroxyl, and formate groups. It is notable that, similar to other pyridine diamino triazine compounds, compound **169** coordinates through the nitrogen atoms of both the pyridine ring and the diamino triazine group. The average bond lengths for $Zn–N_{pyridine}$ and $Zn–N_{triazine}$ are 2.093(2) Å and 2.171(2) Å, respectively, which fall within the normal range when compared to those observed in compound **172** (Table 6.3).[212,213]

Table 6. 2 Crystallographic data of compound **169**.

Compound	**169**
Empirical formula	$C_{54}H_{54}N_{26}O_{18}Zn_4$
Formula weight	1616.71
Temperature/K	150.15
Crystal system	triclinic
Space group	P-1
a/Å	12.1076(6)
b/Å	12.9007(6)
c/Å	13.0664(6)
α/°	81.249(2)
β/°	62.965(2)
γ/°	70.603(2)
Volume/Å^3	1714.73(14)
Z	1
ρ_{calc}g/cm^3	1.566
μ/mm^{-1}	1.528
F(000)	824.0
Crystal size/mm^3	0.13 × 0.1 × 0.09
Radiation	GaKα (λ = 1.34139)
2Θ range for data collection/°	6.32 to 121.21
Index ranges	-15 ≤ h ≤ 15, -16 ≤ k ≤ 16, -16 ≤ l ≤ 16
Reflections collected	46865
Independent reflections	7847 [R_{int} = 0.0474, R_{sigma} = 0.0375]
Data/restraints/parameters	7847/28/509
Goodness-of-fit on F^2	1.064
Final R indexes [I>=2σ (I)]	R_1 = 0.0687, wR_2 = 0.2022
Final R indexes [all data]	R_1 = 0.0722, wR_2 = 0.2079

Table 6. 3 The average coordination bond lengths of compounds **169** and **172**.

Bond	Average bond length of compound **169** (Å)	Average bond length of compound **172** (Å)
$Zn\text{-}O_{hydroxy}$	1.941(2)	---
$Zn\text{-}O_{phenol}$	2.1545(19)	---
$Zn\text{-}O_{formate}$	1.974(2)	---
$Zn\text{-}N_{pyridine}$	2.093(2)	2.1034(13)
$Zn\text{-}N_{triazine}$	2.171(2)	2.2173(13)
$Zn\text{-}O_{nitrate}$	---	2.1808(11)

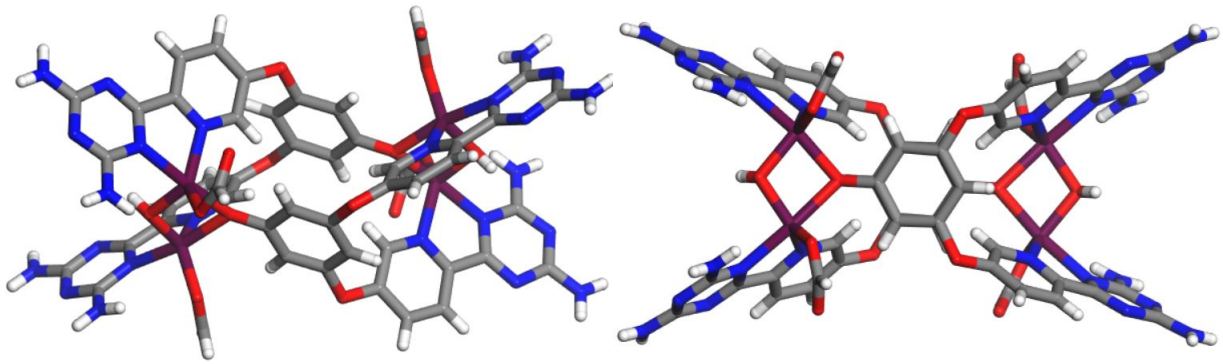

a **b**

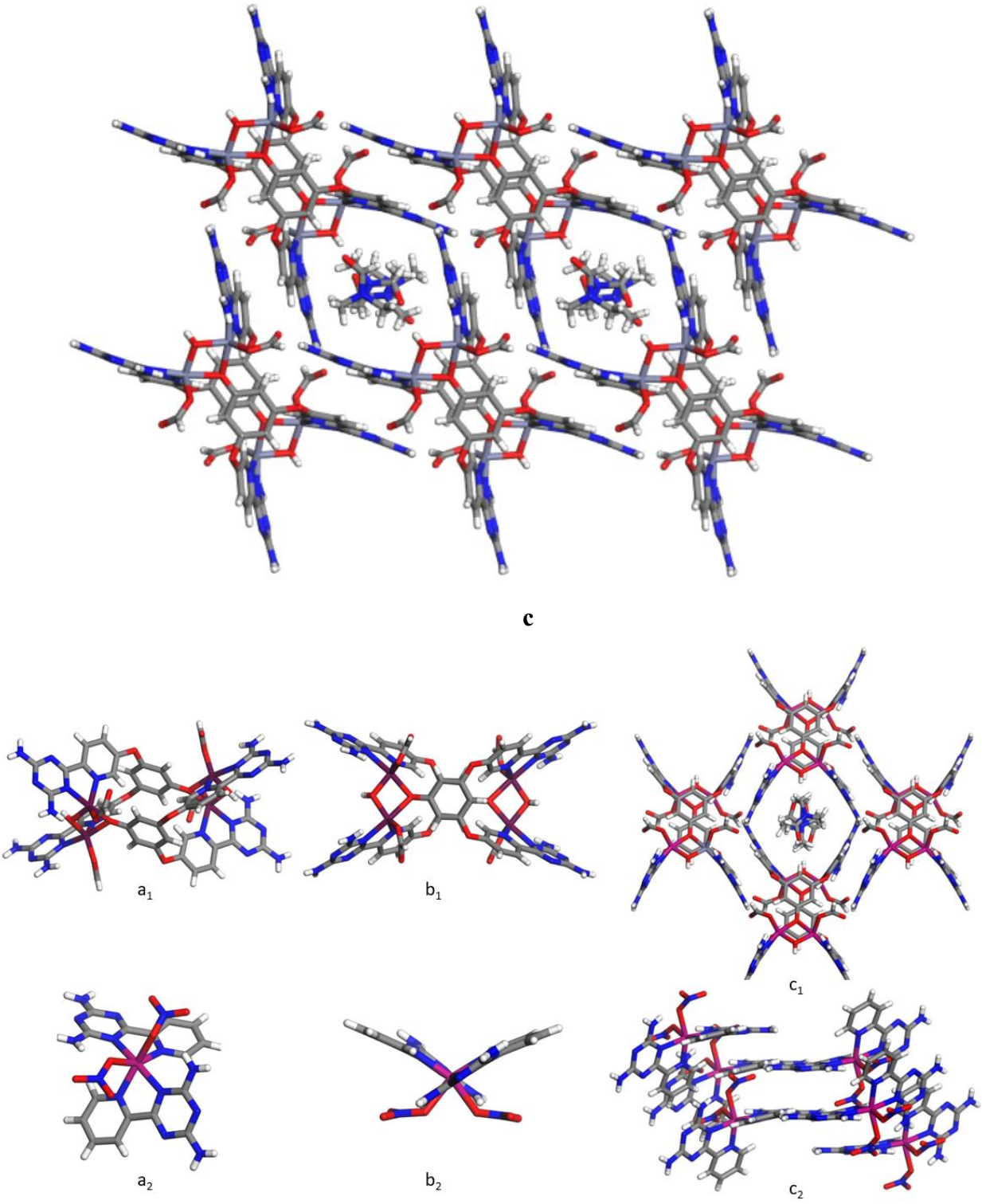

Figure 6. 7 Solid-state structures of molecule **169** in (a_1) and (b_1) are shown, with stereoviews illustrating molecular packing in (c_1). Solid-state structures of molecule **172** in (a_2) and (b_2) are

shown, with stereoviews illustrating molecular packing in (c_2). The atom color scheme is as follows: Zn is pink, C is gray, H is white, N is blue, and O is red.

6.3.5 Hydrogen bonding

Hydrogen bonding simulation in the solid state was conducted for compound **169** and **172** (Figure 6.8), revealing the presence of various weak and strong hydrogen bonds in both compounds (Table 6.4). In compound **169**, strong hydrogen bonds are observed between the hydrogen atoms of the amine group and the solvent (DMF), as well as between the solvent molecules themselves. These interactions likely contribute to the retention of the solvent at elevated temperatures. Additionally, strong hydrogen bonding occurs between the hydrogen of the amine group and the oxygen atom of the formate group.

In contrast, compound **172** exhibits strong hydrogen bonds between the hydrogen atoms of the amine group and the oxygen atoms of the nitrate group, as well as with the nitrogen atoms of the triazine ring. These findings highlight the crucial role of the hydrogen atoms in the amine group in the hydrogen bonding behavior of these compounds.

Table 6. 4 The hydrogen bonding patterns in molecules **169** and **172**. The angle (Θ) between the donor and acceptor atoms, as well as the length (d) of the hydrogen bond.

Cpd.	Bond	θ (°)	d (Å)	Type of hydrogen bond
169	$O_{formate}$…H-N_{amine}	125.44(5)	2.47(1)	Weak
	$O_{formate}$…H-N_{amine}	139.34(5)	2.10(1)	Strong
	$O_{formate}$… H-C_{Bn}	156.16(5)	2.47(1)	Weak
	$O_{hydroxy}$… H-$C_{formaldehyde}$	146.15(5)	2.46(1)	Weak
	$O_{formate}$…H-N_{amine}	145.66(5)	2.38(1)	Weak
	$O_{formate}$…H-N_{amine}	159.19(5)	1.91(1)	Strong
	$N_{triazine}$…H-N_{amine}	159.14(5)	2.23(1)	Weak
	$O_{formate}$…H-C_{py}	129.97(5)	2.41(1)	Weak
	$O_{formate}$…H-N_{amine}	162.23(5)	1.94(1)	Strong
	O_{DMF}…H-$N_{hydroxy}$	148.69(5)	2.071(1)	Strong
	$N_{triazine}$…H-N_{amine}	141.45(5)	2.54(1)	Weak
	N_{DMF}…H-C_{DMF}	120.57(5)	1.92(1)	Strong
	O_{DMF}…H-C_{DMF}	144.06(5)	2.11(1)	Strong
172	$N_{triazine}$…H-C_{py}	102.37(5)	2.43(1)	Weak
	O_{NO3}…H-N_{amine}	156.03(5)	2.09(1)	Strong
	O_{NO3}…H-N_{amine}	145.36(5)	2.42(1)	Weak
	$N_{triazine}$…H-N_{amine}	172.08(5)	2.17(1)	Strong
	O_{NO3}…H-N_{amine}	158.76(5)	2.18(1)	Strong
	O_{NO3}…H-N_{amine}	163.04(5)	2.17(1)	Strong

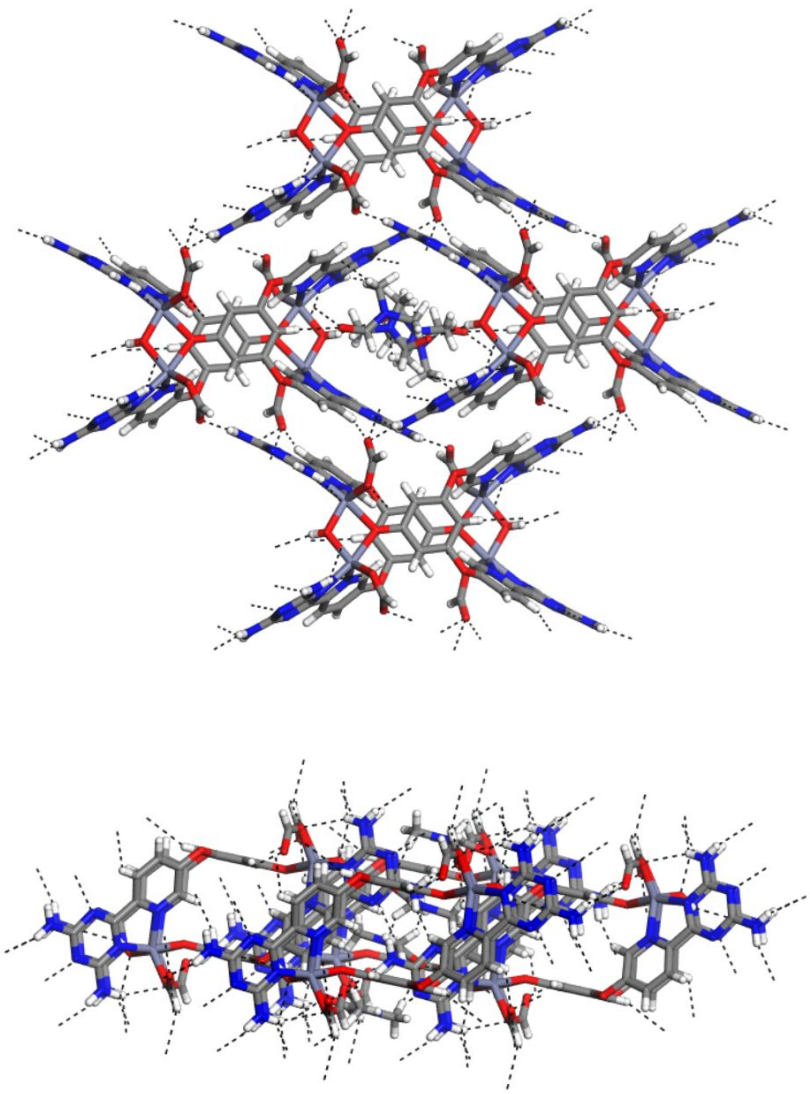

Figure 6. 8 The hydrogen bonding configuration in molecule **169** is depicted. Dashed lines represent the hydrogen bonds. Carbon atoms are depicted in gray, hydrogen atoms in white, nitrogen atoms in blue, oxygen atoms in red, and zinc atoms in pink.

6.3.6 Hirshfeld

To explore the intermolecular interactions of compounds **169** and **172** and compare their properties, a Hirshfeld surface analysis was conducted. Figures 6.9a and 6.9c illustrate the d_{norm} mapping, where short intermolecular contacts involving N···H, O···H, C···H, and H···H interactions are highlighted as red spots. Figures 6.9c and 6.9d present the percentage contributions

of various atomic interactions. For compound **169**, the contributions are as follows: N···H (15.5%), H···H (33.7%), C···H (15.2%), C···N (2.1%), C···C (2.7%), O···H (26.4%), C···O (1.6%), O···N (2.5%), and O···O (0.4%). In contrast, for compound **172**, the contributions are: N···H (19.6%), H···H (23.2%), C···H (12.2%), C···N (3.2%), C···C (1.7%), O···H (31.5%), C···O (5.1%), N···N (0.1%), and O···N (3.4%).

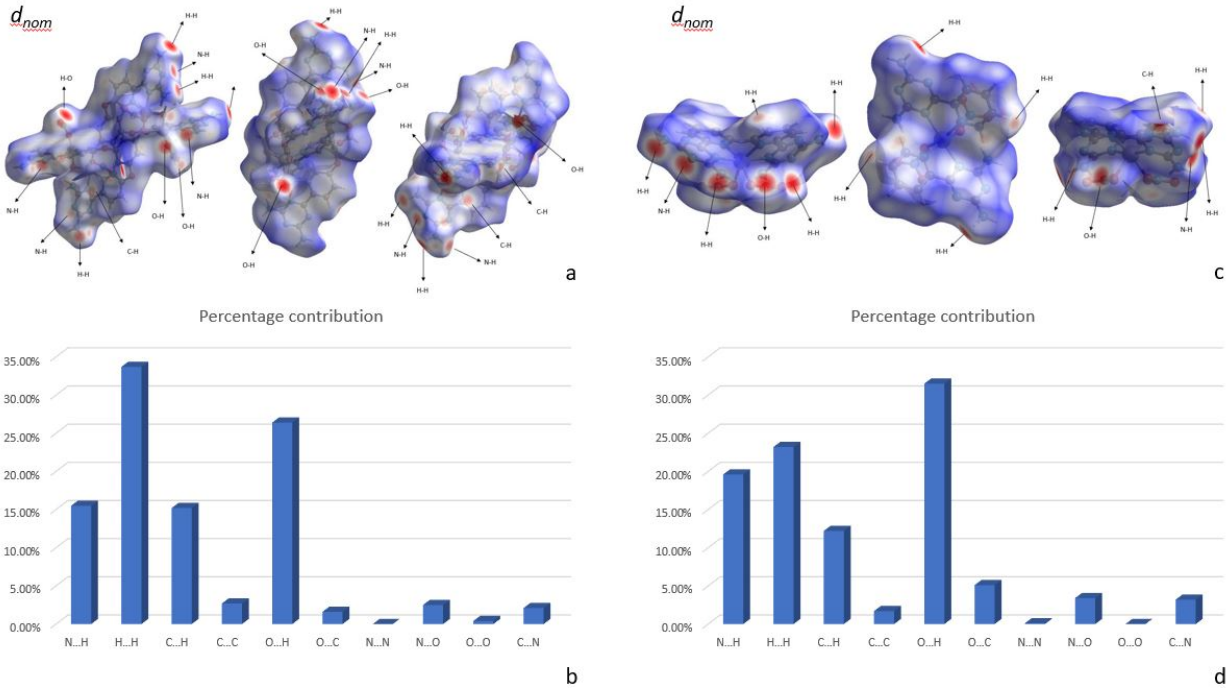

Figure 6. 9 Hirshfeld surfaces for the molecular unit of **169** and **172**. d_{norm} mapping in **169** (a); percentage contribution of intermolecular interaction in **169** (b); d_{norm} mapping in **172** (c); percentage contribution of intermolecular interaction in **172** (d).

The percentage contributions of intermolecular interactions indicate that Zn atoms in both compounds **169** and **172** do not engage in interactions with other atoms. In compound **16**, the highest interaction occurs between H···H atoms, whereas in compound **172**, O···H interactions dominate.

6.4 Conclusion

In conclusion, various organic linkers with different functional groups positioned at the α-position relative to the N-pyridyl atom have been tested for coordination with metal ions under different conditions.

In conclusion, various organic linkers bearing different functional groups at the α-position relative to the N-pyridyl atom were tested for their coordination with metal ions under varying conditions. This study focused on three coordination motifs: cyanopyridine (compounds **150** and **151**), carboxypyridine (compound **137**), and diaminotriazine-pyridine (compound **145**). All three motifs showed potential for metal coordination; however, carboxypyridine reacted too rapidly with metal ions, leading to precipitation rather than crystal formation. Thus, controlling its reactivity is crucial for obtaining high-quality crystals. Notably, the reaction between compound **145** and compound **161** successfully produced well-formed crystals of compound **169**. The compound was characterized using single-crystal X-ray diffraction (scXRD), IR, and UV spectroscopy. ScXRD analysis reveals that in compound **169**, each zinc ion is coordinated by the nitrogen atoms of the pyridine and triazine rings, as well as the oxygen atoms of the hydroxy and formate groups. The coordination bond lengths are found to be within the typical range. The IR spectra reveal shifts in the C=N bond peaks of the pyridine and triazine rings in compound **169** compared to compound **145**, attributed to the effect of coordination between zinc and nitrogen atoms. Additionally, it proposes the formation of formate groups, produced from the oxidation of methanol. The UV spectrum exhibits a $\pi \rightarrow \pi^*$ electronic transition at 300 nm. TGA analysis demonstrates high thermal stability, with degradation occurring above 341 °C. Hydrogen bonding simulations in the solid state indicate a diversity of both strong and weak hydrogen bonds. Hirshfeld analysis provides deeper insights into the molecular packing and interactions. Based on the catalytic applications of similar compounds[154,213], compound **169** shows promise as a candidate for catalytic applications. In addition, by synthesizing compound **171**, we confirmed that the oxidation of the cyano group to an amide group can occur during the coordination reaction.

Chapter 7

Conclusion and prospective

The project is divided into two parts: the organic and inorganic components.

In the organic components, we successfully synthesized 15 new organic linkers for coordination reactions and the formation of metal-organic frameworks (MOFs). These compounds were characterized using NMR, IR, UV-Vis spectroscopy, single-crystal X-ray diffraction (SCXRD), and thermogravimetric analysis (TGA).

The organic linkers are categorized into three groups based on their core structures: benzene, triphenylene, and azacoronene.

For the benzene core, three isomers of cyanopyridine were synthesized using a simple method. These compounds were purified efficiently by washing with solvents, without the need for column chromatography.

We demonstrated that the cyano group can be converted into other functional groups, such as amide, carboxylic acid, and DAT. Through hydrolysis, the cyano group was transformed into amide and carboxylic acid groups under basic conditions, without the use of a catalyst. The resulting compounds were purified by simple filtration of the products.

Our study highlights that reaction the time and the percentage of base are critical factors in this hydrolysis process. Initially, the cyano group undergoes hydrolysis to form amide and carboxylic acid groups. Over time, the percentage of amide decreases, while the percentage of carboxylic acid increases.

To delve deeper into the molecular interactions of these benzene-core compounds, hydrogen bonding simulations and Hirshfeld surface analyses were conducted. These studies revealed that the type of functional groups plays a crucial role in molecular interactions. Compounds with amide and carboxylic acid groups, which have more heteroatoms, exhibit a combination of strong and weak hydrogen bonding, whereas compounds with cyano groups display only weak interactions.

UV-Vis spectroscopy showed $\pi \rightarrow \pi^*$ electronic transitions in these compounds. It was observed that when functional groups are in para positions, a red shift occurs due to the extended conjugation between the oxygen of the etheric group and the functional groups. Additionally, $n \rightarrow \pi^*$ electronic transitions were identified, which can be enhanced by delocalized electrons, further boosting the transition.

Thermogravimetric analysis (TGA) demonstrated high thermal stability for these compounds, likely due to their hydrogen bonding and conjugated structures. The compounds were stable within the temperature range of 200 to 419 °C.

Fluorescence studies indicated that changes in the positions of heteroatoms influence the emission properties of these compounds.

For the triphenylene core, we synthesized four isomers of cyanopyridine using a simple method, achieving yields greater than 90%. Purification was effectively performed by washing with solvents, without the need for column chromatography. The higher yields compared to cyanopyridines with benzene cores can be attributed to the lower solubility of these compounds in common solvents.

Single-crystal X-ray diffraction (SCXRD) analysis revealed that these triphenylene-based compounds do not exhibit the columnar structures typically observed in other triphenylene derivatives. This deviation is likely due to the structural constraints imposed by the cyanopyridine groups.

Hydrogen bonding simulations indicated that these compounds exhibit different behaviors, ranging from weak to strong interactions, depending on the position of the nitrogen and cyano group on the pyridine ring.

UV-Vis spectroscopy showed $\pi \rightarrow \pi^*$ electronic transitions and a red shift when the cyano group is in the para position compared to the meta positions. Additionally, the triphenylene compounds exhibited a red shift relative to the benzene-core analogs, which can be attributed to the higher conjugation in the triphenylene system.

Fluorescence studies demonstrated that the emission properties are influenced by the structural characteristics of the compounds, particularly due to aggregation effects.

In this project, one azacoronene derivative was synthesized with a yield of 89%. UV-Vis spectroscopy revealed several $\pi \rightarrow \pi^*$ transitions at 232, 274, and 366 nm, which can be attributed to the presence of various functional groups within the conjugated system. Thermogravimetric analysis (TGA) demonstrated high thermal stability up to 367 °C, likely due to the compound's aromaticity and the stabilizing effects of hydrogen bonding.

In the inorganic part of the project, we attempted to coordinate organic linkers that had a higher likelihood of forming coordination compounds. It was observed that carboxylic acids exhibited fast kinetics in the coordination reaction, and to obtain crystalline coordination compounds, we needed to slow down the reactions using various methods, such as changing solvents, metal ions, and reaction temperature. Additionally, we confirmed that during the reaction, cyano groups could hydrolysis to form amide groups. This suggests that cyanopyridines can not only directly coordinate with metal ions but also undergo hydrolysis during the reaction, allowing them to coordinate with the metal ions afterward. We also confirmed that the solvent plays an important role in the coordination reaction, as it can be oxidized and participate in the process. Ultimately, these reactions resulted in the formation of one complex which was characterized by IR, UV, and SCXRD.

To gain deeper insights into intermolecular and intramolecular interactions of the complex, hydrogen bonding and Hirshfeld surface studies were conducted. These studies revealed that heteroatoms play a significant role in the interactions of the complex. Moreover, TGA analysis showed high thermal stability up to 341 °C, which can be attributed to strong hydrogen bonding.

For future work on organic linkers, although several attempts to attach a pyridine ring to the benzene core via an etheric bond (compound **176**) (Figure 7.1) using reactions between 1,3,5-trihydroxybenzene **34** and **173** were unsuccessful, an alternative approach could involve synthesizing compound **176** by reacting 1,3,5-tribromobenzene **174** with 4-hydroxypyridine **175** (Figure 7. 1). The resulting compound has the potential to coordinate with metal ions through the nitrogen atoms of the pyridine rings. Furthermore, the presence of flexible ether bonds enhances structural adaptability, facilitating the formation of the desired MOFs.

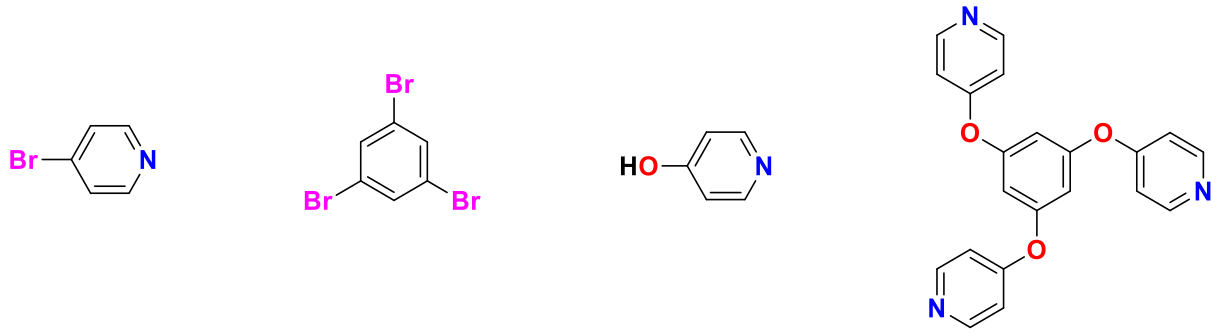

173 **174** **175** **176**

Figure 7. 1 Structure of compounds **173**, **174**, **175**, and **176**.

In addition, although several attempts to hydrolyze cyanopyridine triphenylenes into their corresponding amides and carboxylic acids were unsuccessful, an alternative approach could be explored. Reacting hexahydroxytriphenylene **49** with 5-bromopyridine-2-carboxylic acid methyl ester (**177**), followed by hydrolysis of the resulting ester (**178**), may provide a viable pathway to synthesize the target carboxylic acid (**179**) (Figure 7.2).

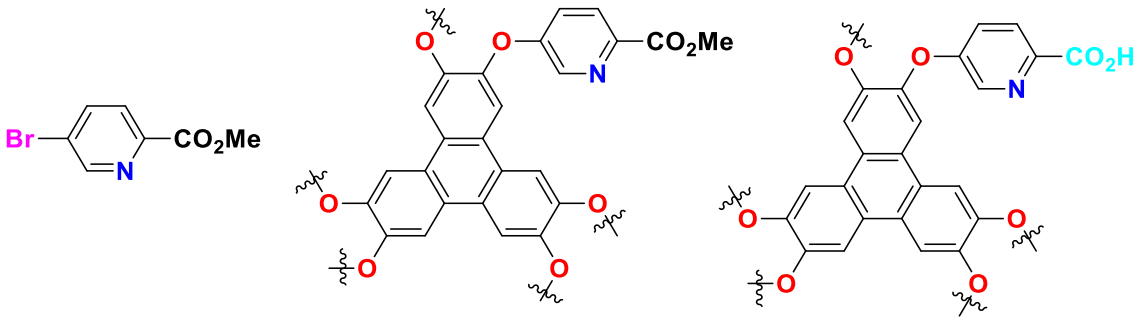

177 **178** **179**

Figure 7. 2 Structure of compound **177**, **178**, **179**.

Furthermore, cyanopyridines can be transformed into their diaminotriazine derivatives, which are rich in heteroatoms and possess an extended conjugated system. These features enable effective interactions with metal ions and other molecules, making them suitable for various applications.

For future work on the inorganic part, there is potential to further explore the cyanopyridine compounds for coordination reactions by modifying reaction conditions and components. This is due to the possibility of hydrolyzing the cyano group to amide and carboxylic acid during the coordination reaction. Additionally, by slowing down the coordination reaction between carboxylic acids, and metal ions through the use of auxiliary ligands, it may be possible to obtain the desired MOF.

Experimental Section

8.1 Chemicals and instruments

All solvents used in this project were purchased from Fisher Chemical. The other chemicals required for the syntheses were purchased from Sigma Aldrich and used without further purification. FTIR spectra were recorded in the range of 550– 4000 cm^{-1} on a Thermo Scientific Nicolet iS10 FT-IR spectrometer, in transmittance mode. UV-visible absorption spectra were measured using a Cary 630 spectrophotometer. Emission spectra were recorded on a Cary Eclipse spectrofluorometer from Agilent. ^{1}H and ^{13}C NMR spectra were recorded in DMSO-d_6 and $CDCl_3$-d6 at room temperature using a Varian Oxford 200 MHz and a Bruker ASCEND 400 MHz Neo Advance spectrophotometer. Chemical shifts (δ) are reported in part per million (ppm) relative to TMS, using the residual solvent protons (2.50 ppm) as reference. Melting points were measured on an Electrothermal IA9300 instrument. Thermal gravimetric analyses (TGA) were performed using a Mettler Toledo TGA1 instrument. The temperature program ranged from an initial temperature of 30 °C to a final temperature of 700 °C, with a ramp rate of 10 °C/ min, while maintaining a nitrogen atmosphere throughout the experiment. The mass spectrometry analyses were performed on Bruker microTOF II and Agilent TOF/Q-TOF instruments by electrospray ionization (ESI) method, in positive mode at the Mass Spectrometry Service at Université de Montréal. The CHN microanalyses were performed on a Thermo Scientific FlashSmart instrument by the Elemental Analysis Service at Université de Montréal. X-ray structure determination was realized on a XtaLAB Synergy, Dualflex, HyPix diffractometer (at 100 K) for **150** and on a Bruker Venture Metaljet diffractometer (at 150 K) for **132**, **137**, **151**, and **172**, and a Rigaku Gemini/Xcalibur diffractometer (at 293 K) (at 100 K) for **131** and **134** respectively. The corresponding crystallographic information files (cifs) for **131**, **132**, **134**, **137**, **150**, **151**, and **169** (CCDC 2223475, 2465679, 2224142, 2465687, 2379447, 2379513, and 2465688 respectively) (for the rest of the compounds I have not submitted) contain complete information on the X-ray structure determination of the compounds.

8.2 General synthesis methods

8.2.1 General synthesis method for 131-133

The tricyanopyridine benzenes **131-133** (Figure 8.1) were synthesized by the reaction of benzene-1,3,5-triol **35** (500 mg, 1 mmol), corresponding bromocyanopyridine (290 mg, 4 mmol), and potassium carbonate (219 mg, 4 mmol) in DMF/Toluene (60:60 mL). The mixture was refluxed for 72 hours. The resultant volatile components were subsequently eliminated via evaporation under reduced pressure. The solid residue was then subjected to extraction using dichloromethane extracted (3 × 50 mL). Afterward, the CH_2Cl_2 was evaporated under reduced pressure, yielding a solid residue. This residue underwent purification through washing with diethyl ether, followed by filtration to isolate the desired pure product.

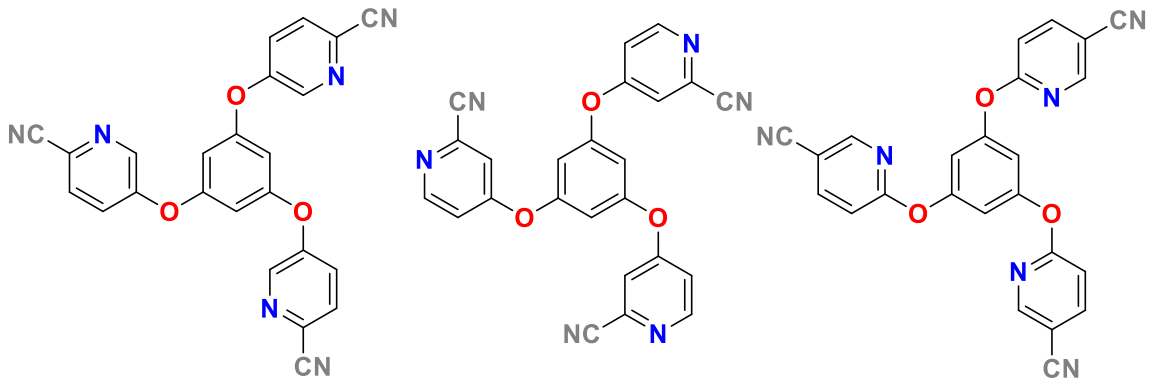

131 **132** **133**

Figure 8. 1 Structures of compounds **131**, **132**, and **133**.

Compound 131

Pale beige powder; Yield 67% (1.14 g, 2.636 mmol) mp 166-169 °C; IR (ATR, solid sample, cm^{-1}) 3086, 2233, 1567, 1455, 1419, 1383, 1288, 1229, 1129, 999 . ^1H NMR (400 MHz, DMSO-d_6) δ Ha 8.64 (d, ^4J = 2.6 Hz, 3H), Hc 8.08 (d, ^3J = 8.7 Hz, 3H), Hb 7.77 (dd, ^3J = 8.6, ^4J = 3.0 Hz, 3 H), Hd 7.10 (s, 3H) ppm. ^{13}C NMR (400 MHz, DMSO-d_6) δ 157.3, 156.5, 142.7, 131.1, 127.2, 126.0, 117.9, 109.7 ppm. HRMS (ESI-TOF) *m/z* $[M + H]^+$ calcd for $C_{24}H_{12}N_6O_3$ 433.10, found 433.10; HRMS (ESI-TOF) *m/z* $[M + H]^+$ calcd for $C_{24}H_{12}N_6O_3$ 937.2006; Found 937.2015. UV

(DMF, r.t, 10^{-4} - 10^{-5} M) λ_{max} = 271 nm, ε = 1.8 × 10^4 $M^{-1}cm^{-1}$. Fluorescence (DMF, r.t, 10^{-4} M): λ_{ex} = 270 nm, $\lambda_{max\ em}$ = 313, 412 nm.

Compound 132

Pale beige powder; Yield 65% (1.11 g, 2.567 mmol) mp 140-143 °C; IR (ATR, solid sample, cm^{-1}) 3067, 2240, 1564, 1450, 1403, 1294, 1267, 1157, 1116, 1006. ^{1}H NMR (400 MHz, DMSO-d_6) δ Hc 8.65 (d, ^3J = 5.8 Hz, 3H), Ha 7.92 (d, ^4J = 2.3 Hz, 3H), Hb 7.48 (dd, ^3J = 5.8, ^4J = 2.5 Hz, 3H), Hd 7.24 (s, 3H) ppm. ^{13}C NMR (400 MHz, DMSO-d_6) δ 164.6, 156.2, 153.6, 134.8, 118.5, 117.6, 116.6, 111.7 ppm. HRMS (ESI-TOF) *m/z* $[M + H]^+$ calcd for $C_{24}H_{12}N_6O_3$ 433.10528; Found 433.10436. UV (DMF, r.t, 10^{-4} - 10^{-5} M) λ_{max} = 267 nm, ε = 6.6 × 10^3 $M^{-1}cm^{-1}$. Fluorescence (DMF, r.t, 10^{-4} M): λ_{ex} = 270 nm, $\lambda_{max\ em}$ = 311, 422 nm. 433.10528.

Compound 133

Pale beige powder; Yield 68% (1.16 g, 2.682 mmol, 68%) mp 179-181 °C; IR (ATR, solid sample, cm^{-1}) 3077, 2233, 1586, 1449, 1378, 1310, 1254, 1132, 1116, 1006. ^{1}H NMR (400 MHz, DMSO-d_6) Ha δ 8.70 (d, ^4J = 2.0 Hz, 3H), Hb 8.34 (dd, ^3J = 8.6, ^4J = 2.3 Hz, 3H), Hc 7.29 (d, ^3J = 8.6 Hz, 3H), Hd 7.10 (s, 3H) ppm. ^{13}C NMR (400 MHz, DMSO-d_6) δ 164.9, 154.3, 152.7, 144.1, 117.4, 112.9, 112.8, 104.6 ppm. HRMS (ESI-TOF) *m/z* $[M + H]^+$ calcd for $C_{24}H_{12}N_6O_3$ 433.10, found 433.10; HRMS (ESI-TOF) *m/z* $[M + H]^+$ calcd for $C_{24}H_{12}N_6O_3$ 433.10436; Found 433.10563. UV (DMF, r.t, 10^{-4} - 10^{-5} M) λ_{max} = 272 nm, ε = 2.0909 × 10^4 $M^{-1}cm^{-1}$. Fluorescence (DMF, r.t, 10^{-4} M): λ_{ex} = 270 nm, $\lambda_{max\ em}$ = 312, 365, 414 nm.

8.2.2 General synthesis method for 134, 136, 137, and 139

The amide pyridine benzenes **134** and **136** and carboxy pyridine benzenes **137** and **139** (Figure 8.2) were synthesized through the hydrolysis of the corresponding cyanopyridine benzenes **131** and **133** (Figure 8.1). Initially, a mixture of cyanopyridine benzenes **131** and **133** (500 mg, 1.16 mmol) and potassium hydroxide (324 mg, 5.77 mmol) was refluxed in 50 ml water at 110 °C. After four hours, a white precipitate formed, which was subsequently filtered and dried in a vacuum oven to obtain the amide pyridine benzenes **134** and **136**. After acidifying the remaining solution beneath the filter with 200 µL of 37% HCl (pH= 4), a precipitate formed. Following

filtration and drying in a vacuum oven, the product obtained was identified as the carboxy pyridine benzenes **137** and **139**.

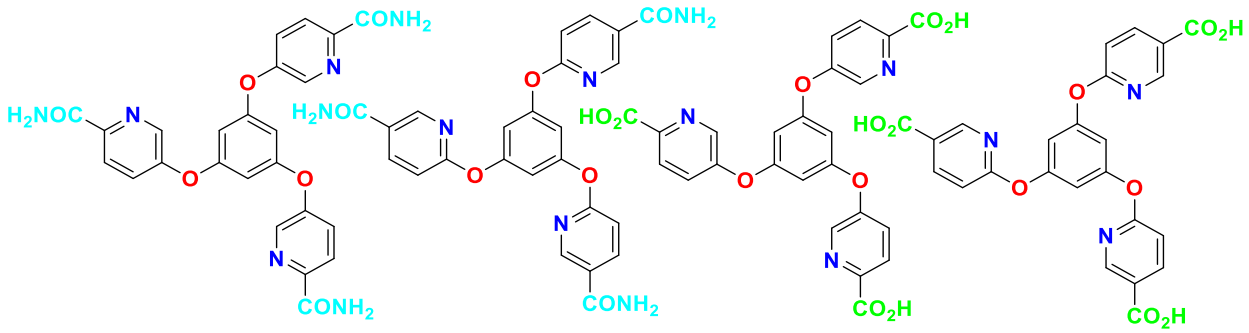

134 **136** **137** **139**

Figure 8. 2 Structures of compounds **134**, **136**, **137**, and **139**.

Compound 134

White powder; Yield 26 % (0.145 g, 0.30 mmol) mp 248-252 ˚C; IR (ATR, solid sample, cm^{-1}) 3462, 3351, 1682, 1614, 1477, 1456, 1409, 1368, 1222, 1123, 1004. ^{1}H NMR (400 MHz, DMSO-d_6) δ Ha 8.46 (d, ^{4}J = 2.7 Hz, 3H), Hc 8.05 (d, ^{3}J = 8.6 Hz, 3H), NH_2 8.02 (s, 3H), Hb 7.68 (dd, ^{3}J = 8.6, ^{4}J = 3 Hz, 2.7 H) NH_2 7.59 (s, 3H), Hd 6.87 (s, 3H) ppm. ^{13}C NMR (100 MHz, DMSO-d_6) δ 165.9, 158.3, 155.4, 146.2, 139.8, 126.6, 124.1, 107.3 ppm; HRMS (ESI-TOF) *m/z* $[M + H]^+$ calcd for $C_{24}H_{18}N_6O_6$ 487.13606; Found 487.13495. UV (DMF, r.t, 10^{-4} - 10^{-5} M) λ_{max} = 271 nm, ε = 1.9275 × 10^4 $M^{-1}cm^{-1}$. Fluorescence (DMF, r.t, 10^{-4} M): λ_{ex} = 270 nm, $\lambda_{max\ em}$ = 314, 414 nm.

Compound 136

White powder; Yield 30 % (0.170 g, 0.35 mmol) mp 270-274 ˚C; IR (ATR, solid sample, cm^{-1}) 3382, 3212, 1662, 1635, 1612, 1591, 1489, 1454, 1400, 1367, 1279, 1249, 1134, 1112, 1004. ^{1}H NMR (400 MHz, DMSO-d_6) δ Ha 8.66 (d, ^{4}J = 2.3 Hz, 3H), Hc 8.27 (dd, ^{3}J = 8.7, ^{4}J = 2.4 Hz, 3H), NH_2 8.07 (s, 3H), Hb 7.50 (s, 3H), NH_2 7.15 (d, ^{3}J = 8.6 Hz, 3H), Hd 6.94 (s, 3H) ppm. ^{13}C NMR (100 MHz, DMSO-d_6) δ 166.3, 164.5, 155.2, 147.9, 140.1, 126.2, 111.6 ppm; HRMS (ESI-TOF) *m/z* $[M + H]^+$ calcd for $C_{24}H_{18}N_6O_6$ 487.13606; Found 487.13550. UV (DMF, r.t, 10^{-4} - 10^{-}

^{5} M) λ_{max} = 272 nm, ε = 1.9902 × 10^{4} $M^{-1}cm^{-1}$. Fluorescence (DMF, r.t, 10^{-4} M): λ_{ex} = 270 nm, $\lambda_{max\ em}$ = 311, 416 nm.

Compound 137

Pale beige powder; Yield 40 % (0.225 g, 0.46 mmol) mp 252-255 °C(not sure); IR (ATR, solid sample, cm^{-1}) 3072, 1736, 1605, 1570, 1452, 1348, 1297, 1220, 993. ^{1}H NMR (400 MHz, DMSO-d_6) δ Ha 8.54 (d, *J* = 3 Hz, 3H), Hc 8.07 (d, *J* = 9 Hz, 3H), Hb 7.68 (dd, *J* = 9, 3 Hz, 2.7 H), Hd 6.96 (s, 3H) ppm. ^{13}C NMR (100 MHz, DMSO-d_6) δ 165.9, 157.4, 155.9, 143.7, 140.7, 126.9, 125.9, 108.2 ppm. HRMS (ESI-TOF) *m/z* [M - H]$^{-}$ calcd for $C_{24}H_{15}N_3O_6$ 488.07355; Found 488.07421. UV (DMF, r.t, 10^{-4} - 10^{-5} M) λ_{max} = 270 nm, ε = 2.1153 × 10^{4} $M^{-1}cm^{-1}$. Fluorescence (DMF, r.t, 10^{-5} M): λ_{ex} = 270 nm, $\lambda_{max\ em}$ = 314, 419 nm.

Compound 139

Pale beige powder; Yield 29 % (0.166 g, 0.34 mmol) mp 270-273 °C; IR (ATR, solid sample, cm^{-1}) 3076, 1698, 1590, 1456, 1419, 1376, 1240, 1113, 998. ^{1}H NMR (400 MHz, DMSO-d_6) δ Ha 8.72 (d, J = 2.4 Hz, 3H), Hc 8.31 (dd, *J* = 8.5, 2.4 Hz, 3H), Hb 7.18 (d, *J* = 8.6 Hz, 3H) Hd 7.03 (s, 3H) ppm. ^{13}C NMR (100 MHz, DMSO-d_6) δ 166.2, 165.4, 154.9, 147.9, 150.0, 141.7, 123.0, 112.2, 111.9 ppm. HRMS (ESI-TOF) *m/z* [M + H]$^{+}$ calcd for $C_{24}H_{12}K_3N_3O_9$ 488.07355; Found 488.07079. UV (DMF, r.t, 10^{-4} - 10^{-5} M) λ_{max} = 272 nm, ε = 2.1987 × 10^{4} $M^{-1}cm^{-1}$. Fluorescence (DMF, r.t, 10^{-4} M): λ_{ex} = 270 nm, $\lambda_{max\ em}$ = 312, 414 nm.

8.2.3 General synthesis method for 135 and 141

The amide pyridine benzenes **135** and carboxylate pyridine benzene **141** (Figure 8.3) were synthesized through the hydrolysis of the corresponding cyanopyridine benzene **132** (Figure 7.1). Initially, a mixture of cyanopyridine benzene **132** (500 mg, 1.16 mmol) and potassium hydroxide (324 mg, 5.77 mmol) was refluxed in 50 ml water at 110 °C. After four hours, a white precipitate formed, which was subsequently filtered and dried in a vacuum oven to obtain the amide pyridine benzene. The remaining solution beneath the filter was acidified with 200 µL of 37% HCl to adjust the pH to approximately 4. Unlike compounds **137** and **139**, compound **141** does not precipitate

upon acidification. The solution was then evaporated under reduced pressure to obtain compound **141**.

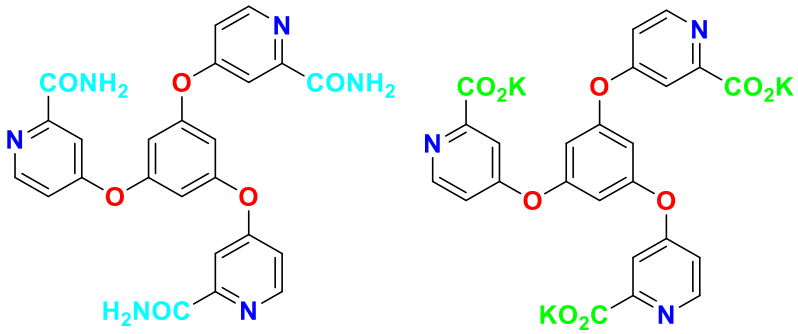

135 **141**

Figure 8. 3 Structures of compounds **135** and **141**.

Compound 135

White powder; Yield 24 % (0.136 g, 0.28 mmol) mp 240-245 °C; IR (ATR, solid sample, cm^{-1}) 3444, 3337, 1678, 1570, 1432, 1364, 1283, 1244, 1133, 1004. ^{1}H NMR (400 MHz, DMSO-d_6) δ Hc 8.55 (d, ^{3}J = 5.6 Hz, 3H), NH_2 8.16 (s, 3H), NH_2 7.72 (s, 3H), Ha 7.61 (d, ^{4}J = 2.1 Hz, 3H), Hb 7.29 (dd, ^{3}J = 5.5, ^{4}J = 2.4 Hz, 3H), Hd 7.14 (s, 3H) ppm. ^{13}C NMR (100 MHz, DMSO-d_6) δ 165.8, 165.0, 156.5, 153.2, 151.2, 115.2, 110.9, 110.8 ppm; HRMS (ESI-TOF) *m/z* $[M + H]^+$ calcd for $C_{24}H_{18}N_6O_6$ 487.13606; Found 487.13495. UV (DMF, r.t, 10^{-4} - 10^{-5} M) λ_{max} = 267 nm, ε = 2.1987×10^4 $M^{-1}cm^{-1}$. Fluorescence (DMF, r.t, 10^{-4} M): λ_{ex} = 270 nm, $\lambda_{max\ em}$ = 310, 423 nm.

Compound 141

Pale beige powder; Yield 76 % (0.531 g, 0.88 mmol) mp 370-375 °C (not sure); IR (ATR, solid sample, cm^{-1}) 3315, 1630, 1563, 1454, 1406, 1366, 1285, 1238, 1136, 1007. ^{1}H NMR (400 MHz, DMSO-d_6) δ Ha 8.49 (d, *J* = 5.6 Hz, 3H), Hc 7.51 (d, *J* = 2.5 Hz, 3H), Hb 7.14 (dd, *J* = 5.6, 2.5 Hz, 3H), Hc 7.00 (s, 3H) ppm. ^{13}C NMR (100 MHz, DMSO-d_6) δ 166.2, 165.4, 156.5, 153.2, 151.2, 115.2, 110.9, 110.8 ppm. HRMS (ESI-TOF) *m/z* [M-3Na+2H-e] calcd for $C_{24}H_{14}N_3O_9$

488.07355; Found 488.06973. UV (DMF, r.t) λ_{max} = 310, 443 nm. Fluorescence (DMF, r.t): λ_{ex} = 270 nm, $\lambda_{max\ em}$ = 309, 418 nm.

8.2.4 Synthesis method of 145

To synthesize compound **145** (Figure 8.4), a mixture of 1,3,5-tri-cyanopyridine-benzene **131** (0.30 g, 0.69 mmol), dicyandiamide (0.18 g, 2.42 mmol), and KOH (0.12 g, 2.08 mmol) in 10 mL of 2-methoxyethanol was refluxed for 4 hours. After cooling down, 10 ml of water was added to the solution, and the pH was adjusted to around 3 by using 200 µl HCl 37%. Upon acid addition, a precipitate formed. The supernatant was filtered, and the yellow residue was dried under a vacuum oven to obtain the final product.

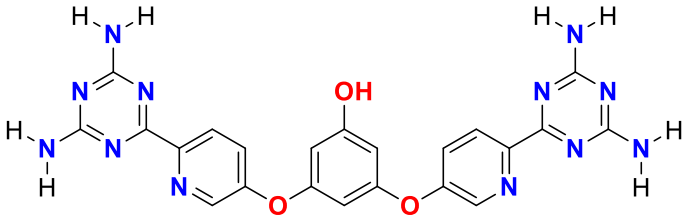

145

Figure 8. 4 Structure of compound **145**.

Compound 145

Yellow powder; Yield 72% (0.247 g, 497 mmol); mp 225-235 ˚C; UV (acetonitrile) λ_{max} = 300 nm; IR (neat) ν_{max} = 3470, 3313, 3188, 1605, 1531, 1435, 1398, 1220, 1141, 1114, 992 cm^{-1}. ^{1}H NMR (400 MHz, DMSO-d_6) δ Hd 8.46 (s, 3H, CH), Ha 8.25 (d, ^{3}J = 8.6 Hz, 3H, CH), Hb 7.58 (dd, ^{3}J = 8.6, ^{4}J = 2.0 Hz, 3 H, CH), H_{NH2} 6.84 (s, 12H, NH), Hc 6.34 (d, ^{3}J = 11.5 Hz, 3H, CH) ppm; ^{13}C NMR (100 MHz, DMSO-d_6) δ = 169.9, 168.0, 160.6, 158.3, 154.53, 150.3, 140.7, 126.1, 124.9, 102.6, 101.2 ppm; HRMS (ESI-TOF) *m/z* $[M + H]^+$ calcd for $C_{22}H_{18}N_{12}O_3$ 499.46; Found 499.17.

8.2.5 General synthesis method for compounds 150-153

To synthesis compounds **150-153** (Figure 8.5), a mixture of triphenylene-2,3,6,7,10,11-hexaol (0.5 g, 1.54 mmol), corresponding bromocyanopyridine (2.5 g, 13.8 mmol), and K_2CO_3 (1.9 g, 13.8 mmol) in DMF/toluene (1/1) was heated at reflux for 72 hours. Volatiles were then removed from the mixture by evaporation under reduced pressure, and the solid residue was extracted with CH_2Cl_2 (4 × 50 mL). CH_2Cl_2 was removed by evaporation under reduced pressure, and the solid residue was washed with hot methanol. A subsequent filtration allowed the pure product to be isolated.

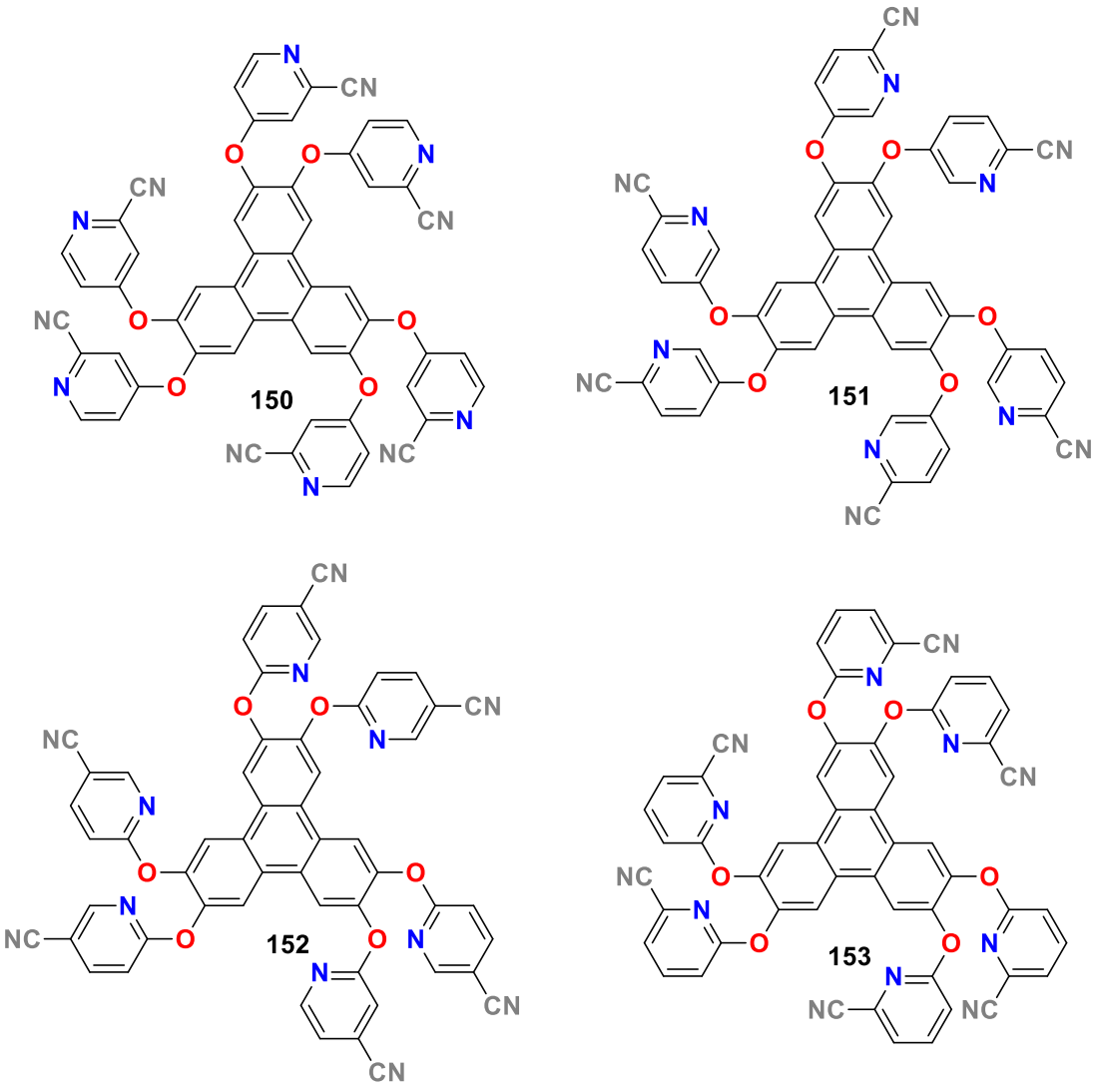

Figure 8. 5 Structures of compounds **150-153**.

Compound 150

Pale beige powder. Yield 90% (0.94 g, 1.003 mmol). mp 333-337 ˚C; ^{1}H NMR (DMSO-d_6, 200 MHz), δ, ppm: Hd 9.05 (s, 6H, CH), Hc 8.56 (d, ^{3}J = 5.8 Hz, 6H, CH), Ha 7.82 (d, ^{4}J = 2.5 Hz, 6H, CH), Hb 7.31 (dd, ^{3}J = 5.8, ^{4}J=2.6 Hz, 6 H, CH). ^{13}C NMR (DMSO-d_6, 100 MHz) δ, ppm: 164.6, 153.5, 144.9, 134.7, 129.1, 120.3, 117.5, 117.3, 115.4. HRMS (ESI-TOF) *m/z* $[M+H]^+$ calcd for $C_{54}H_{24}N_{12}O_6$ 937.20145; Found 937.20139; (relative error -0.07). Elemental analysis: Calcd. (%) for $C_{54}H_{25}N_{12}O_6$ (CH_3OH): C 68.18, H 2.91, N 17.35; Found: C 68.06, H 2.72, N 17.64; IR (ATR, solid sample, cm^{-1}): 3060, 2240, 1571, 1464, 1419, 1419, 1297, 1270, 1160, 1007. UV (acetonitrile, r.t, 10^{-4} - 10^{-6} M) λ_{max} = 271 nm. Fluorescence (acetonitrile, r.t): λ_{ex} = 270 nm, $\lambda_{max\ em}$ = 377, 360, 369 nm. X-ray quality crystals were obtained at 25 ˚C by slow evaporation of a solution of the compound in DMSO (~5 mg/mL).

Compound 151

Pale beige powder. Yield 87% (0.92 g, 0.982 mmol). mp 274-278 ˚C. ^{1}H NMR (DMSO-d_6, 200 MHz) δ, ppm: Hd 8.96 (s, 6H, CH), Ha 8.48 (d, ^{4}J = 2.5 Hz, 6H, CH), Hc 7.98 (d, ^{3}J = 8.7 Hz, 6H, CH), Hb 7.58 (dd, ^{3}J = 8.7, ^{4}J = 2.9 Hz, 6H, CH). ^{13}C NMR (DMSO-d_6, 100 MHz) δ, ppm: 156.6, 145.5, 141.3, 131.1, 128.9, 126.9, 124.4, 119.6, 117.7. HRMS (ESI-TOF) *m/z* $[M + H]^+$ calcd for $C_{54}H_{25}N_{12}O_6$ 937.2015; Found 937.2006 (relative error 0.96 ppm).Elemental analysis: Calcd (%) for $C_{54}H_{25}N_{12}O_6(H_2O)_{1.8}(CH_3OH)$: C 65.97, H 3.18. N 16.79; Found: C 66.46, H 2.71, N 16.53. IR (ATR, solid sample, cm^{-1}): 3059, 2234, 1570, 1503, 1463, 1416, 1283, 1227, 1129,1013. UV (acetonitrile, r.t, 10^{-4} - 10^{-6} M) λ_{max} = 275 nm. Fluorescence (acetonitrile, r.t, 10^{-5} M**):** λ_{ex} = 270 nm, $\lambda_{max\ em}$ = 380, 363, 398 nm. X-ray quality crystals were obtained at 25 ˚C by slow evaporation of a solution of the compound in acetonitrile (~5 mg/mL).

Compound 152

Pale beige powder. Yield 92% (0.89 g, 0.949 mmol). mp 366 ˚C. ^{1}H NMR (DMSO-d_6, 200 MHz) δ, ppm: Hd 8.86 (s, 6H, CH), Ha 8.59 (d, ^{4}J = 1.9 Hz, 6H, CH), Hc 8.26 (dd, ^{3}J = 8.7, ^{4}J = 2.3 Hz, 6H, CH), Hb 7.13 (d, ^{3}J = 8.7 Hz, 6H, CH). ^{13}C NMR (DMSO-d_6, 100 MHz) δ, ppm: 164.9, 152.6, 144.0, 145.1, 128.1, 119.8, 117.3, 111.8, 104.5. HRMS (ESI-TOF) *m/z* $[M+H]^+$ calcd for $C_{54}H_{25}N_{12}O_6$ 937.2015; Found 937.2046 (relative error -3.31 ppm). Elemental analysis: Calcd (%) for $C_{54}H_{25}N_{12}O_6(H_2O)$: C 67.92, H 2.74. N 17.60; Found: C 67.61, H 2.72, N 17.60 .IR (ATR,

solid sample, cm^{-1}) 3074, 2232, 1595, 1504, 1472, 1414, 1288, 1255, 1117, 1017. UV (acetonitrile, r.t, 10^{-4} - 10^{-6} M) λ_{max} = 273 nm. Fluorescence (acetonitrile, r.t, 10^{-5} M**):** λ_{ex} = 270 nm, $\lambda_{max\ em}$ = 375, 364, 393 nm.

Compound 153

Pale beige powder. Yield 89% (0.87 g, 0.928 mmol). mp 332-336 °C. ^{1}H NMR (DMSO-d_6, 200 MHz) δ, ppm: Hd 8.91 (s, 6H, CH), Hc 8.01 (dd, ^{3}J = 8.5, ^{3}J = 7.4 Hz, 6H, CH), Ha 7.73 (dd, ^{3}J = 7.3, ^{4}J = 0.7 Hz, 6H, CH), Hb 7.31 (dd, ^{3}J = 8.5, ^{4}J = 0.7 Hz, 6H, CH). ^{13}C NMR (DMSO-d_6, 200 MHz) δ, ppm: 163.0, 145.0, 142.3, 129.8, 128.1, 125.3, 119.8, 117.1, 116.5. HRMS (ESI-TOF) *m/z* $[M+H]^+$ calcd for $C_{54}H_{25}N_{12}O_6$ 937.20145; Found 937.20265; (relative error 1.28). Elemental analysis: Calcd (%) for $C_{54}H_{25}N_{12}O_6(CH_3OH)_2$: C 67.20, H 3.22, N 16.79; Found: C 67.77, H 2.77, N 16.88. IR (ATR, solid sample, cm^{-1}) 3088, 2236, 1589, 1505, 1436, 1413, 1321, 1269, 1205, 1130, 1010. UV (acetonitrile, r.t, 10^{-4} - 10^{-6} M) λ_{max} = 269 nm. Fluorescence (acetonitrile, r.t, 10^{-5} M**):** λ_{ex} = 270 nm, $\lambda_{max\ em}$ = 362, 394, 473 nm.

8.2.6 Synthesis method of 2,3,6,7,10,11-hexamethoxytriphenylene (52)

To synthesize compound **51** (Figure 8.6), according to the reported study[214], in a 1000 mL round-bottom flask equipped with a magnetic stirrer, veratrole **50** (21.3 mL, 166.5 mmol) was gradually introduced into a well-stirred suspension of $FeCl_3$ (81.0 g, 499.4 mmol) in dichloromethane (500 mL) with concentrated sulfuric acid (0.9 mL, 16.3 mmol). As the veratrole **50** was added, hydrogen chloride gas was released, causing the temperature to rise until the dichloromethane began boiling. The reaction mixture was then stirred for an additional 2 hours. To halt the reaction, methanol (300 mL) was carefully added (this step generates heat and formaldehyde, so it is recommended to perform it in a well-ventilated fume hood). After complete addition of methanol, the mixture was stirred for another 30 minutes, then filtered. The remaining solid was thoroughly washed with methanol (5 × 80 mL) and vacuum dried, yielding 2,3,6,7,10,11-hexamethoxytriphenylene **51** as a grey solid. ^{1}H NMR (400 MHz, DMSO-d6) Ha δ 7.99 (s, 6H), Hb 4.04 (s, 18H) ppm. The melting point is more than 300°C as reported (19.7 g, 87%).

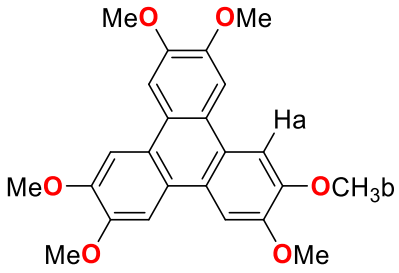

52

Figure 8. 6 Structure of compound **52**.

8.2.7 Synthesis method of 1,5,9-trinitro-2,3,6,7,10,11-hexamethoxytriphenylene (165)

To synthesize compound **165** (Figure 8.7), according to the reported study[214], in a 500 mL round-bottom flask fitted with a magnetic stirrer, dry $CHCl_3$ (250 mL) was added along with TBAB (7.9 g, 24.5 mmol), $AgNO_3$ (25.0 g, 147.0 mmol), and 2,3,6,7,10,11-hexamethoxytriphenylene **52** (10.0 g, 24.5 mmol). Benzene sulfonyl chloride (18.8 mL, 147.0 mmol) was then slowly introduced, and the mixture was heated to 60 °C for three days. Afterward, the reaction mixture was filtered, and the resulting solution was added to water and extracted with CH_2Cl_2. The organic phase was washed with water, dried over anhydrous Na_2SO_4, and concentrated under reduced pressure. The product was purified through silica gel column chromatography (PE : DCM = 4 : 1, v/v) and recrystallized in ethanol, yielding a yellow solid **165**. ^{1}H NMR (400 MHz, $CDCl_3$-d_6) δ 7.61 (s, 3H), Hb 4.08 (s, 9H), Hc 4.01 (s, 9H) ppm. The melting point is between 245-246°C as reported (7.2 g, 54%).

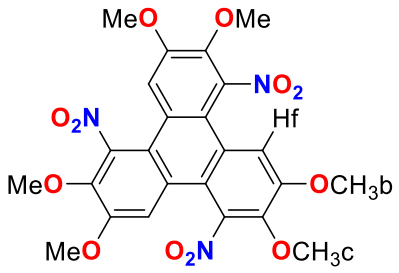

165

Figure 8. 7 Structure of compound **165**.

8.2.8 Synthesis method for 2,3,6,7,10,11-hexamethoxytriphenylene-1,5,9-triamine (166)

To synthesize compound **166** (Figure 8.8), according to the reported study[214], in a 500 mL round-bottom flask equipped with a magnetic stirrer, a solution of 1,5,9-trinitro-2,3,6,7,10,11-hexamethoxytriphenylene **165** (5.0 g, 9.2 mmol) was prepared in a 200 mL THF/MeOH mixture (4:1 v/v). To this solution, $Ni(OAc)_2•4H_2O$ (2.3 g, 9.2 mmol) was added, and the mixture was stirred for 5 minutes. Finely powdered $NaBH_4$ (5.22 g, 138.0 mmol) was then gradually introduced, leading to the immediate formation of a fine black precipitate. The mixture was stirred until thin-layer chromatography (TLC) indicated the reaction was complete. At the end, 100 mL of water was added, the mixture was filtered, and the solvents were evaporated under reduced pressure. The remaining solid was recrystallized from ethanol to yield a gray solid **166**. ^{1}H NMR (400 MHz, DMSO-d6) δ Hf 8.10 (s, 3H), NH_2 5.14 (s, 6H), Hb 3.79 (s, 9H), Hc 3.90 (s, 9H) ppm. The melting point is between 173-174°C as reported (4.0 g, 96%).

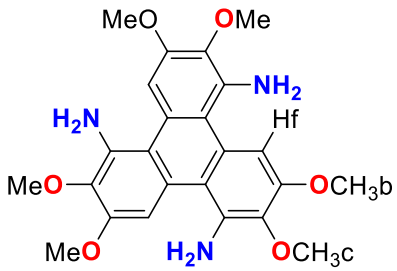

166

Figure 8. 8 Structure of compound **166**.

8.2.9 Synthesis method of compound 165

To synthesize compound **165** (Figure 8.9), 1,5,9-triamino-2,3,6,7,10,11-hexamethoxytriphenylene **159** (50 mg, 0.11 mmol) and 4-formylbenzoate (91 mg, 0.55 mmol) were placed in a dried 25 mL schlenk tube. The tube was purged with nitrogen, followed by the addition of 5 mL of DMSO. The reaction mixture was heated at 150 °C for 24 hours under a nitrogen atmosphere. Subsequently, the reaction was continued under an oxygen atmosphere at 120 °C and monitored by TLC until completion. After cooling to room temperature, the mixture was extracted with water (15 mL) and dichloromethane (2 × 40 mL). The organic layer was separated, and the solvent was evaporated. The resulting yellow residue was washed with water and acetone, then dried under vacuum to afford the final product, compound **165**.

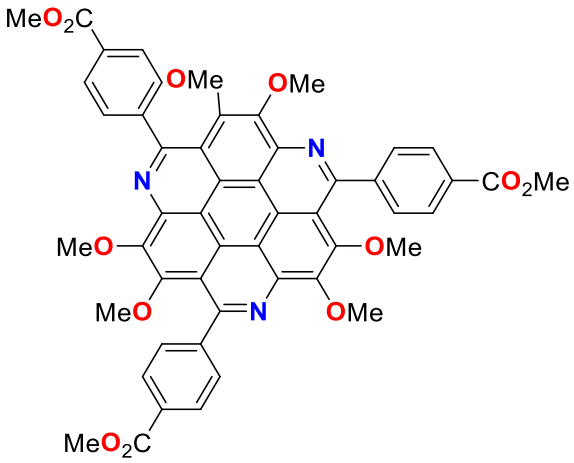

165

Figure 8. 9 Structure of compound **165**.

Compound 165

Yellow powder; Yield 89% (0.868 g, 0.098 mmol) mp 227-232 ˚C; ^{1}H NMR (400 MHz, $CDCl_3$-d_6)) δ Hb 8.33 (d, ^{3}J = 8.5 Hz, 6H, CH), Ha 7.99 (d, ^{3}J = 8.5 Hz, 6H, CH), Hc 4.53 (s, 9H, CH_3), He 4.06 (s, 9H, CH_3), Hd 3.82 (s, 9H, CH_3) ppm; ^{13}C NMR (100 MHz, $CDCl_3$-d_6) δ 167.2, 158.6, 150.1, 148.4, 147.6, 140.0, 129.6, 129.5, 128.7, 123.5, 116.5, 112.6, 63.1, 61.9, 52.3 ppm; IR (ATR, solid sample, cm^{-1}) 2945, 1716, 1610, 1564, 1455, 1407, 1374, 1272, 1188, 1103 cm^{-1};

HRMS (ESI-TOF) *m/z* $[M + H]^+$ calcd for $C_{51}H_{39}N_3O_{12}$ 885.87; Found 890.2929; UV (acetonitrile, r.t, 10^{-4} - 10^{-6} M) λ_{max} = 232, 274, 366 nm.

8.2.10 Synthesis method of 169

To synthesize compound **169** (Figure 8.10), a solution of one equivalent compound **145** (10 mg, 0.020 mmol) and three equivalents of $Zn(ClO_4)_2 \cdot 6H_2O$ **168** (16.32 mg, 0.044 mmol) dissolved in a mixture of 3 mL of DMF and 6 mL of methanol was prepared. The solution was then transferred to a 25 mL sealed vial and heated in an oven at 80 °C for 48 hours. After heating, the vial was allowed to slowly cool to room temperature, resulting in the formation of crystals of the final compound **169** (Figure 7.11).

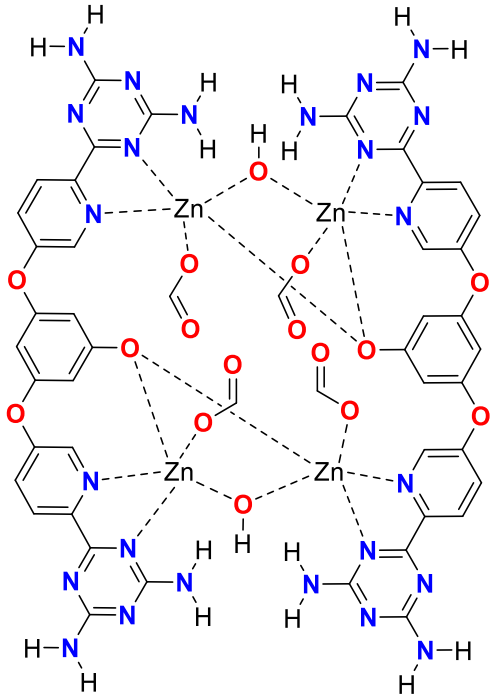

Figure 8. 10 Structure of compound **169**.

Compound 169

Yellow crystal (Figure 8.11); Yield 65% (0.098 g, 0.065 mmol); IR (ATR) 3395, 2934, 2360, 1652, 1494, 1456, 1412, 1387, 1339, 1253, 1150, 1099, 1016, 995 cm^{-1}; HRMS (ESI-TOF) *m/z*.

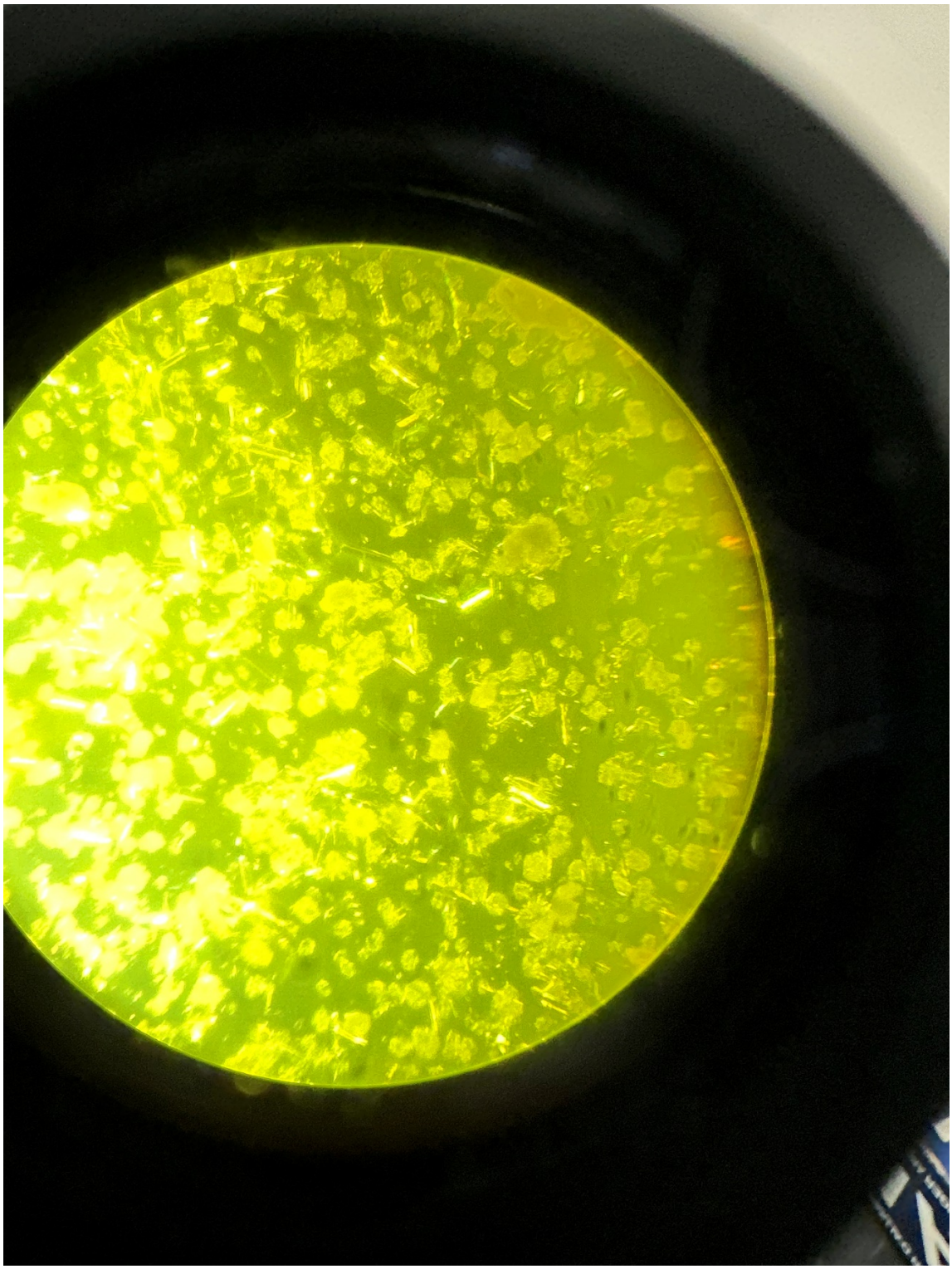

Figure 8. 11 Photo of crystal of compound **169**.

Annex

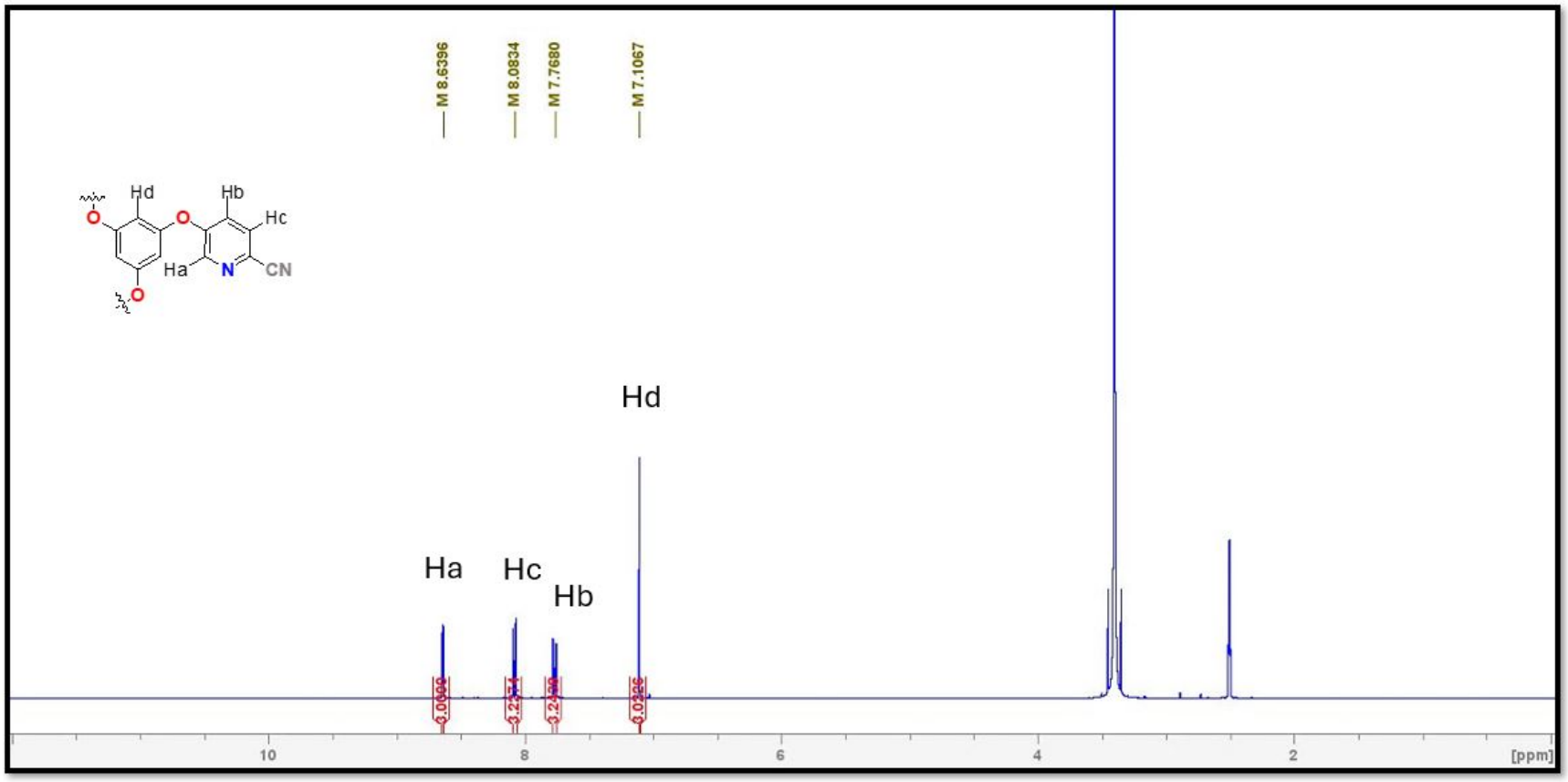

Figure S. 1 ^{1}H NMR (400 MHz) spectrum of compound **131**. Solvent: DMSO-d_6.

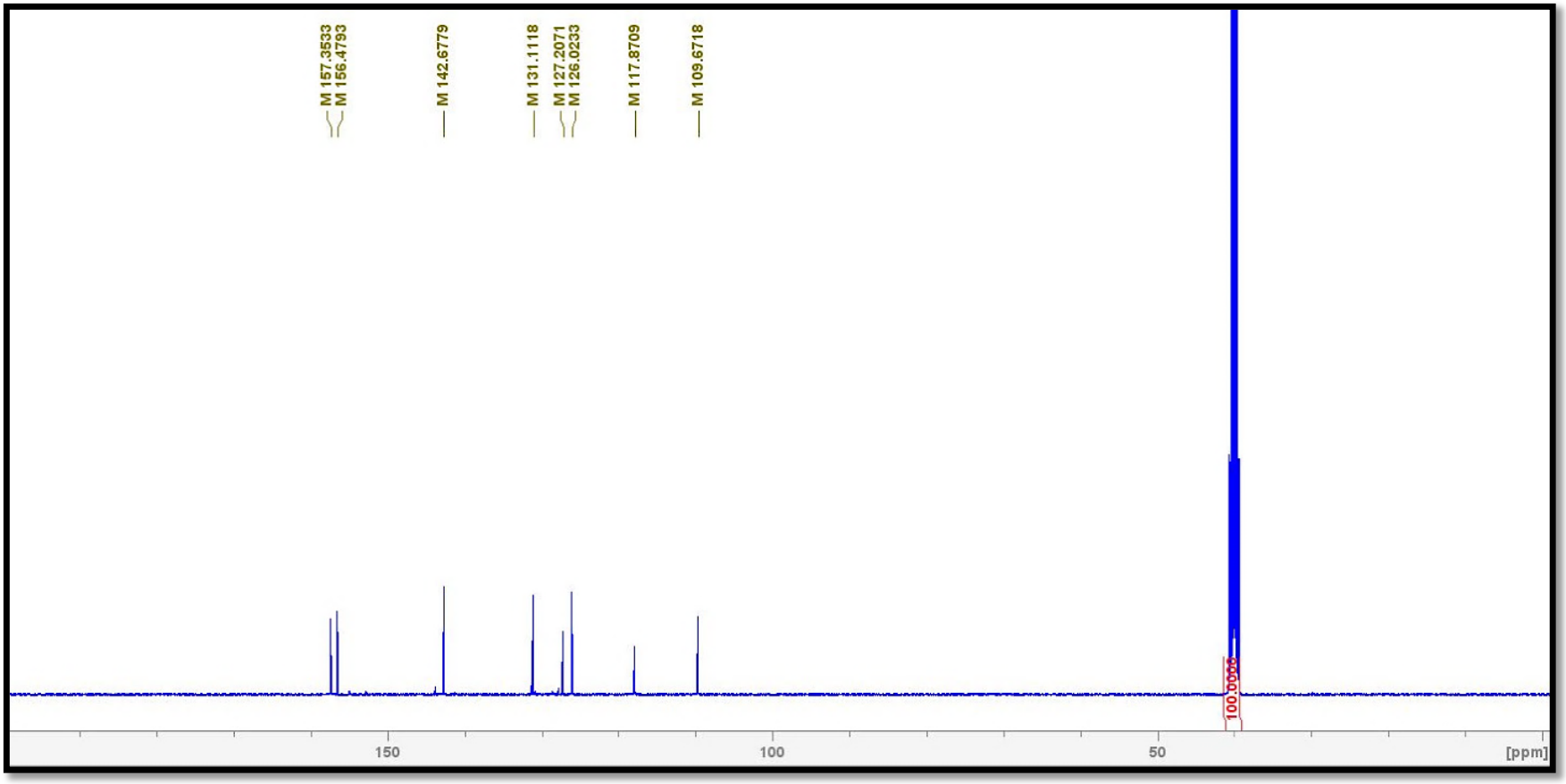

Figure S. 2 ^{13}C NMR (100 MHz) spectrum of compound **131**. Solvent: DMSO-d_6.

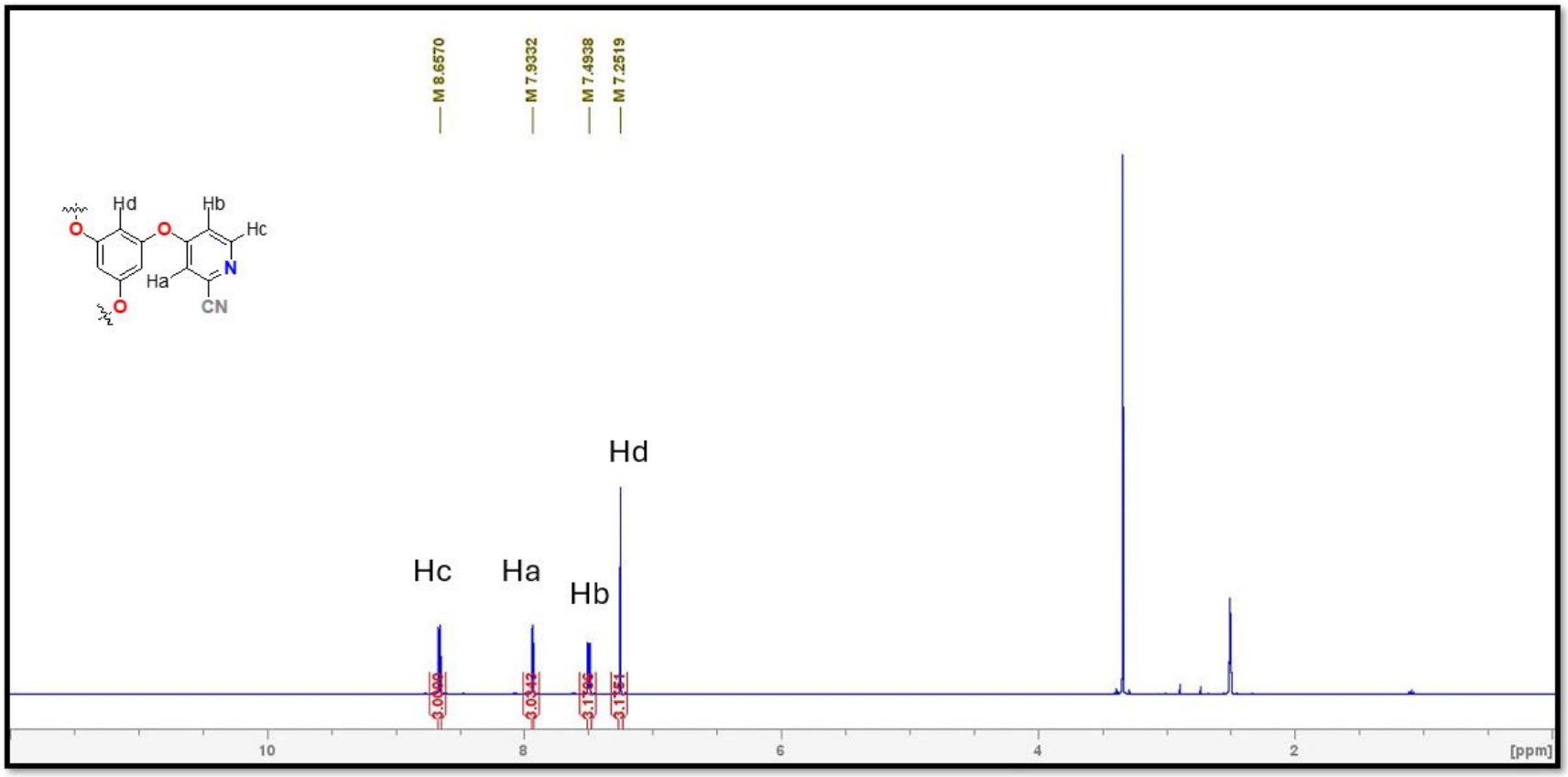

Figure S. 3 ^{1}H NMR (400 MHz) spectrum of compound **132**. Solvent: DMSO-d_6.

d

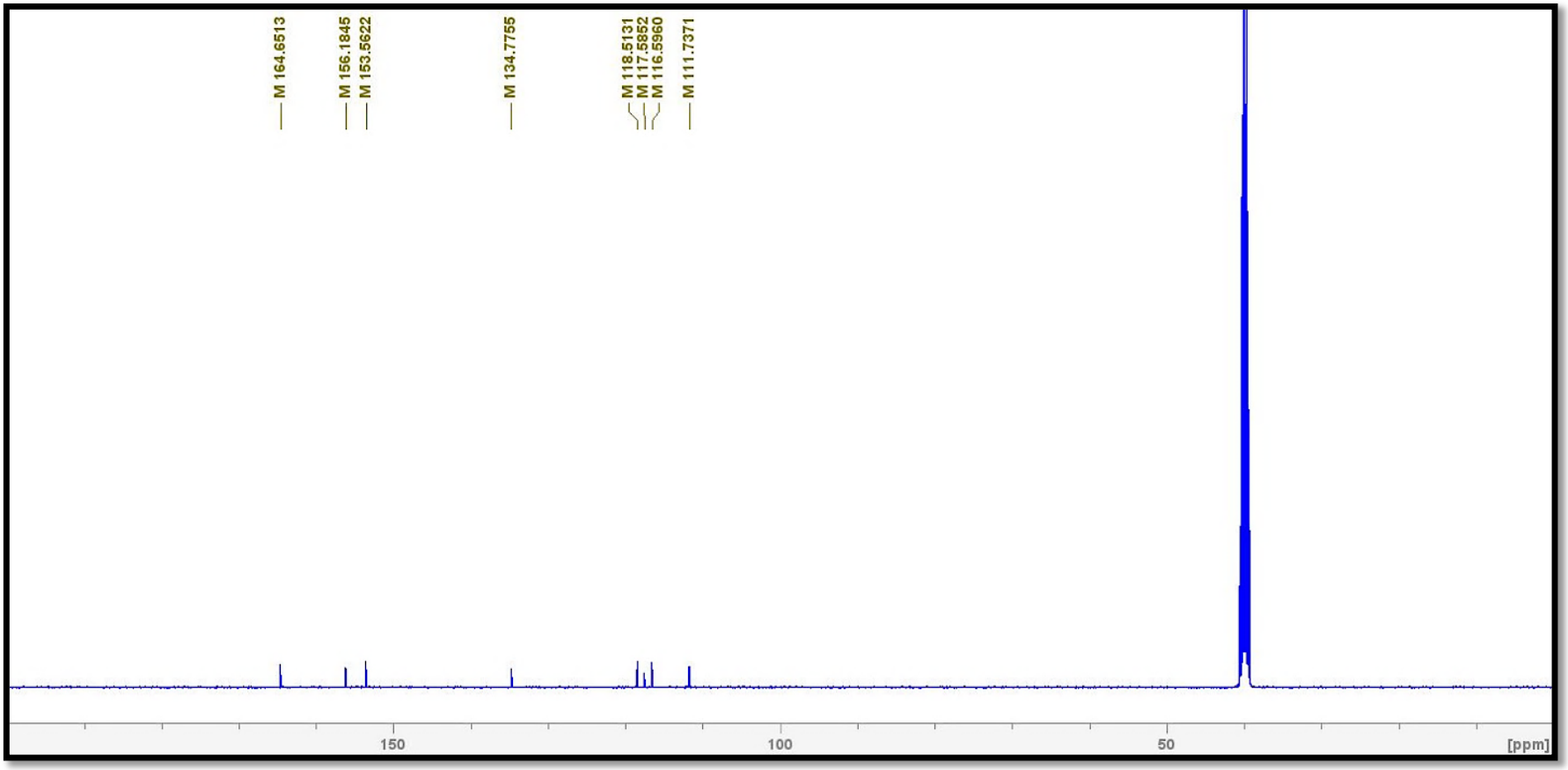

Figure S. 4 ^{13}C NMR (100 MHz) spectrum of compound **132**. Solvent: DMSO-d_6.

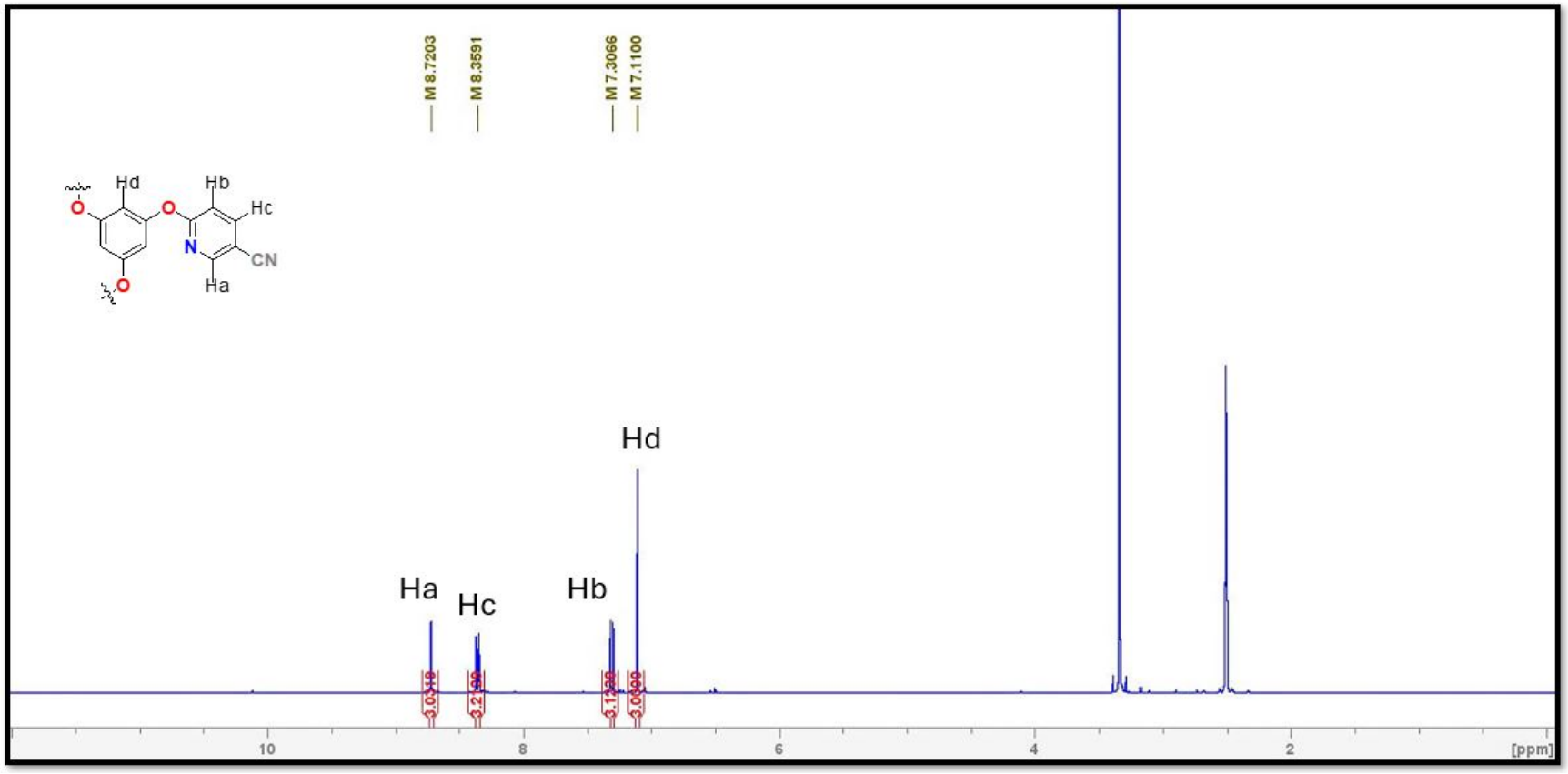

Figure S. 5 ^{1}H NMR (400 MHz) spectrum of compound **133**. Solvent: DMSO-d_6.

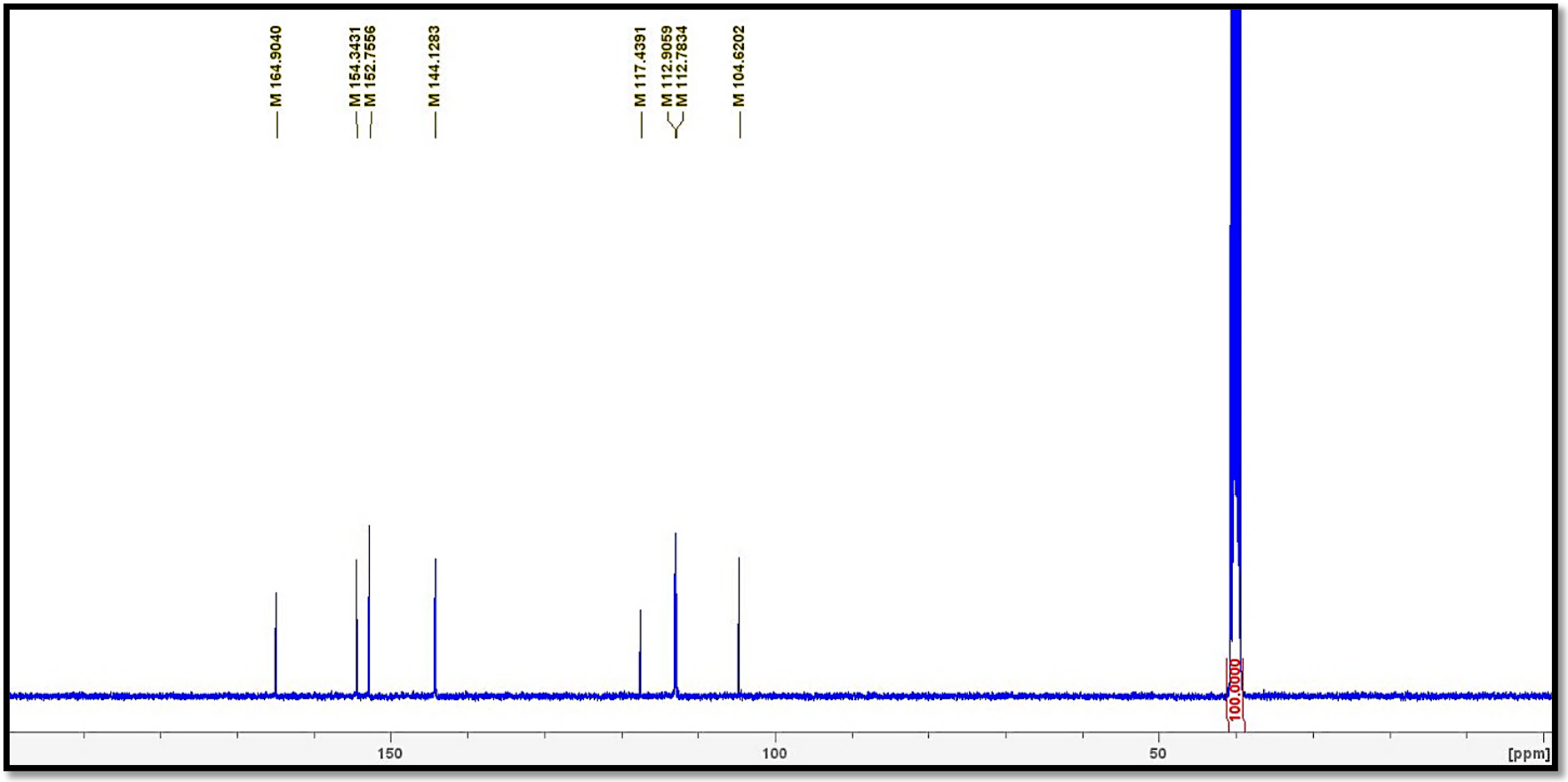

Figure S. 6 ^{13}C NMR (100 MHz) spectrum of compound **133**. Solvent: DMSO-d_6.

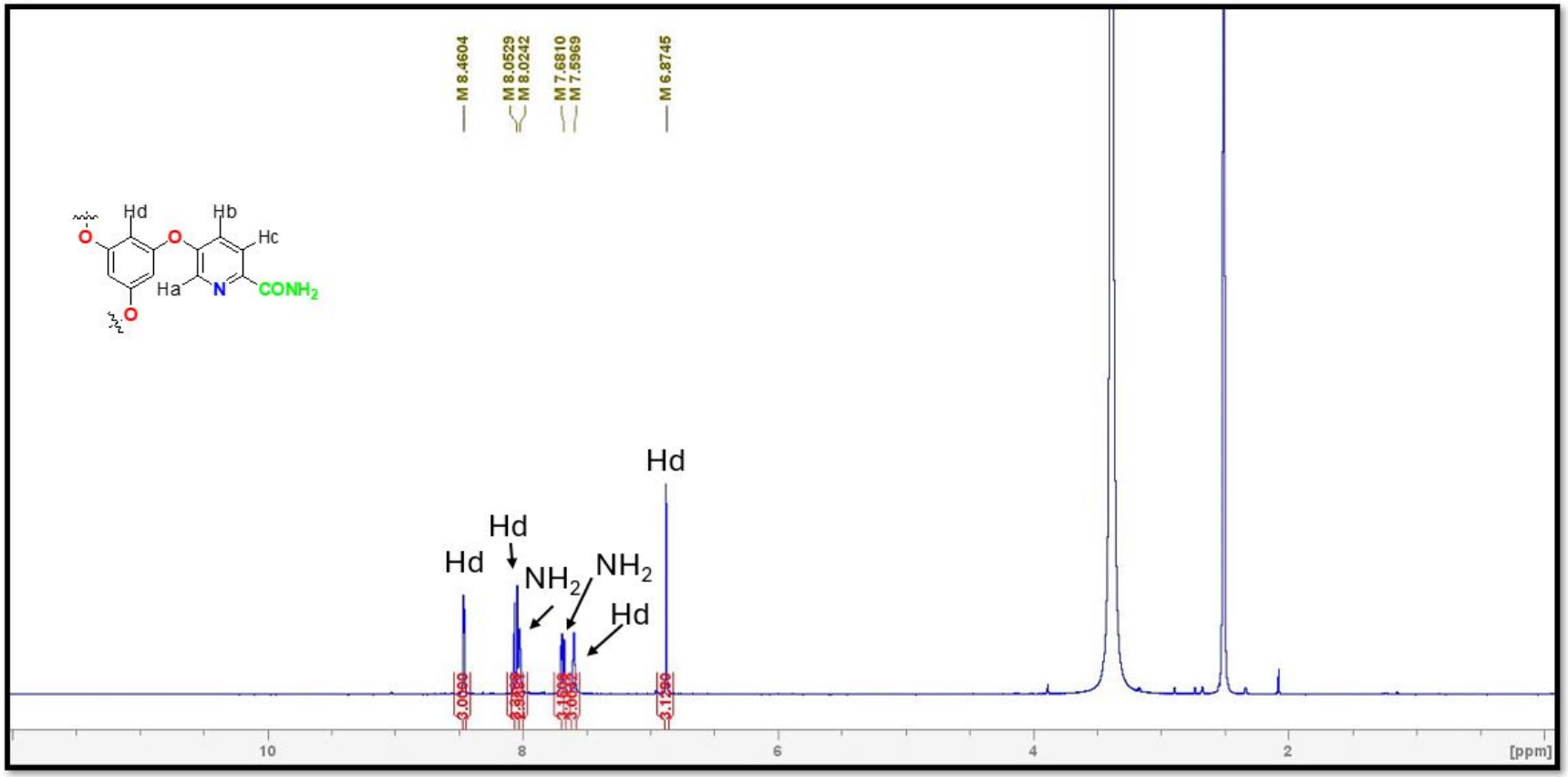

Figure S. 7 ^{1}H NMR (400 MHz) spectrum of compound **134**. Solvent: DMSO-d_6.

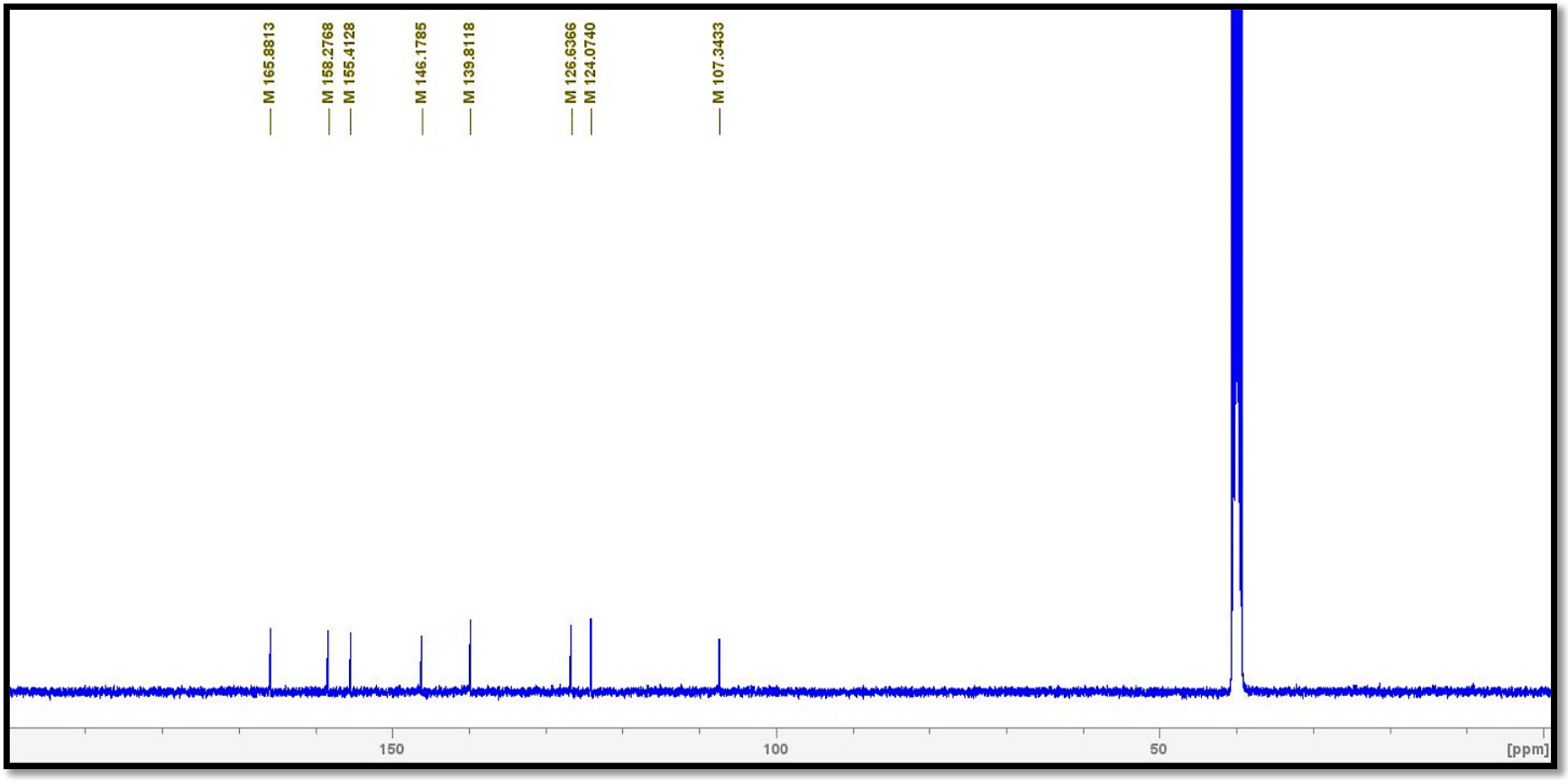

Figure S. 8 ^{13}C NMR (100 MHz) spectrum of compound **134**. Solvent: DMSO-d_6.

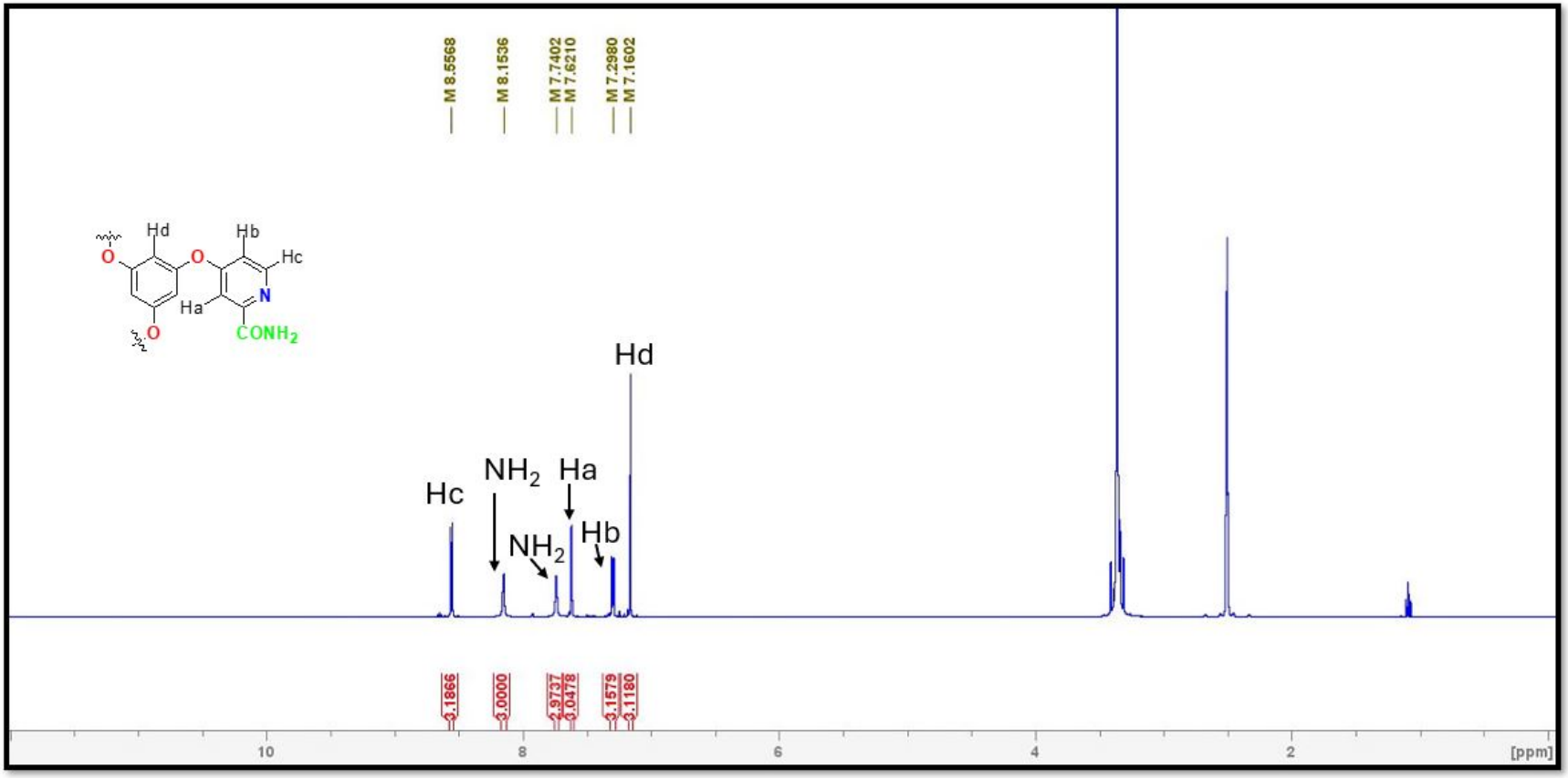

Figure S. 9 ^{1}H NMR (400 MHz) spectrum of compound **135**. Solvent: DMSO-d_6.

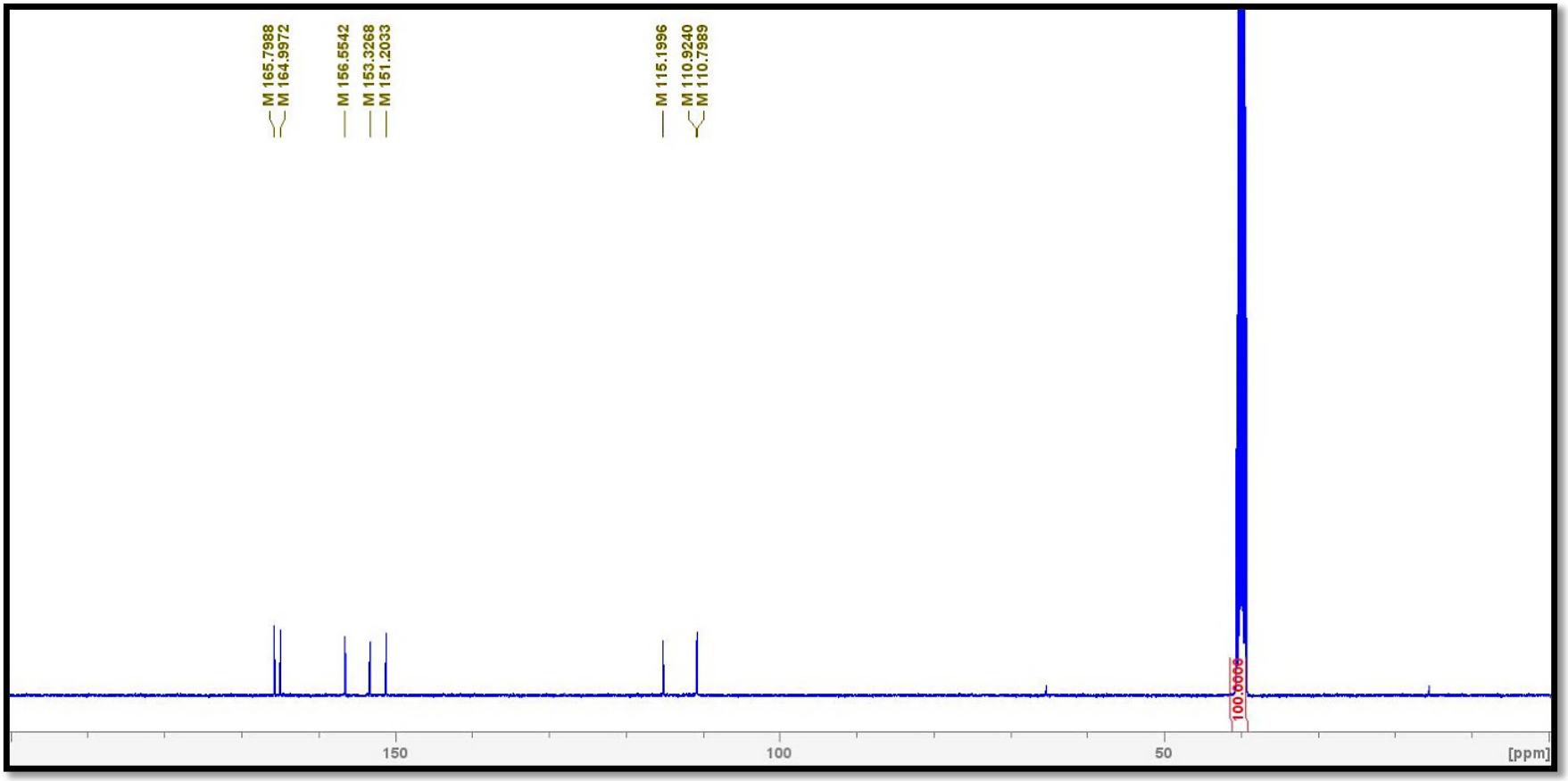

Figure S. 10 ^{13}C NMR (100 MHz) spectrum of compound **135**. Solvent: DMSO-d_6.

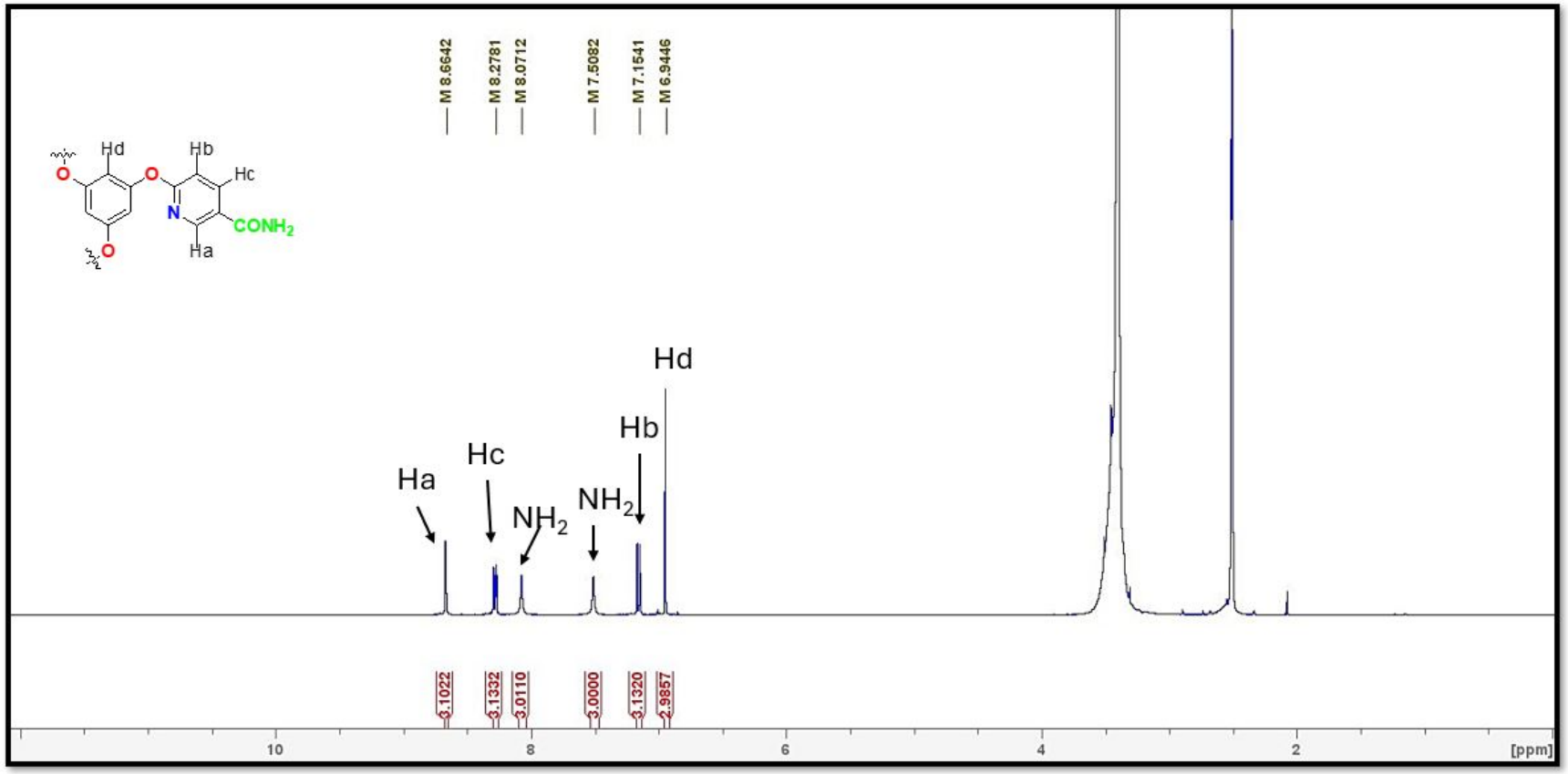

Figure S. 11 ^{1}H NMR (400 MHz) spectrum of compound **136**. Solvent: DMSO-d_6.

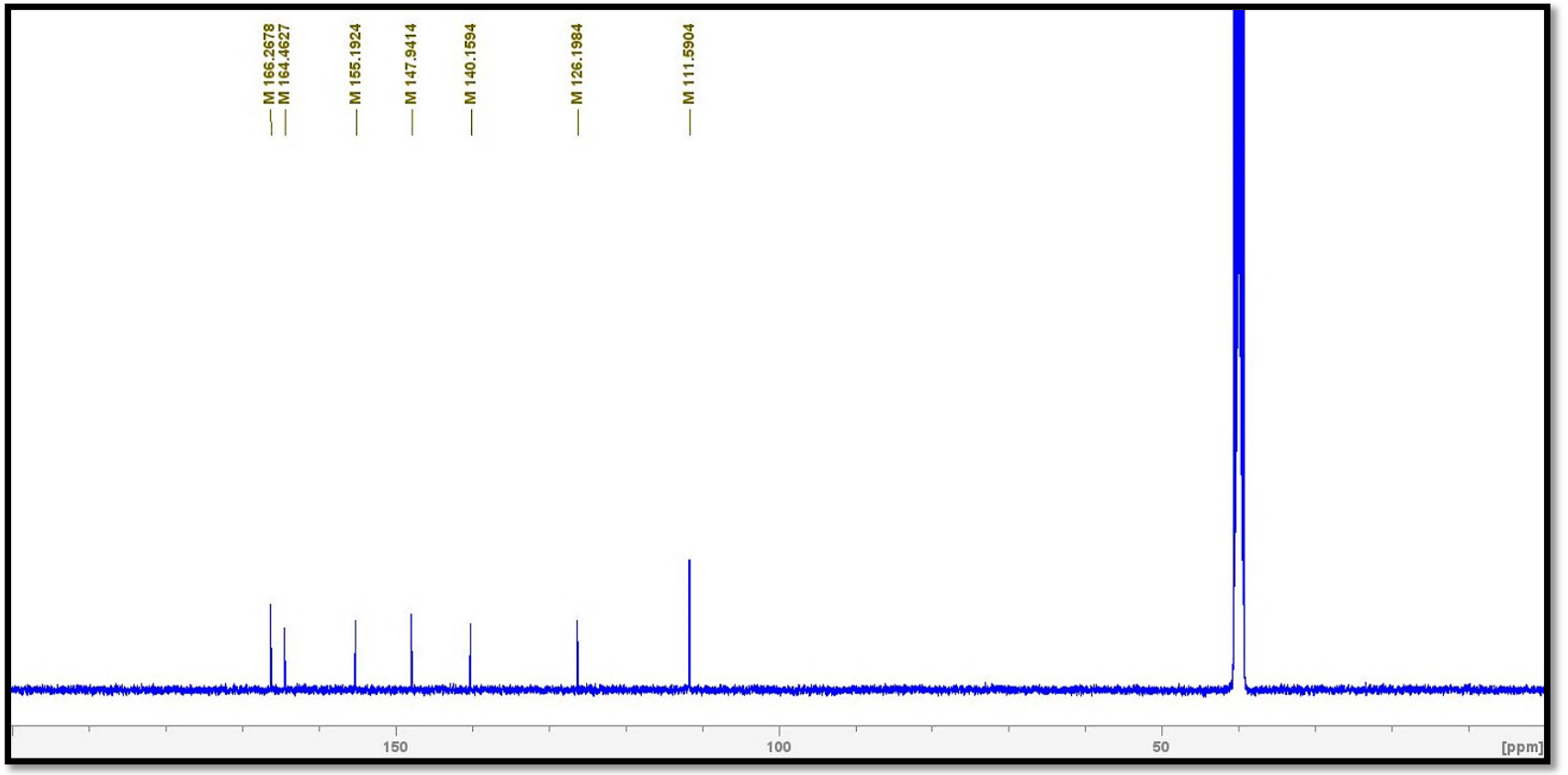

Figure S. 12 ^{13}C NMR (100 MHz) spectrum of compound **136**. Solvent: DMSO-d_6.

m

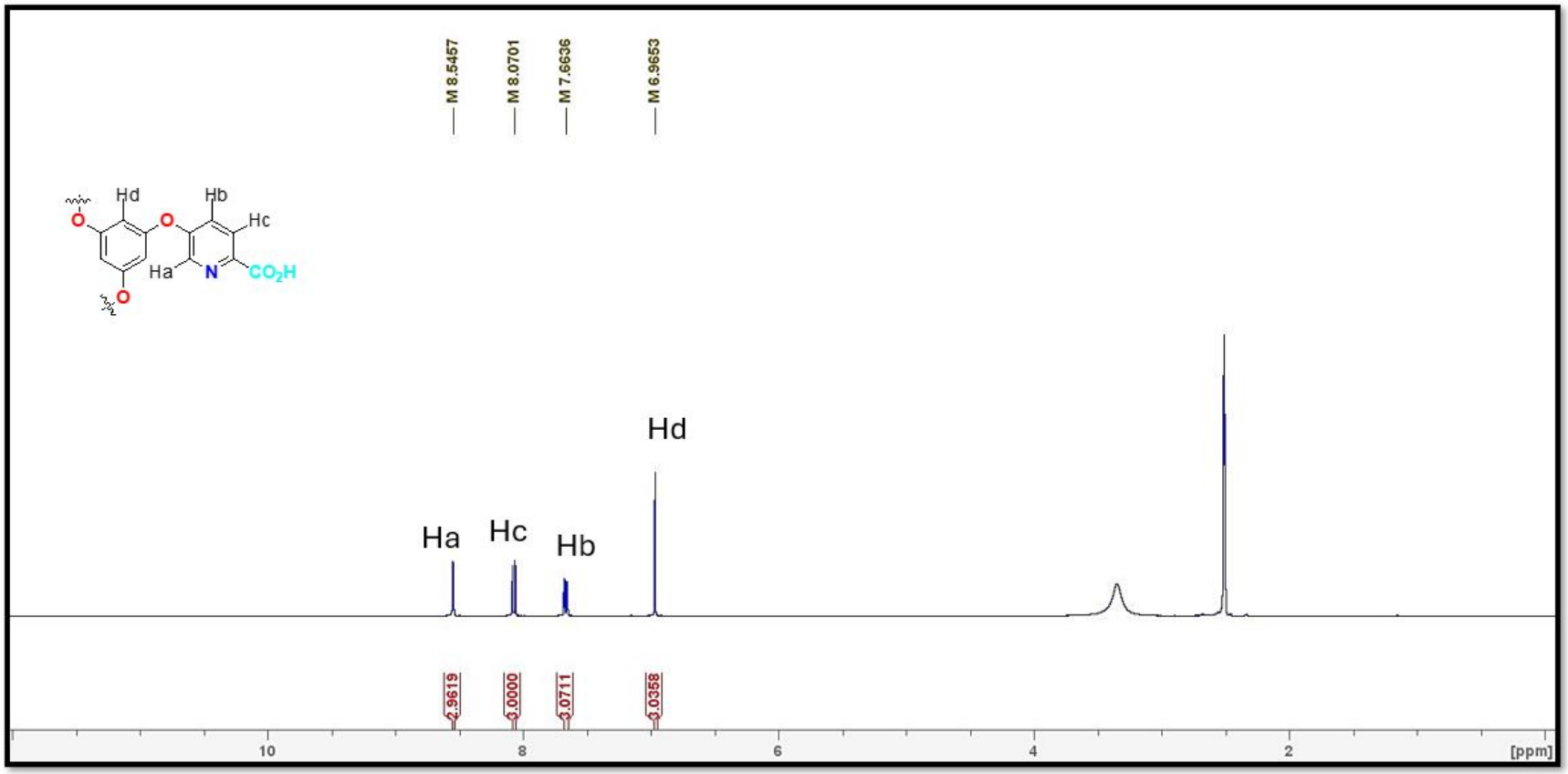

Figure S. 13 ^{1}H NMR (400 MHz) spectrum of compound **137**. Solvent: DMSO-d_6.

n

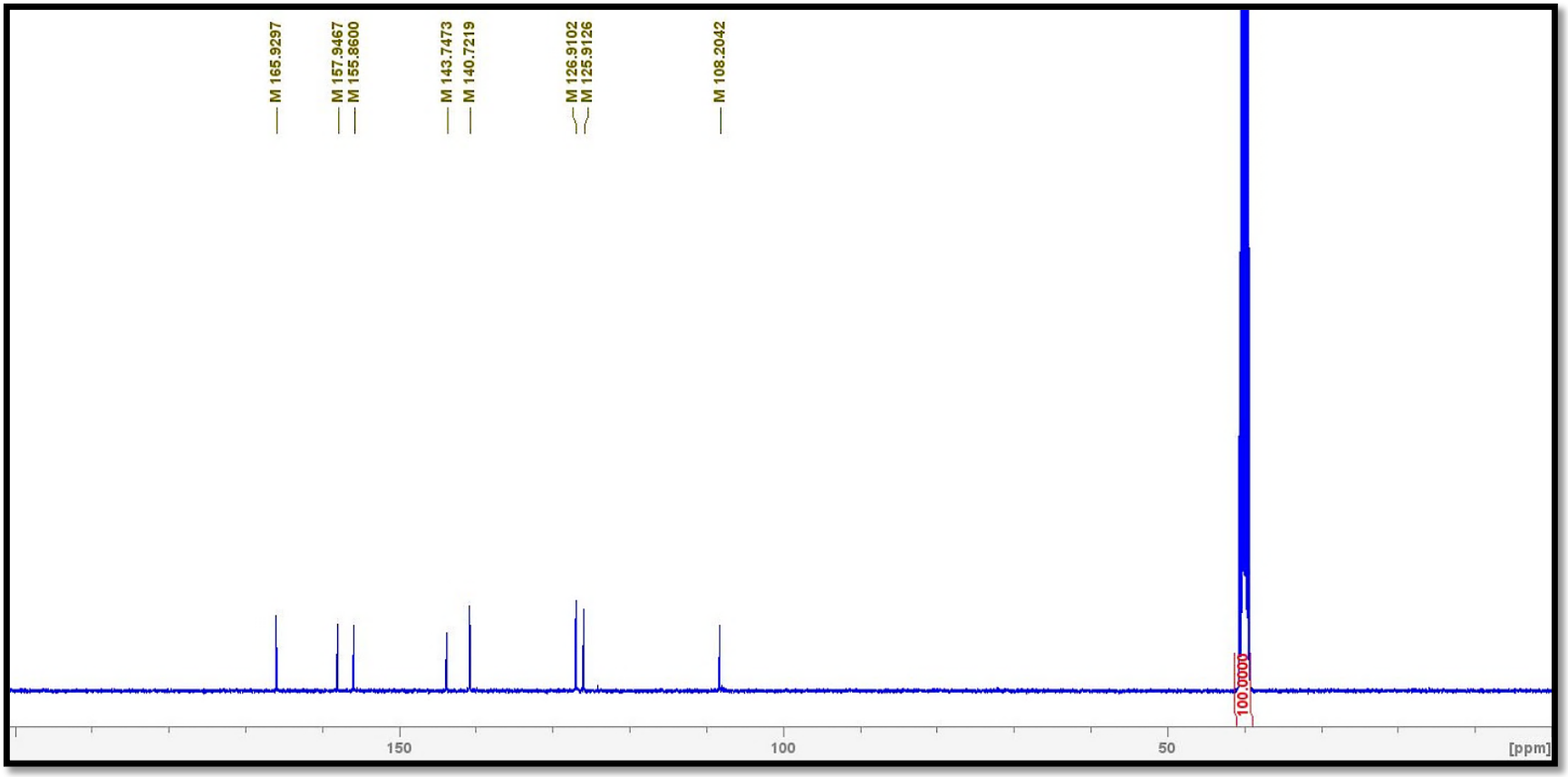

Figure S. 14 ^{13}C NMR (100 MHz) spectrum of compound **137**. Solvent: DMSO-d_6.

o

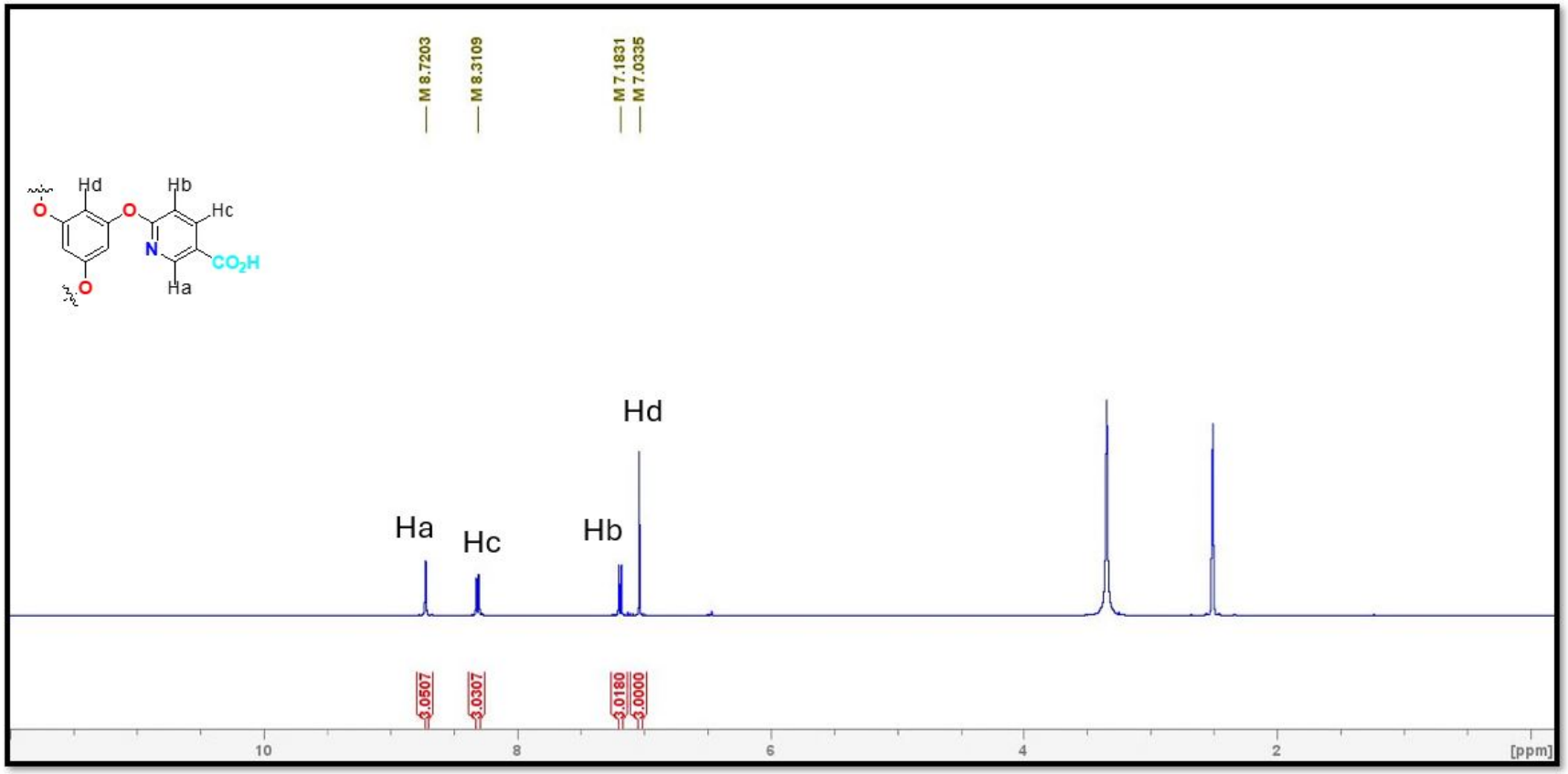

Figure S. 15 ^{1}H NMR (400 MHz) spectrum of compound **139**. Solvent: DMSO-d_6.

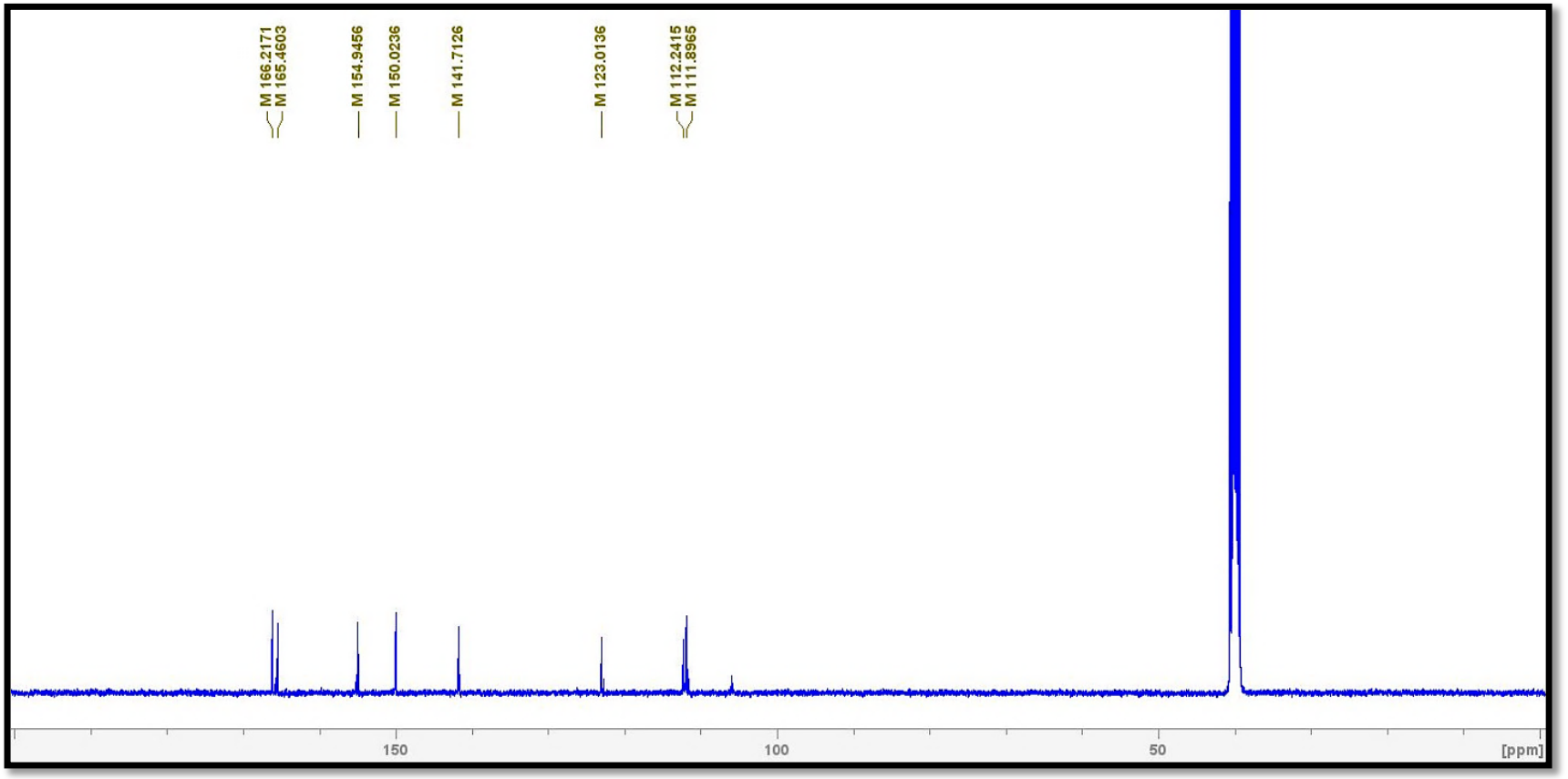

Figure S. 16 ^{13}C NMR (100 MHz) spectrum of compound **139**. Solvent: DMSO-d_6.

q

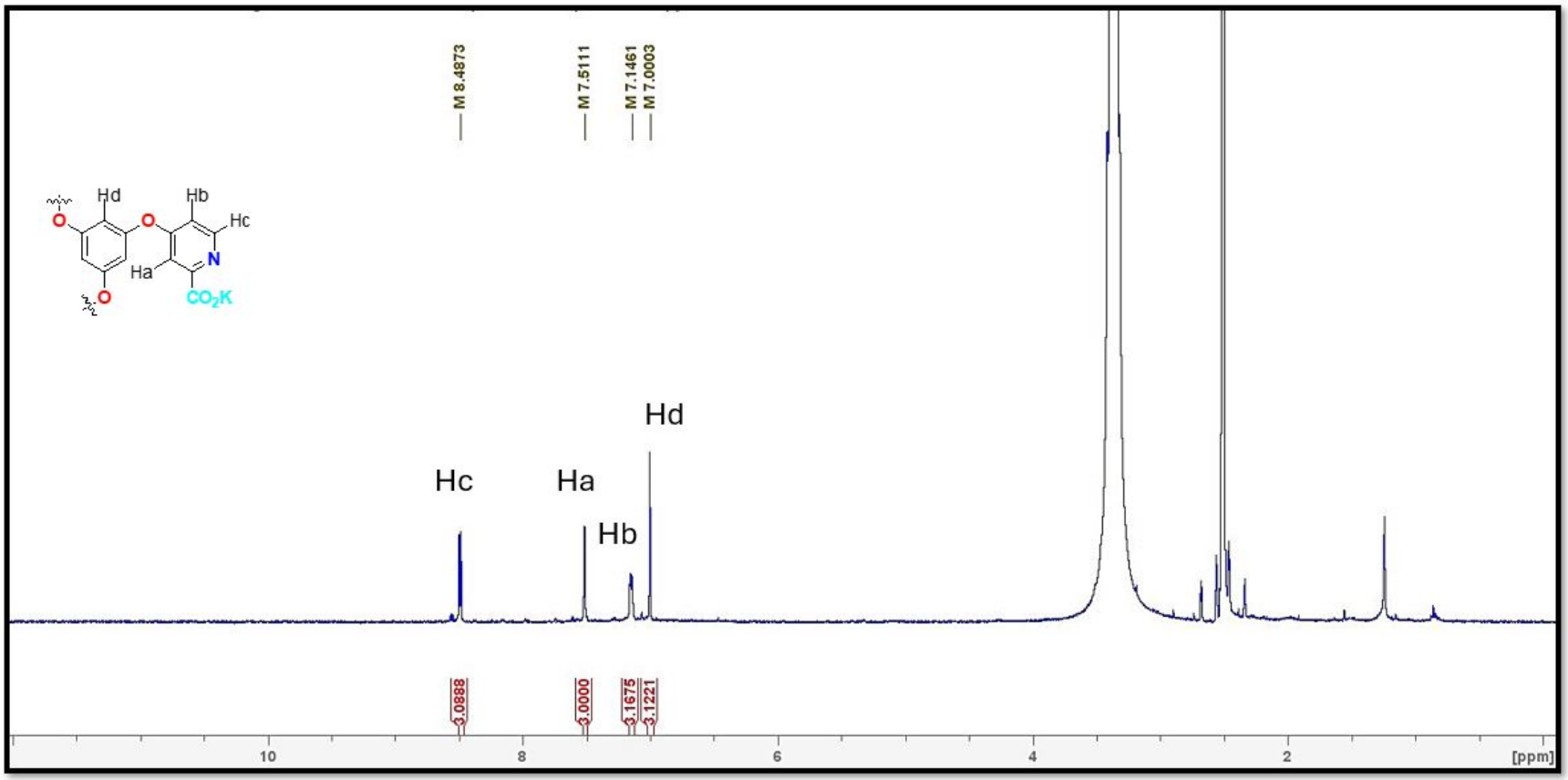

Figure S. 17 ^{1}H NMR (400 MHz) spectrum of compound **141**. Solvent: DMSO-d_6.

r

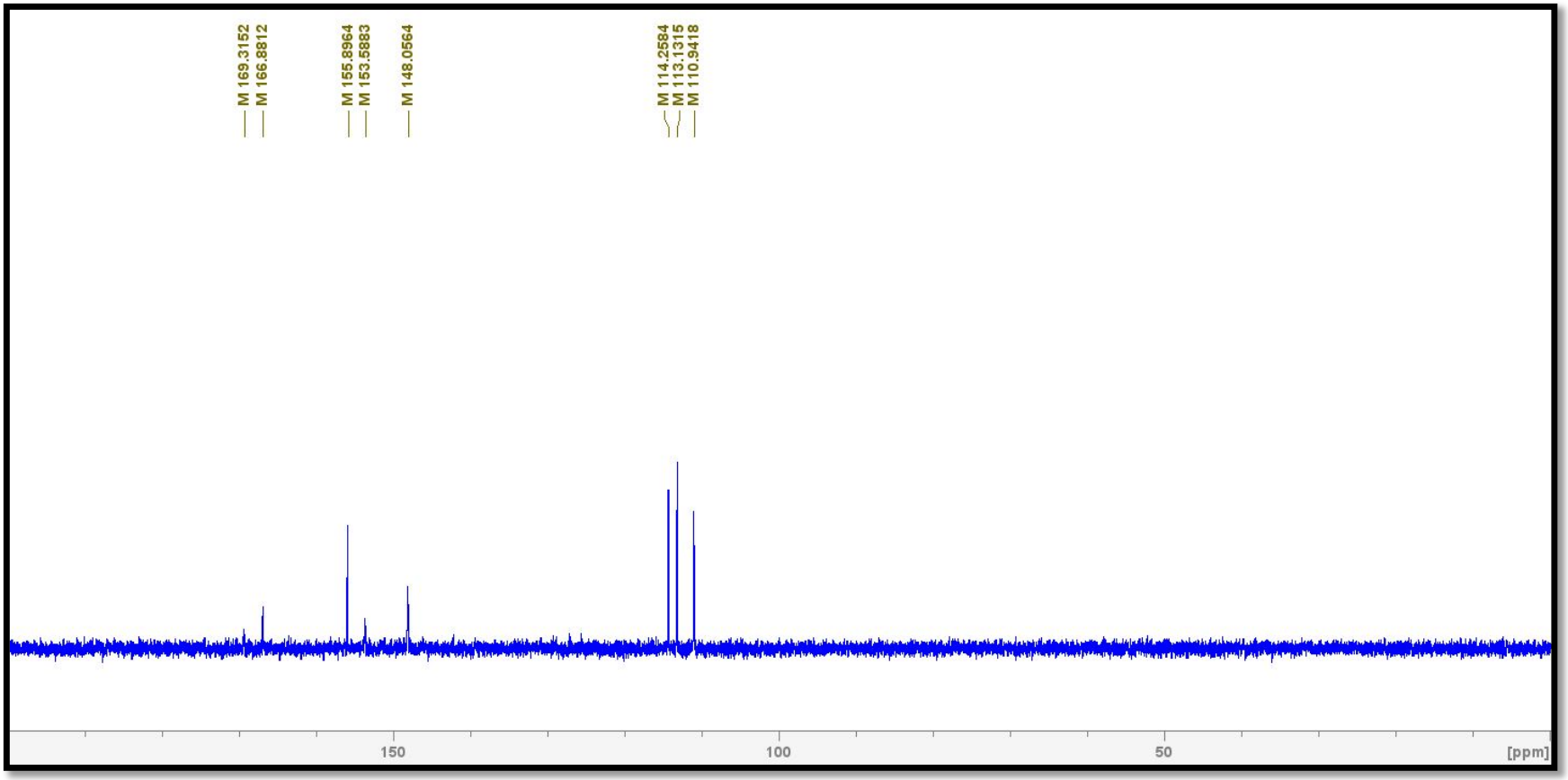

Figure S. 18 ^{13}C NMR (100 MHz) spectrum of compound **141**. Solvent: DMSO-d_6.

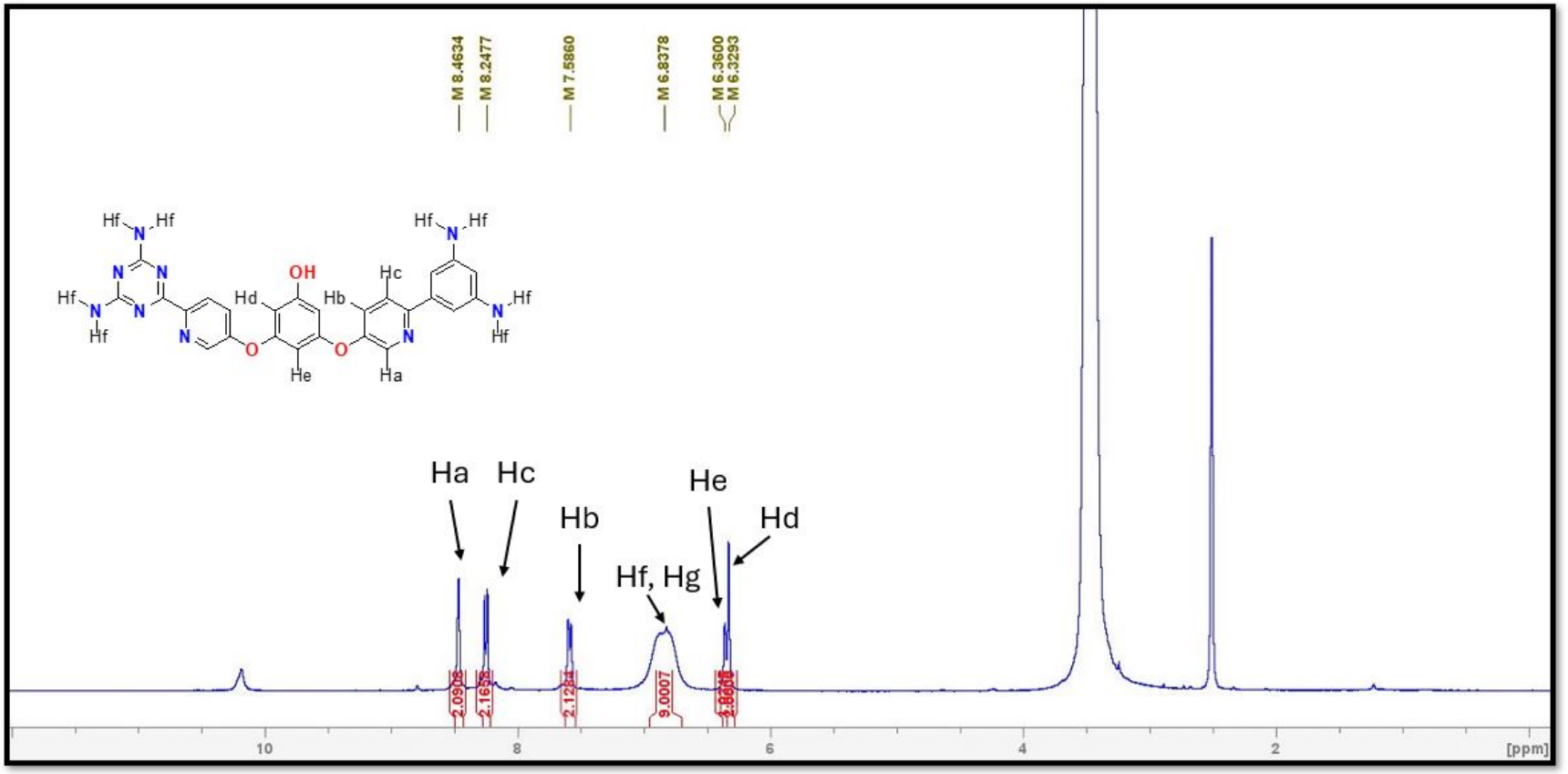

Figure S. 19 ^{1}H NMR (400 MHz) spectrum of compound **145**. Solvent: DMSO-d_6.

t

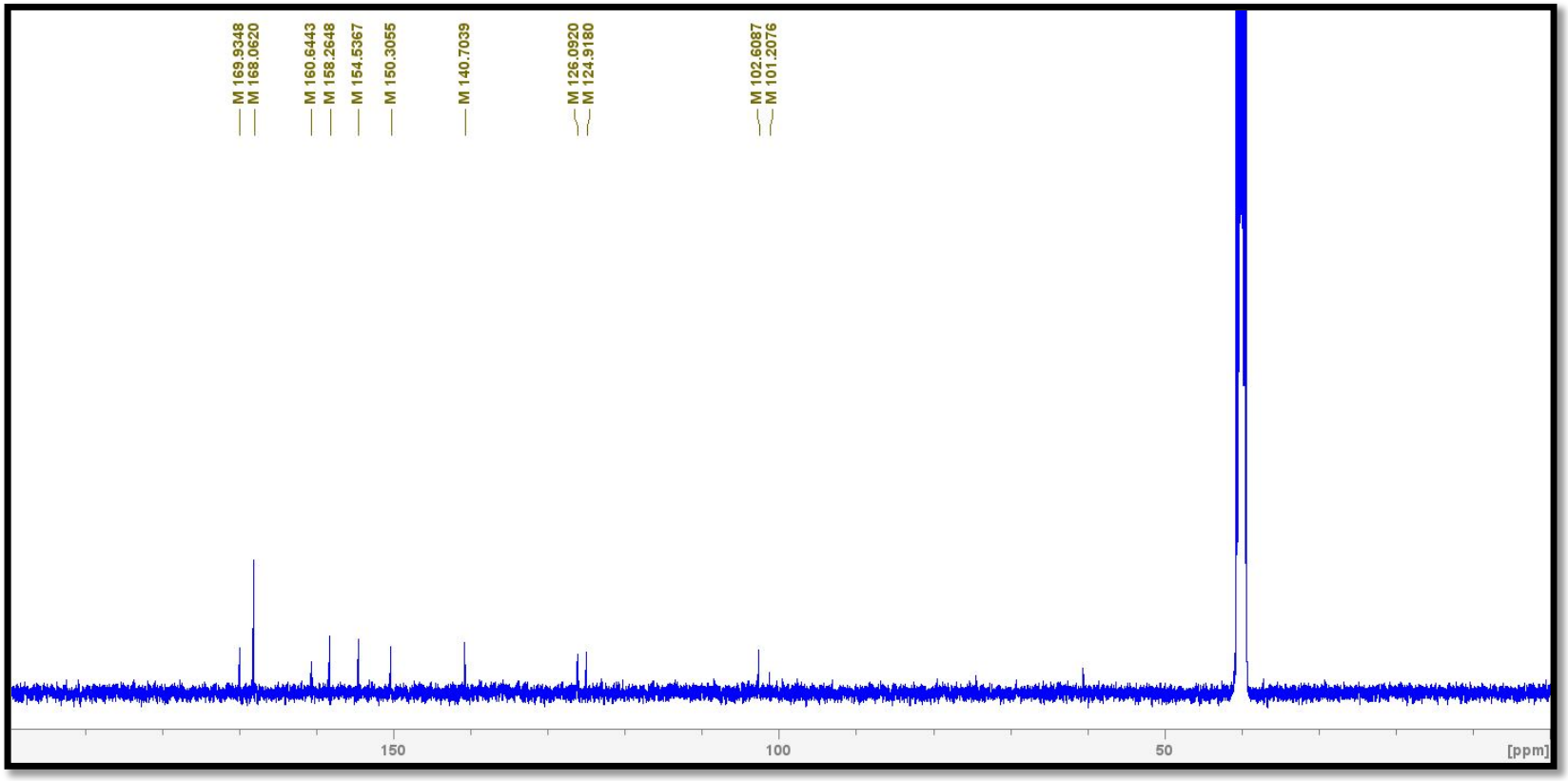

Figure S. 20 ^{13}C NMR (100 MHz) spectrum of compound **145**. Solvent: DMSO-d_6.

u

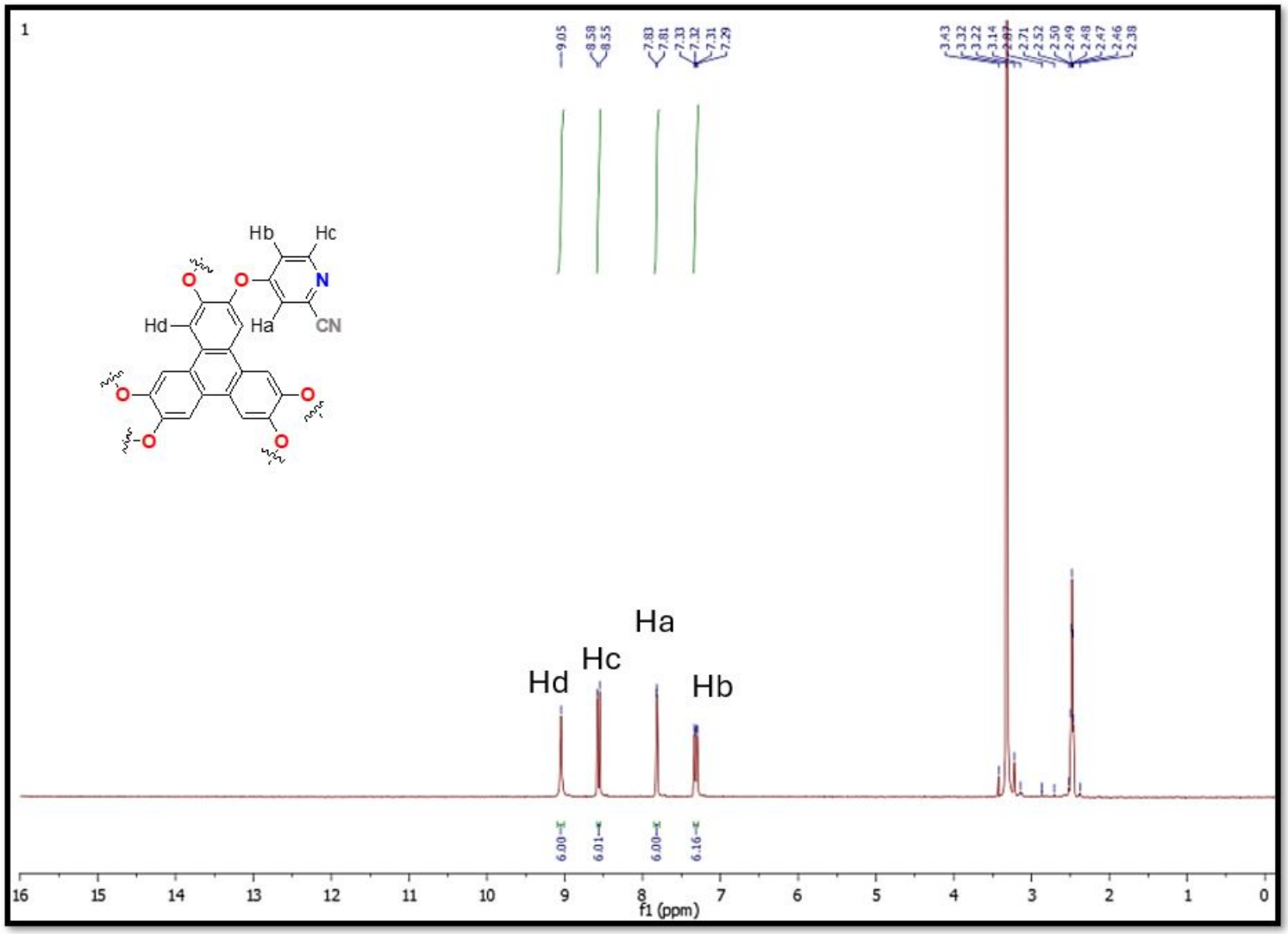

Figure S. 21 ^{1}H NMR (200 MHz) spectrum of compound **150**. Solvent: DMSO-d6.

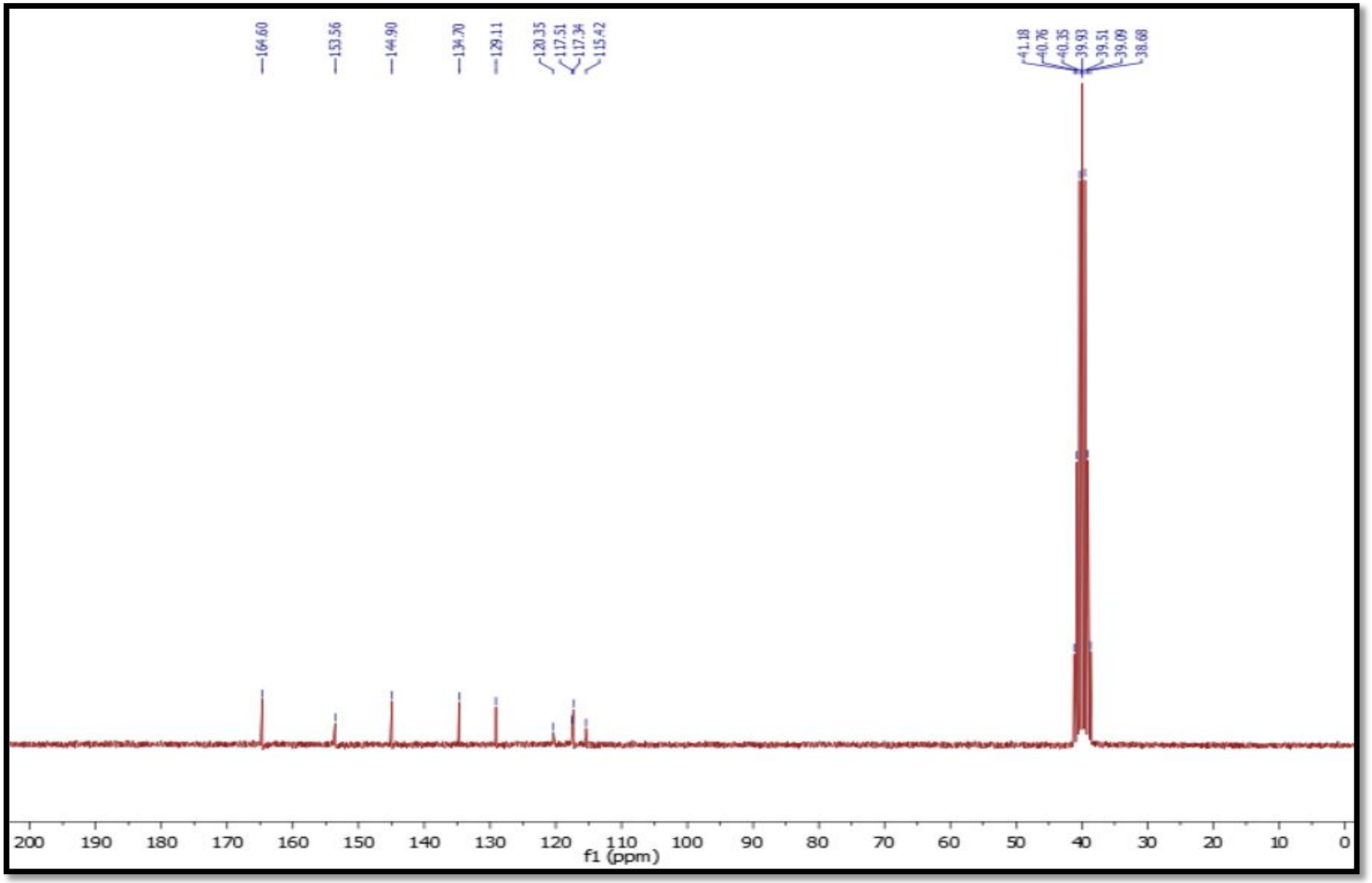

Figure S. 22 ^{13}C NMR (100 MHz) spectrum of compound **150**. Solvent: DMSO-d_6.

w

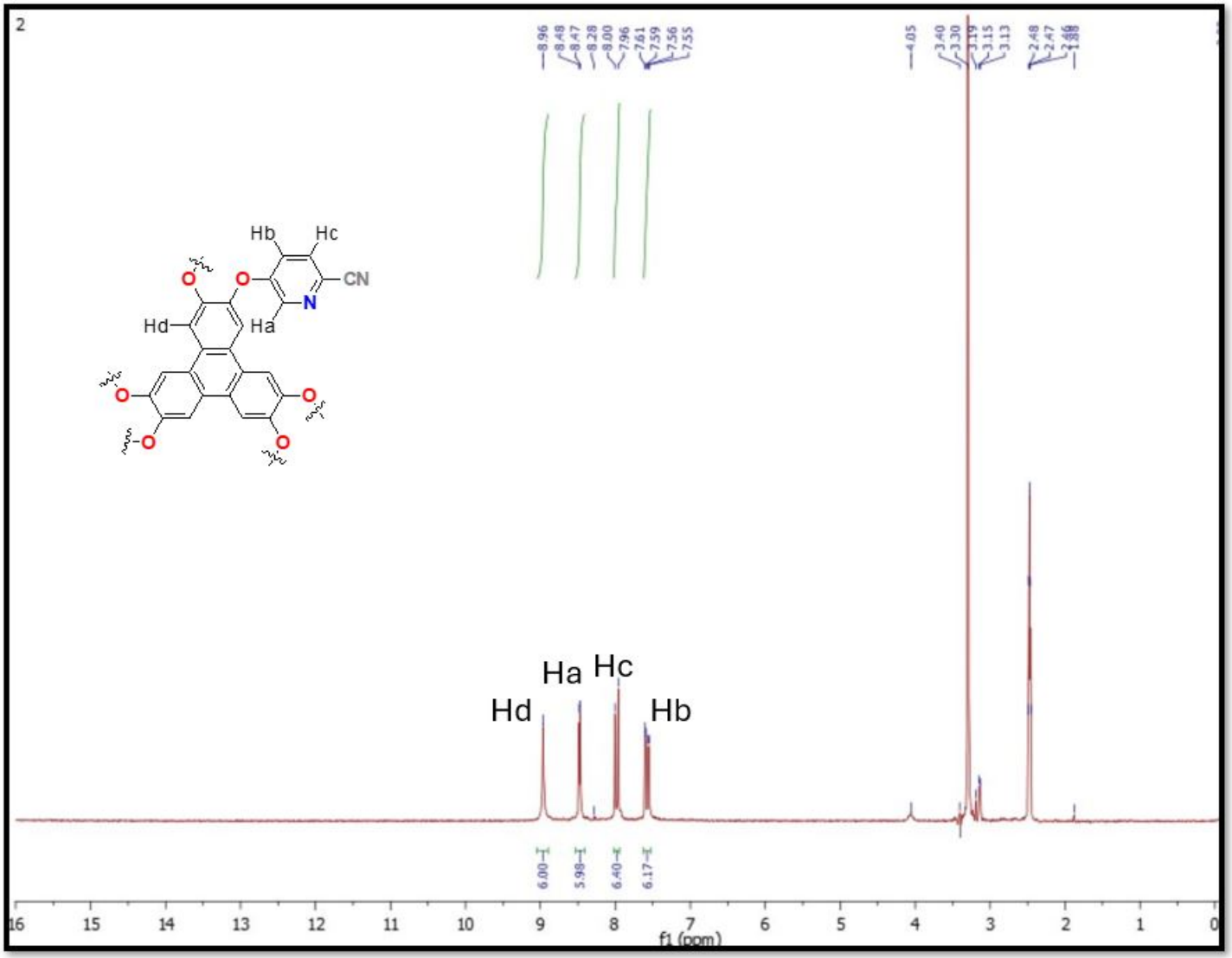

Figure S. 23 ^{1}H NMR (200 MHz) spectrum of compound **151**. Solvent: DMSO-d_6.

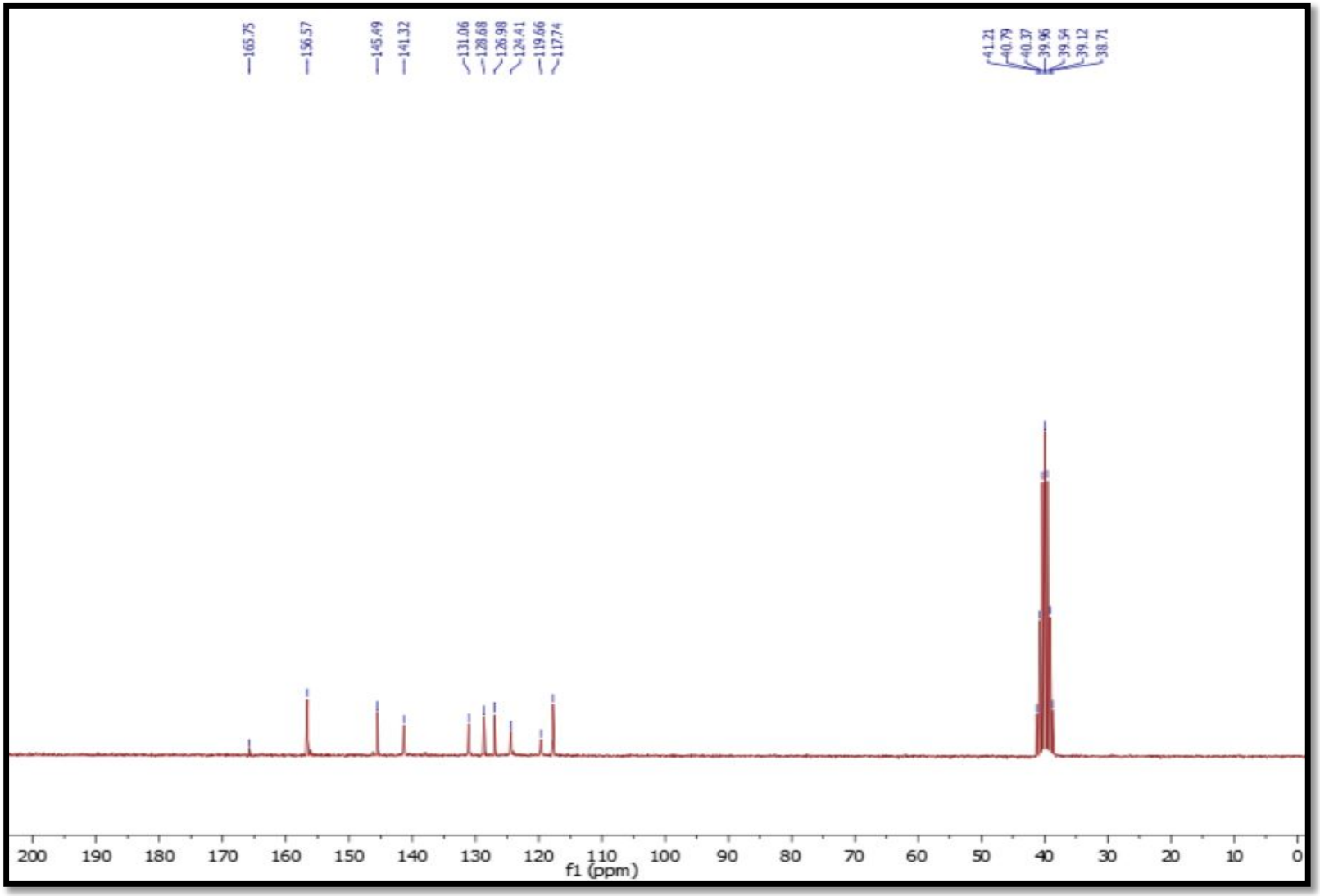

Figure S. 24 ^{13}C NMR (100 MHz) spectrum of compound **151**. Solvent: DMSO-d_6.

y

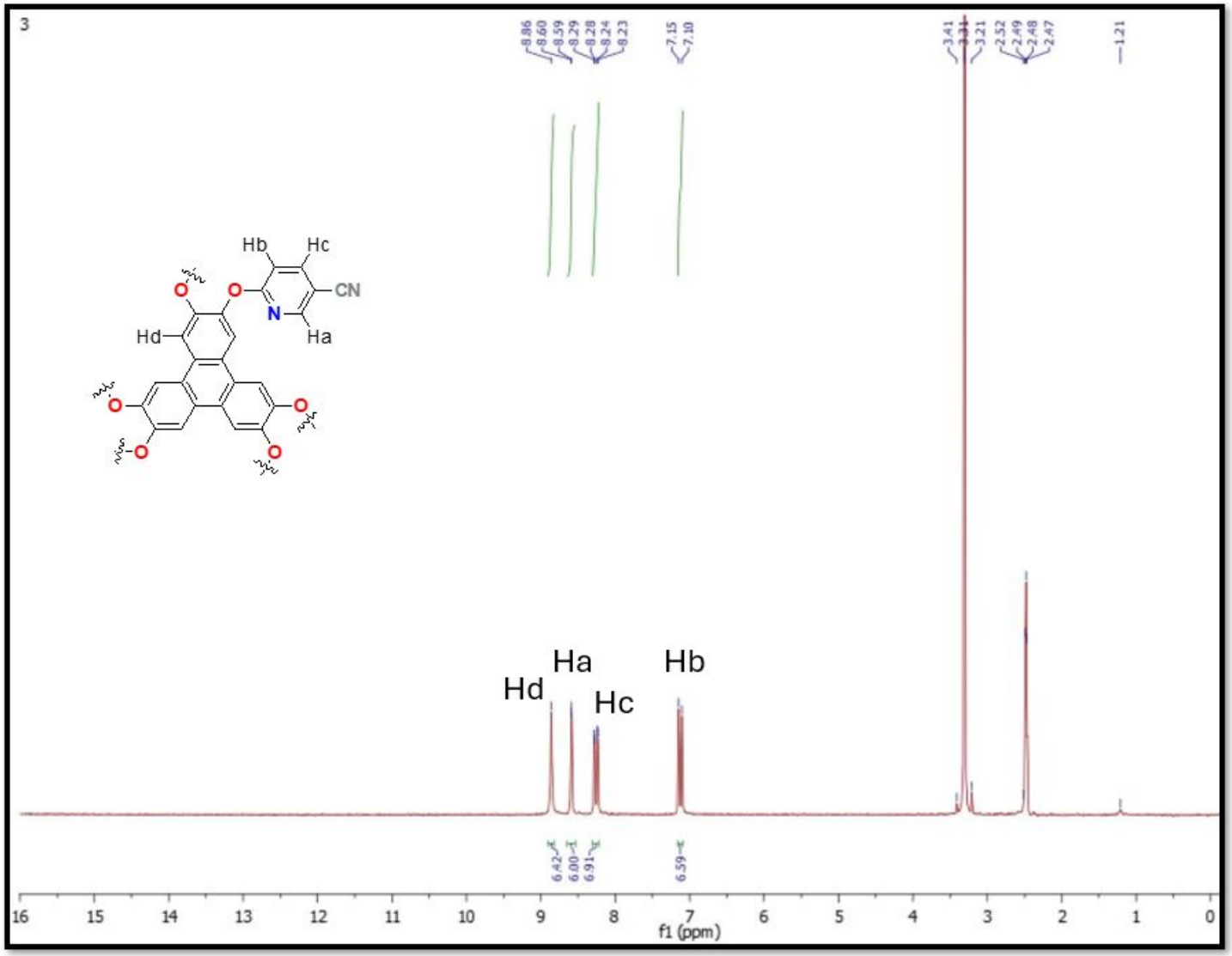

Figure S. 25 ^{1}H NMR (200 MHz) spectrum of compound **152**. Solvent: DMSO-d_6.

z

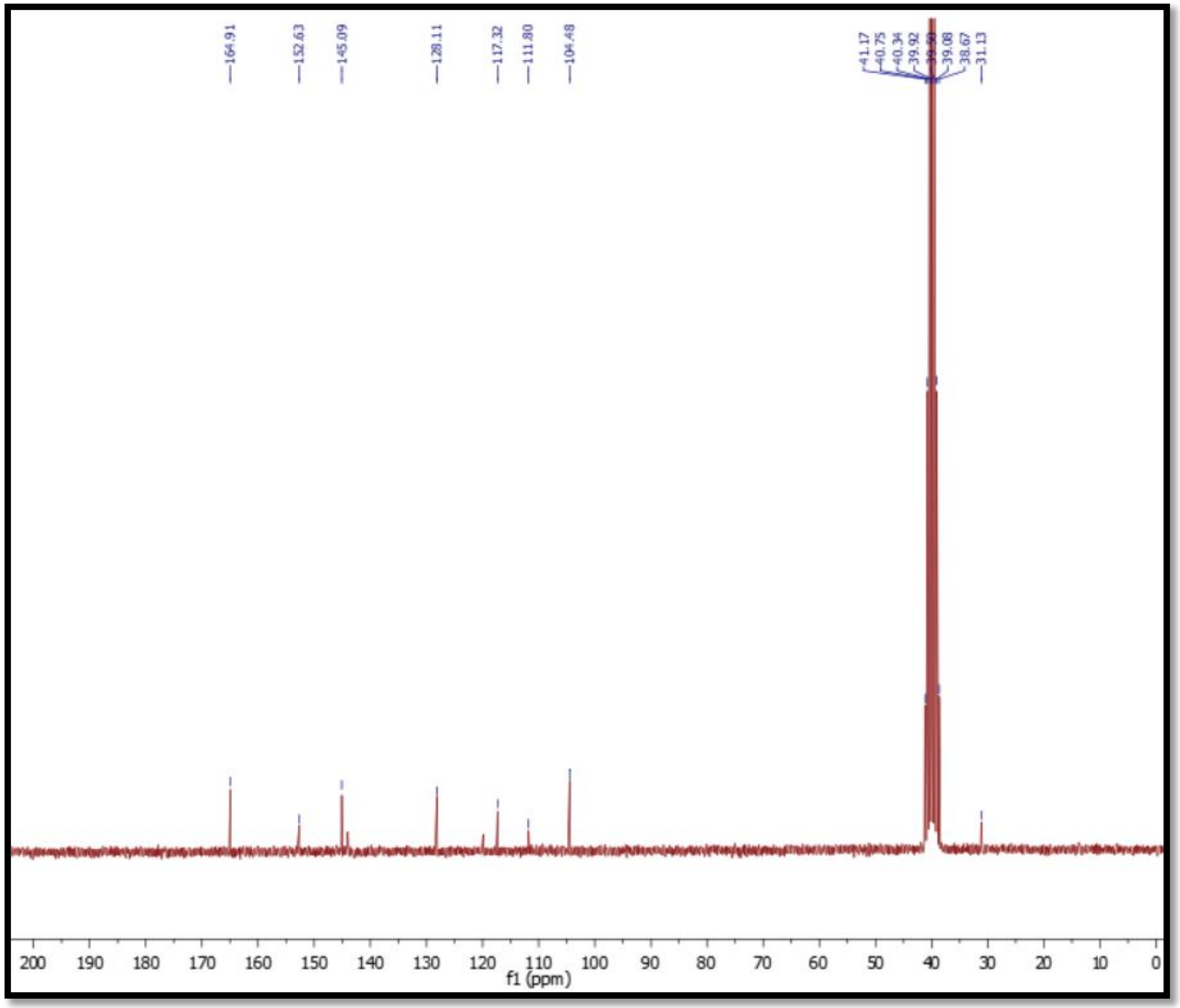

Figure S. 26 ^{13}C NMR (100 MHz) spectrum of compound **152**. Solvent: DMSO-d_6.

aa

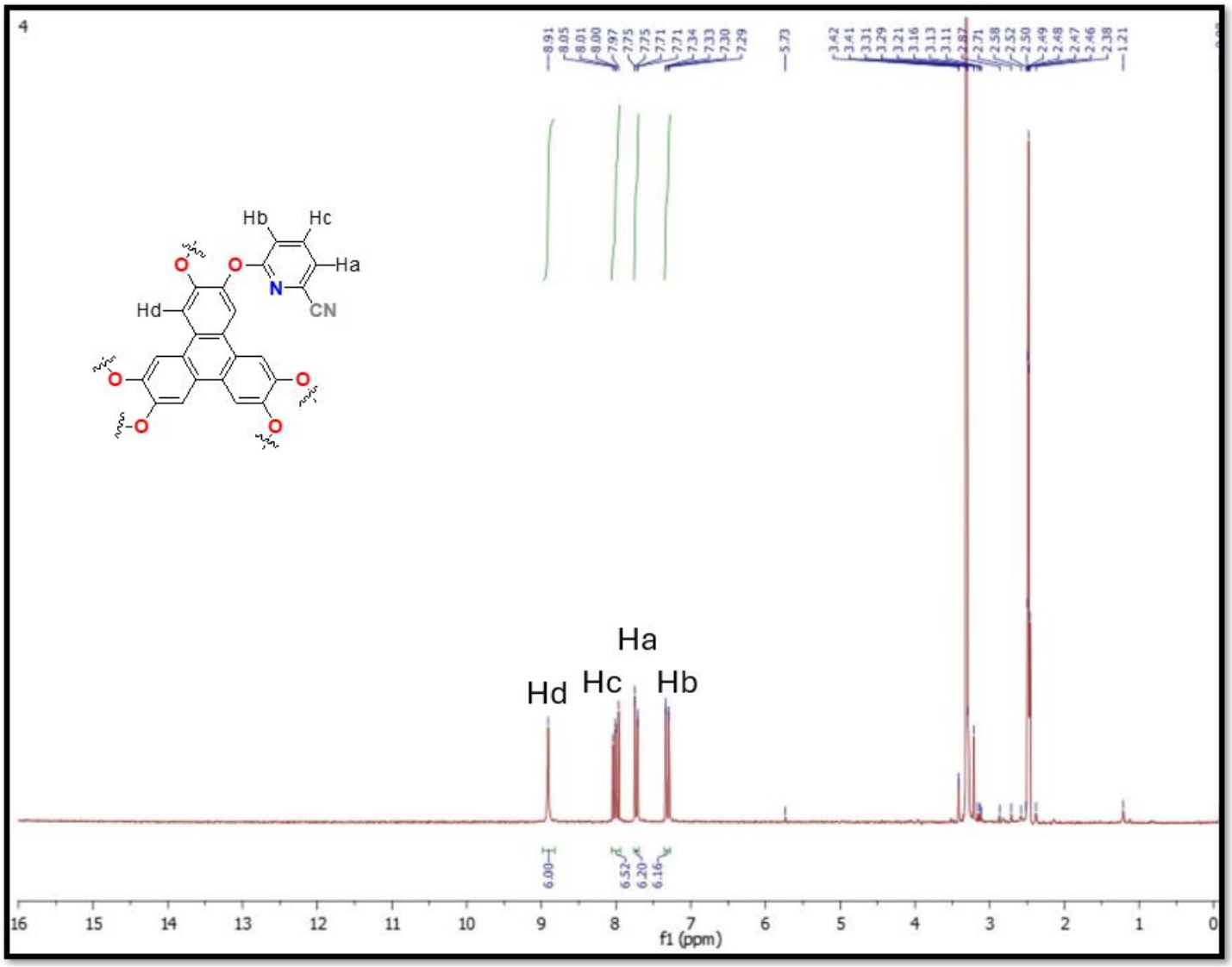

Figure S. 27 ^{1}H NMR (200 MHz) spectrum of compound **153**. Solvent: DMSO-d_6.

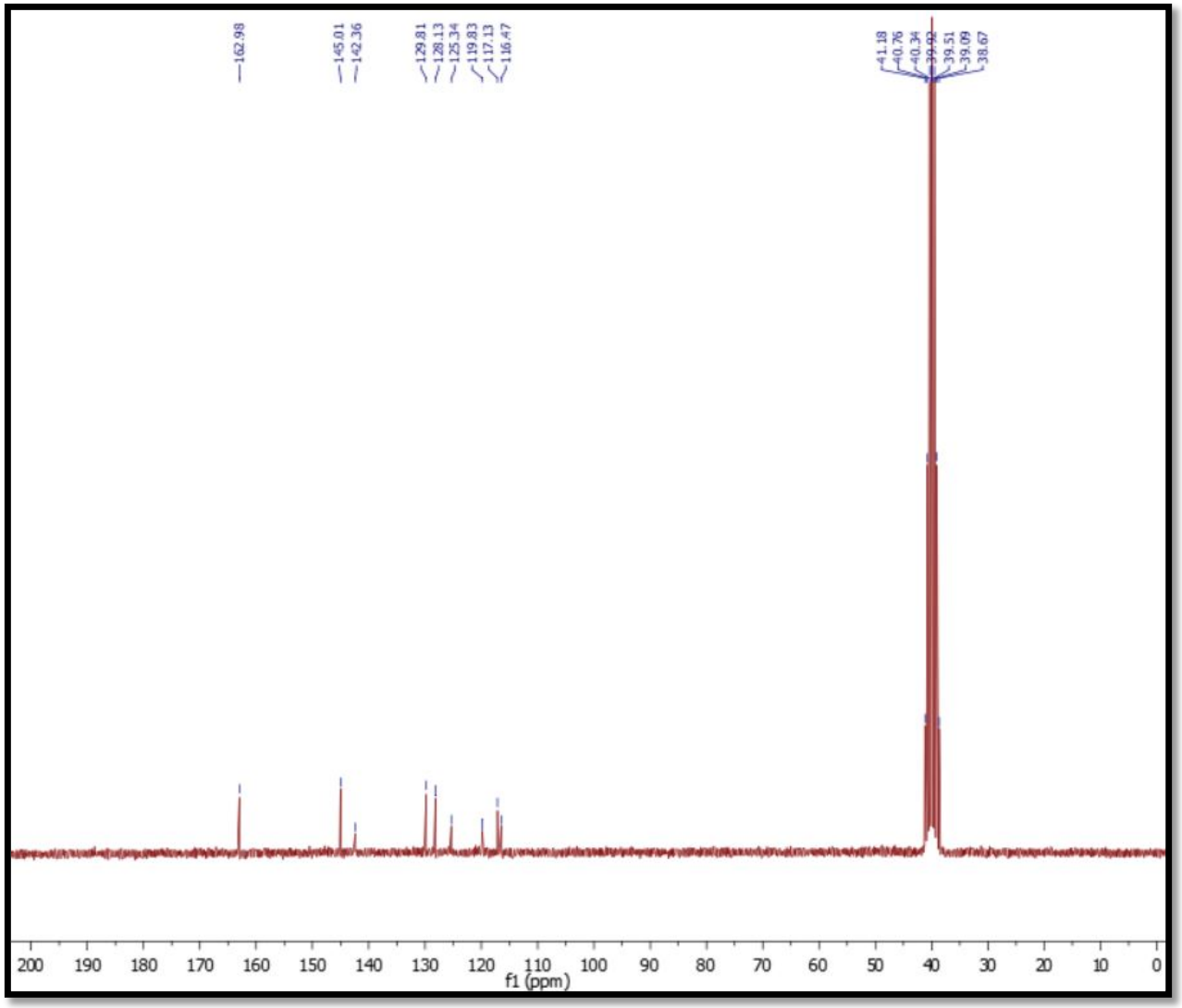

Figure S. 28 ^{13}C NMR (100 MHz) spectrum of compound **153**. Solvent: DMSO-d_6.

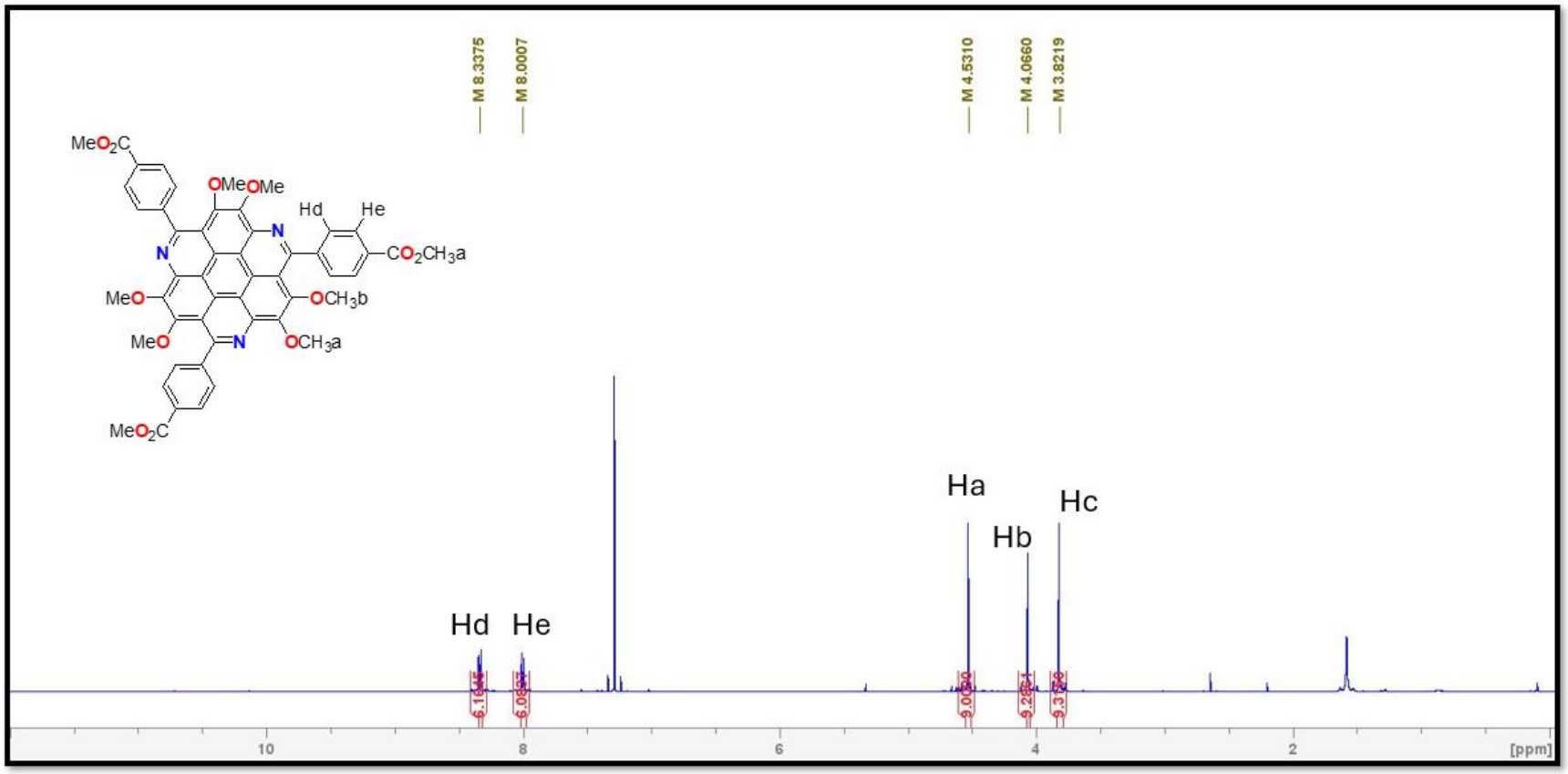

Figure S. 29 ^{1}H NMR (400 MHz) spectrum of compound **164**. Solvent: $CDCl_3$-d_6.

dd

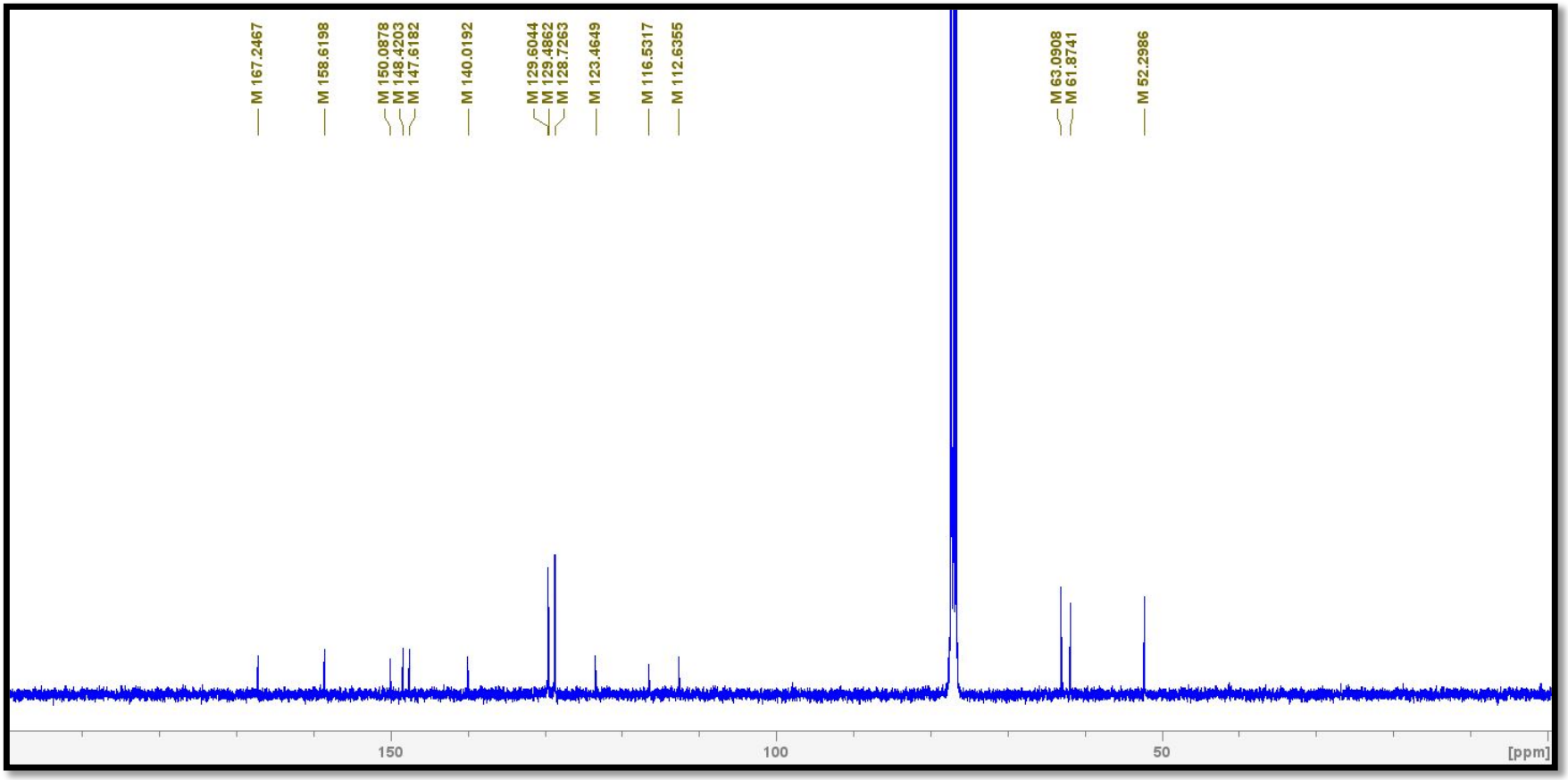

Figure S. 30 ^{13}C NMR (100 MHz) spectrum of compound 164. Solvent: $CDCl_3$-d_6.

ee

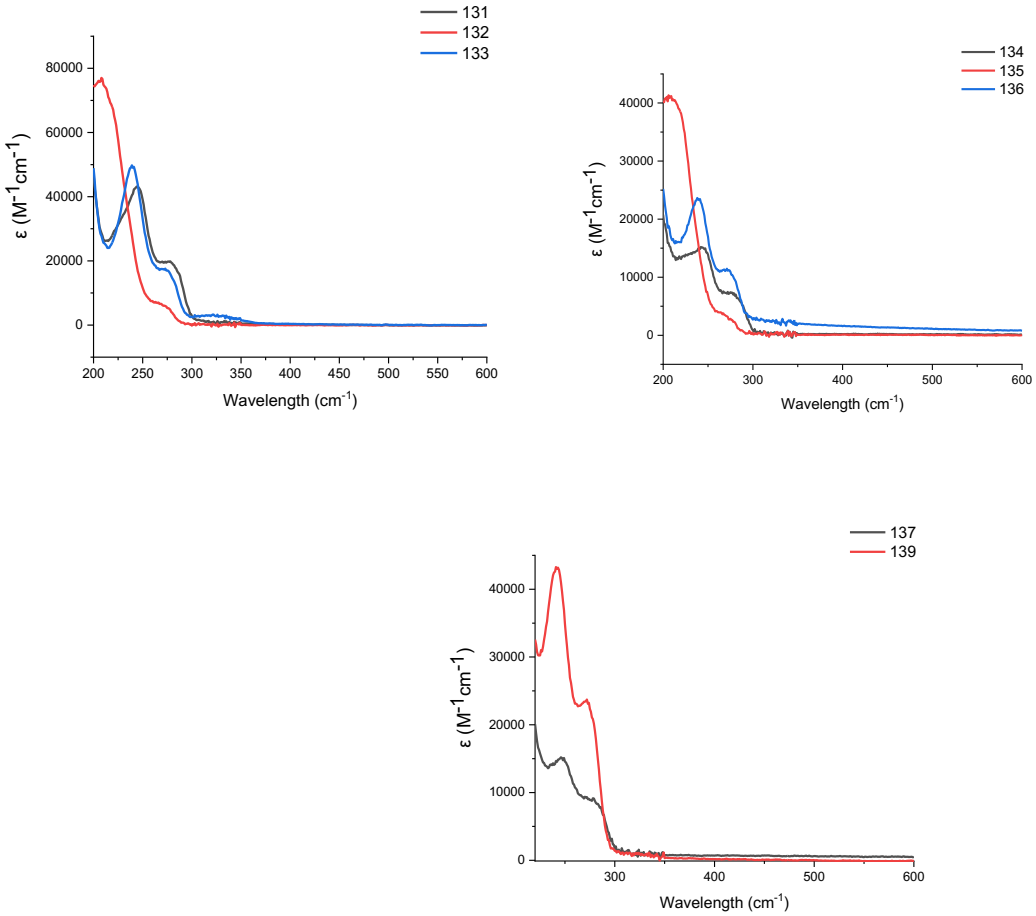

Figure S. 31 Emission spectra of compounds **131**, **132**, **133**, **134**, **135**, **136**, **137**, and **139** in Acetonitrile at room temperature.

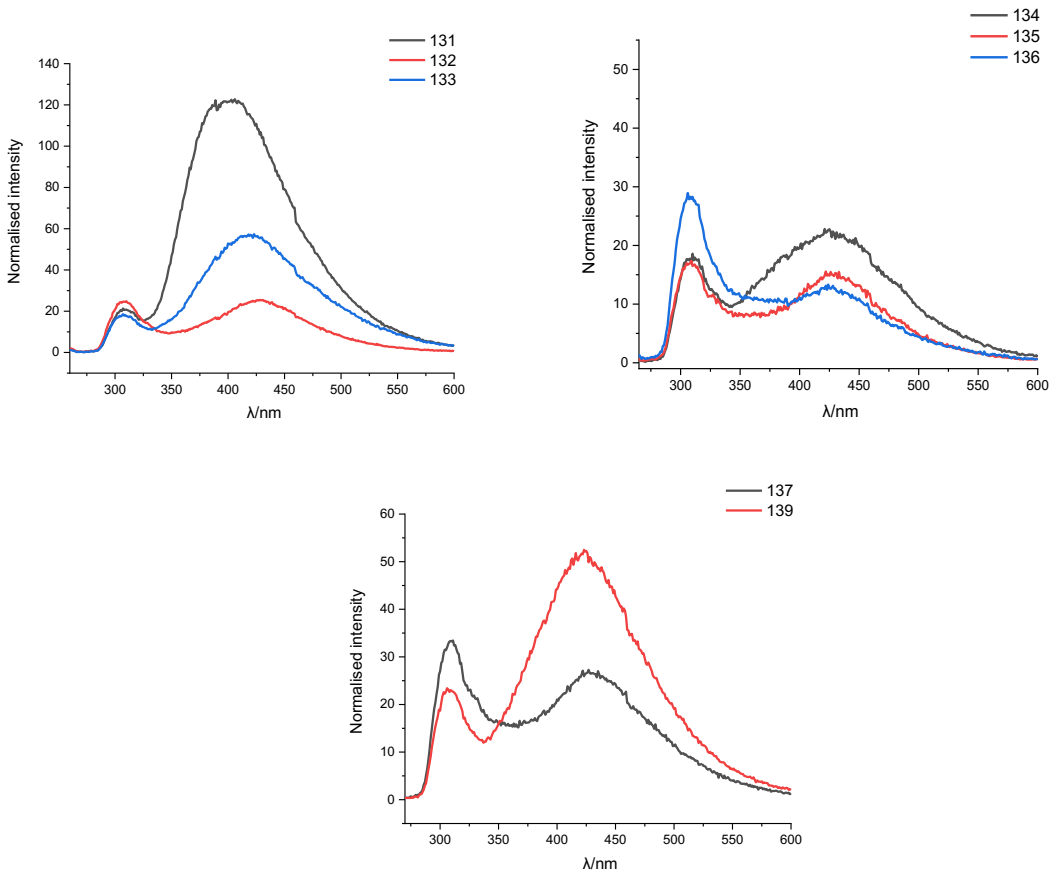

Figure S. 32 Emission spectra of compounds **131**, **132**, **133**, **134**, **135**, **136**, **137**, and **139** in Acetonitrile at room temperature. λ_{ex} = 240 nm.

gg

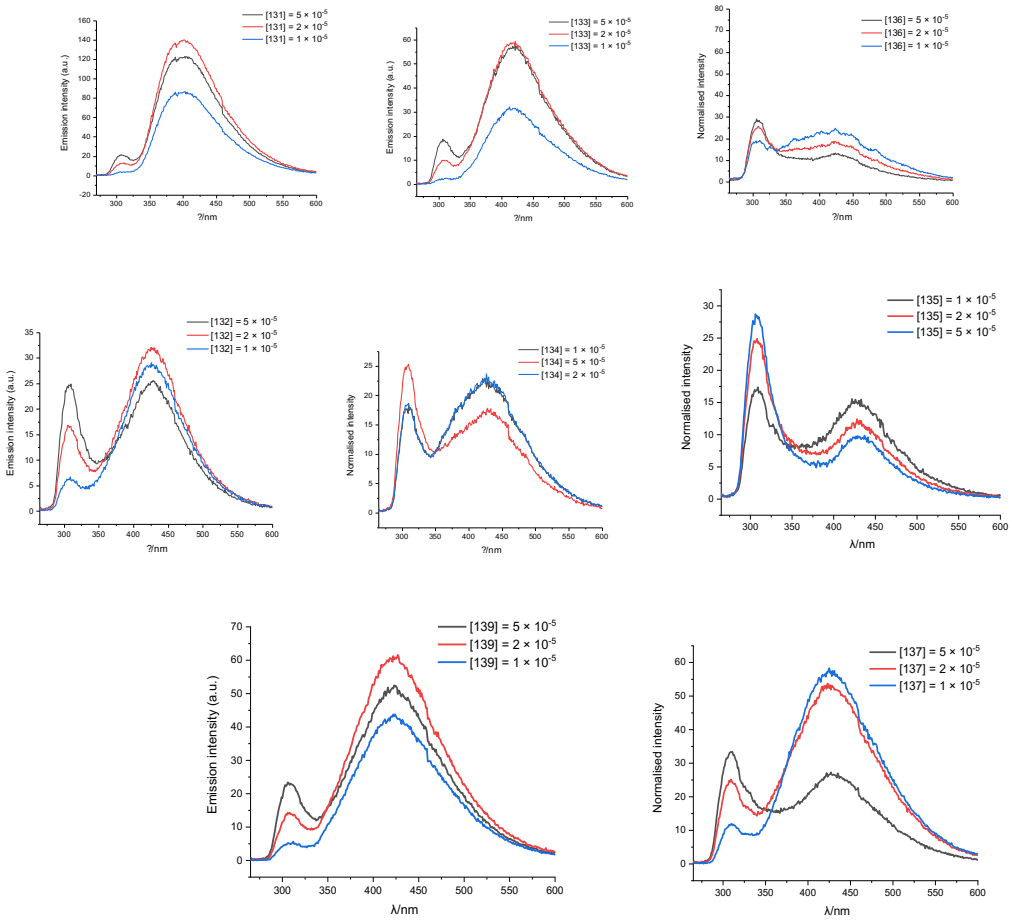

Figure S. 33 Emission spectra of compounds **131**, **132**, **133**, **134**, **135, 136**, **137**, and **139** in acetonitrile at room temperature at different concentrations. λ_{ex} = 240 nm.

hh

References:

(1) Sosnilo, A.; Gorovoy, A. Assessing Global Trends in World Energy: Genesis of the New Energy Transition. In *Lecture Notes in Networks and Systems*; Springer Science and Business Media Deutschland GmbH, **2023**; Vol. 684 LNNS, pp 398–415. https://doi.org/10.1007/978-3-031-32719-3_31.

(2) Dong, K.; Dong, X.; Jiang, Q. How Renewable Energy Consumption Lower Global CO2 Emissions? Evidence from Countries with Different Income Levels. *World Economy* **2020**, *43* (6), 1665–1698. https://doi.org/10.1111/twec.12898.

(3) Rublee, C.; Inglis, R.; Maibach, E. Review of United States Senators' Website Position Statements on Climate Change and Health. *The Journal of Climate Change and Health* **2022**, *6*, 100104. https://doi.org/10.1016/j.joclim.2021.100104.

(4) Karduri, R. K. R. *Impacts of Fossil Fuels on Rural Communities*. http://www.ijert.org.

(5) Clarke, L.; Curtis, M.; Eisenberg, A.; Grubert, E.; Haggerty, J. H.; James, A.; Jensen, N.; Kaufman, N.; Krause, E.; Raimi, D.; Tingley, D.; Weber, J. A Research Agenda for Economic Resilience in Fossil Fuel–Dependent Communities. *Environmental Research: Energy* **2024**, *1* (3), 033004. https://doi.org/10.1088/2753-3751/ad6d70.

(6) King, A. Mitigating Criticality, Part II: Source Diversification. *Critical Materials* **2021**, 161–203. https://doi.org/10.1016/B978-0-12-818789-0.00006-2.

(7) Keesing, J.; Gartner, A.; Westera, M.; Edgar, G.; Myers, J.; Hardman-Mounford, N.; Bailey, M. Impacts and Environmental Risks of Oil Spills on Marine Invertebrates, Algae and Seagrass. In *Oceanography and Marine Biology*; Hawkins, S., Evans, A., Dale, A., Firth, L., Smith, I., Eds.; **2018**; Vol. 56.

(8) *Renewable Energy: Sources and Types*. https://www.greenesa.com/article/renewable-energy-sources-types (accessed **2023**-03-27).

(9) Nwaigwe, K. N.; Mutabilwa, P.; Dintwa, E. An Overview of Solar Power (PV Systems) Integration into Electricity Grids. *Materials Science for Energy Technologies*. KeAi Communications Co. December 1, **2019**, pp 629–633. https://doi.org/10.1016/j.mset.2019.07.002.

(10) Msigwa, G.; Ighalo, J. O.; Yap, P. S. Considerations on Environmental, Economic, and Energy Impacts of Wind Energy Generation: Projections towards Sustainability Initiatives. *Science of the Total Environment*. Elsevier B.V. November 25, 2022. https://doi.org/10.1016/j.scitotenv.**2022**.157755.

(11) *Hydropower Energy is The "Forgotten Giant" of Clean Electricity | World Economic Forum*. https://www.weforum.org/agenda/2021/07/hydropower-energy-low-carbon-clean-electricity-iea (accessed **2022**-11-05).

(12) Ren, Y.; Yao, X.; Liu, D.; Qiao, R.; Zhang, L.; Zhang, K.; Jin, K.; Li, H.; Ran, Y.; Li, F. Optimal Design of Hydro-Wind-PV Multi-Energy Complementary Systems Considering Smooth Power Output. *Sustainable Energy Technologies and Assessments* **2022**, *50*. https://doi.org/10.1016/j.seta.2021.101832.

(13) Chowdhury, M. S.; Rahman, K. S.; Selvanathan, V.; Nuthammachot, N.; Suklueng, M.; Mostafaeipour, A.; Habib, A.; Akhtaruzzaman, M.; Amin, N.; Techato, K. Current Trends and Prospects of Tidal Energy Technology. *Environment, Development and Sustainability*. Springer Science and Business Media B.V. June 1, **2021**, pp 8179–8194. https://doi.org/10.1007/s10668-020-01013-4.

(14) Romanov, D.; Leiss, B. Geothermal Energy at Different Depths for District Heating and Cooling of Existing and Future Building Stock. *Renewable and Sustainable Energy Reviews*. Elsevier Ltd October 1, **2022**, p 112727. https://doi.org/10.1016/j.rser.2022.112727.

(15) Chen, J.; Abazari, R.; Adegoke, K. A.; Maxakato, N. W.; Bello, O. S.; Tahir, M.; Tasleem, S.; Sanati, S.; Kirillov, A. M.; Zhou, Y. Metal–Organic Frameworks and Derived Materials as Photocatalysts for Water Splitting and Carbon Dioxide Reduction. *Coordination Chemistry Reviews*. Elsevier B.V. October 15, **2022**, p 214664. https://doi.org/10.1016/j.ccr.2022.214664.

(16) Fan, W.; Zhang, X.; Kang, Z.; Liu, X.; Sun, D. Isoreticular Chemistry within Metal–Organic Frameworks for Gas Storage and Separation. *Coordination Chemistry Reviews*. Elsevier B.V. September 15, **2021**, p 213968. https://doi.org/10.1016/j.ccr.2021.213968.

(17) Qian, Q.; Asinger, P. A.; Lee, M. J.; Han, G.; Mizrahi Rodriguez, K.; Lin, S.; Benedetti, F. M.; Wu, A. X.; Chi, W. S.; Smith, Z. P. MOF-Based Membranes for Gas Separations. *Chemical Reviews*. American Chemical Society August 26, **2020**, pp 8161–8266. https://doi.org/10.1021/acs.chemrev.0c00119.

(18) Delaporte, N.; Rivard, E.; Natarajan, S. K.; Benard, P.; Trudeau, M. L.; Zaghib, K. Synthesis and Performance of Mof-Based Non-Noble Metal Catalysts for the Oxygen Reduction Reaction in Proton-Exchange Membrane Fuel Cells: A Review. *Nanomaterials*. MDPI AG October 1, **2020**, pp 1–61. https://doi.org/10.3390/nano10101947.

(19) Dou, J.; Zhu, C.; Wang, H.; Han, Y.; Ma, S.; Niu, X.; Li, N.; Shi, C.; Qiu, Z.; Zhou, H.; Bai, Y.; Chen, Q. Synergistic Effects of Eu-MOF on Perovskite Solar Cells with Improved Stability. *Advanced Materials* **2021**, *33* (39), 2102947. https://doi.org/10.1002/adma.202102947.

(20) Tahir, M. A.; Arshad, N.; Akram, M. Recent Advances in Metal Organic Framework (MOF) as Electrode Material for Super Capacitor: A Mini Review. *Journal of Energy Storage*. Elsevier Ltd March 1, **2022**, p 103530. https://doi.org/10.1016/j.est.2021.103530.

(21) Ye, Z.; Jiang, Y.; Li, L.; Wu, F.; Chen, R. Rational Design of MOF-Based Materials for Next-Generation Rechargeable Batteries. *Nano-Micro Letters*. Springer Science and Business Media B.V. December 1, **2021**, pp 1–37. https://doi.org/10.1007/s40820-021-00726-z.

(22) Dou, J.; Zhu, C.; Wang, H.; Han, Y.; Ma, S.; Niu, X.; Li, N.; Shi, C.; Qiu, Z.; Zhou, H.; Bai, Y.; Chen, Q. Synergistic Effects of Eu-MOF on Perovskite Solar Cells with Improved Stability. *Advanced Materials* **2021**, *33* (39), 2102947. https://doi.org/10.1002/adma.202102947.

(23) Carrasco, S. Metal-Organic Frameworks for the Development of Biosensors: A Current Overview. *Biosensors*. MDPI October 16, **2018**, p 92. https://doi.org/10.3390/bios8040092.

(24) Łuczak, J.; Kroczewska, M.; Baluk, M.; Sowik, J.; Mazierski, P.; Zaleska-Medynska, A. Morphology Control through the Synthesis of Metal-Organic Frameworks. *Advances in Colloid and Interface Science*. Elsevier B.V. April 1, **2023**, p 102864. https://doi.org/10.1016/j.cis.2023.102864.

(25) Stavila, V.; Talin, A. A.; Allendorf, M. D. MOF-Based Electronic and Opto-Electronic Devices. *Chemical Society Reviews*. Royal Society of Chemistry August 21, **2014**, pp 5994–6010. https://doi.org/10.1039/c4cs00096j.

(26) Matsumura, M.; Matsuhashi, Y.; Kawakubo, M.; Hyodo, T.; Murata, Y.; Kawahata, M.; Yamaguchi, K.; Yasuike, S. Synthesis, Structural Characterization, and Optical Properties of Benzene-Fused Tetracyclic and Pentacyclic Stiboles. *Molecules* **2021**, *26* (1), 222. https://doi.org/10.3390/MOLECULES26010222.

(27) Zahir Iqbal, M.; Waqas Khan, M.; Shaheen, M.; Sharif, S.; Mohammad Wabaidur, S.; Ansari, M. Z.; Aftab, S. 1,2,4,5-Benzene-Tetra-Carboxylic Acid and 2-Methylimidazole Bi-Linker Intercalated Redox Active Copper Organic Framework for Advanced Battery-Supercapacitor Hybrids. *Journal of Electroanalytical Chemistry* **2023**, *941*, 117505. https://doi.org/10.1016/j.jelechem.2023.117505.

(28) Shoukat, W.; Iqbal, M. Z.; Khizar, A.; Murtaza, I.; Alam, S.; Ali, R.; Wabaidur, S. M.; Faisal, M. M. Investigating the Influence of Copper Benzene-1,2-Dicarboxylate (Cu-BDC) and Benzene-1,3,5-Tricarboxylate Ligands (Cu-BTC) on the Electrochemical Capacity of Hybrid Supercapacitors. *Current Applied Physics* **2024**, *64*, 40–47. https://doi.org/10.1016/j.cap.2024.05.002.

(29) Moloto, W.; Mbule, P.; Nxumalo, E.; Ntsendwana, B. Stabilizing Effects of Zinc(II)-Benzene-1,3,5-Tricarboxylate Metal Organic Frameworks on the Performance of TiO2 Photoanodes for Use in Dye-Sensitized Solar Cells. *J Photochem Photobiol A Chem* **2021**, *407*, 113063. https://doi.org/10.1016/j.jphotochem.2020.113063.

(30) Song, Z.; Cheng, N.; Lushington, A.; Sun, X. Recent Progress on MOF-Derived Nanomaterials as Advanced Electrocatalysts in Fuel Cells. *Catalysts*. MDPI August 2, **2016**, p 116. https://doi.org/10.3390/catal6080116.

(31) Li, Y.; Yang, R. T. Gas Adsorption and Storage in Metal-Organic Framework MOF-177. *Langmuir* **2007**, *23* (26), 12937–12944. https://doi.org/10.1021/la702466d.

(32) Chen, J.; Li, X.; Wang, Y.; Huang, J.; Li, K.; Nie, X.; Jiang, J. Synthesis and Application Performance of Environmentally-Friendly Plasticizer Cardanol Acetate for PVC. *Nongye Gongcheng Xuebao/Transactions of the Chinese Society of Agricultural Engineering* **2015**, *31* (14), 303–308. https://doi.org/10.11975/j.issn.1002-6819.2015.14.042.

(33) Zhang, G.; Zhang, Z.; Zeng, R. Photoinduced FeCl3-Catalyzed Alkyl Aromatics Oxidation toward Degradation of Polystyrene at Room Temperature†. *Chin J Chem* **2021**, *39* (12), 3225–3230. https://doi.org/10.1002/cjoc.202100420.

(34) Ghiaci, M.; Mostajeran, M.; Gil, A. Synthesis and Characterization of Co-Mn Nanoparticles Immobilized on a Modified Bentonite and Its Application for Oxidation of p -Xylene to Terephthalic Acid. *Ind Eng Chem Res* **2012**, *51* (49), 15821–15831. https://doi.org/10.1021/ie3021939.

(35) Malineni, J.; Singh, S.; Tillmann, S.; Keul, H.; Möller, M. Aliphatic Polyethers with Sulfate, Carboxylate, and Hydroxyl Side Groups—Do They Show Anticoagulant Properties? *Macromol Biosci* **2017**, *17* (5). https://doi.org/10.1002/mabi.201600274.

(36) Yu, H.; Wang, Y.; Chen, L.; Wei, C.; Mu, T.; Xue, Z. Biobased Dimethyl Isosorbide as an Efficient Solvent for Alkaline Hydrolysis of Waste Polyethylene Terephthalate to Terephthalic Acid. *Green Chemistry* **2023**, *25* (19), 7807–7816. https://doi.org/10.1039/d3gc02308g.

(37) Trejo-Carbajal, N.; Ambriz-Luna, K. I.; Herrera-González, A. M. Efficient Method and Mechanism of Depolymerization of PET under Conventional Heating and Microwave Radiation Using T-BuNH2/Lewis Acids. *Eur Polym J* **2022**, *175*, 111388. https://doi.org/10.1016/j.eurpolymj.2022.111388.

(38) Cavka, J. H.; Jakobsen, S.; Olsbye, U.; Guillou, N.; Lamberti, C.; Bordiga, S.; Lillerud, K. P. A New Zirconium Inorganic Building Brick Forming Metal Organic Frameworks with Exceptional Stability. *J Am Chem Soc* **2008**, *130* (42), 13850–13851. https://doi.org/10.1021/ja8057953.

(39) Serre, C.; Millange, F.; Thouvenot, C.; Noguès, M.; Marsolier, G.; Louër, D.; Férey, G. Very Large Breathing Effect in the First Nanoporous Chromium(III)-Based Solids: MIL-53 or CrIII(OH)·{O2C-C6H4- CO2}·{HO2C-C6H4 -CO2H}x·H2Oy. *J Am Chem Soc* **2002**, *124* (45), 13519–13526. https://doi.org/10.1021/ja0276974.

(40) Férey, C.; Mellot-Draznieks, C.; Serre, C.; Millange, F.; Dutour, J.; Surblé, S.; Margiolaki, I. Chemistry: A Chromium Terephthalate-Based Solid with Unusually Large Pore Volumes and Surface Area. *Science (1979)* **2005**, *309* (5743), 2040–2042. https://doi.org/10.1126/science.1116275.

(41) Rosi, N. L.; Eckert, J.; Eddaoudi, M.; Vodak, D. T.; Kim, J.; O'Keeffe, M.; Yaghi, O. M. Hydrogen Storage in Microporous Metal-Organic Frameworks. *Science (1979)* **2003**, *300* (5622), 1127–1129. https://doi.org/10.1126/science.1083440.

(42) Short, G. N.; Nguyen, H. T. H.; Scheurle, P. I.; Miller, S. A. Aromatic Polyesters from Biosuccinic Acid. *Polym Chem* **2018**, *9* (30), 4113–4119. https://doi.org/10.1039/c8py00862k.

(43) Chen, W. T.; Tsai, M. J.; Wu, J. Y. A Thermally Stable Undulated Coordination Layer Showing a Sequentially Interweaving 2D → 3D Net as a Turn-On Sensor for Luminescence Detection of Al3+ in Water. *Cryst Growth Des* **2022**, *22* (1), 228–236. https://doi.org/10.1021/acs.cgd.1c00876.

(44) Jadhav, M. M.; Rhyman, L.; Ramasami, P.; Sekar, N. Unfolding ESIPT in Bis-2,5-(2-Benzoxazolyl) Hydroquinone and 2,5-Bis(Benzo[d]Oxazol-2-Yl)-4-Methoxyphenol: A Comprehensive Computational Approach. *J Fluoresc* **2016**, *26* (4), 1295–1307. https://doi.org/10.1007/s10895-016-1816-1.

(45) Kudelin, A. I.; Papathanasiou, K.; Isaeva, V.; Caro, J.; Salmi, T.; Kustov, L. M. Microwave-Assisted Synthesis, Characterization and Modeling of Cpo-27-Mg Metal-Organic Framework for Drug Delivery. *Molecules* **2021**, *26* (2). https://doi.org/10.3390/molecules26020426.

(46) Cadot, S.; Veyre, L.; Luneau, D.; Farrusseng, D.; Alessandra Quadrelli, E. A Water-Based and High Space-Time Yield Synthetic Route to MOF Ni2(Dhtp) and Its Linker 2,5-Dihydroxyterephthalic Acid. *J Mater Chem A Mater* **2014**, *2* (42), 17757–17763. https://doi.org/10.1039/c4ta03066d.

(47) Wu, H.; Utomo, W. P.; Tian, Y.; Mak, C. H.; Chung, H. Y.; Hsu, H. Y.; Shang, J.; Ng, Y. H. Enhanced Visible-Light-Driven Heterogeneous Photocatalytic CO2 Methanation Using a Cu2O@Cu-MOF-74 Thin Film. *ChemPhysMater* **2023**, *2* (2), 126–133. https://doi.org/10.1016/j.chphma.2022.05.003.

(48) Bi, D.; Zhao, T.; Lai, Q.; Zhao, J.; Grigoriev, S. A.; liang, Y. In Situ Preparation of MOF-74 for Compact Zincophilic Surfaces Enhancing the Stability of Aqueous Zinc-Ion Battery Anodes. *J Alloys Compd* **2024**, *1002*, 175448. https://doi.org/10.1016/j.jallcom.2024.175448.

(49) Paridala, K.; Lu, S. M.; Wang, M. M.; Li, C. Tandem One-Pot CO2 Reduction by PMHS and Silyloxycarbonylation of Aryl/Vinyl Halides to Access Carboxylic Acids. *Chemical Communications* **2018**, *54* (82), 11574–11577. https://doi.org/10.1039/c8cc06820h.

(50) Under Photostimulation, A.; Kashimura, T.; Kudo, K.; Mori, S.; Sugita, N. *COBALT CARBONYL CATALYZED POLYCARBONYLATION OF POLYHALOGENATED*; **1986**.

(51) Kolotuchin, S. V.; Thiessen, P. A.; Fenlon, E. E.; Wilson, S. R.; Loweth, C. J.; Zimmerman, S. C. Self-Assembly of 1,3,5-Benzenetricarboxylic (Trimesic) Acid and Its Analogues. *Chemistry - A European Journal* **1999**, *5* (9), 2537–2547. https://doi.org/10.1002/(SICI)1521-3765(19990903)5:9<2537::AID-CHEM2537>3.0.CO;2-3.

(52) Navarrete, A.; Manquian, C.; Vivas, L.; Serafini, D.; Singh, D. P. Controlled Growth-Dependent Electrochemical Behavior of Cobalt and 1,3,5 Benzene-Tricarboxylic Acid-Based MOFs for Efficient Supercapacitor Applications. *Mater Chem Phys* **2024**, *317*, 129142. https://doi.org/10.1016/j.matchemphys.2024.129142.

(53) Zhao, G.; Liu, Q.; Tian, N.; Yu, L.; Dai, W. Highly Efficient Benzothiophene Capture with a Metal-Modified Copper-1,3,5-Benzenetricarboxylic Acid Adsorbent. *Energy and Fuels* **2018**, *32* (6), 6763–6769. https://doi.org/10.1021/acs.energyfuels.8b01223.

(54) Duan, C.; Yu, Y.; Yang, P.; Zhang, X.; Li, F.; Li, L.; Xi, H. Engineering New Defects in MIL-100(Fe) via a Mixed-Ligand Approach to Effect Enhanced Volatile Organic Compound Adsorption Capacity. *Ind Eng Chem Res* **2020**, *59* (2), 774–782. https://doi.org/10.1021/acs.iecr.9b05751.

(55) Boyarskii, V. P.; Zhesko, T. E.; Lanina, S. A. Synthesis of Aromatic Carboxylic Acids by Carbonylation of Aryl Halides in the Presence of Epoxide-Modified Cobalt Carbonyls as Catalysts. *Russian Journal of Applied Chemistry* **2005**, *78* (11), 1844–1848. https://doi.org/10.1007/s11167-005-0619-y.

(56) *Synthesis Method of 4, 4' -Diphenyl Ether Dicarboxylic Acid*; 2019.

(57) Li, X. X.; Wei, Z. Q.; Yue, S. T.; Wang, N.; Mo, H. H.; Liu, Y. L. A New Lanthanide Coordination Polymer with 4,4′-Oxybis (Benzoic Acid) Ligand: Hydrothermal Synthesis, Crystal Structure and Photoluminescence. *J Chem Crystallogr* **2011**, *41* (5), 757–761. https://doi.org/10.1007/s10870-010-9969-2.

(58) Ma, D.; Li, X.; Huo, R. A High-Efficiency White Light-Emitting Lanthanide-Organic Framework Assembled from 4,4′-Oxybis(Benzoic Acid), 1,10-Phenanthroline and Oxalate. *J Mater Chem C Mater* **2014**, *2* (43), 9073–9076. https://doi.org/10.1039/c4tc01409j.

(59) Einkauf, J. D.; Chan, B. C.; de Lill, D. T. Reversible Solvent-Induced Transformation of a One-Dimensional Uranyl Coordination Polymer Using 4,4′-Oxybis(Benzoate). *Polyhedron* **2017**, *128* (128), 149–153. https://doi.org/10.1016/j.poly.2017.03.004.

(60) Park, H. J.; Oh, J.; Kim, J.; Kim, J. Two-Step Gas Adsorption Induced by the Transmetallation in a Two-Dimensional Metal-Organic Framework. *Chemical Communications* **2020**, *56* (67), 9727–9730. https://doi.org/10.1039/d0cc03007d.

(61) Maaskant, E.; Vogel, W.; Dingemans, T. J.; Benes, N. E. The Use of a Star-Shaped Trifunctional Acyl Chloride for the Preparation of Polyamide Thin Film Composite Membranes. *J Memb Sci* **2018**, *567*, 321–328. https://doi.org/10.1016/j.memsci.2018.09.032.

(62) Phang, W. J.; Lee, W. R.; Yoo, K.; Kim, B.; Hong, C. S. Selective CO2 Adsorption and Proton Conductivity in the Two-Dimensional Zn(Ii) Framework with Protruded Water Molecules and Flexible Ether Linkers. *Dalton Transactions* **2013**, *42* (22), 7850–7853. https://doi.org/10.1039/c3dt50896j.

(63) Zhang, J.; Huo, L.; Wang, X.; Fang, K.; Fan, L.; Hu, T. Structural Diversity, Magnetic Properties, and Luminescent Sensing of the Flexible Tripodal Ligand of 1,3,5-Tris(4-Carbonylphenyloxy)Benzene Based Mn(II)/Cd(II) Coordination Polymers. *Cryst Growth Des* **2017**, *17* (11), 5887–5897. https://doi.org/10.1021/acs.cgd.7b00986.

(64) Chen, L. T.; Zhang, X. L.; Hu, G. F.; Seik Weng, N.; Zhao, J. S.; Liu, C. Y. The Construct of a Novel Threefold Interpenetrating Uranium-Organic Framework as a Sensor for Detecting Ru3+. *Chemical Papers* **2023**, *77* (3), 1721–1727. https://doi.org/10.1007/s11696-022-02587-1.

(65) Park, H. J.; Oh, J.; Kim, J.; Kim, J. Two-Step Gas Adsorption Induced by the Transmetallation in a Two-Dimensional Metal-Organic Framework. *Chemical Communications* **2020**, *56* (67), 9727–9730. https://doi.org/10.1039/d0cc03007d.

(66) Chaudhari, A. K.; Nagarkar, S. S.; Joarder, B.; Ghosh, S. K. A Continuous π-Stacked Starfish Array of Two-Dimensional Luminescent MOF for Detection of Nitro Explosives. *Cryst Growth Des* **2013**, *13* (8), 3716–3721. https://doi.org/10.1021/cg400749m.

(67) Chen, L. T.; Zhang, X. L.; Hu, G. F.; Seik Weng, N.; Zhao, J. S.; Liu, C. Y. The Construct of a Novel Threefold Interpenetrating Uranium-Organic Framework as a Sensor for Detecting Ru3+. *Chemical Papers* **2023**, *77* (3), 1721–1727. https://doi.org/10.1007/s11696-022-02587-1.

(68) Li, R.; Li, S.; Zhang, Q.; Li, Y.; Wang, H. Layer-by-Layer Assembled Triphenylene-Based MOFs Films for Electrochromic Electrode. *Inorg Chem Commun* **2021**, *123*, 108354. https://doi.org/10.1016/j.inoche.2020.108354.

(69) Sonet, D.; Bibal, B. Triphenylene: A Versatile Molecular Receptor. *Tetrahedron Lett* **2019**, *60* (12), 872–884. https://doi.org/10.1016/j.tetlet.2019.02.033.

(70) Contreras-Pereda, N.; Pané, S.; Puigmartí-Luis, J.; Ruiz-Molina, D. Conductive Properties of Triphenylene MOFs and COFs. *Coordination Chemistry Reviews*. Elsevier B.V. June 1, **2022**, p 214459. https://doi.org/10.1016/j.ccr.2022.214459.

(71) Vasanthakannan, V. M.; Pavithrakumar, M.; Senthilkumar, K. First Principle Studies on Triphenylene-Hexathiol-Based Metal-Organic Framework for Hydrogen Storage Application. *J Energy Storage* **2024**, *78*, 110077. https://doi.org/10.1016/j.est.2023.110077.

(72) Reinhard, D.; Zhang, W. S.; Vaynzof, Y.; Rominger, F.; Schröder, R. R.; Mastalerz, M. Triptycene-Based Porous Metal-Assisted Salphen Organic Frameworks: Influence of the Metal Ions on Formation and Gas Sorption. *Chemistry of Materials* **2018**, *30* (8), 2781–2790. https://doi.org/10.1021/acs.chemmater.8b00614.

(73) Sonet, D.; Bibal, B. Triphenylene: A Versatile Molecular Receptor. *Tetrahedron Lett* **2019**, *60* (12), 872–884. https://doi.org/10.1016/j.tetlet.2019.02.033.

(74) Bajpai, M.; Yadav, N.; Kumar, S.; Srivastava, R.; Dhar, R. Incorporation of Liquid Crystalline Triphenylene Derivative in Bulk Heterojunction Solar Cell with Molybdenum Oxide as Buffer Layer for Improved Efficiency. *Liq Cryst* **2016**, *43* (7), 928–936. https://doi.org/10.1080/02678292.2016.1149239.

(75) Sakamoto, R.; Kambe, T.; Tsukada, S.; Takada, K.; Hoshiko, K.; Kitagawa, Y.; Okumura, M.; Nishihara, H. π-Conjugated Trinuclear Group-9 Metalladithiolenes with a Triphenylene Backbone. *Inorg Chem* **2013**, *52* (13), 7411–7416. https://doi.org/10.1021/ic400110z.

(76) Dong, R.; Pfeffermann, M.; Liang, H.; Zheng, Z.; Zhu, X.; Zhang, J.; Feng, X. Large-Area, Free-Standing, Two-Dimensional Supramolecular Polymer Single-Layer Sheets for Highly Efficient Electrocatalytic Hydrogen Evolution. *Angewandte Chemie - International Edition* **2015**, *54* (41), 12058–12063. https://doi.org/10.1002/anie.201506048.

(77) Clough, A. J.; Yoo, J. W.; Mecklenburg, M. H.; Marinescu, S. C. Two-Dimensional Metal-Organic Surfaces for Efficient Hydrogen Evolution from Water. *J Am Chem Soc* **2015**, *137* (1), 118–121. https://doi.org/10.1021/ja5116937.

(78) Shakirov, I. I.; Boronoev, M. P.; Sinikova, N. A.; Karakhanov, E. A.; Maksimov, A. L. Selective Hydrogenation of Phenylacetylene on a Pd-Containing Catalyst Based on a Polymer Layered Substrate. *Russian Journal of Applied Chemistry* **2020**, *93* (2), 258–267. https://doi.org/10.1134/S1070427220020159.

(79) Morimoto, K.; Dohi, T.; Kita, Y. Oxidative Trimerization of Catechol to Hexahydroxytriphenylene. *European J Org Chem* **2013**, No. 9, 1659–1662. https://doi.org/10.1002/ejoc.201201515.

(80) Nam, K. W.; Park, S. S.; dos Reis, R.; Dravid, V. P.; Kim, H.; Mirkin, C. A.; Stoddart, J. F. Conductive 2D Metal-Organic Framework for High-Performance Cathodes in Aqueous Rechargeable Zinc Batteries. *Nat Commun* **2019**, *10* (1), 1–10. https://doi.org/10.1038/s41467-019-12857-4.

(81) Wu, H.; Zhang, W.; Kandambeth, S.; Shekhah, O.; Eddaoudi, M.; Alshareef, H. N. Conductive Metal–Organic Frameworks Selectively Grown on Laser-Scribed Graphene for Electrochemical Microsupercapacitors. *Adv Energy Mater* **2019**, *9* (21), 1900482. https://doi.org/10.1002/aenm.201900482.

(82) Miner, E. M.; Wang, L.; Dincă, M. Modular O2 Electroreduction Activity in Triphenylene-Based Metal-Organic Frameworks. *Chem Sci* **2018**, *9* (29), 6286–6291. https://doi.org/10.1039/c8sc02049c.

(83) De Lourdes Gonzalez-Juarez, M.; Morales, C.; Flege, J. I.; Flores, E.; Martin-Gonzalez, M.; Nandhakumar, I.; Bradshaw, D. Tunable Carrier Type of a Semiconducting 2D Metal-Organic Framework Cu3(HHTP)2. *ACS Appl Mater Interfaces* **2022**, *14* (10), 12404–12411. https://doi.org/10.1021/acsami.2c00089.

(84) Gong, Y. N.; Wei, X. W.; He, L. H.; Wen, Y. Q.; Ren, Y. W.; Xie, Y. R.; Zhong, D. C. Two Bilayer Metal-Organic Frameworks with Rare Trinuclear Heterometal Clusters and Tunable Photoluminescence. *Dalton Transactions* **2017**, *46* (23), 7403–7407. https://doi.org/10.1039/c7dt01242j.

(85) Gong, Y. N.; Jiang, L.; Lu, T. B. A Highly Stable Dynamic Fluorescent Metal-Organic Framework for Selective Sensing of Nitroaromatic Explosives. *Chemical Communications* **2013**, *49* (94), 11113–11115. https://doi.org/10.1039/c3cc46530f.

(86) Gong, Y. N.; Lu, T. B. Fast Detection of Oxygen by the Naked Eye Using a Stable Metal–Organic Framework Containing Methyl Viologen Cations. *Chemical Communications* **2013**, *49* (70), 7711–7713. https://doi.org/10.1039/c3cc42268b.

(87) Mocci, P.; Cardia, R.; Cappellini, G. Si-Atoms Substitutions Effects on the Electronic and Optical Properties of Coronene and Ovalene. *New J Phys* **2018**, *20* (11), 113008. https://doi.org/10.1088/1367-2630/aae7f0.

(88) Ejuh, G. W.; Tchangnwa Nya, F.; Ottou Abe, M. T.; Jean-Baptiste, F. F.; Ndjaka, J. M. B. Electronic Structure, Physico-Chemical, Linear and Non Linear Optical Properties Analysis of Coronene, 6B-, 6N-, 3B3N- Substituted C24H12 Using RHF, B3LYP and WB97XD Methods. *Opt Quantum Electron* **2017**, *49* (11), 1–14. https://doi.org/10.1007/s11082-017-1221-2.

(89) Prodhan, S.; Mazumdar, S.; Ramasesha, S. Correlated Electronic Properties of a Graphene Nanoflake: Coronene. *Molecules* **2019**, *24* (4), 730. https://doi.org/10.3390/molecules24040730.

(90) Ejuh, G. W.; Tchangnwa Nya, F.; Djongyang, N.; Ndjaka, J. M. B. Theoretical Study on the Electronic, Optoelectronic, Linear and Non Linear Optical Properties and UV–Vis Spectrum of Coronene and Coronene Substituted with Chlorine. *SN Appl Sci* **2020**, *2* (7), 1–11. https://doi.org/10.1007/s42452-020-3028-1.

(91) Chakravarty, C.; Mandal, B.; Sarkar, P. Coronene-Based Metal-Organic Framework: A Theoretical Exploration. *Physical Chemistry Chemical Physics* **2016**, *18* (36), 25277–25283. https://doi.org/10.1039/c6cp05495a.

(92) Dong, R.; Pfeffermann, M.; Skidin, D.; Wang, F.; Fu, Y.; Narita, A.; Tommasini, M.; Moresco, F.; Cuniberti, G.; Berger, R.; Müllen, K.; Feng, X. Persulfurated Coronene: A New Generation of "Sulflower." *J Am Chem Soc* **2017**, *139* (6), 2168–2171. https://doi.org/10.1021/jacs.6b12630.

(93) Wang, J.; Wang, J.; Song, X.; Qi, S.; Zhao, M. Multifunctional Electrocatalytic Activity of Coronene-Based Two-Dimensional Metal-Organic Frameworks: TM-PTC. *Appl Surf Sci* **2020**, *511*, 145393. https://doi.org/10.1016/j.apsusc.2020.145393.

(94) Chen, Z.; Cui, Y.; Ye, C.; Liu, L.; Wu, X.; Sun, Y.; Xu, W.; Zhu, D. Highly Conductive Cobalt Perthiolated Coronene Complex for Efficient Hydrogen Evolution. *Chemistry – A European Journal* **2020**, *26* (56), 12868–12873. https://doi.org/10.1002/chem.202001792.

(95) Yin, J. C.; Lian, X.; Li, Z. G.; Cheng, M.; Liu, M.; Xu, J.; Li, W.; Xu, Y.; Li, N.; Bu, X. H. Triazacoronene-Based 2D Conductive Metal–Organic Framework for High-Capacity Lithium Storage. *Adv Funct Mater* **2024**, *34* (41), 2403656. https://doi.org/10.1002/adfm.202403656.

(96) Mahesha, P.; Shetty, N. S. Pharmacological Perspectives of 2-Alkoxy-3-Cyanopyridine Scaffolds: An Up-to-Date Review. *ChemistrySelect*. John Wiley and Sons Inc May 27, **2024**. https://doi.org/10.1002/slct.202401770.

(97) Clarke, R. E.; Ford, P. C. Cyanopyridine Complexes of Pentaammineruthenium(II)1. *Inorg Chem* **1970**, *9* (3), 495–499. https://doi.org/10.1021/ic50085a013.

(98) Zhao, H.; Bodach, A.; Heine, M.; Krysiak, Y.; Glinnemann, J.; Alig, E.; Fink, L.; Schmidt, M. U. 4-Cyanopyridine, a Versatile Mono- and Bidentate Ligand. Crystal Structures of Related Coordination Polymers Determined by X-Ray Powder Diffraction. *CrystEngComm* **2017**, *19* (16), 2216–2228. https://doi.org/10.1039/c7ce00425g.

(99) Heine, M.; Fink, L.; Schmidt, M. U. 3-Cyanopyridine as a Bridging and Terminal Ligand in Coordination Polymers. *CrystEngComm* **2018**, *20* (46), 7556–7566. https://doi.org/10.1039/c8ce01568f.

(100) Heine, M.; Fink, L.; Schmidt, M. U. 3-Cyanopyridine as a Bridging and Terminal Ligand in Coordination Polymers. *CrystEngComm* **2018**, *20* (46), 7556–7566. https://doi.org/10.1039/c8ce01568f.

(101) Lin, P.; Henderson, R. A.; Harrington, R. W.; Clegg, W.; Wu, C. De; Wu, X. T. New 1- and 2-Dimensional Polymeric Structures of Cyanopyridine Complexes of Ag1 and Cu1. *Inorg Chem* **2004**, *43* (1), 181–188. https://doi.org/10.1021/ic030254w.

(102) Sun, D.; Wei, Z. H.; Yang, C. F.; Wang, D. F.; Zhang, N.; Huang, R. Bin; Zheng, L. S. PH-Dependent Ag(i) Coordination Architectures Constructed from 4-Cyanopyridine and Phthalic Acid: From Discrete Structure to 2D Sheet. *CrystEngComm* **2011**, *13* (5), 1591–1601. https://doi.org/10.1039/c0ce00539h.

(103) Jochim, A.; Jess, I.; Näther, C. Structural Diversity in Cd(NCS)2-3-Cyanopyridine Coordination Compounds: Synthesis, Crystal Structures and Thermal Properties. *Zeitschrift fur Naturforschung - Section B Journal of Chemical Sciences* **2020**, *75* (1), 163–172. https://doi.org/10.1515/znb-2019-0175.

(104) Wellm, C.; Neumann, T.; Gallo, G.; Dziubyna, A. M.; Rams, M.; Dinnebier, R. E.; Näther, C. Structural Variety in Mn(NCS)2 4-Cyanopyridine Coordination Compounds: Synthesis, Structures, Isomerism, and Magnetic Properties. *Cryst Growth Des* **2020**, *20* (5), 3374–3385. https://doi.org/10.1021/acs.cgd.0c00157.

(105) Jochim, A.; Jess, I.; Näther, C. Zn(NCS) 2 -3-Cyanopyridine Coordination Compounds: Synthesis, Crystal Structures, and Thermal Properties. *Z Anorg Allg Chem* **2019**, *645* (3), 212–218. https://doi.org/10.1002/zaac.201800428.

(106) Chand, T.; Savitri, B. Vitamin <scp> B $_3$ </Scp> , Niacin. In *Industrial Biotechnology of Vitamins, Biopigments, and Antioxidants*; Wiley, **2016**; pp 41–65. https://doi.org/10.1002/9783527681754.ch3.

(107) Xue, J.; Hua, X.; Yang, L.; Li, W.; Xu, Y.; Zhao, G.; Zhang, G.; Liu, L.; Liu, K.; Chen, J.; Wu, J. Cobalt(II) and Strontium(II) Complexes of Three Isomers, Nicotinamide, Isonicotinamide and Picolinamide. *J Mol Struct* **2014**, *1059* (1), 108–117. https://doi.org/10.1016/j.molstruc.2013.11.001.

(108) Lumb, I.; Sran, B. S.; Sood, H.; Arora, D. S.; Hundal, G. Coordination Chemistry of Cu(II), Co(II), Zn(II) and Ag(I) Complexes of Isomeric Pyridine 2- and 4-Carboxamides and Their Biological Activity Evaluation. *Polyhedron* **2017**, *127*, 153–166. https://doi.org/10.1016/j.poly.2017.01.063.

(109) Kwiatek, D.; Kubicki, M.; Toliński, T.; Ferenc, W.; Lis, S.; Hnatejko, Z. A Series of New Pyridine Carboxamide Complexes and Self-Assemblies with Tb(III), Eu(III), Zn(II), Cu(II) Ions and Their Luminescent and Magnetic Properties. *J Coord Chem* **2019**, *72* (4), 727–748. https://doi.org/10.1080/00958972.2019.1574344.

(110) Hamdy, L. B. *Developing New Hydrogen Bonded Alkaline Earth Metal-Organic Complexes*; **2015**.

(111) Mirzaei, M.; Eshtiagh-Hosseini, H.; Alfi, N.; Aghabozorg, H.; Attar Gharamaleki, J.; Beyramabadi, S. A.; Khavasi, H. R.; Salimi, A. R.; Shokrollahi, A.; Aghaei, R.; Karami, E. Syntheses, Crystal, Molecular Structures, and Solution Studies of Cu(II), Co(II), and Zn(II) Coordination Compounds Containing Pyridine-2,6-Dicarboxylic Acid and 1,4-Pyrazine-2,3-Dicarboxylic Acid: Comparative Computational Studies of Cu(II) and Zn(II) Complexes. *Struct Chem* **2011**, *22* (6), 1365–1377. https://doi.org/10.1007/s11224-011-9829-5.

(112) Wei, R.; Liu, Z.; Wei, W.; Liang, C.; Han, G.; Zhan, L. Synthesis, Crystal Structure and Characterization of Two Cobalt (II) Complexes Based on Pyridine Carboxylic Acid Ligands. *Z Anorg Allg Chem* **2022**, *648* (9), e202000418. https://doi.org/10.1002/zaac.202000418.

(113) Sun, Y. G.; Sun, D.; Yu, W.; Zhu, M. C.; Ding, F.; Liu, Y. N.; Gao, E. J.; Wang, S. J.; Xiong, G.; Dragutan, I.; Dragutan, V. Synthesis, Characterization, Interaction with DNA and Cytotoxicity of Pd(Ii) and Pt(Ii) Complexes Containing Pyridine Carboxylic Acid Ligands. *Dalton Transactions* **2013**, *42* (11), 3957–3967. https://doi.org/10.1039/c2dt32114a.

(114) Beattie, K.; Phadke, G.; Novakovic, J. Lamotrigine. In *Profiles of Drug Substances, Excipients and Related Methodology*; Academic Press Inc., **2012**; Vol. 37, pp 245–285. https://doi.org/10.1016/B978-0-12-397220-0.00006-4.

(115) Rajak, S.; Mohan, M.; Tremblay, A. A.; Maris, T.; Leal Do Santos, S.; Venancio, E. C.; Ferreira Santos, S.; Duong, A. Programmed Molecular Construction: Driving the Self-Assembly by Coordination and Hydrogen Bonds Using 6-(Pyridin-2-Yl)-1,3,5-Triazine-2,4-Diamine with M(NO3)2 Salts. *ACS Omega* **2019**, *4* (2), 2708–2718. https://doi.org/10.1021/acsomega.8b03517.

(116) Chu, J.; Chen, W.; Su, G.; Song, Y. F. Four New Copper(II) Complexes with Di-Substituted s-Triazine-Based Ligands. *Inorganica Chim Acta* **2011**, *376* (1), 350–357. https://doi.org/10.1016/j.ica.2011.06.041.

(117) Manna, B.; Mukherjee, S.; Desai, A. V.; Sharma, S.; Krishna, R.; Ghosh, S. K. A π-Electron Deficient Diaminotriazine Functionalized MOF for Selective Sorption of Benzene over Cyclohexane. *Chemical Communications* **2015**, *51* (84), 15386–15389. https://doi.org/10.1039/c5cc06128h.

(118) Sifnaiou, E.; Garypidou, A.; Ypsilantis, K.; Plakatouras, J. C.; Garoufis, A. Synthesis, Characterization and Photophysical Properties of Mixed Ligand Cyclometalated Platinum(II) Complexes Containing 2-Phenylpyridine and Pyridine Carboxylic Acids. *Polyhedron* **2023**, *231*, 116252. https://doi.org/10.1016/j.poly.2022.116252.

(119) Patra, R.; Titi, H. M.; Goldberg, I. Coordination Polymers of Flexible Polycarboxylic Acids with Metal Ions. V. Polymeric Frameworks of 5-(3,5-Dicarboxybenzyloxy)-3-Pyridine Carboxylic Acid with Cd(Ii), Cu(Ii), Co(Ii), Mn(Ii) and Ni(Ii) Ions; Synthesis, Structure, and Magnetic Properties. *CrystEngComm* **2013**, *15* (15), 2863–2872. https://doi.org/10.1039/c3ce27023h.

(120) Song, J. F.; Jia, Y. Y.; Zhou, R. S.; Li, S. Z.; Qiu, X. M.; Liu, J. Six New Coordination Compounds Based on Rigid 5-(3-Carboxy-Phenyl)-Pyridine-2-Carboxylic Acid: Synthesis, Structural Variations and Properties. *RSC Adv* **2017**, *7* (12), 7217–7226. https://doi.org/10.1039/c6ra26966d.

(121) Zhang, X. Y.; Wen, H. F.; Yang, Q. F.; Zhou, R. S.; Song, J. F. Eight New Coordination Polymers Containing Rigid 4-(4-Carboxy-Phenyl)-Pyridine-2-Carboxylic Acid: Synthesis, Structural Diversity, Fluorescence and Magnetic Properties. *Inorganica Chim Acta* **2020**, *507*, 119600. https://doi.org/10.1016/j.ica.2020.119600.

(122) Heine, M.; Fink, L.; Schmidt, M. U. 3-Cyanopyridine as a Bridging and Terminal Ligand in Coordination Polymers. *CrystEngComm* **2018**, *20* (46), 7556–7566. https://doi.org/10.1039/c8ce01568f.

(123) Krebs, C.; Foltyn, M.; Jess, I.; Mangelsen, S.; Rams, M.; Näther, C. Synthesis, Crystal Structures, Thermal and Magnetic Properties of Mn(NCS)2 Coordination Compounds with 3-Cyanopyridine. *Inorganica Chim Acta* **2023**, *554*, 121495. https://doi.org/10.1016/j.ica.2023.121495.

(124) Zhao, H.; Bodach, A.; Heine, M.; Krysiak, Y.; Glinnemann, J.; Alig, E.; Fink, L.; Schmidt, M. U. 4-Cyanopyridine, a Versatile Mono- and Bidentate Ligand. Crystal Structures of Related Coordination Polymers Determined by X-Ray Powder Diffraction. *CrystEngComm* **2017**, *19* (16), 2216–2228. https://doi.org/10.1039/c7ce00425g.

(125) Wu, Y.; Wu, T.; Huang, Y. A Review: Biological Activities of Novel Cyanopyridine Derivatives. *Archiv der Pharmazie*. John Wiley and Sons Inc July 1, **2023**, p 2300067. https://doi.org/10.1002/ardp.202300067.

(126) Bakhite, E. A.; Abd-Ella, A. A.; El-Sayed, M. E. A.; Abdel-Raheem, S. A. A. Pyridine Derivatives as Insecticides. Part 2: Synthesis of Some Piperidinium and Morpholinium Cyanopyridinethiolates and Their Insecticidal Activity. *Journal of Saudi Chemical Society* **2017**, *21* (1), 95–104. https://doi.org/10.1016/j.jscs.2016.02.005.

(127) Ismail, M. M. F.; Farrag, A. M.; Harras, M. F.; Ibrahim, M. H.; Mehany, A. B. M. Apoptosis: A Target for Anticancer Therapy with Novel Cyanopyridines. *Bioorg Chem* **2020**, *94*, 103481. https://doi.org/10.1016/j.bioorg.2019.103481.

(128) Kukushkin, V. Y.; Pombeiro, A. J. L. Metal-Mediated and Metal-Catalyzed Hydrolysis of Nitriles. *Inorganica Chimica Acta*. Elsevier S.A. January 1, **2005**, pp 1–21. https://doi.org/10.1016/j.ica.2004.04.029.

(129) Kilpatrick, M. L. A Mechanism for the Hydrolysis of Cyanamide in Acid Solution. *J Am Chem Soc* **1947**, *69* (1), 40–46. https://doi.org/10.1021/ja01193a010.

(130) Kosower, E. M.; Patton, J. W. The Products and Kinetics of Hydrolysis of Cyanopyridinium Ions. *Tetrahedron* **1966**, *22* (7), 2081–2093. https://doi.org/10.1016/S0040-4020(01)82128-1.

(131) Rajput, A.; Mukherjee, R. Coordination Chemistry with Pyridine/Pyrazine Amide Ligands. Some Noteworthy Results. *Coordination Chemistry Reviews*. Elsevier January 5, **2013**, pp 350–368. https://doi.org/10.1016/j.ccr.2012.03.024.

(132) Lumb, I.; Sran, B. S.; Sood, H.; Arora, D. S.; Hundal, G. Coordination Chemistry of Cu(II), Co(II), Zn(II) and Ag(I) Complexes of Isomeric Pyridine 2- and 4-Carboxamides and Their Biological Activity Evaluation. *Polyhedron* **2017**, *127*, 153–166. https://doi.org/10.1016/j.poly.2017.01.063.

(133) Muthu, S.; Yip, J. H. K.; Vittal, J. J. Coordination Networks of Ag(I) and N,N′ - Bis(3-Pyridinecarboxainide)-1,6-Hexane: Structures and Anion Exchange. *Journal of the Chemical Society. Dalton Transactions* **2002**, No. 24, 4561–4568. https://doi.org/10.1039/B206680G.

(134) Wang, L.; Zhang, P.; Chen, K.; Dong, J.; Luo, F.; Huang, Q.; Sun, Z.; Zou, X.; Zhu, G. Synthetic Subnanochannels in Porous Aromatic Frameworks Accelerate Selective Water Permeation in Membrane Desalination. *Sci China Mater* **2022**, *65* (7), 1920–1928. https://doi.org/10.1007/s40843-021-1993-7.

(135) Zhao, X.; Deng, C.; Meng, D.; Ji, H.; Chen, C.; Song, W.; Zhao, J. Nickel-Coordinated Carbon Nitride as a Metallaphotoredox Platform for the Cross-Coupling of Aryl Halides with Alcohols. *ACS Catal* **2020**, *10* (24), 15178–15185. https://doi.org/10.1021/acscatal.0c04725.

(136) Gerig, J. T.; Reinheimer, J. D. NMR Studies of Substituted Pyridines. *Organic Magnetic Resonance* **1969**, *1* (3), 239–247. https://doi.org/10.1002/mrc.1270010309.

(137) Karmakar, A.; Kumar, A.; Chaudhari, A. K.; Samanta, P.; Desai, A. V.; Krishna, R.; Ghosh, S. K. Bimodal Functionality in a Porous Covalent Triazine Framework by Rational Integration of an Electron-Rich and -Deficient Pore Surface. *Chemistry - A European Journal* **2016**, *22* (14), 4931–4937. https://doi.org/10.1002/chem.201600109.

(138) Gerig, J. T.; Reinheimer, J. D. NMR Studies of Substituted Pyridines. *Organic Magnetic Resonance* **1969**, *1* (3), 239–247. https://doi.org/10.1002/mrc.1270010309.

(139) Han, W.; Jin, F.; Zhao, Q.; Du, H.; Yao, L. Acid-Free Silver-Catalyzed Cross-Dehydrogenative Carbamoylation of Pyridines with Formamides. *Synlett* **2016**, *27* (12), 1854–1859. https://doi.org/10.1055/s-0035-1561975.

(140) Park, H. J.; Oh, J.; Kim, J.; Kim, J. Two-Step Gas Adsorption Induced by the Transmetallation in a Two-Dimensional Metal-Organic Framework. *Chemical Communications* **2020**, *56* (67), 9727–9730. https://doi.org/10.1039/d0cc03007d.

(141) Ohishi, T.; Nishiura, M.; Hou, Z. Carboxylation of Organoboronic Esters Catalyzed by N-Heterocyclic Carbene Copper(I) Complexes. *Angewandte Chemie International Edition* **2008**, *47* (31), 5792–5795. https://doi.org/10.1002/anie.200801857.

(142) Tolstorozhev, G. B.; Belkov, M. V.; Skornyakov, I. V.; Bazyl, O. K.; Artyukhov, V. Y.; Mayer, G. V.; Shadyro, O. I.; Kuzovkov, P. V.; Brinkevich, S. D.; Samovich, S. N. Infrared Spectroscopy of Hydrogen Bonds in Benzoic Acid Derivatives. *J Appl Spectrosc* **2014**, *81* (1), 109–117. https://doi.org/10.1007/s10812-014-9895-8.

(143) Manohara, H. M.; Trupthi Devaiah, C.; Hemavathi, B.; Ahipa, T. N. Synthesis, Optical and Electrochemical Properties of New Cyanopyridine Derivatives. *J Lumin* **2019**, *206*, 284–291. https://doi.org/10.1016/j.jlumin.2018.10.070.

(144) Andresen, T. L.; Krebs, F. C.; Thorup, N.; Bechgaard, K. Crystal Structures of 2,3,6,7,10,11-Oxytriphenylenes. Implications for Columnar Discotic Mesophases. *Chemistry of Materials* **2000**, *12* (8), 2428–2433. https://doi.org/10.1021/cm0003020.

(145) Chaudhari, A. K.; Nagarkar, S. S.; Joarder, B.; Ghosh, S. K. A Continuous π-Stacked Starfish Array of Two-Dimensional Luminescent MOF for Detection of Nitro Explosives. *Cryst Growth Des* **2013**, *13* (8), 3716–3721. https://doi.org/10.1021/cg400749m.

(146) Dey, A.; Desiraju, G. R. Correlation between Molecular Dipole Moment and Centrosymmetry in Some Crystalline Diphenyl Ethers. *Chemical Communications* **2005**, No. 19, 2486–2488. https://doi.org/10.1039/b502516h.

(147) Handy, J. V.; Ayala, G.; Pike, R. D. Structural Comparison of Copper(II) Thiocyanate Pyridine Complexes. *Inorganica Chim Acta* **2017**, *456*, 64–75. https://doi.org/10.1016/j.ica.2016.11.013.

(148) Karmakar, A.; Kumar, A.; Chaudhari, A. K.; Samanta, P.; Desai, A. V.; Krishna, R.; Ghosh, S. K. Bimodal Functionality in a Porous Covalent Triazine Framework by Rational Integration of an Electron-Rich and -Deficient Pore Surface. *Chemistry - A European Journal* **2016**, *22* (14), 4931–4937. https://doi.org/10.1002/chem.201600109.

(149) Yuan, H.; Xu, J.; Van Dam, E. P.; Giubertoni, G.; Rezus, Y. L. A.; Hammink, R.; Bakker, H. J.; Zhan, Y.; Rowan, A. E.; Xing, C.; Kouwer, P. H. J. Strategies to Increase the Thermal Stability of Truly Biomimetic Hydrogels: Combining Hydrophobicity and Directed Hydrogen Bonding. *Macromolecules* **2017**, *50* (22), 9058–9065. https://doi.org/10.1021/acs.macromol.7b01832.

(150) Lakowicz, J. R.; Weber, G. Quenching of Fluorescence by Oxygen. a Probe for Structural Fluctuations in Macromolecules. *Biochemistry* **1973**, *12* (21), 4161–4170. https://doi.org/10.1021/bi00745a020.

(151) Hawes, C. S. Coordination Sphere Hydrogen Bonding as a Structural Element in Metal-Organic Frameworks. *Dalton Transactions*. Royal Society of Chemistry May 14, **2021**, pp 6034–6049. https://doi.org/10.1039/d1dt00675d.

(152) Li, J. Y.; Xie, M. J.; Jiang, J.; Chang, Q. W.; Ye, Q. S.; Liu, W. P.; Chen, J. L.; Ning, P. Synthesis and Crystal Structure of Two Polydimensional Molecular Architectures from Cobalt(II), Copper(II) Complexes of 2,4-Diamino-6-Pyridyl-1, 3,5-Triazine. *Asian Journal of Chemistry* **2014**, *26* (2), 419–422. https://doi.org/10.14233/ajchem.2014.15424.

(153) Li, J. Y.; Xie, M. J.; Jiang, J.; Chang, Q. W.; Ye, Q. S.; Liu, W. P.; Chen, J. L.; Ning, P. Synthesis and Crystal Structure of Two Polydimensional Molecular Architectures from Cobalt(II), Copper(II) Complexes of 2,4-Diamino-6-Pyridyl-1, 3,5-Triazine. *Asian Journal of Chemistry* **2014**, *26* (2), 419–422. https://doi.org/10.14233/ajchem.2014.15424.

(154) Rajak, S.; Chair, K.; Karan Rana, L.; Kaur, P.; Maris, T.; Duong, A. Amidine/Amidinate Cobalt Complexes: One-Pot Synthesis, Mechanism, and Photocatalytic Application for Hydrogen Production. **2020**, *16*, 11. https://doi.org/10.1021/acs.inorgchem.0c01495.

(155) Sonet, D.; Bibal, B. Triphenylene: A Versatile Molecular Receptor. *Tetrahedron Lett* **2019**, *60* (12), 872–884. https://doi.org/10.1016/j.tetlet.2019.02.033.

(156) Kumar, S. Recent Developments in the Chemistry of Triphenylene-Based Discotic Liquid Crystals. *Liq Cryst* **2004**, *31* (8), 1037–1059. https://doi.org/10.1080/02678290410001724746.

(157) Thiessen, A.; Wettach, H.; Meerholz, K.; Neese, F.; Höger, S.; Hertel, D. Control of Electronic Properties of Triphenylene by Substitution. *Org Electron* **2012**, *13* (1), 71–83. https://doi.org/10.1016/j.orgel.2011.10.005.

(158) Ibáñez, S.; Peris, E. A Rigid Trigonal-Prismatic Hexagold Metallocage That Behaves as a Coronene Trap. *Angewandte Chemie* **2019**, *131* (20), 6765–6769. https://doi.org/10.1002/ange.201902568.

(159) Cong, G.; Wang, W.; Lai, N. C.; Liang, Z.; Lu, Y. C. A High-Rate and Long-Life Organic–Oxygen Battery. *Nat Mater* **2019**, *18* (4), 390–396. https://doi.org/10.1038/s41563-019-0286-7.

(160) Togashi, K.; Nomura, S.; Yokoyama, N.; Yasuda, T.; Adachi, C. Low Driving Voltage Characteristics of Triphenylene Derivatives as Electron Transport Materials in Organic Light-Emitting Diodes. *J Mater Chem* **2012**, *22* (38), 20689–20695. https://doi.org/10.1039/c2jm33669c.

(161) Kim, Y. T.; Lee, S.; Park, S.; Lee, C. Y. Graphene Chemiresistors Modified with Functionalized Triphenylene for Highly Sensitive and Selective Detection of Dimethyl Methylphosphonate. *RSC Adv* **2019**, *9* (58), 33976–33980. https://doi.org/10.1039/c9ra07186e.

(162) Wang, H.; Xu, X.; Kojtari, A.; Ji, H. F. Triphenylene Nano/Microwires for Sensing Nitroaromatics. *Journal of Physical Chemistry C* **2011**, *115* (41), 20091–20096. https://doi.org/10.1021/jp204786f.

(163) Chuang, M. Y.; Lin, Y. T.; Tung, T. W.; Chang, L. Y.; Zan, H. W.; Meng, H. F.; Lu, C. J.; Tao, Y. T. Room-Temperature-Operated Organic-Based Acetone Gas Sensor for Breath Analysis. *Sens Actuators B Chem* **2018**, *260*, 593–600. https://doi.org/10.1016/j.snb.2017.12.168.

(164) CHEN, J.-R.; CAI, J.; XU, B.-Y.; LI, Q.; ZHAO, K.-Q. DFT Study on the Effect of Different Peripheral Chains on Charge Transport Properties of Triphenylene Derivatives. *Chin J Chem* **2008**, *26* (12), 2292–2296. https://doi.org/10.1002/cjoc.200890406.

(165) Hoang, M. H.; Cho, M. J.; Kim, K. H.; Cho, M. Y.; Joo, J. soo; Choi, D. H. New Semiconducting Multi-Branched Conjugated Molecules Based on π-Extended Triphenylene and Its Application to Organic Field-Effect Transistor. *Thin Solid Films* **2009**, *518* (2), 501–506. https://doi.org/10.1016/j.tsf.2009.07.030.

(166) Chen, W.; Zhang, H.; Zheng, H.; Li, H.; Guo, F.; Ni, G.; Ma, M.; Shi, C.; Ghadari, R.; Hu, L. Two-Dimensional Triphenylene Cored Hole-Transporting Materials for Efficient Perovskite Solar Cells. *Chemical Communications* **2020**, *56* (12), 1879–1882. https://doi.org/10.1039/c9cc08248d.

(167) Contreras-Pereda, N.; Pané, S.; Puigmartí-Luis, J.; Ruiz-Molina, D. Conductive Properties of Triphenylene MOFs and COFs. *Coordination Chemistry Reviews*. Elsevier B.V. June 1, **2022**, p 214459. https://doi.org/10.1016/j.ccr.2022.214459.

(168) Mahringer, A.; Jakowetz, A. C.; Rotter, J. M.; Bohn, B. J.; Stolarczyk, J. K.; Feldmann, J.; Bein, T.; Medina, D. D. Oriented Thin Films of Electroactive Triphenylene Catecholate-Based Two-Dimensional MetalOrganic Frameworks. *ACS Nano* **2019**, *13* (6), 6711–6719. https://doi.org/10.1021/acsnano.9b01137.

(169) Gowda, A.; Jacob, L.; Singh, D. P.; Douali, R.; Kumar, S. Charge Transport in Novel Phenazine Fused Triphenylene Supramolecular Systems. *ChemistrySelect* **2018**, *3* (23), 6551–6560. https://doi.org/10.1002/slct.201801412.

(170) Oukachmih, M.; Destruel, P.; Seguy, I.; Ablart, G.; Jolinat, P.; Archambeau, S.; Mabiala, M.; Fouet, S.; Bock, H. New Organic Discotic Materials for Photovoltaic Conversion. *Solar Energy Materials and Solar Cells* **2005**, *85* (4), 535–543. https://doi.org/10.1016/j.solmat.2004.05.012.

(171) Guo, H.; Zhu, M.; Wang, Z.; Yang, F. Triphenylene–Perylene–Triphenylene Triads with Bay-Substituents: Synthesis, Mesomorphism, and Electron Transfer Properties. *Tetrahedron Lett* **2016**, *57* (37), 4191–4195. https://doi.org/10.1016/j.tetlet.2016.08.004.

(172) Hoang, M. H.; Nguyen, D. N.; Ngo, T. T.; Cho, M. J.; Lee, S. J.; Choi, D. H. New π-Extended Triphenylene-Based Organic Semiconductors in Field-Effect Transistors. *Synth Met* **2015**, *209*, 434–440. https://doi.org/10.1016/j.synthmet.2015.08.022.

(173) Hoang, M. H.; Nguyen, D. N.; Choi, D. H. Extended Conjugated Semiconducting Molecules Based on Triphenylene. *Advances in Natural Sciences: Nanoscience and Nanotechnology* **2011**, *2* (3), 035002. https://doi.org/10.1088/2043-6262/2/3/035002.

(174) Demir, A.; Atahan, A.; Bağcı, S.; Aslan, M.; Saif Islam, M. Organic/Inorganic Interfaced Field-Effect Transistor Properties with a Novel Organic Semiconducting Material. *Philosophical Magazine* **2016**, *96* (3), 274–285. https://doi.org/10.1080/14786435.2015.1130277.

(175) Sonet, D.; Bibal, B. Triphenylene: A Versatile Molecular Receptor. *Tetrahedron Lett* **2019**, *60* (12), 872–884. https://doi.org/10.1016/j.tetlet.2019.02.033.

(176) Van De Craats, A. M.; Siebbeles, L. D. A.; Bleyl, I.; Haarer, D.; Berlin, Y. A.; Zharikov, A. A.; Warman, J. M. Mechanism of Charge Transport along Columnar Stacks of a Triphenylene Dimer. *Journal of Physical Chemistry B* **1998**, *102* (48), 9625–9634. https://doi.org/10.1021/jp9828989.

(177) Cinacchi, G.; Colle, R.; Tani, A. Atomistic Molecular Dynamics Simulation of Hexakis(Pentyloxy)Triphenylene: Structure and Translational Dynamics of Its Columnar State. *Journal of Physical Chemistry B* **2004**, *108* (23), 7969–7977. https://doi.org/10.1021/jp049654a.

(178) Kumar, S.; Pal, S. K.; Kumar, P. S.; Lakshminarayanan, V. Novel Conducting Nanocomposites: Synthesis of Triphenylene-Covered Gold Nanoparticles and Their Insertion into a Columnar Matrix. *Soft Matter* **2007**, *3* (7), 896–900. https://doi.org/10.1039/b701380a.

(179) Gupta, M.; Pal, S. K. Triphenylene-Based Room-Temperature Discotic Liquid Crystals: A New Class of Blue-Light-Emitting Materials with Long-Range Columnar Self-Assembly. *Langmuir* **2016**, *32* (4), 1120–1126. https://doi.org/10.1021/acs.langmuir.5b03353.

(180) Cinacchi, G.; Prampolini, G. Estimate of Benzene-Triphenylene and Triphenylene-Triphenylene Interactions: A Topic Relevant to Columnar Discotic Liquid Crystals. *Journal of Physical Chemistry C* **2008**, *112* (25), 9501–9509. https://doi.org/10.1021/jp0776917.

(181) Heine, M.; Fink, L.; Schmidt, M. U. 3-Cyanopyridine as a Bridging and Terminal Ligand in Coordination Polymers. *CrystEngComm* **2018**, *20* (46), 7556–7566. https://doi.org/10.1039/c8ce01568f.

(182) Sakai, K.; Ito, T.; Watanabe, K. Studies of Organic Catalytic Reactions. V. The Function of the Chelates Formed in the Hydrolysis of 2-Cyanopyridine with Metal Oxide Catalysts. *Bull Chem Soc Jpn* **1967**, *40* (7), 1660–1665. https://doi.org/10.1246/bcsj.40.1660.

(183) Kumar, D.; Chouhan, A.; Jeanneau, E.; Mishra, S.; Pandey, A. Syntheses and Characterizations of Calcium and Strontium Based Coordination Compounds with the 5-(2-Pyridyl)Tetrazolate Ligand, Respectively Exhibiting Extended 1 D and 2 D Structures. *J Mol Struct* **2022**, *1260*, 132757. https://doi.org/10.1016/j.molstruc.2022.132757.

(184) Das, A.; Sharma, P.; Frontera, A.; Verma, A. K.; Barcelo-Oliver, M.; Hussain, S.; Bhattacharyya, M. K. Energetically Significant Nitrile⋯nitrile and Unconventional C–H⋯π(Nitrile) Interactions in Pyridine Based Ni(II) and Zn(II) Coordination Compounds: Antiproliferative Evaluation and Theoretical Studies. *J Mol Struct* **2021**, *1223*, 129246. https://doi.org/10.1016/j.molstruc.2020.129246.

(185) Krebs, C.; Thiele, S.; Ceglarska, M.; Näther, C. Synthesis, Crystal Structures and Properties of Ni(NCS) $_2$ -3-Cyanopyridine Coordination Compounds Including a Ferromagnetic Layered Compound. *Z Anorg Allg Chem* **2021**, *647* (22), 2122–2129. https://doi.org/10.1002/zaac.202100204.

(186) Pisačić, M.; Kodrin, I.; Trninić, A.; Daković, M. Two-Dimensional Anisotropic Flexibility of Mechanically Responsive Crystalline Cadmium(II) Coordination Polymers. *Chemistry of Materials* **2022**, *34* (5), 2439–2448. https://doi.org/10.1021/acs.chemmater.2c00062.

(187) Krebs, F. C.; Schiodt, N. C.; Batsberg, W.; Bechgaard, K. Purification of 2,3,6,7,10,11-Hexamethoxytriphenylene and Preparation of Hexakiscarbonylmethyl and Hexakiscyanomethyl Derivatives of 2,3,6,7,10,11-Hexahydroxytriphenylene. *Synthesis (Stuttg)* **1997**, *1997* (11), 1285–1290. https://doi.org/10.1055/s-1997-3188.

(188) Wei, J.; Han, B.; Guo, Q.; Shi, X.; Wang, W.; Wei, N. 1,5,9-Triazacoronenes: A Family of Polycyclic Heteroarenes Synthesized by a Threefold Pictet-Spengler Reaction. *Angewandte Chemie - International Edition* **2010**, *49* (44), 8209–8213. https://doi.org/10.1002/anie.201002369.

(189) Chou, C. E.; Wang, D.; Bagui, M.; Hsu, J.; Chakraborty, S.; Peng, Z. Syntheses and Optical Properties of Triphenylene-Containing Conjugated Polymers. *J Lumin* **2010**, *130* (6), 986–994. https://doi.org/10.1016/j.jlumin.2010.01.010.

(190) Ikeda, M.; Takeuchi, M.; Shinkai, S. Unusual Emission Properties of a Triphenylene-Based Organogel System. *Chemical Communications* **2003**, *3* (12), 1354–1355. https://doi.org/10.1039/b302415f.

(191) Psutka, K. M.; Ledrew, J.; Taing, H.; Eichhorn, S. H.; Maly, K. E. Synthesis and Self-Assembly of Liquid Crystalline Triphenylenedicarboxythioimides. *Journal of Organic Chemistry* **2019**, *84* (17), 10796–10804. https://doi.org/10.1021/acs.joc.9b01330.

(192) Wu, D.; Zhang, H.; Liang, J.; Ge, H.; Chi, C.; Wu, J.; Liu, S. H.; Yin, J. Functionalized Coronenes: Synthesis, Solid Structure, and Properties. *Journal of Organic Chemistry* **2012**, *77* (24), 11319–11324. https://doi.org/10.1021/jo302093t.

(193) Eriksson, J.; Eriksson, L.; Jakobsson, E. Decabromodiphenyl Ether. *Acta Crystallogr C* **1999**, *55* (12), 2169–2171. https://doi.org/10.1107/S0108270199008884.

(194) Desiraju, G. R.; Steiner, T. *The Weak Hydrogen Bond: In Structural Chemistry and Biology*; International Union of Crystal, **2001**; Vol. 9.

(195) Andresen, T. L.; Krebs, F. C.; Thorup, N.; Bechgaard, K. Crystal Structures of 2,3,6,7,10,11-Oxytriphenylenes. Implications for Columnar Discotic Mesophases. *Chemistry of Materials* **2000**, *12* (8), 2428–2433. https://doi.org/10.1021/cm0003020.

(196) Osawa, T.; Kajitani, T.; Hashizume, D.; Ohsumi, H.; Sasaki, S.; Takata, M.; Koizumi, Y.; Saeki, A.; Seki, S.; Fukushima, T.; Aida, T. Wide-Range 2D Lattice Correlation Unveiled for Columnarly Assembled Triphenylene Hexacarboxylic Esters. *Angewandte Chemie International Edition* **2012**, *51* (32), 7990–7993. https://doi.org/10.1002/anie.201203077.

(197) Desiraju, G.; Steiner, T. *The Weak Hydrogen Bond*; Oxford University Press, **2010**. https://doi.org/10.1093/acprof:oso/9780198509707.001.0001.

(198) Srinivasa Rao, B.; Srivani, A.; Dhana Lakshmi, D.; Lingaiah, N. Selective Hydration of Nitriles to Amides Over Titania Supported Palladium Exchanged Vanadium Incorporated Molybdophosphoric Acid Catalysts. *Catal Letters* **2016**, *146* (10), 2025–2031. https://doi.org/10.1007/s10562-016-1816-4.

(199) Rajak, S.; Schott, O.; Kaur, P.; Maris, T.; Hanan, G. S.; Duong, A. Synthesis, Crystal Structure, Characterization of Pyrazine Diaminotriazine Based Complexes and Their Systematic Comparative Study with Pyridyl Diaminotriazine Based Complexes for Light-Driven Hydrogen Production. *Polyhedron* **2020**, *180*, 114412. https://doi.org/10.1016/j.poly.2020.114412.

(200) Liu, L.; Zhang, C.; Zhang, L. X.; Li, Q.; Yin, Y. Y.; Wang, H. Y.; Sun, R. H.; Li, J. Y.; Hou, X. Y.; Dong, H.; Bie, L. J. A 2D Coordination Polymer of [Cd(TMA)(4-CNPy)(H2O)]n (H2TMA = 3-Thiophenemalonic Acid, 4-CNPy = 4-Cyanopyridine) with Impedimetric Humidity Sensing Performance. *Inorg Chem Commun* **2020**, *111*, 107636. https://doi.org/10.1016/j.inoche.2019.107636.

(201) Gross, M.; Müller, D. C.; Nothofer, H. G.; Scherf, U.; Neher, D.; Bräuchle, C.; Meerholz, K. Improving the Performance of Doped π-Conjugated Polymers for Use in Organic Light-Emitting Diodes. *Nature* **2000**, *405* (6787), 661–665. https://doi.org/10.1038/35015037.

(202) Yang, J.; Zhao, Z.; Wang, S.; Guo, Y.; Liu, Y. Insight into High-Performance Conjugated Polymers for Organic Field-Effect Transistors. *Chem*. Elsevier Inc December 13, **2018**, pp 2748–2785. https://doi.org/10.1016/j.chempr.2018.08.005.

ggg

(203) Moliton, A.; Hiorns, R. C. Review of Electronic and Optical Properties of Semiconducting π-Conjugated Polymers: Applications in Optoelectronics. *Polym Int* **2004**, *53* (10), 1397–1412. https://doi.org/10.1002/pi.1587.

(204) Meier, H.; Stalmach, U.; Kolshorn, H. Effective Conjugation Length and UV/Vis Spectra of Oligomers. *Acta Polymerica* **1997**, *48* (9), 379–384. https://doi.org/10.1002/actp.1997.010480905.

(205) Chen, J.; Peng, H.; Law, C. C. W.; Dong, Y.; Lam, J. W. Y.; Williams, I. D.; Tang, B. Z. Hyperbranched Poly(Phenylenesilolene)s: Synthesis, Thermal Stability, Electronic Conjugation, Optical Power Limiting, and Cooling-Enhanced Light Emission. *Macromolecules* **2003**, *36* (12), 4319–4327. https://doi.org/10.1021/ma034012r.

(206) Wei, J.; Han, B.; Guo, Q.; Shi, X.; Wang, W.; Wei, N. Erratum: 1,5,9-Triazacoronenes: A Family of Polycyclic Heteroarenes Synthesized by a Threefold Pictet-Spengler Reaction (Angewandte Chemie - International Edition (2010) 49 (8209-8213) DOI: 10.1002/Anie.201002369). *Angewandte Chemie - International Edition*. John Wiley & Sons, Ltd December 17, **2010**, p 9803. https://doi.org/10.1002/anie.201090161.

(207) Sun, Y. X.; Wang, X. G.; Shen, G. D.; Yang, T.; Yang, Y. H.; Li, J.; Yang, M. Y.; Sun, H. M.; Wei, J. F. A 6π Azaelectrocyclization Strategy towards the 1,5,9-Triazacoronenes. *Adv Synth Catal* **2020**, *362* (8), 1651–1656. https://doi.org/10.1002/adsc.201901433.

(208) Żyła-Karwowska, M.; Zhylitskaya, H.; Cybińska, J.; Lis, T.; Chmielewski, P. J.; Stępień, M. An Electron-Deficient Azacoronene Obtained by Radial π Extension. *Angewandte Chemie* **2016**, *128* (47), 14878–14882. https://doi.org/10.1002/ange.201608400.

(209) Yin, J. C.; Lian, X.; Li, Z. G.; Cheng, M.; Liu, M.; Xu, J.; Li, W.; Xu, Y.; Li, N.; Bu, X. H. Triazacoronene-Based 2D Conductive Metal–Organic Framework for High-Capacity Lithium Storage. *Adv Funct Mater* **2024**. https://doi.org/10.1002/adfm.202403656.

(210) Moliton, A.; Hiorns, R. C. Review of Electronic and Optical Properties of Semiconducting π-Conjugated Polymers: Applications in Optoelectronics. *Polym Int* **2004**, *53* (10), 1397–1412. https://doi.org/10.1002/pi.1587.

(211) McKinstry, C.; Cathcart, R. J.; Cussen, E. J.; Fletcher, A. J.; Patwardhan, S. V.; Sefcik, J. Scalable Continuous Solvothermal Synthesis of Metal Organic Framework (MOF-5) Crystals. *Chemical Engineering Journal* **2016**, *285*, 718–725. https://doi.org/10.1016/j.cej.2015.10.023.

(212) Rajak, S.; Mohan, M.; Tremblay, A. A.; Maris, T.; Leal Do Santos, S.; Venancio, E. C.; Ferreira Santos, S.; Duong, A. Programmed Molecular Construction: Driving the Self-Assembly by Coordination and Hydrogen Bonds Using 6-(Pyridin-2-Yl)-1,3,5-Triazine-2,4-Diamine with M(NO3)2 Salts. *ACS Omega* **2019**, *4* (2), 2708–2718. https://doi.org/10.1021/acsomega.8b03517.

(213) Rajak, S.; Schott, O.; Kaur, P.; Maris, T.; Hanan, G. S.; Duong, A. Synthesis, Crystal Structure, Characterization of Pyrazine Diaminotriazine Based Complexes and Their Systematic Comparative Study with Pyridyl Diaminotriazine Based Complexes for Light-Driven Hydrogen Production. *Polyhedron* **2020**, *180*, 114412. https://doi.org/10.1016/j.poly.2020.114412.

(214) Sun, Y.; Wang, X.; Shen, G.; Yang, T.; Yang, Y.; Li, J.; Yang, M.; Sun, H.; Wei, J. A 6π Azaelectrocyclization Strategy towards the 1,5,9-Triazacoronenes. *Adv Synth Catal* **2020**, *362* (8), 1651–1656. https://doi.org/10.1002/adsc.201901433.